

# Thermopower in Two-Dimensional Electron Systems

Thesis by

William Elbridge Chickering

In Partial Fulfillment of the Requirements

for the Degree of

Doctor of Philosophy

California Institute of Technology

Pasadena, California

2016

(Defended December 10, 2015)

© 2016

William Elbridge Chickering

All Rights Reserved

# Acknowledgements

This thesis and the several years of research that preceded it could not have been completed without the love and support of my colleagues, friends, and family. First and foremost, I want to thank my incredibly patient wife, Theresa, who was always there for me, vicariously enduring the highs and lows of my extended academic journey.

I was fortunate to share my time at Caltech with many brilliant labmates. I am particularly indebted to Ghislain Granger who tutored me in the art of low temperature physics and device fabrication. Many thanks also go to Erik Henriksen and Johannes Pollanen who animated our underground laboratory with their good humor and endless curiosity. And to Debaleena Nandi and Trupti Khaire for our many conversations about life and the world above ground.

Finally, I must express profound gratitude to my advisor, Professor Jim Eisenstein. His passion, integrity, and generosity was not only instrumental for the work described in this thesis, but also provided me a model to aspire to both professionally and personally.

# Abstract

The subject of this thesis is the measurement and interpretation of thermopower in high-mobility two-dimensional electron systems (2DESs). These 2DESs are realized within state-of-the-art GaAs/AlGaAs heterostructures that are cooled to temperatures as low as  $T = 20$  mK. Much of this work takes place within strong magnetic fields where the single-particle density of states quantizes into discrete Landau levels (LLs), a regime best known for the quantum Hall effect (QHE). In addition, we review a novel hot-electron technique for measuring thermopower of 2DESs that dramatically reduces the influence of phonon drag.

Early chapters concentrate on experimental materials and methods. A brief overview of GaAs/AlGaAs heterostructures and device fabrication is followed by details of our cryogenic setup. Next, we provide a primer on thermopower that focuses on 2DESs at low temperatures. We then review our experimental devices, temperature calibration methods, as well as measurement circuits and protocols.

Latter chapters focus on the physics and thermopower results in the QHE regime. After reviewing the basic phenomena associated with the QHE, we discuss thermopower in this regime. Emphasis is given to the relationship between diffusion thermopower and entropy. Experimental results demonstrate this relationship persists well into the fractional quantum Hall (FQH) regime.

Several experimental results are reviewed. Unprecedented observations of the diffusion thermopower of a high-mobility 2DES at temperatures as high as  $T = 2$  K are achieved using our hot-electron technique. The composite fermion (CF) effective mass is extracted from measurements of thermopower at LL filling factor  $\nu = 3/2$ . The thermopower versus magnetic field in the FQH regime is shown to be qualitatively

consistent with a simple entropic model of CFs. The thermopower at  $\nu = 5/2$  is shown to be quantitatively consistent with the presence of non-Abelian anyons. An abrupt collapse of thermopower is observed at the onset of the reentrant integer quantum Hall effect (RIQHE). And the thermopower at temperatures just above the RIQHE transition suggests the existence of an unconventional conducting phase.

# Contents

<b>Acknowledgements</b>	<b>iii</b>
<b>Abstract</b>	<b>iv</b>
<b>Introduction and Summary</b>	<b>1</b>
<b>1 Two-Dimensional Electron System</b>	<b>7</b>
1.1 GaAs/AlGaAs Heterostructures . . . . .	9
1.2 Device Fabrication . . . . .	15
1.2.1 Hot-Electron Thermocouple . . . . .	19
1.2.2 2DES Diving Boards . . . . .	20
1.3 Summary . . . . .	22
<b>2 Cryogenic Environment</b>	<b>24</b>
2.1 Energy/Temperature Scales . . . . .	24
2.2 Dilution Refrigerators . . . . .	26
2.3 Cold Finger . . . . .	28
2.4 Connecting and Cooling the 2DES . . . . .	30
2.5 Sample Illumination . . . . .	32
2.6 “High” Temperature Regulation . . . . .	33
2.7 Summary . . . . .	33
<b>3 Thermopower of 2D Electrons</b>	<b>35</b>
3.1 The Seebeck Effect . . . . .	35
3.2 Classical Transport: Drude Model . . . . .	38

3.3	Mott's Formula . . . . .	39
3.4	Thermopower vs Entropy . . . . .	42
3.5	Phonon Drag Thermopower . . . . .	44
3.6	Summary . . . . .	48
<b>4</b>	<b>Diving Board Technique</b>	<b>49</b>
4.1	Diving Board A . . . . .	50
4.1.1	Temperature Calibration . . . . .	51
4.1.2	Measurement Protocol . . . . .	56
4.1.3	Experimental Results at Zero Field . . . . .	59
4.1.4	Long Thermal Relaxation Times . . . . .	63
4.2	Diving Board B . . . . .	65
4.2.1	Short Thermal Relaxation Times . . . . .	67
4.2.2	Temperature Calibration . . . . .	68
4.2.3	Measurement Protocol . . . . .	70
4.3	Summary . . . . .	71
<b>5</b>	<b>Hot-Electron Thermocouple</b>	<b>73</b>
5.1	Device Layout . . . . .	74
5.2	Temperature Calibration . . . . .	77
5.3	Measurement Protocol . . . . .	81
5.4	Experimental Results . . . . .	82
5.5	Future Work: Metal-Insulator Transition . . . . .	88
5.6	Summary . . . . .	92
<b>6</b>	<b>Quantum Hall Effect</b>	<b>94</b>
6.1	Classical Hall Effect . . . . .	95
6.2	Landau Level Quantization . . . . .	98
6.3	Electron Spin . . . . .	102
6.4	Filling Factor . . . . .	103
6.5	Disorder Broadening . . . . .	104

6.6	Compressibility . . . . .	106
6.7	Edge States . . . . .	108
6.8	Quantum Magnetotransport . . . . .	110
6.9	Quantum Lifetime . . . . .	115
6.10	Summary . . . . .	116
<b>7</b>	<b>Thermopower in the Quantum Hall Regime</b>	<b>119</b>
7.1	Classical 2DES in a Magnetic Field . . . . .	120
7.2	Thermoelectric Currents . . . . .	123
7.3	Thermopower with LL Quantization . . . . .	125
7.4	Entropic Model . . . . .	129
7.5	Disorder and the Generalized Mott Formula . . . . .	132
7.6	Computing $S_{xx}^d$ and $S_{xy}^d$ . . . . .	133
7.7	Phonon Drag in the QH Regime . . . . .	136
7.8	Experimental Results at Low Fields . . . . .	138
7.9	Summary . . . . .	144
<b>8</b>	<b>Fractional Quantum Hall Regime</b>	<b>146</b>
8.1	Fractional Quantum Hall Effect . . . . .	147
8.1.1	Laughlin States . . . . .	148
8.1.2	Composite Fermions . . . . .	149
8.1.3	Wigner Crystal . . . . .	152
8.2	Thermopower in the FQH Regime . . . . .	153
8.2.1	CFs at $B^* = 0$ . . . . .	154
8.2.2	Entropic Model . . . . .	158
8.2.3	Disorder . . . . .	160
8.3	Experimental Results at High Fields . . . . .	162
8.3.1	$S_{xx}$ vs $T$ at $\nu = 3/2$ . . . . .	163
8.3.2	Comparison to Experiment on 2D Holes . . . . .	166
8.3.3	Comparison to Noninteracting Disordered Model . . . . .	168
8.3.4	$S_{xx}$ vs $B$ in FQH Regime . . . . .	168

8.3.5	Low-Temperature Fluctuations . . . . .	174
8.3.6	Comparison to Entropic Model . . . . .	176
8.4	Summary . . . . .	179
<b>9</b>	<b>The First Excited Landau Level</b>	<b>181</b>
9.1	FQH State at $\nu = 5/2$ . . . . .	182
9.1.1	Non-Abelian Anyons . . . . .	184
9.1.2	Thermopower of Non-Abelian Anyons . . . . .	186
9.1.3	Experimental Results . . . . .	188
9.2	Reentrant Integer Quantum Hall Effect . . . . .	192
9.2.1	$N \geq 2$ LLs . . . . .	192
9.2.2	$N = 1$ LL . . . . .	194
9.2.3	Experimental Results . . . . .	197
9.3	Summary . . . . .	200
<b>A</b>	<b>Properties of a 2DES in GaAs</b>	<b>202</b>
<b>B</b>	<b>Sample Processing</b>	<b>203</b>
B.1	Sample Cleaving . . . . .	203
B.2	Cleaning the Sample . . . . .	204
B.3	Photolithography . . . . .	204
B.4	Etching the Mesa . . . . .	206
B.5	Ohmic Contacts . . . . .	206
B.5.1	InSn Ohmic Contacts . . . . .	207
B.5.2	Ni/AuGe Ohmic Contacts . . . . .	208
B.6	Al Top Gates . . . . .	209
B.7	Thin Sample . . . . .	209
B.8	Mount Diving Board . . . . .	211
B.9	Attach Heater . . . . .	213
B.10	Wire Up . . . . .	214

<b>C</b>	<b>Narrow Band Lock-In Detection</b>	<b>216</b>
C.1	Example: Four-Point Resistance Measurement . . . . .	216
<b>D</b>	<b>Long Thermal Relaxation Times</b>	<b>218</b>
<b>E</b>	<b>Electrical Resistance as a Hot-Electron Thermometer</b>	<b>221</b>
E.1	Introduction . . . . .	221
E.2	Error in $\Delta R$ Due to Joule Heating . . . . .	222
E.3	Error in $\Delta T$ Due to Joule Heating . . . . .	223
E.4	Impact on Thermopower Measurement . . . . .	224
<b>F</b>	<b>Corbino Thermopower</b>	<b>225</b>
F.1	Corbino vs Hall Bar . . . . .	229
<b>G</b>	<b>Diffusion Thermopower of a Band Insulator</b>	<b>232</b>
	<b>Bibliography</b>	<b>236</b>

# List of Figures

1.1	Band structure of a AlGaAs-GaAs heterojunction . . . . .	10
1.2	Illustration of AlGaAs-GaAs-AlGaAs quantum well . . . . .	11
1.3	MBE grown epilayers of a quantum well heterostructure . . . . .	12
1.4	Conduction band of delta-doped GaAs/AlGaAs quantum well . . . . .	14
1.5	Simple 2DES device. . . . .	15
1.6	Lithographically patterned 2DES device. . . . .	17
1.7	2DES diving board A . . . . .	21
2.1	Functional diagram of dilution refrigerator . . . . .	27
2.2	Oxford 200 TL dilution refrigerator . . . . .	29
3.1	Illustration of Seebeck effect . . . . .	36
4.1	2DES thermopower diving board technique . . . . .	51
4.2	Temperature calibration using $R_{xx}$ vs $B$ . . . . .	53
4.3	Thermal conductance of diving board A . . . . .	55
4.4	Quasi-DC thermovoltage measurement . . . . .	57
4.5	$S/T$ vs $T$ at $B = 0$ from diving board . . . . .	59
4.6	$S$ vs $T$ at $B = 0$ from diving board A . . . . .	61
4.7	Thermal relaxation of diving board A . . . . .	64
4.8	Layout of diving board B . . . . .	66
4.9	2DES diving board B . . . . .	67
4.10	Thermal relaxation of diving board B . . . . .	68
4.11	Thermal conductance of diving board B . . . . .	69

5.1	Layout of 2D hot-electron thermocouple . . . . .	74
5.2	Hot-electron thermocouple device . . . . .	76
5.3	Temperature calibration at $B = 0$ using 2DES resistance . . . . .	78
5.4	Hot-electron thermocouple measurement circuit . . . . .	80
5.5	$\Delta S/T$ vs $T$ at $B = 0$ . . . . .	83
5.6	$\Delta S$ vs $\Delta(1/n)$ at $B = 0$ . . . . .	86
5.7	Thermopower in vicinity of metal-insulator transition . . . . .	91
6.1	Classical magnetotransport . . . . .	97
6.2	Illustration of Landau levels . . . . .	101
6.3	Disorder broadened Landau levels . . . . .	105
6.4	Extended and localized states within LLs . . . . .	108
6.5	Classical skipping orbit . . . . .	109
6.6	Illustration of QH edge states . . . . .	110
6.7	Magnetotransport measurement setup . . . . .	111
6.8	Integer quantum Hall effect . . . . .	113
6.9	Determination of quantum lifetime . . . . .	117
7.1	Thermopower of classical 2DES in magnetic field . . . . .	123
7.2	Thermoelectric current distributions in strong field . . . . .	125
7.3	$\sigma_{xy}$ and $\epsilon_{xy}$ vs $\mu$ in IQH regime . . . . .	126
7.4	$S^d$ vs $\mu$ in disorder-free IQH regime . . . . .	127
7.5	$S^d$ vs $B$ in disorder-free IQH regime . . . . .	131
7.6	$S_{xx}^d$ and $S_{xy}^d$ vs $B$ in IQH regime . . . . .	134
7.7	$S^g$ vs $B$ in IQH regime . . . . .	137
7.8	$\Delta V/\Delta T_{\text{app}}$ vs $B$ in low field regime . . . . .	140
7.9	Comparison of theory and experiment at low fields . . . . .	143
8.1	Partial hierarchy of FQH states within CF theory . . . . .	151
8.2	Disorder-free entropic thermopower of CFs in lowest LL . . . . .	159
8.3	$S_{xx}$ vs $T$ at $\nu = 3/2$ . . . . .	163

8.4	$S_{xx}$ vs $T$ at $\nu = 1/2, 3/2$ , and $B = 0$ in 2D hole system . . . . .	167
8.5	$S_{xx}$ and $R_{xx}$ vs $B$ in FQH regime . . . . .	169
8.6	$S_{xx}$ vs $B$ at various $T$ in FQH regime . . . . .	172
8.7	Low-temperature thermopower fluctuations in FQH regime . . . . .	175
8.8	Comparison of theory and experiment in FQH regime . . . . .	177
9.1	$R_{xx}$ vs $B$ in $N = 1$ LL . . . . .	183
9.2	Temperature dependence of $S_{xx}$ at $\nu = 5/2$ . . . . .	189
9.3	Comparison of $T$ -dependence of FQH states in $N = 1$ LL . . . . .	190
9.4	Comparison of theory and experiment at $\nu = 5/2$ . . . . .	191
9.5	Anisotropy and RIQHE in higher ( $N \geq 2$ ) LLs . . . . .	193
9.6	RIQHE in $N = 1$ LL . . . . .	195
9.7	$R_{xy}$ and $R_{xx}$ vs $T$ in vicinity of RIQHE . . . . .	196
9.8	$S_{xx}$ vs $B$ in vicinity of RIQHE . . . . .	197
9.9	$S_{xx}$ vs $T$ in vicinity of RIQHE . . . . .	198
B.1	Custom vacuum chuck . . . . .	212
B.2	2DES diving board A prior to installation . . . . .	215
C.1	Four-point resistance measurement of 2DES hall bar . . . . .	217
D.1	$T$ - and $B$ -dependence of thermal relaxation times . . . . .	219
F.1	Corbino thermopower measurement . . . . .	226
F.2	Corbino thermopower vs energy . . . . .	228

# Introduction and Summary

The study of two-dimensional electron systems (2DESs) has yielded many of the most important discoveries in condensed matter physics of the past several decades. Chief among these is the integer quantum Hall effect (IQHE), a rare instance of a macroscopic manifestation of quantum mechanics in which the transverse conductance becomes quantized into integer multiples of universal constants [1]. The IQHE is a single-particle phenomenon that nonetheless quickly led to the discovery of several strongly correlated many-body phases of matter. The most prominent example is the *fractional* quantum Hall effect (FQHE) in which collective behavior results in the conductance quantizing to particular rational number  $p/q$  multiples of the IQHE values [2]. Adding to this list of collective phases are Wigner crystallization at high fields [3], nematic ordering in high Landau levels [4], excitonic Bose-Einstein condensates in bilayer quantum Hall systems [5], and exotic even-denominator FQHEs believed to exhibit non-Abelian exchange statistics [6].

The exploration of the rich worlds realized within 2DESs has been dominated by measurements of electrical transport. And for good reason. Compared to optical, acoustic, and thermal experiments, measurements of conductance and resistance tend to be more easily achieved. Indeed, this is evidenced by the fact that the most famous discoveries in these systems (e.g. IQHE, FQHE) are defined in terms of electrical transport coefficients. At the same time, the information contained within these coefficients is limited. This thesis presents thermopower studies of 2DESs with the goal of augmenting our picture of these systems and the collective phases found therein.

A key value of thermopower is its simple relationship to entropy under certain

conditions. At sufficiently low temperatures, the thermopower of a high-mobility electron system is directly proportional to the entropy per electron. Originally shown [7] to hold for noninteracting electrons, this unique relationship between a transport coefficient and a thermodynamic variable theoretically also holds in many circumstances for an interacting 2DES in a quantizing magnetic field [8]. Providing both explanatory and predictive power, the relationship between thermopower and entropy plays a prominent role in this thesis.

The experimental studies performed for this thesis mainly focus on the lowest and first excited Landau levels, within the fractional quantum Hall (FQH) regime. This is achieved by subjecting ultra-pure GaAs/AlGaAs semiconductor heterostructures to low temperatures (down to  $T = 20$  mK) and high magnetic fields (up to  $B = 12$  T). Within this regime, special attention is given to particular collective states. These include the composite fermion metal at filling factor  $\nu = 3/2$ , the enigmatic even-denominator FQH state at  $\nu = 5/2$ , and insulating phases associated with reentrant integer quantum Hall effects. Odd-denominator FQH states are examined more broadly. To provide context, we also consider thermopower data at lower magnetic fields where Landau level quantization is evident but Coulomb interactions can be ignored. Away from the quantum Hall regime, we also present a novel method for measuring the zero-field diffusion thermopower of a 2DES at high temperatures and low electron densities.

In addition to experimental methods and results, a significant portion of this thesis is dedicated to providing the reader with the context necessary for appreciating and understanding this work. Material is often presented in a pedagogical style that reflects the author's understanding. Given the limited scope of this thesis, many subjects are treated only superficially. Nonetheless, this unique compilation of topics can hopefully serve as a helpful guide to experimentalists interested in venturing into the realm of thermoelectric phenomena in 2D systems. This thesis is organized as follows:

**Chapter 1** introduces the *two-dimensional electron system* (2DES), a gas of electrons that is free to move in-plane but constrained from moving out-of-plane. The

idiosyncrasies of the 2DES make it both incredibly useful and in many ways ideal for studying correlated many-body phenomena. We discuss the significance of ultra-clean 2DESs as well as how they are realized within GaAs/AlGaAs semiconductor *heterostructures*. The building-block features of the 2DES devices fabricated for this thesis as well as the devices as a whole are described here.

**Chapter 2** describes the cryogenic environment in which we perform experiments on the 2DES. To motivate the discussion, we consider several temperature scales that are relevant to our research. Next, we review the working principles of *dilution refrigeration* by which temperatures lower than  $T = 20$  mK are achieved. We then survey our experimental setup, describing how our 2DES devices are electrically connected to, yet thermally isolated from, the outside world. Our illumination technique, which releases stubborn carriers in order to achieve the highest electron mobilities, is then discussed. Finally, we explain our method of “high” temperature regulation in which we operate a dilution refrigerator in an unconventional manner to maintain a particular set of experiments at higher than usual temperatures (e.g.  $0.6 \lesssim T \lesssim 6$  K).

In **Chapter 3** we explain the basic physics of thermopower in the absence of an externally applied magnetic field. We show how thermopower, also known as the *Seebeck coefficient*, can be understood in terms of more fundamental transport coefficients. After a brief digression into the semiclassical Drude model of electronic transport, we derive *Mott’s formula*, a relatively simple expression of low-temperature thermopower in terms of often measurable quantities. We then consider the relationship between thermopower and entropy. The chapter concludes with a discussion of the *phonon drag* contribution to thermopower. In the context of our research, we consider this contribution a parasitic effect to be avoided. We reveal the origin of phonon drag as well as some basic strategies for minimizing its effects.

**Chapter 4** reviews our *diving board technique* for measuring thermopower of a high-mobility 2DES. Ours is a modification of a standard method of imposing a temperature difference across a material system. One end of our sample is thermally anchored to a cold reservoir while the other end is suspended in space with a heating element attached. Heat then flows along the thermally resistive sample to establish a

temperature gradient. However, departing from standard practice, we do not employ external thermometry to measure this temperature gradient. Rather, we exploit temperature dependent properties of the 2DES itself for this purpose. We explain both why and how our temperature calibration is implemented in this way. This method is employed for both diving board devices introduced in this chapter. Our original device, diving board A, suffers from long thermal relaxation times. We outline our quasi-DC measurement protocol, which accommodates these delays and analyze our thermopower results in zero magnetic field. We then introduce an improved device, diving board B, which overcomes the long relaxation times via an improved design thereby facilitating much faster data acquisition.

In **Chapter 5** we consider an alternative approach to measuring two-dimensional thermopower by reviewing our *hot-electron thermocouple*. Just as a junction of dissimilar metals will produce a voltage in response to a temperature difference, so too will a junction of 2DESs with dissimilar Fermi levels. This is the working principle of our hot-electron thermocouple, which is realized by electrostatically establishing different electron densities in each half of a 2DES mesa. This thermocouple forms one “bar” of a cross patterned 2DES mesa. Current is passed along the other “bar” in order to heat the electrons at the center of the thermocouple. An advantage of this heating method is that it produces far fewer phonons compared to the external heaters employed by traditional diving board devices. This results in a dramatic reduction in the parasitic effects of phonon drag allowing the unprecedented measurement of the diffusion thermopower of a high-mobility 2DES at temperatures as high as  $T = 2$  K. In this chapter, we discuss the device layout, temperature calibration, measurement protocol, as well as experimental results of this novel technique. We conclude the chapter with a proposal to utilize this technique to study the enigmatic *two-dimensional metal-insulator transition*.

With **Chapter 6** we digress from the topic of thermopower to introduce and review the *integer quantum Hall effect* (IQHE). When a 2DES is subjected to a strong out-of-plane magnetic field, the orbital motion of the electrons quantizes. The most famous manifestations of this phenomenon are plateaus at precisely  $h/\nu e^2$ , for

integers  $\nu$ , that appear in the transverse resistance with the simultaneous vanishing of the longitudinal resistance. In this chapter, we survey the essential features of quantum Hall phenomena in the absence of appreciable electron-electron interactions. We begin with the classical Hall effect, proceed to *Landau level* (LL) quantization, explain filling factors, the impact of disorder, the notion of compressibility, and the role of edge states. Once equipped with these concepts, we are able to understand typical quantum magnetotransport measurements. We conclude this chapter with a discussion and measurement of the quantum lifetime, a quantity we reference in subsequent chapters.

**Chapter 7** reviews thermopower in the quantum Hall regime. To establish context, we begin with a discussion of a classical 2DES in a magnetic field. We then consider how disorder-broadened LLs dramatically alter the thermoelectric response of the 2DES. In part to demonstrate that the relationship between thermopower and entropy persists in the presence of a strong magnetic field, we demonstrate that the diffusion thermopower of a disorder-free 2DES in the IQH regime can be derived by merely counting single-electron states. This chapter touches upon many subjects including how a disorder potential gives rise to a transverse thermopower, known as the *Nernst-Ettingshausen effect*, the current distributions during a thermopower measurement, a model for computing the thermopower tensor, and phonon drag in the quantum Hall regime. We conclude with an analysis of the results of our low-field thermopower measurements.

**Chapter 8** delves into the fractional quantum Hall regime. First we introduce the *fractional quantum Hall effect* (FQHE), a higher order manifestation of the IQHE, which can largely be understood by recasting the problem of many strongly interacting electrons into one of many weakly interacting *composite fermions* (CFs). Armed with the notion of CFs, we again exploit the thermopower-entropy relation to anticipate the low-temperature thermopower of the FQH regime. Toward that end, we review the theory of CF thermopower at LL filling factors where the effective magnetic field is zero. Several experimental results are included in this chapter. The thermopower at LL filling factor  $\nu = 3/2$  is analyzed and shown to be consistent with a Fermi sea

of CFs. The CF effective mass is extracted and compared to theory and previous measurements. The wealth of FQH state signatures in thermopower versus magnetic field measurements is demonstrated and compared to those in more familiar resistance data. More generally, the temperature and field dependence of thermopower in the FQH regime is shown to be at least qualitatively consistent with the entropy per CF for two species of CFs (2-flux and 4-flux quanta attached).

Finally, in **Chapter 9** we explore the rich phenomena of the first excited LL. This unique LL shares features of both the lowest and higher LLs by exhibiting both FQHEs and so-called *reentrant integer quantum Hall effects* (RIQHEs). Moreover, this LL is home to the enigmatic  $\nu = 5/2$  FQH state believed to exhibit *non-Abelian exchange statistics*. In this chapter we briefly discuss the putative nature of this state as well as that of its excitations, known as *non-Abelian anyons*, and why they have generated so much interest. We then review a recent theory of enhanced thermopower at  $\nu = 5/2$  that results from the uniquely large degeneracy of non-Abelian anyons. Experimental thermopower results at  $\nu = 5/2$  are then discussed and compared with the theory. Our focus then shifts to the phenomena surrounding RIQHEs. After going over the salient features of RIQHEs, we review measurements of thermopower in the vicinity of these dramatic transitions. The RIQHE is correlated with an abrupt collapse of the thermopower that is clearly distinct from QH phenomena. At temperatures just above the RIQHE transition, we find surprising thermopower behavior suggestive of an unconventional conducting phase.

# Chapter 1

## Two-Dimensional Electron System

A *two-dimensional electron system* or 2DES is a gas of electrons that is free to move in-plane but constrained from moving out-of-plane<sup>1</sup>. Such a system is of great utility to those of us interested in many-body correlated physics for several reasons. First, as discussed below, it is quite practicable to separate the donor ions from the electrons that comprise a 2DES. This liberates the electrons from interacting strongly with a background potential as is the case for electrons in a metal, such as copper, or a typical doped semiconductor. In addition, being confined to two dimensions, the electrons are limited in their ability to screen the charge of neighboring electrons. Finally, when subjected to a strong out-of-plane magnetic field, the kinetic energy of low-temperature 2D electrons quantizes into discrete levels yielding the *quantum Hall effect* (see Chapter 6). All of these circumstances enhance the role of electron-electron interactions.

Historically there are many ways to realize a 2DES. Early studies exploited weakly polarizable surfaces such as that of solid hydrogen or liquid helium [10]. More recently, graphene—atomic sheets of carbon that form a honeycomb lattice—have attracted a great deal attention due to its many exceptional properties, including its electronic characteristics, which are governed by two-dimensional electron (and/or hole) systems [11]. Another approach involves trapping electrons in a potential energy well formed at a material interface. Using this latter technique, we are today surrounded by 2DESs formed within transistors such as the ubiquitous metal-oxide-semiconductor

---

<sup>1</sup>For a review of low dimensional systems, see Davies [9].

field-effect transistor or MOSFET that forms a technological cornerstone of modern electronics.

In enhancement mode MOSFETs a voltage between the 'metal' and the semiconductor results in the formation of a 2DES at the oxide-semiconductor interface. Known as an inversion layer, this 2DES allows conduction between the transistor's source and drain. In 1980 Klaus von Klitzing made one of the most dramatic discoveries [1] in the field of condensed matter physics by studying such inversion layers at low temperatures and within large magnetic fields. He found that at certain values of the magnetic field the transverse, or Hall, conductance became precisely equal to integer multiples of a universal value. This macroscopic manifestation of quantum mechanics, now known as the *integer quantum Hall effect* (IQHE), plays an important role in this thesis and is discussed in detail in Chapter 6.

The quality of the 2DES formed within MOSFETs is limited, however, due to its relatively high scattering rate. A simple way to formalize the quality of a 2DES is through a quantity known as *electron mobility*  $\mu_e$  defined as the ratio of the electronic drift velocity  $v_d$  to the electric field; that is,  $v_d = \mu_e E$ . Unlike the crystalline silicon that forms the conduction channel of a MOSFET, the silicon dioxide that electrically isolates the 2DES from the 'metal' electrode is glassy resulting in an *interface roughness* that scatters the electrons thereby limiting their mobility. As a result, a 'high-mobility' silicon MOSFET at low temperature has  $\mu_e \lesssim 40,000 \text{ cm}^2/\text{Vs}$  [9]. While this is indeed a high-mobility when compared, for example, to electrons in a copper wire at room temperature ( $\mu_e \sim 30 \text{ cm}^2/\text{Vs}$ ), we require mobilities more than two orders larger in magnitude to realize the delicate many-body phases of interest in our studies.

This chapter provides an overview of the devices within which the ultra-high-mobility 2DESs are realized and studied for this thesis. We begin with a discussion of GaAs/AlGaAs heterostructures and the band engineering made possible via the parameters of these layered crystalline semiconductors. We then introduce the specific devices studied along with a basic<sup>2</sup> description of the techniques employed in their

---

<sup>2</sup>A detailed account of the actual processing recipes used to create these devices is provided in

fabrication. Subsequent chapters elaborate on these devices and how they are used to measure the thermoelectric properties of the 2DES.

## 1.1 GaAs/AlGaAs Heterostructures

The problem of interface roughness is largely overcome within the ultra-clean, layered semiconductors known as *heterostructures* [12]. Using *molecular beam epitaxy* or MBE, extremely pure material may be grown on a substrate with nearly atomic resolution. The most common heterostructures are made from group III-V compounds; in particular, GaAs and AlAs. These two compounds are very well matched due to having the same zinc-blende crystal structure and lattice constants that differ by less than 0.15% allowing them to be grown on top of one another without introducing appreciable stress or defects. At the same time, the *band gaps*  $E_g$  of these two compounds are quite different: at low temperatures<sup>3</sup>, GaAs has a direct gap  $E_g = 1.52$  eV while AlAs has an indirect gap  $E_g = 2.25$  eV. The goal of heterostructure growth using these compounds is to manipulate the electrical and/or optical properties of the material by layering alloys of the form  $\text{Al}_x\text{Ga}_{1-x}\text{As}$ , where  $x$  is a number between 0 and 1 indicating the Al concentration. This process is known as *band engineering*.

As an example, let us consider the band structure at a *heterojunction* between the alloy  $\text{Al}_{0.3}\text{Ga}_{0.7}\text{As}$ , which has a direct energy gap  $E_g = 1.93$  eV at low temperatures, and pure GaAs. A simple model [13] known as *Anderson's rule* states that the vacuum levels of two materials are aligned at a heterojunction. The band structure is then determined by the difference between the bottom of the conduction band and the vacuum level, known as a material's *electron affinity*  $\chi$ . The difference in the electron affinities then governs the discontinuity in the conduction band  $\Delta E_c$  as illustrated in Fig. 1.1. In reality, Anderson's rule is overly simplistic and in the case of a heterojunction formed by  $\text{Al}_{0.3}\text{Ga}_{0.7}\text{As}$  and GaAs it overestimates  $\Delta E_c$ . The actual discontinuity has been measured as  $\Delta E_c = 250$  meV [14].

---

Appendix B.

<sup>3</sup>These values are for  $T \lesssim 4$  K. At room temperature, GaAs has a direct gap  $E_g = 1.42$  eV and AlAs has an indirect gap  $E_g = 2.16$  eV.

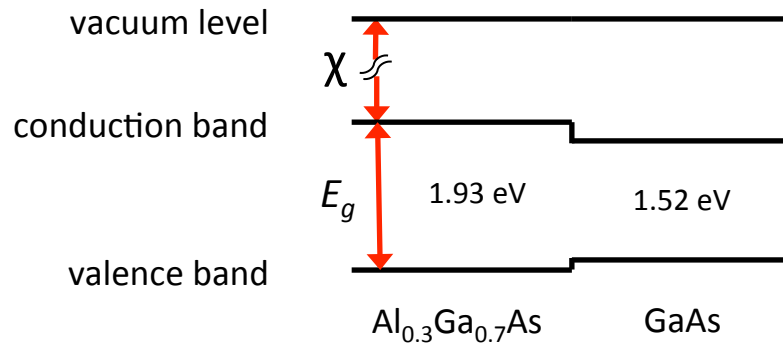


Figure 1.1: Band structure of a AlGaAs-GaAs heterojunction.

By sandwiching a layer of GaAs between layers of AlGaAs a *quantum well* is created that can confine electrons of the conduction band<sup>4</sup> in the growth or  $z$ -direction. In Fig. 1.2 we illustrate a quantum well resulting from 20 nm of GaAs sandwiched between layers of Al<sub>0.3</sub>Ga<sub>0.7</sub>As. The dashed line in the figure represents a Fermi level that lies below the confinement potential, or in the band gap, of the flanking AlGaAs resulting in a spatially localized electron system. Importantly, such a finite quantum well supports multiple localized modes or *subbands* (not shown). By positioning the Fermi level appropriately, only the lowest subband is populated. Of course, these structures are in fact three dimensional and Fig. 1.2 only shows the variation of the potential in the  $z$ -direction. Well away from the edges of the sample, electrons are unbound and free to move in the  $x$ - $y$  plane thus establishing a 2DES.

But how is the Fermi level determined? Up to now we have neglected a critical aspect of heterostructure band engineering. Intrinsic semiconductors like GaAs, AlAs, and their alloys have Fermi levels that lie in band gaps. To create a metallic or *compressible* system we must therefore introduce additional carriers. An obvious way to achieve this would be to dope a quantum well with donors. The problem with this approach, however, is that the donors, ionized after contributing their electrons, would

<sup>4</sup>In Fig. 1.1 we see the valence band of the GaAs lies about 0.04 eV above that of the Al<sub>0.3</sub>Ga<sub>0.7</sub>As such that by sandwiching a layer of GaAs between layers of AlGaAs a quantum well is also created for holes in the valence band. The position of the Fermi level determines whether the quantum well contains a metallic system of electrons or holes; or neither, as is the case when the Fermi level lies in the band gap.

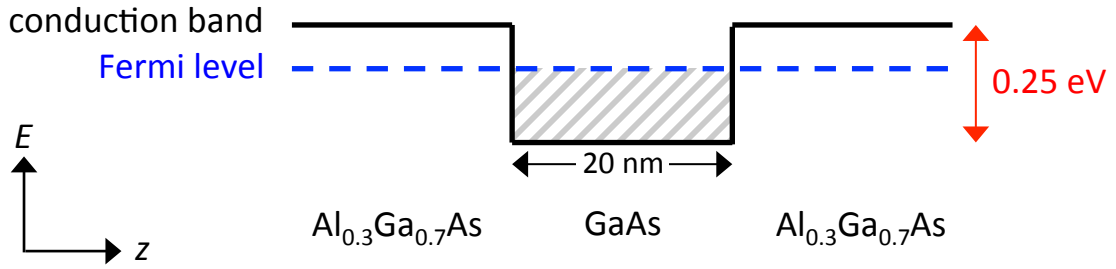


Figure 1.2: Illustration of a quantum well created by sandwiching 20 nm of GaAs between layers of AlGaAs.

scatter the 2DES via Coulomb interactions thereby limiting their mobility  $\mu_e$  and preventing the formation of the delicate many-body phases we desire. The solution is to utilize the important invention by Störmer et al. [15] of *modulation doping* in which dopants are spatially separated from the quantum well, far enough that scattering from donor ions is minimized but close enough that donated carriers migrate to the well. Exotic many-body phases aside, modulation doping is also extremely important to the realm of modern device physics. It has allowed the realization of high gain FETs with ultra-high switching speeds that are a crucial ingredient in the front-end amplification stages of the now ubiquitous cellular phone.

The samples studied in this thesis employ a particular variant known as *delta-doping* where a monolayer of silicon is grown, separated from the GaAs quantum well by a relatively thick layer of AlGaAs. An example of MBE grown epilayers forming a delta-doped quantum well are shown in Fig. 1.3. The layers in the figure are similar to, and capture the salient features of, the parent wafer of the diving board devices studied for this thesis. The 30 nm quantum well is doped from both above and below by silicon monolayers with a setback distance of 80 nm. This setback distance is a key factor in determining the ultimate character of our 2DES. For a given Al concentration  $x$ , and hence a given conduction band offset, the closer the donors are to the quantum well, the higher the density of electrons in the 2DES. A higher density is often desirable since it means the Fermi level is larger relative to

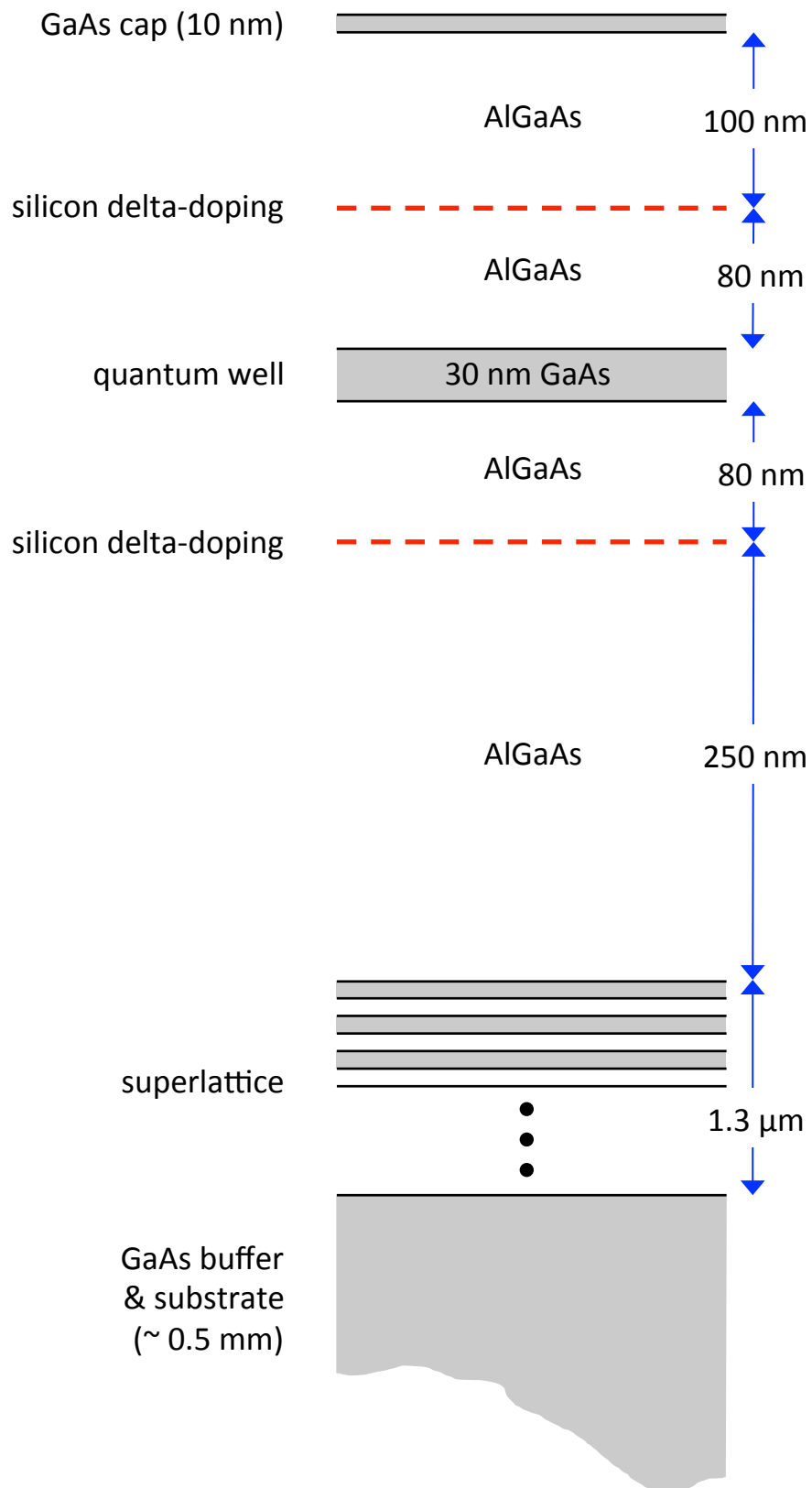


Figure 1.3: MBE grown epilayers of a delta-doped GaAs/AlGaAs quantum well heterostructure similar to that of the devices studied for this thesis.

fluctuations in the background potential, and therefore, can result in higher electron mobilities. However, placing the donors too close to the quantum well defeats the whole purpose of modulation doping, which is to separate the 2DES from the donor ions. This implies there is an optimal setback distance—given the quantum well width, aluminum concentration in the AlGaAs, and other parameters beyond the scope of this thesis—that will maximize the electron mobility.

Continuing our tour of Fig. 1.3, the MBE growth begins by depositing a buffer layer of 500 nm of GaAs onto a 0.5 mm thick (100)-oriented GaAs substrate. This is followed by the growth of a filtering superlattice; that is, an array of one hundred narrow, 3 nm wide GaAs quantum wells each separated by 10 nm of AlGaAs. The superlattice traps impurities that percolate up from the substrate during growth and also prepares an atomically flat surface onto which the critical layers of the heterostructure may be grown. Growth then proceeds with 250 nm of AlGaAs<sup>5</sup> followed by the lower donor layer and then the AlGaAs-GaAs-AlGaAs quantum well structure. Moving upward, after the upper donor layer, an additional 100 nm of AlGaAs is deposited followed by a 10 nm GaAs cap to protect the aluminum from oxidation.

Now that we have a better picture of the full structure involved in realizing an ultra-high-mobility 2DES, we may refine our diagram of the band structure. Heretofore we have neglected the effect of the donor ion charge as well as that of the 2DES itself on the conduction band. The bands shown in Fig. 1.1 and 1.2 reflect only the kinetic energy of the electrons in each material layer. The actual bands include an additional contribution from the electrostatic potential that arises from separating electrons from their donor ions. As a rule, bands bend within charged regions with a curvature proportional to the charge density. In Fig. 1.4 we illustrate the conduction band along the  $z$ -direction for a delta-doped quantum well that includes this electrostatic potential contribution. The dashed line in the figure represents a Fermi level that is positioned above the bottom of the band within the well, thereby

---

<sup>5</sup>The parent wafer of the diving board devices studied in this thesis contain the alloy  $\text{Al}_{0.24}\text{Ga}_{0.76}\text{As}$  whereas that of the hot-electron thermocouple device contains  $\text{Al}_{0.3}\text{Ga}_{0.7}\text{As}$ .

populating its lowest subband whose wave function is also depicted in the figure. At the same time, the Fermi level remains below the local band minima at the donor layers precluding the formation of parallel electron systems<sup>6</sup>.

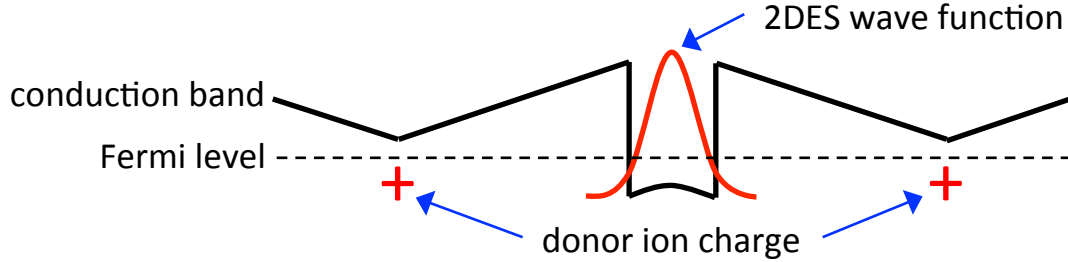


Figure 1.4: Illustration of the conduction band of a delta-doped GaAs/AlGaAs quantum well that includes the contribution from the electrostatic potential resulting from separating electrons from their donor ions. The dashed line represents a Fermi level resulting in the population the lowest subband of the quantum well.

Determining the actual position of the Fermi level relative to the quantum well is not only a function of the heterostructure layers but is also governed by the situation at the GaAs cap’s exposed surface. Exposed GaAs has a high density of surface states near the middle of its band gap [9]. These states are in fact so numerous that they pin the Fermi level to their narrow band of energies lying about 0.8 eV below the bottom of the conduction band. In many cases the ability to adjust the Fermi level, and hence the 2DES’s density, is desirable. Metal may be deposited onto the surface of many<sup>7</sup> heterostructures in order to capacitively modulate or *gate* the 2DES’s density by adjusting the Fermi level. Gating in this manner plays a critical role in the thermopower measurements made via our hot-electron thermocouple. We will further discuss the fabrication and behavior of gates in Section 1.2.

The combined effect of the atomically sharp interfaces and remotely located donor ions of GaAs/AlGaAs heterostructures are 2DESs with electron mobilities that can

<sup>6</sup>A common failure-mode for heterostructure growth is the manifestation of *parallel conduction* resulting from a Fermi level that sits above the local minima of the conduction band at the donor layers. Fortunately, this issue is readily identified through basic magnetotransport (see Chapter 6).

<sup>7</sup>Not all heterostructures are “gatable” in this manner. See Section 1.2 for a discussion of the limits of electrostatic gating.

exceed  $3 \times 10^7 \text{ cm}^2/\text{Vs}$ . This is the highest of any electron system and nearly three orders of magnitude greater than that of the “high-mobility” silicon MOSFETs discussed in the previous section. Moreover, an ultra-high-mobility 2DES with a density of  $3 \times 10^{11} \text{ cm}^{-2}$  will have a mean free path<sup>8</sup> of  $\sim 300 \text{ }\mu\text{m}$ ! These state of the art heterostructures are therefore a critical ingredient to a study such as ours. We are therefore quite fortunate in our collaboration with Loren Pfeiffer and Ken West of Princeton University who consistently produce wafers of the highest quality, without which our research would not be possible.

## 1.2 Device Fabrication

Once a GaAs/AlGaAs heterostructure is grown, specialized 2DES devices may be constructed through subsequent fabrication or *sample processing*. This section presents a qualitative overview of commonly fabricated features. A detailed account of the actual processing recipes used to create these features is provided in Appendix B.

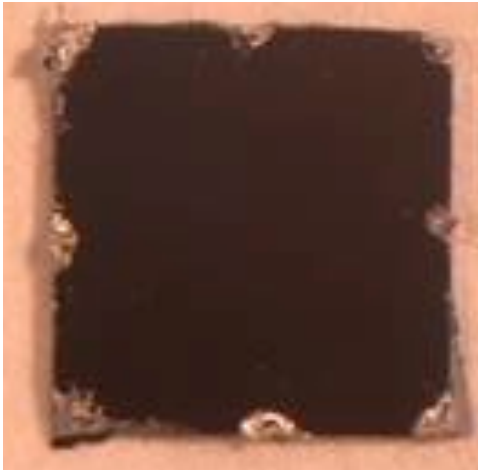


Figure 1.5: Image of a simple 2DES device. This cleaved sample is about  $5 \times 5 \text{ mm}^2$  with eight indium ohmic contacts placed along its periphery. Simple devices like this are routinely used to characterize their parent wafers.

---

<sup>8</sup>See Appendix A for a list of properties of a 2DES in GaAs.

The most simple devices merely involve making electrical contact to the 2DES. Figure 1.5 shows a  $5 \times 5 \text{ mm}^2$  sample cleaved from a parent wafer with *ohmic contact* material—in this case, pure indium—placed at the corners and midpoints of its periphery. The term “ohmic contact” originates from their approximate adherence to Ohm’s law, as opposed, to say, a non-linear diode-like behavior. To fabricate these contacts the indium is carefully applied to the sample’s surface using a soldering pen. It is then diffused into the heterostructure by annealing the sample in a forming gas atmosphere. Wires are then attached through the dextrous use of tweezers, soldering pen, and a microscope. Simple devices like this are routinely used to characterize the quality of their parent wafers through measurements of the 2DES’s electrical resistivity (Appendix C) as well as magnetotransport (Sec. 6.8) in order to determine electron mobility.

Using lithographic techniques the surface of a sample may be patterned in ways to create more sophisticated devices. For example, the 2DES may be confined to an arbitrary geometry in the  $x$ - $y$  plane by wet etching a lithographically patterned sample<sup>9</sup>. The 2DES is destroyed within the etched region. The remaining, unetched region is referred to as a *2DES mesa* in analogy to the table-top shaped hills common to the American Southwest. Figure 1.6 shows a sample with several patterned features including a 2DES mesa consisting of  $60 \mu\text{m}$  channels.

The ability to modulate the density of the 2DES or to even fully deplete the quantum well is often desirable. Patterned metal, typically aluminum, may be thermally evaporated onto a sample’s surface allowing electrostatic manipulation of the Fermi level. In this way, a metallic top gate forms a capacitor with the 2DES allowing the reduction or even enhancement of the number of electrons within the quantum well (this manner of gating is critical to the operation of our hot-electron thermocouple).

---

<sup>9</sup>While it is common practice during mesa processing to etch sufficiently deep that the quantum well is removed, this is not actually necessary. Like GaAs (see Section 1.1) an exposed AlGaAs surface has a high density of states in its energy gap that pins the Fermi level [9]. By etching away the GaAs cap and a significant fraction of the AlGaAs spacer layer—perhaps even leaving the silicon doping layer—the Fermi level can be lowered well below the bottom of the conduction band within the GaAs quantum well such that a 2DES will not form. A more shallow etch can be desirable in situations where delicate metallization must climb up the 2DES mesa from an etched region. In such a scenario, a 2DES mesa that is too tall can result in a discontinuity in the metal.

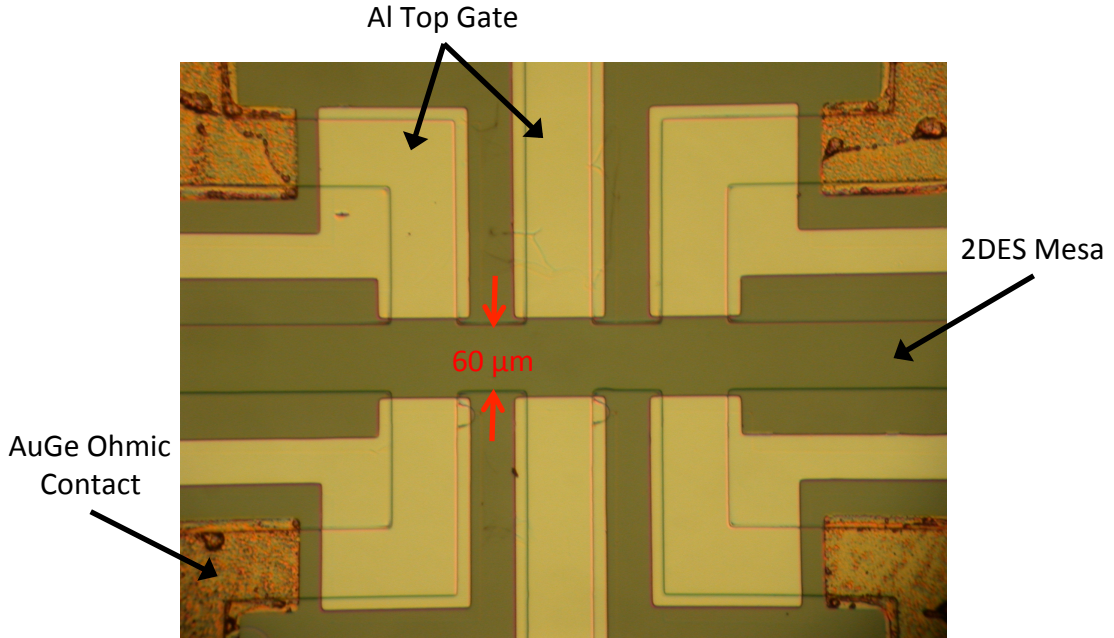


Figure 1.6: A lithographically patterned 2DES device. The image is filtered to enhance color contrast.

As an example, refer to Fig. 1.6; the six mesa arms extending vertically from the central  $60 \mu\text{m}$  channel are covered by aluminum top gates. Another, very simple technique is to place copper tape beneath the  $0.5 \text{ mm}$  substrate, positioned between a sample and its plastic header, to form a back gate. There are limits to this gating technique, however. In enhancement mode, a sufficiently large positive voltage (e.g.  $\sim 0.5 \text{ V}$ ) can produce quantum mechanical tunneling between the 2DES and top gate. At the same time, GaAs has a dielectric breakdown field of  $3 - 9 \times 10^5 \text{ V/cm}$  [16] setting an upper limit on the magnitude of voltage that can be applied to an external gate without damaging the sample. Copper back gates, meanwhile, have relatively small capacitances due to the thick substrate<sup>10</sup>. Dielectric breakdown within the wiring will therefore determine the maximum voltage (e.g.  $\sim \pm 200 \text{ V}$ ) for these

<sup>10</sup>Back gates can be evaporated onto thinned samples to achieve relatively high capacitances allowing full depletion of a 2DES with  $n = 1.5 \times 10^{11} \text{ cm}^{-2}$ . While this technique was not employed for the devices studied for this thesis, it is routinely applied in our lab to double quantum well samples.

gates, thereby limiting density adjustments to  $\Delta n \sim \pm 10^{10} \text{ cm}^{-2}$ ; often less than 10% of the ungated density.

Many, though not all, GaAs/AlGaAs heterostructures are “gatable”. Samples of the highest mobility—such as those used to fabricate the diving board devices studied for this thesis—are not amenable to electrostatic gating due to mobile carriers in their donor layers that screen an electric field originating from an external metal gate. In order to achieve the highest electron mobilities these heterostructures are said to be “over-doped” resulting in potential wells at the donor layers that actually dip below the Fermi level resulting in a small degree of parallel conduction. While this parallel conductance is negligible relative to that of the 2DES it is advantageous in its smoothing of the remote impurity potential seen by the 2DES. Achieving the highest electron mobilities therefore comes at the cost of electrostatic gatability.

Another key feature of the sample presented in Fig. 1.6 are its ohmic contacts seen in the corners of the image. An alternative to the indium used for the simple device shown in Fig. 1.5, ohmic contacts may also be constructed from an evaporated AuGe alloy. To assist with adhesion, a thin, “sticky” layer of nickel is first evaporated onto the GaAs surface. Like indium, AuGe diffuses into the GaAs/AlGaAs heterostructure during an annealing treatment to make contact with the quantum well. Compared with indium, evaporated AuGe contacts usually provide a less resistive connection to the 2DES and have the added benefit of being lithographically defined. As such, they can be formed into arbitrary geometries; an important feature for the hot-electron thermocouple discussed in the next section. The only downside of evaporated contacts is the overhead involved with the requisite lithographic methods.

The patterned sample shown in Fig. 1.6 along with all of the devices studied for this thesis were fabricated using *photolithography*. This technique begins with the application of a thin, uniform coating of a type of polymer known as *photoresist*. A patterned mask containing regions that are opaque and others that are transparent to ultraviolet light is then placed over the sample. In places where the ultraviolet light is incident upon the photoresist, it is chemically altered. Immersion in a special solution known as a *developer* then selectively removes either the exposed or unexposed regions

of the photoresist, depending on its polarity. The remaining photoresist acts as a protective layer and the exposed areas may be etched or metalized.

This patterning technique is capable of feature sizes down to about  $5\ \mu\text{m}$ , a number set by the diffraction limit of the ultraviolet light used. One can go beyond this limit, achieving nano-scale feature sizes through the use of electron beam lithography. Modern scanning electron microscopes are readily capable of achieving dimensions as small as  $50\ \text{nm}$ , a limit set by the de Broglie wavelength of the energetic electrons used. The experiments performed for this thesis, however, focus on the diffusion transport of ultra-high-mobility electrons. As already mentioned, these systems can have mean free paths of hundreds of microns. This sets a lower bound for the feature sizes permitted in our devices if we want to avoid ballistic behavior. For this type of experiment, therefore, bigger is better and photolithography is the appropriate fabrication technique.

### 1.2.1 Hot-Electron Thermocouple

The hot-electron thermocouple utilizes all of the features described in the previous section. In fact, the image of Fig. 1.6 is the interior region of the sample used to acquire all of the hot-electron data presented in this thesis. A lower magnification image of the device is provided in Chapter 5 along with an explanation of the protocol used to measure thermopower.

The device originates from a  $5 \times 5\ \text{mm}^2$  sample cleaved from a GaAs/Ga<sub>0.3</sub>Al<sub>0.7</sub>As heterostructure that includes a symmetrically doped  $20\ \text{nm}$  quantum well grown via MBE onto a (100)-oriented GaAs substrate. The sample has an ungated density of  $n = 1.6 \times 10^{11}\ \text{cm}^{-2}$  and an electron mobility of  $\mu_e = 3.3 \times 10^6\ \text{cm}^2/\text{Vs}$ , at low temperatures. The mobility of this 2DES is nearly an order of magnitude less than that within the diving board devices described in subsequent sections. As such, the sample does not suffer from the type of parallel conduction discussed in the previous section and the 2DES density is readily modulated by applying voltages to the top gates. At the same time, many of the most delicate many-body phases cannot be

realized in this device, which is designed with noninteracting electrons in mind.

The device was patterned into a 1 mm-long, 60  $\mu\text{m}$ -wide 2DES mesa with ohmic contacts at each end for driving current along it. Three arms extend away from each side of this central channel and terminate at ohmic contacts. The actual *thermocouple* consists of the two opposing arms in the center of the device which are overlaid with top gates. The remaining arms, which are also equipped with top gates, are normally used as voltage probes enabling measurements of the resistance of the 2DES in the central region of the device.

The ohmic contacts are the evaporated Ni-AuGe variety and in addition to enabling electrical measurements they also serve to thermally anchor the electron gas in their immediate vicinity to the lattice temperature. Away from the contacts, however, the electrons can easily be heated out of equilibrium with the lattice; hence the term “hot-electron”. This fact is critical to the operation of the device and will be elaborated upon in Chapter 5.

## 1.2.2 2DES Diving Boards

In Chapter 4 we explain our diving board technique for measuring the thermopower of the 2DES. The 2DES diving board devices employed by this technique are both cleaved from a GaAs/Al<sub>0.24</sub>Ga<sub>0.76</sub>As heterostructure grown via MBE onto a (100)-oriented GaAs substrate. The crucial epilayers of their parent wafer correspond to those shown in Fig. 1.3. After illumination<sup>11</sup> by a red LED, the density and mobility of the 2DES are  $n = 2.9 \times 10^{11} \text{ cm}^{-2}$  and  $\mu_e = 3.1 \times 10^7 \text{ cm}^2/\text{Vs}$ , respectively, at low temperatures. The ultra-high-mobility 2DESs originating from this wafer exhibit a wealth of fractional quantum Hall (FQH) states and other many-body correlated phenomena.

The original diving board, which we designate with the letter ‘A’, is shown in Fig. 1.7. The sample is bar shaped,  $L = 12 \text{ mm}$  long by  $W = 3 \text{ mm}$  wide. A strain gauge<sup>12</sup> acting as a heater is attached to one end of the sample while the other end

<sup>11</sup>See Section 2.5 for a discussion of sample illumination.

<sup>12</sup>We use GE/IMI 7031 varnish to attach a Vishay WK-06-031CF-350 strain gauge to our sample.

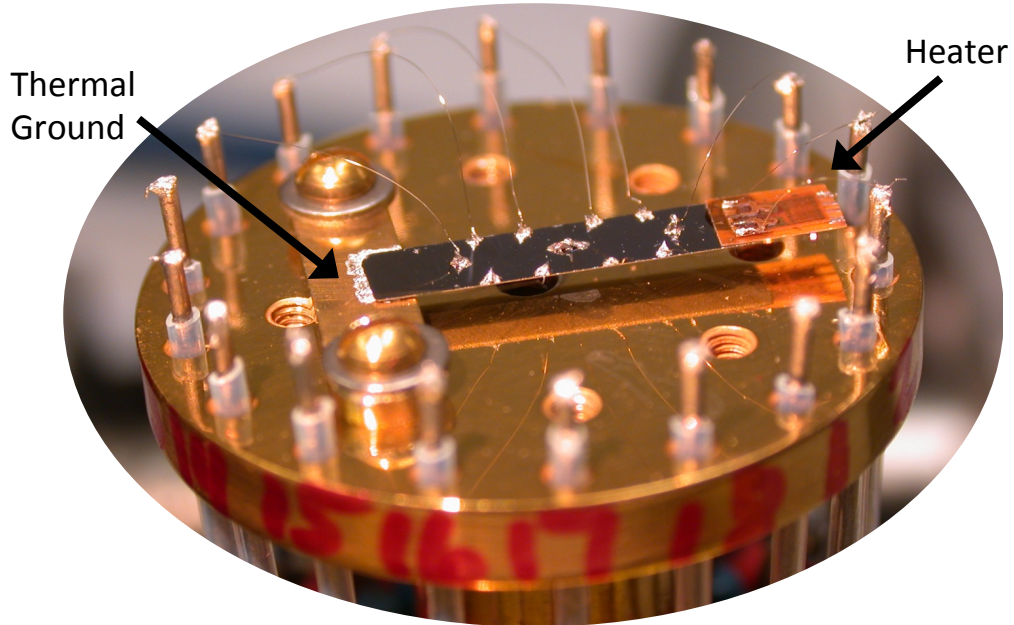


Figure 1.7: 2DES diving board A installed into a special sample stage. The gold-plated silver disc is about one inch in diameter.

is indium-soldered to a small Au-plated copper slab that serves as thermal ground. The copper slab is, in turn, bolted to the cold finger of a dilution refrigerator<sup>13</sup>. This configuration allows a heat flux to flow along the length of the diving board establishing a temperature gradient along the 2DES.

The sample's surface is patterned into two square  $3 \times 3 \text{ mm}^2$  2DES mesas, separated by 1 mm and positioned symmetrically about the midpoint of the bar. Electrical contact to the 2DESs is enabled by six small eutectic InSn<sup>14</sup> ohmic contacts diffused onto the mesa perimeters. Close inspection of Fig. 1.7 reveals that the two mesas share one ohmic contact and are thereby connected in series. Manganin wires,  $25 \mu\text{m}$  in diameter and approximately 1 cm long, are attached to these contacts (and to the resistive heater). Manganin was chosen because the thermal conductance and thermopower [17] of these wires is negligible in comparison to the thermal conductance

<sup>13</sup>See Sec. 2.2 for a discussion of dilution refrigeration.

<sup>14</sup>We find that ohmic contacts made from eutectic InSn yield marginally lower resistances when compared to those made from pure indium.

of the sample bar and the thermopower of the 2DES within it.

For reasons that will be made clear in subsequent chapters, we want to maximize the thermal resistance of the diving board. This is achieved by thinning the substrate to about  $t = 130 \text{ }\mu\text{m}$  via a chemical etch<sup>15</sup> and then sandblasting its backside to ensure diffuse phonon scattering [18]. This latter step is important, for otherwise highly specular phonon boundary scattering can lead to nonuniform temperature gradients along the bar.

It turns out that diving board A suffers from a problem that limits its ability to measure thermopower at low temperatures and high magnetic fields. Using fabrication methods covered in this chapter and Appendix B, an improved diving board device is constructed that overcomes these issues. We defer the discussion of both the problem presented by diving board A along with the improved diving board to Chapter 4.

### 1.3 Summary

In this chapter we introduced the two-dimensional electron system (2DES). Interesting in and of itself and yielding highly impactful applications (e.g. in enhancement-mode MOSFETs), the 2DES provides an ideal forum for studying strongly correlated quantum systems. The cleanest, highest mobility 2DESs are realized within GaAs/AlGaAs heterostructures grown via molecular beam epitaxy. These layered materials are grown such that when cooled, potential energy wells trap electrons away from their donor ions and are confined to two dimensions. By separating the negatively charged electrons from their positively charged donor ions, their interlayer interaction can be made negligible in comparison to the intralayer coupling of neighboring electrons within the 2DES. By minimizing this background charge potential within an all but defect-free crystal lattice, inelastic scattering rates are dramatically reduced resulting in ultra-high electron mobilities.

Many years of research have resulted in a number of fabrication techniques used to create specialized devices from the wafers of these state of the art GaAs/AlGaAs

---

<sup>15</sup>See Appendix B for the thinning procedure.

heterostructures. In particular, through patterning techniques, such as photolithography, combined with chemical etching, the 2DES may be confined to arbitrary two-dimensional geometries. And by depositing particular metals such as pure indium onto a sample's surface and annealing such that the metal diffuses into the crystal, ohmic contacts are formed providing electrical and thermal connections to the 2DES. Depositing an aluminum film onto a sample's surface allows capacitive control over the density of the 2DES. We combine these techniques to construct a novel hot-electron thermocouple discussed in Chapter 5. With help of other procedures for substrate thinning and sample mounting, we also fabricate diving board style devices, which are introduced in Chapter 4 and set the stage for the experiments explored in subsequent chapters. But first, in the next chapter, we describe the cryogenic environment, which is necessary for the formation of ultra-high-mobility 2DESs and particularly critical to the realization of the delicate many-body states we wish to study.

# Chapter 2

## Cryogenic Environment

The art of achieving, maintaining, and modulating extremely low temperatures, known as *cryogenics*, advanced by leaps and bounds during the 20th century. This greatly facilitated experimental condensed matter research in numerous areas including magnetism, lattice dynamics, electronic properties of materials, superconductivity, and superfluidity. Likewise, in order to realize the delicate correlated electron phases that are the focus of this thesis, it is necessary to perform our experiments at sub-Kelvin temperatures.

In this chapter we first consider the energy, or temperature, scales relevant to our research. This motivates the discussion that follows on dilution refrigeration which is the means by which we cool our experiments. After a brief description of how the sample is positioned within the core of a powerful magnet, we examine both the electrical and thermal connections to the 2DES. We conclude with some words on the technique of sample illumination whereby additional carriers are coaxed into the quantum well in an effort to maximize the electron mobility.

### 2.1 Energy/Temperature Scales

To better appreciate our need for cryogenic temperatures, it is helpful to consider several relevant energy scales. For starters, before any quantum mechanical behavior can be resolved, our electrons must be cooled well below their Fermi temperature  $T_F$ . In the case of our diving board samples, which have 2DESs of density  $n =$

$2.9 \times 10^{11} \text{ cm}^{-2}$ ,  $T_F = 120 \text{ K}$ . At temperatures much less than this the 2DES is said to be a *degenerate electron gas*, as the lowest energy states are completely filled, and its fermionic nature emerges.

A comparable energy scale is found within the heterostructure band structure we discussed in Section 1.1. The GaAs quantum well contains several modes or subbands. To ensure that our electron system is indeed confined to two dimensions, it is incumbent on us to only populate the lowest energy subband<sup>1</sup>. For a heterostructure like that shown in Fig. 1.3 the energy difference between the lowest and first excited subband is  $E_1 - E_0 \sim 100 \text{ K}$ . We must therefore operate at temperatures much less than 100 K if we are to guarantee a negligible thermal population of carriers in the quantum well's first excited mode.

In Chapter 6 we will discuss the physics of two-dimensional electrons in a magnetic field. Ignoring electron-electron interactions for a moment, at sufficiently high fields the electrons will follow quantized cyclotron orbits in a manner somewhat similar to the quantized orbits of an atom. In order to resolve this phenomenon we must cool the electrons to a temperature well below the energy difference of these orbits. The actual energy differences in question are functions<sup>2</sup> of electron density and magnetic field strength but a representative value for the regime studied for this thesis corresponds to  $T \sim 10 \text{ K}$ .

The most delicate many-body electron states require we go colder still. A key motivation for our work is the interest surrounding the even-denominator fractionalized quantum Hall state at Landau level filling factor  $\nu = 5/2$ , which is believed to exhibit exotic quantum statistics. In our samples, as we will see, this state is associated with an energy gap of  $\Delta \approx 450 \text{ mK}$ . Fortunately, we have tools for achieving such extreme cold, most important of which is dilution refrigeration.

---

<sup>1</sup>In Chapter 6 we explain how to experimentally demonstrate the two-dimensional nature of the electrons.

<sup>2</sup>See Chapter 6 for a discussion of the integer quantum Hall effect.

## 2.2 Dilution Refrigerators

The standard approach to reaching temperatures below about 300 mK is through *dilution refrigeration* [19]. A relatively recent invention of the 1960s [20], this method of refrigeration relies upon some fortunate properties of  $^3\text{He}$ – $^4\text{He}$  mixtures. Below about  $T = 0.87$  K, a mixture of liquid  $^3\text{He}$  and  $^4\text{He}$  will separate into a  $^3\text{He}$ -rich phase and a  $^3\text{He}$ -poor phase. As absolute zero temperature is approached, the  $^3\text{He}$ -rich phase will become pure  $^3\text{He}$ . Importantly, however, the  $^3\text{He}$ -poor phase will always contain a small fraction of  $^3\text{He}$ , approaching the universal value of 6.6% as  $T \rightarrow 0$ . This surprising fact is critical to the operation of a dilution refrigerator (DR).

Cooling occurs via the transfer of  $^3\text{He}$  atoms from the  $^3\text{He}$ -rich phase to the dilute,  $^3\text{He}$ -poor phase, due to the higher enthalpy of the atoms in the latter phase. This can be qualitatively understood in analogy to evaporation in which a pure liquid cools as some of its molecules transition to a gaseous phase. By creating a situation in which  $^3\text{He}$  atoms are continuously moved from the  $^3\text{He}$ -rich to poor phase, a state of the art DR can cool the mixture to temperatures below 10 mK!

Figure 2.1 contains a functional diagram of a generic DR. To thermally isolate the DR it is enclosed within an *inner vacuum can* or IVC. On the other side of the IVC wall the *main helium bath* shields the DR from the hot electromagnetic radiation of the outside world. Inside the DR, the amount of helium along with the precise  $^3\text{He}$  to  $^4\text{He}$  ratio must be such that the phase boundary occurs in the *mixing chamber*. Due to the  $^3\text{He}$ -rich phase's smaller mass density, it floats on top of the  $^3\text{He}$ -poor phase. A carefully positioned tube connects the lower portion of the mixing chamber—and hence, the  $^3\text{He}$ -poor phase—with a chamber called a *still*, in reference to the distillation-like nature of the DR. The still is maintained at  $T \approx 0.7$  K through the use of an external heater (not shown), a temperature at which the vapor pressure of  $^3\text{He}$  is about three orders of magnitude larger than that of  $^4\text{He}$ . Pumping on the still therefore removes almost exclusively  $^3\text{He}$  atoms. Removal of the  $^3\text{He}$  from the still produces an osmotic pressure that forces  $^3\text{He}$  up from the mixing chamber and, in turn, the transfer of  $^3\text{He}$  across the  $^3\text{He}$ -rich-poor phase interface.

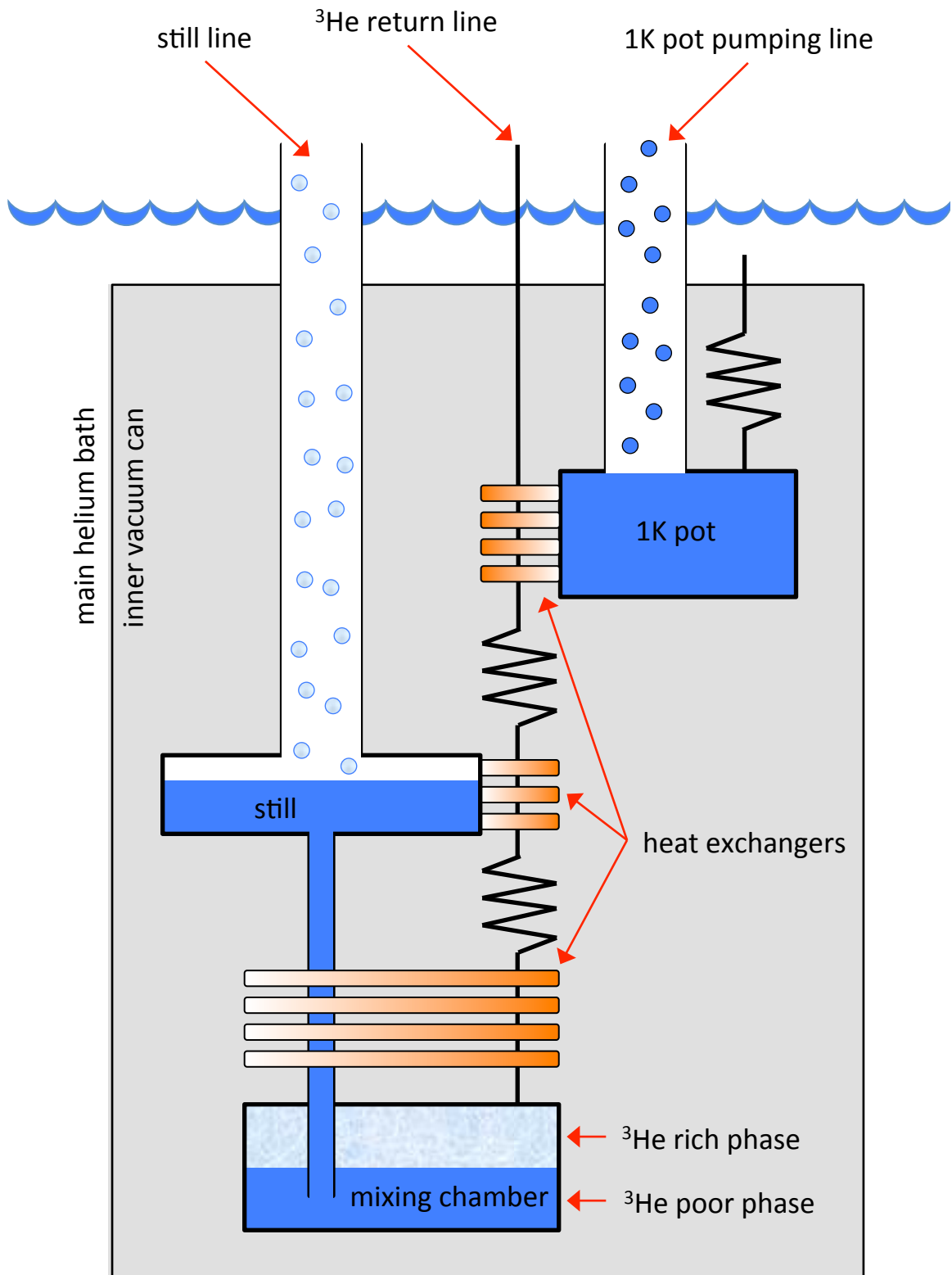


Figure 2.1: Functional diagram of a dilution refrigerator.

To achieve continuous cooling, the  $^3\text{He}$  removed from the still must find its way back to the  $^3\text{He}$ -rich phase within the mixing chamber. Toward this end, the exhaust of the still pump is routed back into the cryostat via a high-impedance capillary called the *return line*. A set of heat exchangers thermalize the  $^3\text{He}$  with a volume known as the *1K pot*. The 1K pot is a small reservoir of  $^4\text{He}$ —independent of the closed dilution circuit—that is continuously fed from the main helium bath. Pumping on the vapor of this  $^4\text{He}$  cools it to  $T \approx 1.2$  K, a temperature at which the  $^3\text{He}$  in the low-pressure (e.g. 10 mBar) return line readily re-condenses.

Following liquification, the  $^3\text{He}$  encounters the primary impedance of the return line before further cooling via another set of heat exchangers coupled to the still. Now at  $T \approx 0.7$  K, a second impedance is overcome prior to arriving at the final set of heat exchangers where thermalization with the  $^3\text{He}$ -poor phase between the still and mixing chamber occurs. Finally returning to the mixing chamber, we have come full-circle, completing the dilution refrigeration circuit.

The cooling power of a DR is harnessed by thermally anchoring an experiment to its mixing chamber (not shown in the figure). In our research we employed two different DR models. Our coldest experiments, involving the diving board devices, took place within an Oxford 200 TL shown in Fig. 2.2, which has a cooling power of about  $200 \mu\text{W}$  at  $T = 100$  mK and a base temperature of  $T \approx 17$  mK. Meanwhile, the hot-electron thermocouple experiments were conducted within an enhanced Oxford KelvinOx 25 ( $50 \mu\text{W}$  at  $T = 100$  mK with a base temperature of  $T \approx 30$  mK), however, we did not use this DR in a conventional manner as explained below in Section 2.6.

## 2.3 Cold Finger

As will be explained in Chapter 6, the usual method of realizing many-body, correlated physics within a 2DES is through the application of large magnetic fields. We can achieve field strengths as large as 14 T in our lab using a superconducting solenoid immersed in the helium of the cryostat's main bath. To minimize eddy currents in-

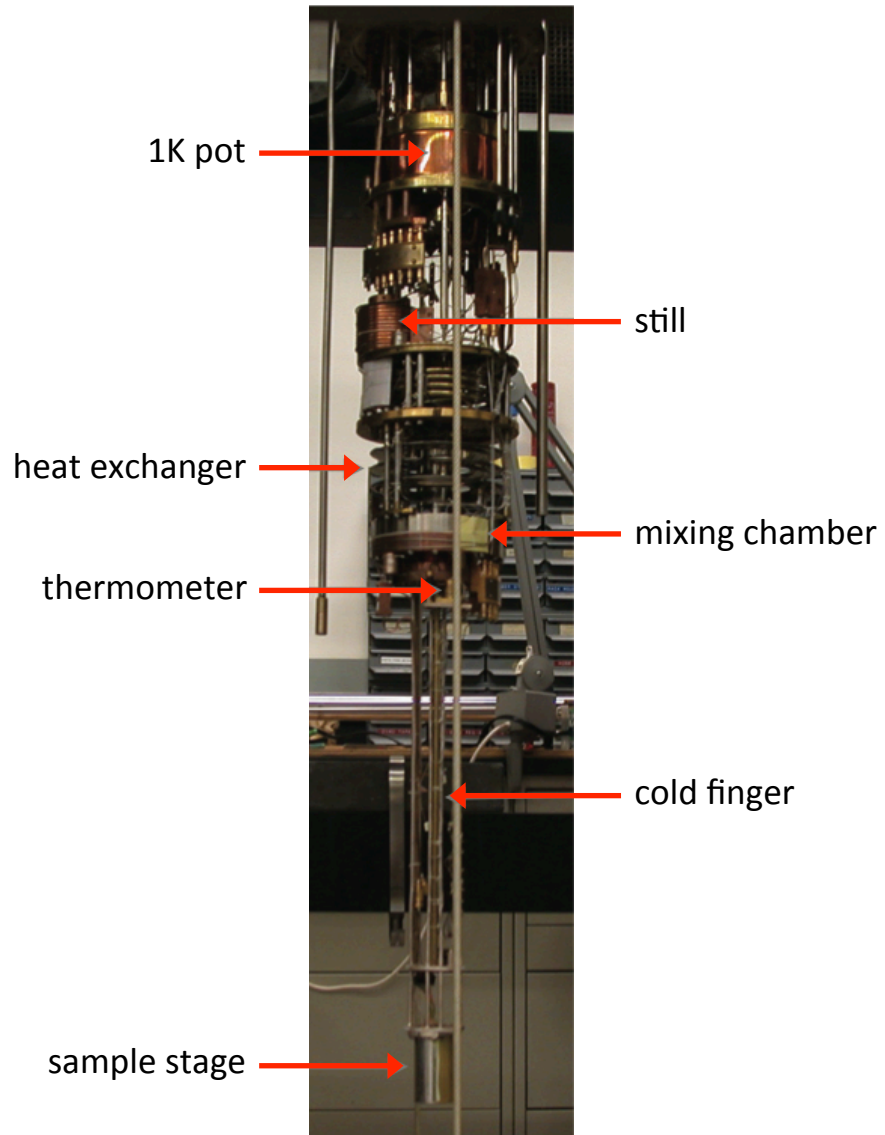


Figure 2.2: Oxford 200 TL dilution refrigerator equipped with cold finger and sample stage.

duced in the metal parts of the DR while changing the field strength, the magnet is located well below the mixing chamber. The sample stage is precisely positioned in the center of the magnet core via a long, highly thermally conducting set of rods collectively known as the *cold finger* (see Fig. 2.2). Interestingly, cold fingers are typically made using annealed silver rather than copper because the latter contains nuclear magnetic moments resulting in a strongly field dependent specific heat<sup>3</sup>. As the thermal link between the DR and the sample, an ideal cold finger would lack a temperature gradient and respond instantly to changes in mixing chamber temperature.

## 2.4 Connecting and Cooling the 2DES

The substrates of the diving board samples are anchored to the DR’s mixing chamber via a special gold-plated silver *sample stage* that is shown in Figs. 1.7 and 2.2. Indium soldering one end of the sample to a gold-plated bar that is bolted to a solid silver part that is in turn attached to the cold finger provides thermal ground to these devices. While this effectively cools the sample’s GaAs substrate, achieving the lowest temperatures for the 2DES itself is another matter.

Cooling electrons below  $T \sim 100$  mK is a key challenge of low-temperature condensed matter physics. High-mobility 2DESs such as ours are limited in their ability to cool via phonon emission in this so-called *Bloch-Grüneisen regime*, with measured energy relaxation rates varying as strongly as  $\propto T^5$  [22, 23]. To mitigate this issue, we connect low-pass filters in series with the 2DES ohmic contacts. In the case of our diving board experiments, these filters are formed by a 5 k $\Omega$  metal-film resistor and a 500 pF capacitor, which eliminates high frequency noise that would otherwise heat the 2DES. Perhaps even more importantly, we ground the capacitors to the cold finger. The idea is that while the capacitor acts like an open circuit with respect to our quasi-DC electrical measurements, it is thermally a short circuit, connecting the

---

<sup>3</sup>Some cryostats exploit this property of copper, or other materials with large nuclear moments like the intermetallic compound PrNi<sub>5</sub>, to construct cooling stages that utilize the principle of adiabatic nuclear demagnetization [21].

2DES to a reservoir of cold electrons.

A challenge complimentary to that of cooling electrons is determining their precise temperature. While a calibrated carbon resistance thermometer attached to the mixing chamber (see Fig. 2.2) reliably reports the temperature of a sample's lattice, the actual temperature of the 2DES is more elusive. Direct methods of measuring electronic temperature, such as Coulomb blockade [24], do exist but are difficult to implement. As will be discussed in this thesis, under certain circumstances, the 2DES's diffusion thermopower in the form of a thermocouple provides a relatively simple way of determining the electron temperature. For now, we may rest assured that any decoupling between the DR and the 2DES in our experiments is mild as evidenced by the fact that features of the electric and thermoelectric transport continue to evolve down to the DR's lowest temperatures.

Electrical connection to the outside world is made via twisted pairs of manganin wire that run up and out of the cryostat to a break-out box where measurement equipment may connect using BNC co-axial cables. The utility of the twisted pairs is that ambient electromagnetism will tend to thread adjacent loops formed by a pair such that induced voltages will mutually cancel out. To minimize the role of these wires as heat leaks, we heat-sink them at several points within the cryostat including the mixing chamber, still, 1K pot, and a flange at  $T = 4$  K.

The above considerations are very important to achieving the extremely low electron temperatures of our diving board experiments. The hot-electron thermocouple experiments, on the other hand, were more forgiving due to their operation at temperatures above  $\sim 0.5$  K. At these elevated temperatures electrons readily thermalize with the lattice in which they inhabit. In this case, setup is similar to that described above with the exception that the low-pass filters are omitted. And unlike the diving board devices, the thermocouple sample is simply affixed to a standard 18-pin plastic header that plugs into a socket of a standard sample stage located at the end of the KelvinOx's cold finger.

## 2.5 Sample Illumination

Achieving the ultra-high electron mobilities within our diving board samples requires one last critical step: sample illumination. During the initial cool-down of the cryostat, a red light-emitting diode, or LED, illuminates these samples continuously from room temperature down to  $\sim 10$  K. Unlike in a classical semiconductor, carriers from the silicon donors within AlGaAs can originate from both loosely bound hydrogenic states and more deeply bound *DX centers* [9]. In the latter case, the would-be carrier causes the lattice to relax around the donor resulting in a larger binding energy. Photons from the LED excite these trapped electrons resulting in their liberation, which in turn alters the lattice potential surrounding the donor in a way that prevents their recapture. This effect, known as *persistent photoconductivity*, often increases the 2DES's conductivity  $\sigma$ , density  $n$ , as well as mobility  $\mu_e$ .

Of the devices studied for this thesis, we only illuminate the diving board samples, which are cleaved from an ultra-high-mobility heterostructure wafer designed for this treatment. The hot-electron thermocouple, on the other hand, contains a number of aluminum top gates, which shield the underlying 2DES from incident photons. Illumination of this latter device would result in a non-uniform electron gas, which is not desirable for the associated experiments. In the case of the diving boards, we expose the sample to a red LED positioned directly overhead  $\sim 1$  cm away energized by a 1.5 mA current. The illumination occurs during the initial cooling of an experiment from room temperature down to  $T = 10$  K at which point the LED is turned off.

In practice, the precise consequences of illumination are not well understood. In our lab we have explored various illumination schemes and find that different procedures yield better results for other samples. For example, in previous experiments on a different heterostructure it was found that a one minute illumination at  $T = 1.6$  K worked best [25].

## 2.6 “High” Temperature Regulation

One regulates the temperature of a dilution refrigerator by applying heat to its mixing chamber. Commercial temperature controllers<sup>4</sup> utilizing control loop feedback mechanisms modulate the power to the mixing chamber heater in order to regulate the cryostat at a particular temperature. In normal operation a dilution refrigerator can be maintained at temperatures as high as  $T \sim 500$  mK in this manner. At higher temperatures the  $^3\text{He}$ - $^4\text{He}$  mixture can no longer separate into distinct liquid phases [19] and the cryostat becomes unstable.

The hot-electron thermocouple experiment described in Chapter 5 requires stable regulation at temperatures much higher than those accessible via dilution refrigeration. At the same time, other factors—in particular, the ability to continuously regulate temperature—made the Oxford KelvinOx an attractive venue for the experiment. Fortunately, an ad hoc method is known in our lab that allows operation of a dilution refrigerator at temperatures in the range 0.6 – 6.0 K. By circulating only 15% of the  $^3\text{He}$ - $^4\text{He}$  mixture, maintaining the normal molar fraction of  $^3\text{He}$ , a nominal dilution refrigerator provides continuous thermal stability at temperatures between  $T \approx 0.6$  and 6 K. In this mode, the  $^3\text{He}$ - $^4\text{He}$  mixture comprises a single liquid phase and cooling occurs primarily through pumping on the vapor of the  $^3\text{He}$ .

## 2.7 Summary

The cryogenic environment explored in this chapter is an essential ingredient for all of the experiments discussed in this thesis. We have seen how experimental temperatures map to characteristic energies such as the Fermi energy of the 2DES as well as that of the first excited subband of the GaAs quantum well. Even lower temperatures are required to resolve the spectra of the quantum Hall regime.

Dilution refrigerators, the workhorses of low-temperature laboratories such as ours, provide the means for achieving such extreme cold (as low as 10 mK!). We

---

<sup>4</sup>We use Linear Research models LR-400 and LR-700 temperature controllers.

have outlined the principles by which these cryostats operate as well as described the manner in which the 2DES is situated within and thermally coupled to them. We also discussed how sample illumination uses persistent photoconductivity to liberate additional carriers in order to achieve the highest electron mobilities. Finally, we described how a dilution refrigerator can be run in an unconventional mode that allows stable temperature regulation within the elevated range of 0.6 to 6 K, which is ideal for the hot-electron thermocouple experiments covered in Chapter 5.

## Chapter 3

# Thermopower of 2D Electrons

The conversion of heat to electricity is enabled by phenomena collectively known as the *thermoelectric effect*. The singular form is a misnomer as the thermoelectric “effect” actually comprises three effects: the *Seebeck effect*, *Peltier effect*, and *Thomson effect*. Our focus is on the first of these, which is referred to as simply *thermopower* throughout this thesis. This chapter reviews the basic theory of thermopower within the 2DES in the absence of an externally applied magnetic field. We discuss the two contributions, *diffusion thermopower* and *phonon drag*, as well as the former’s relationship to entropy and the latter’s undesirability. The two chapters that follow will describe experimental setups for measuring diffusion thermopower while minimizing phonon drag. In Chapter 7 we extend our theoretical foundation into the strong magnetic field regime.

### 3.1 The Seebeck Effect

In 1821 the German physicist Thomas Johann Seebeck discovered that a metallic loop consisting of two dissimilar metals produces a voltage when the junctions are held at different temperatures. He found the voltage to depend only on the temperature difference between the junctions; that is, the voltage is indifferent to the distribution of the temperature along the metals. A variation on this original experiment which employs an open-circuit consisting of a single junction between the metals forms the essence of a *thermocouple*, a simple technology with countless applications including

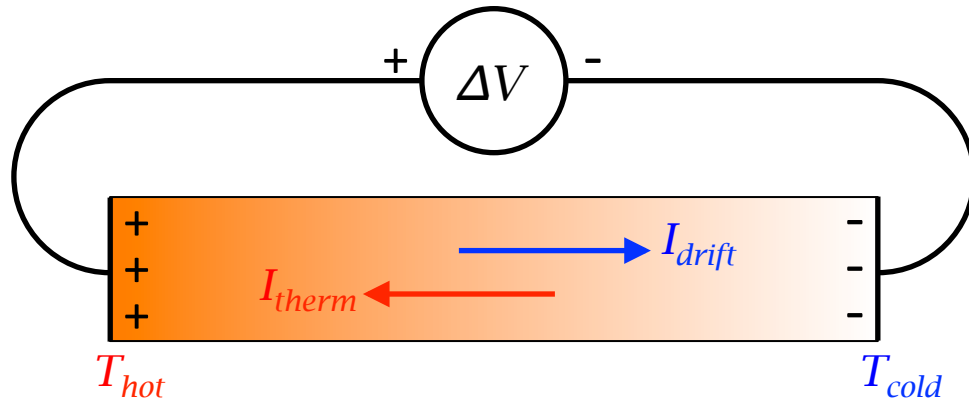


Figure 3.1: Illustration of Seebeck effect. A temperature gradient along an open-circuited metallic system results in mutually canceling thermoelectric and drift currents  $I_{therm}$  and  $I_{drift}$ . The charge separation producing  $I_{drift}$  yields a thermovoltage  $\Delta V$ .

temperature sensors, pressure gauges, bolometers, and energy conversion.

We can qualitatively understand thermopower by considering a single metallic system whose ends are held at different temperatures: the left end at  $T_{hot}$  and the right end at  $T_{cold}$  as illustrated in Fig. 3.1. In this particular metal, let us suppose that electrons are the only carriers. To the ends of our metal we will attach the probes of an ideal voltmeter, which draws no current and whose leads have no thermoelectric response of their own. The positive probe is connected to the end held at  $T_{hot}$  and the negative probe is connected to the end held at  $T_{cold}$ . What would our ideal voltmeter measure?

Due to thermal diffusion and phonon scattering, more electrons from the hotter end will migrate toward the colder end than vice versa such that a net leftward (electrons have negative charge!) thermoelectric current  $I_{therm}$  is established. (Do not misconstrue  $I_{therm}$  as a thermal or energy current; it is an electrical current that arises in response to a temperature gradient.) Since no current is drawn from the end of the metal an excess of electrons will accumulate on the right side. This results in a net negative charge density on the right side and a net positive charge density on the left side of the metal. The separation of charge produces an electric field pointing

rightward thereby establishing a rightward drift current  $I_{drift}$ . In steady state,  $I_{drift}$  is equal in magnitude but opposite in direction to  $I_{therm}$  such that zero net current flows. The voltmeter measures a voltage  $\Delta V$  resulting from the electric field produced by the charge separation.

For sufficiently small differences between  $T_{hot}$  and  $T_{cold}$  we may write

$$\Delta V = -S \cdot (T_{hot} - T_{cold}), \quad (3.1)$$

where  $S$  is an intrinsic material parameter known as the *Seebeck coefficient* or thermopower. Note that for our n-type metal,  $S < 0$  such that  $\Delta V > 0$ . For a p-type system, where holes are the dominant carriers,  $S > 0$ ; that is, like a Hall measurement, thermopower reveals the sign of the charge carriers. Common metals typically have values of  $S$  on the order of microvolts per Kelvin at room temperature [26].

A more general expression than that of Eq. 3.1, which is only valid for small temperature differences, can be written in terms of the local electric field

$$E = S(T) \cdot \nabla T|_{j=0}, \quad (3.2)$$

where  $S(T)$  is the local temperature dependent thermopower,  $\nabla T$  is the local temperature gradient, and  $|_{j=0}$  indicates that no electrical current is allowed to flow. By integrating Eq. 3.2 over the length of the metal we may derive the general expression for the thermovoltage

$$\Delta V = - \int_{T_{cold}}^{T_{hot}} S(T) \cdot dT. \quad (3.3)$$

Let us pursue the picture offered by Fig. 3.1 of thermopower in terms of mutually canceling electrical currents. An electrical current density  $j$  consists of two terms:

$$j = \sigma E + \epsilon \nabla T, \quad (3.4)$$

where  $\sigma$  is the familiar electrical conductivity and  $\epsilon$  is the *thermoelectric conductivity*. The first term of Eq. 3.4 is well known as Ohm's Law. We typically neglect the second

term since more than often it is much smaller than the first term. In fact, only in special cases, such as that of a perfect superconductor or a perfect insulator, does the  $\epsilon\nabla T$  term truly vanish. Setting  $j = 0$  in Eq. 3.4 yields

$$E = - \frac{\epsilon}{\sigma} \nabla T \Big|_{j=0}, \quad (3.5)$$

from which it follows

$$S(T) \equiv -\frac{\epsilon}{\sigma}. \quad (3.6)$$

Thus we see that thermopower  $S(T)$ , a transport coefficient, may be defined in terms of two other, more fundamental, transport coefficients  $\sigma$  and  $\epsilon$ . Moreover, these more fundamental coefficients are associated with the drift and thermoelectric currents  $I_{drift}$  and  $I_{therm}$  of Fig. 3.1.

Importantly, since ideal voltmeters like that of Fig. 3.1 do not exist, one cannot directly measure the thermopower of a single material. Real voltmeters have leads with thermopowers of their own, which also develop a thermoelectric response. For instance, in the limit of small temperature differences, substituting a real voltmeter into Fig. 3.1 would yield

$$\Delta V = - (S - S_{lead}) \cdot (T_{hot} - T_{cold}), \quad (3.7)$$

where  $S_{lead}$  is the thermopower of voltmeter's leads. During real measurements one always has a thermocouple with which one observes a thermoelectric response due to the difference between two thermopowers.

## 3.2 Classical Transport: Drude Model

Before delving into the details of thermoelectric transport within electron systems, it is helpful to briefly consider the classic model of electronic transport in matter. The motion of electrons inside the periodic potential of an ideal semiconductor can

be modeled as that of free electrons with a modified *effective mass*  $m^*$ . In the case of our GaAs heterostructures, the relevant value is the  $\Gamma$ -point conduction-band mass such that  $m^* = 0.067m_0$ , where  $m_0$  is the bare electron mass<sup>1</sup>. At the same time, no crystal structure is perfect, and even the ultra-clean samples we study have impurities and lattice imperfections. We can therefore model the motion of our 2D electrons like frictionless pinballs that occasionally bounce off obstacles.

The Drude model [26] does just this by applying classical kinetic theory to describe electronic transport through a disordered medium. The *momentum lifetime*  $\tau_m$  limits an electron's time averaged velocity  $v_d$ —known as the *drift velocity*—when subjected to an electric field  $E$  such that  $v_d = -eE\tau_m/m^*$  (let us assume  $\nabla T = 0$ ). With the relation  $j = -nev_d$  between the drift velocity and the current density  $j$ , together with Ohm's law,  $j = \sigma E$ , we arrive at an expression for the electrical conductivity:  $\sigma = ne^2\tau_m/m^*$ . Note that, given the definition of electron mobility,  $v_d = \mu_e E$ , we may also write the conductivity as  $\sigma = ne\mu_e$ , making explicit the intuitive result that conductivity scales with the mobility of the system. In the next section we will use this relationship between conductivity and electron density to derive a simple expression for the diffusion thermopower of a 2DES.

### 3.3 Mott's Formula

In the low-temperature limit we may ignore thermoelectric effects from phonons, and therefore, consider the thermoelectric response of an electron system as driven solely by diffusion. Using the linear response transport coefficients obtained through the Chester-Thellung-Kubo-Greenwood formalism [27, 28, 29] we may derive an expression for the *diffusion thermopower*  $S^d$ . An electronic system subjected to both an electric field  $E$  and a temperature gradient  $\nabla T$  will experience the current density

$$j = - \int_{-\infty}^{\infty} \sigma_0(\varepsilon) \frac{\partial f}{\partial \varepsilon}(\varepsilon, \mu, T) d\varepsilon \cdot E + \frac{1}{e} \int_{-\infty}^{\infty} \sigma_0(\varepsilon) \frac{\partial f}{\partial T}(\varepsilon, \mu, T) d\varepsilon \cdot \nabla T, \quad (3.8)$$

---

<sup>1</sup>See Appendix A for a list of properties of a 2DES.

where  $f(\varepsilon, \mu, T)$  is the Fermi-Dirac distribution and  $\sigma_0(\varepsilon)$  is the electrical conductivity of carriers at energy  $\varepsilon$ , which equals the total electrical conductivity at  $T = 0$  for  $\mu = \varepsilon$ . Comparing Eqs. 3.4 and 3.8 we see that

$$\sigma(\mu, T) = - \int_{-\infty}^{\infty} \sigma_0(\varepsilon) \frac{\partial f}{\partial \varepsilon}(\varepsilon, \mu, T) d\varepsilon \quad (3.9)$$

and

$$\epsilon(\mu, T) = \frac{1}{e} \int_{-\infty}^{\infty} \sigma_0(\varepsilon) \frac{\partial f}{\partial T}(\varepsilon, \mu, T) d\varepsilon. \quad (3.10)$$

Given that  $S \equiv -\epsilon/\sigma$  (Eq. 3.6) we may write

$$S^d(\mu, T) = -\frac{1}{\sigma(\mu, T)} \frac{1}{e} \int_{-\infty}^{\infty} \sigma_0(\varepsilon) \frac{\partial f}{\partial T}(\varepsilon, \mu, T) d\varepsilon. \quad (3.11)$$

Since  $f(\varepsilon, \mu, T)$  is a function of  $(\varepsilon - \mu)/k_B T$ , it follows that  $\partial f/\partial T = -(\varepsilon - \mu)/k_B T \cdot \partial f/\partial \varepsilon$ , where  $k_B$  is Boltzmann's constant, such that

$$S^d(\mu, T) = \frac{1}{\sigma(\mu, T)} \frac{1}{ek_B T} \int_{-\infty}^{\infty} \sigma_0(\varepsilon) (\varepsilon - \mu) \frac{\partial f}{\partial \varepsilon}(\varepsilon, \mu, T) d\varepsilon. \quad (3.12)$$

Equation 3.12, known as the *Cutler-Mott formula*, is a linear response expression for the diffusion thermopower of noninteracting, free electrons at zero magnetic field that is valid at all temperatures. The factor  $(\varepsilon - \mu)$  makes explicit how the contributions to the thermopower from electrons and holes have opposite sign. Meanwhile, at low temperatures, the factor  $\partial f/\partial \varepsilon$  causes the integrand to vanish everywhere except within a range of energy on the order of  $k_B T$  about  $\mu$ . Thus we see that the variation of  $\sigma_0(\varepsilon)$  about  $\mu$  governs the behavior of  $S^d$ . In particular, for  $S^d$  to be nonvanishing  $\sigma_0(\varepsilon)$  must break the particle-hole symmetry about  $\mu$ . Moreover, since  $\sigma_0(\varepsilon)$  is directly proportional to the density of extended states at  $\varepsilon$  [30], we see that  $S^d$  is a highly sensitive probe of the states at the Fermi surface.

In the limit of zero temperature we may derive a more simple expression for  $S^d$ . By deferring the temperature derivative in Eq. 3.11 until after approximating the integral  $\int_{-\infty}^{\infty} \sigma_0(\varepsilon) f(\varepsilon, \mu, T) d\varepsilon$  with a *Sommerfeld expansion* [31] and then retaining only the

lowest order term in temperature  $T$ , we arrive at *Mott's formula* for thermopower [32]:

$$S^d(\varepsilon_F, T) \simeq -\frac{\pi^2 k_B^2}{3e} \frac{1}{\sigma} \left. \frac{d\sigma}{d\varepsilon} \right|_{\varepsilon=\varepsilon_F} T, \quad (3.13)$$

where we use the fact that  $\mu \rightarrow \varepsilon_F$  as  $T \rightarrow 0$ .

The value of Mott's formula lies in its simplicity compared to the integral expression of Eq. 3.12. By evaluating Mott's formula in the context of the Drude model we can obtain an even more efficacious expression for thermopower in terms of often readily measurable quantities. In Section 3.2 we saw that the Drude model yields a simple expression for electrical conductivity:  $\sigma = ne^2\tau_m/m^*$ , where  $n$  is the electron density,  $m^*$  the electron effective mass, and  $\tau_m$  the momentum lifetime. Meanwhile, the density (and hence energy) dependence of  $\tau_m$  will follow a simple power law over a large range of parameter values; that is,  $\tau_m = \tau_{m,0}n^p$ , where  $\tau_{m,0}$  and  $p$  are constants. The value of the exponent  $p$  depends on the details of the scattering mechanisms and is typically  $0.5 \lesssim p \lesssim 1.5$  for 2DESs in modulation-doped GaAs heterostructures at low temperatures where  $\tau_m$  is dominated by impurity scattering [33]. The conductivity in our Drude picture is then related to the electron density as  $\sigma \propto n^{1+p}$  such that the Mott formula may be expressed as a function of  $n$  and  $T$ :

$$S^d(n, T) \simeq -\frac{\pi^2 k_B^2}{3e} \frac{1}{\sigma} \frac{d\sigma}{dn} \frac{dn}{d\varepsilon} T = -\frac{\pi k_B^2 m^*}{3\hbar^2 e} (1+p) \frac{T}{n}. \quad (3.14)$$

In deriving Eq. 3.14 we used the fact that noninteracting and otherwise free electrons confined to two dimensions have a constant density of states due to their parabolic dispersion relation,  $\varepsilon = \hbar^2 \mathbf{k}^2 / 2m^*$ , given by

$$\frac{dn}{d\varepsilon} = \frac{m^*}{\pi \hbar^2}. \quad (3.15)$$

Thus we have arrived at a surprisingly simple result. Equation 3.14 says that at sufficiently low temperatures (i.e.  $k_B T \ll \varepsilon_F$ ), the thermopower of a two-dimensional metal is given by the ratio of the temperature  $T$  to the electron density  $n$ . Equally

surprising, it so happens that this ratio is simply related to the entropy of our electron system.

### 3.4 Thermopower vs Entropy

The low-temperature (i.e.  $k_B T \ll \varepsilon_F$ ) entropy per area of the 2DES is given by [34]

$$\mathcal{S} = \frac{\pi^2 k_B^2}{3} \frac{dn}{d\varepsilon} T = \frac{\pi k_B^2 m^*}{3\hbar^2} T. \quad (3.16)$$

The diffusion thermopower may therefore be regarded as the entropy per carrier per carrier charge modulo the factor  $(1 + p)$ . That is,

$$S^d = (1 + p) \frac{\mathcal{S}}{qn}, \quad (3.17)$$

where  $q$  is the carrier charge (e.g.  $q = -e$  in the case of electrons). In fact, while we have only demonstrated the relationship between entropy and diffusion thermopower for 2D electrons in the limit of zero temperature and in zero magnetic field, it is rigorously established [7] that this proportionality holds in general for both degenerate and nondegenerate noninteracting electrons in both 2D and 3D.

We have already seen that thermopower reveals the sign of the charge of the carriers in a system. Moreover, while deriving Mott's formula we argued that  $S^d$  is highly sensitive to the states at the Fermi surface. Here we are going further, contending that in the special case of noninteracting free electrons diffusion thermopower  $S^d$ , a transport coefficient, is directly proportional to the entropy per carrier  $\mathcal{S}/n$ , a thermodynamic variable! In Chapter 7 we will extend this claim to otherwise free two-dimensional electrons in a strong magnetic field and in Chapters 8 and 9 we will see that this relationship is believed to hold, at least in special cases, to strongly correlated electron systems. Indeed, this deep connection between entropy and  $S^d$  looms large in motivating our efforts to improve our measurement capabilities.

One must exercise caution in over-interpreting the results of thermoelectric measurements, however. The validity of simple interpretations of thermopower are limited

to simple systems. Even when determining the sign of the charge carriers one must be circumspect. For example, if a system consists of both electrons and holes in parallel (e.g. a semimetal) their contributions to the thermopower will be of opposite sign. This contrasts with the electrical conductivity in which their contributions sum constructively:  $\sigma = \sigma_e + \sigma_h$ , where  $\sigma_e$  is the contribution from electrons and  $\sigma_h$  that from holes. Applying Mott's formula (Eq. 3.13) we find

$$S^d \simeq -\frac{\pi^2 k_B^2}{3e} T \frac{1}{\sigma_e + \sigma_h} \left( \frac{d\sigma_e}{d\varepsilon} - \frac{d\sigma_h}{d\varepsilon} \right) \Big|_{\varepsilon=\varepsilon_F}, \quad (3.18)$$

which may be written as

$$S^d \simeq \frac{\sigma_e}{\sigma_e + \sigma_h} S_e^d + \frac{\sigma_h}{\sigma_e + \sigma_h} S_h^d, \quad (3.19)$$

where  $S_e^d$  is the diffusion thermopower that would exist in the absence of the holes and  $S_h^d$  that in the absence of the electrons. If  $S_e^d$  and  $S_h^d$  were both large but equal in magnitude and, at the same time,  $\sigma_e = \sigma_h$ , the total diffusion thermopower  $S^d$  would be zero. The naive (incorrect) interpretation would be that the carriers have little, if any, entropy! While the proportionality between diffusion thermopower and entropy per carrier holds for the electrons or holes individually, it is not valid for the system as a whole.

It so happens that an expression similar to Eq. 3.19 applies generally to an arbitrary collection of species of varying attributes (e.g. charge, effective mass, scattering times). To see this, consider the electrical current for an arbitrary system consisting of several parallel conducting carrier species:

$$j = \sum_i \sigma_i E + \sum_i \epsilon_i \nabla T, \quad (3.20)$$

where  $\sigma_i$  and  $\epsilon_i$  are the electrical conductivity and thermoelectric conductivity of species  $i$ , respectively. Setting  $j = 0$  yields

$$E = - \left( \sum_i \sigma_i \right)^{-1} \sum_i \epsilon_i \nabla T \Big|_{j=0}, \quad (3.21)$$

from which it follows

$$S = - \left( \sum_i \sigma_i \right)^{-1} \sum_i \epsilon_i = \left( \sum_i \sigma_i \right)^{-1} \sum_i \sigma_i S_i, \quad (3.22)$$

where  $S_i \equiv -\epsilon_i/\sigma_i$  is the thermopower that would exist if only species  $i$  were present. Note that Eq. 3.22 is neither limited to low temperatures nor diffusion thermopower; rather, it holds as long as Eq. 3.20 is valid. In the case of diffusion thermopower arising from multiple carrier species conducting in parallel, combining Eq. 3.17 and Eq. 3.22 yields

$$S^d = \left( \sum_i \sigma_i \right)^{-1} \sum_i \sigma_i (1 + p_i) \frac{\mathcal{S}_i}{q_i n_i}, \quad (3.23)$$

where  $p_i$ ,  $\mathcal{S}_i$ ,  $q_i$ , and  $n_i$  are the scattering parameter, entropy per area, carrier charge, and carrier density of species  $i$ , respectively.

### 3.5 Phonon Drag Thermopower

Even in the case of a single species system the entropic interpretation of thermopower can be misleading since it is only valid for the diffusion contribution  $S^d$ . Another contribution, known as *phonon drag*  $S^g$ , arises from the transfer of momentum between the thermally excited vibrational modes of the three-dimensional lattice and the two-dimensional electrons. The contributions from diffusion and phonon drag are additive yielding a total thermopower  $S = S^d + S^g$ , while the above arguments connecting thermopower and the entropy of the 2DES only apply to the former. Unfortunately, in the majority of experimental thermopower studies of the 2DES in GaAs at low temperatures,  $S^g$  dominates the thermoelectric response making observations of  $S^d$

difficult<sup>2</sup>.

A detailed description of the complicated mechanics behind phonon drag is beyond the scope of this thesis, but the essence of the phenomenon is quite simple<sup>3</sup>. In the presence of a temperature gradient  $\nabla T$  a net phonon current will flow in the substrate from hot to cold. Referring once again to our picture of mutually canceling currents (see Fig. 3.1), electron-phonon scattering events transfer momentum to the electrons, which produces a thermoelectric current that adds constructively to that from electron diffusion (Eq. 3.10) to yield the total  $I_{therm}$ . The drift current  $I_{drift}$  required to cancel  $I_{therm}$  is therefore larger resulting in a larger net thermopower.

In a regime where impurity scattering limits the electrical conductivity, we may express the net thermopower as

$$S = S^d + S^g = -\frac{\epsilon^d + \epsilon^g}{\sigma}, \quad (3.24)$$

where  $\epsilon^d$  is the thermoelectric conductivity associated with electron diffusion given by Eq. 3.10 and  $\epsilon^g$  is the thermoelectric conductivity due to phonon drag. Semiclassically, and by employing Debye approximations, Nicholas [38]—whose results were extended by Miele et al. [39]—found that the thermoelectric conductivity can be written as

$$\epsilon^g = \sum_s \frac{m^* v_s \Lambda_s}{e T \tau_{ep}^s} \sigma, \quad (3.25)$$

where  $\Lambda_s$  is the phonon mean free path,  $v_s$  is the velocity, and  $\tau_{ep}^s$  is the electron-phonon momentum relaxation time associated with vibrational mode  $s$ . Equation 3.25 assumes a low-temperature 2DES that is highly degenerate and does not appreciably impact the phonon distribution, which is appropriate for our experimental situation

---

<sup>2</sup>In non-piezoelectric material systems, such as Si-MOSFETs and graphene, the phonon drag contribution is much less than that of diffusion thermopower at temperatures where the former dominates the thermoelectric response of 2D electrons in GaAs. At the same time, the electron mobilities achieved in these systems are orders of magnitude less than that of electrons in GaAs heterostructures.

<sup>3</sup>For an overview of theoretical and experimental studies of phonon drag, see reviews by Gallagher and Butcher [35] and Fletcher et al. [36, 37].

in the absence of a magnetic field<sup>4</sup>. In contrast, Eq. 3.25 is not valid in the case of a bulk metal where electron-phonon interactions do significantly alter the phonon distribution. The relaxation time  $\tau_{ep}^s$  is analogous to the momentum lifetime  $\tau_m$  used in our discussion of the Drude model in Section 3.2. Pursuing this analogy, we may define the quantity  $\mu_{ep}^s = e\tau_{ep}^s/m^*$  as the mobility the electrons would have if the only scattering events were those with phonons of mode  $s$ . (Note, however, that in the current model the actual electron mobility is impurity limited such that  $\mu_e = e\tau_m/m^*$ .) The phonon drag contribution to thermopower is therefore

$$S^g = -\frac{\epsilon^g}{\sigma} = -\sum_s \frac{v_s \Lambda_s}{\mu_{ep}^s T}. \quad (3.26)$$

An interesting aspect of this result is that even though its validity requires that the actual electron mobility  $\mu_e$  be impurity limited, it says that  $S^g$  is independent of  $\mu_e$ . And this is indeed verified experimentally [36].

A key feature of this expression for phonon drag is the appearance of  $\mu_{ep}^s$  in the denominator. We mentioned in Section 2.4 that cooling a high-mobility GaAs/AlGaAs 2DES below about  $T = 100$  mK, well into the so-called Bloch-Grüneisen regime, is challenging due to the rapid decline in phonon emission rates with falling temperature. This is precisely the physics represented by  $\mu_{ep}^s$ , which is inversely proportional to the rate at which momentum may be transferred between the electrons and phonons of mode  $s$ . Through measurements of electrical conductivity, Störmer et al. [22] showed that  $\mu_{ep}^s \propto T^{-5}$  for piezoelectric electron-phonon scattering in this regime, which is characterized by phase-space restrictions resulting from the size of phonon wave vectors relative to  $k_F$  of the 2DES. Combining this result with Eq. 3.26 leads us to expect  $S^g \propto T^4$ . Experimentally, measurements attributed to phonon drag behave like  $S \propto T^p$  with values of  $p$  between 2 and 4 [40, 41, 42, 43]. The lower values of  $p$  are likely due to the enhancement of electron-phonon interactions that occur away from the Bloch-Grüneisen regime.

---

<sup>4</sup>Equation 3.25 is only valid in a semiclassical regime and is no longer applicable in the presence of a strong magnetic field. We discuss the consequences of a strong magnetic field in chapters 6 and 7.

Given our interest in diffusion thermopower  $S^d$  and the information contained therein, in our view the phonon drag contribution  $S^g$  is a parasitic effect to be minimized. In practice this has proven difficult as, historically, measurements of high-mobility degenerate 2DES thermopower are dominated by phonon drag at all but the lowest accessible temperatures. The traditional experimental approach utilizes a diving board setup similar to our own described in Chapter 4. In such experiments that target high-mobility two-dimensional electrons or holes in GaAs/AlGaAs [40, 41, 42, 43] a crossover from the diffusion dominated to the phonon drag dominated regimes occurs below  $T \sim 400$  mK, the exact temperature depending on the details of the sample and experimental setup. Being confined to such low temperatures limits the precision of measurements of temperature dependence. Moreover, the magnitude of  $S^d$  signals decline rapidly with temperature making low-temperature measurements a further challenge.

The study of two-dimensional holes rather than electrons offers some advantage. The first observation of Mott-like thermopower in a high-mobility ( $\mu_h \approx 700,000$  cm<sup>2</sup>/Vs) two-dimensional system was in a p-type GaAs/AlGaAs heterostructure [40]. This can be understood as a consequence of the larger hole effective mass (see Eq. 3.14), which is typically about four times that of two-dimensional electrons in GaAs [44].

Modest reductions in phonon drag can be achieved by reducing the phonon mean free path  $\Lambda_s$ . In Chapter 4 we discuss how thinning the GaAs substrate of our diving board devices can, in principle, reduce the value of  $\Lambda_s$  by more than a factor of three. At the same time, the crossover temperature into the Bloch-Grüneisen regime can be increased through enhancement of the electron density  $n$ , and hence,  $k_F$  [22], which should also increase the diffusion-phonon drag crossover temperature [42]. These tactics have a small impact, however, compared to the suppression of phonon drag achieved by heating the 2DES directly as in the case of our hot-electron thermocouple technique, which is discussed in Chapter 5.

### 3.6 Summary

The thermoelectric effect gives rise to an electric field within the 2DES in response to a temperature gradient. For a given temperature gradient, the magnitude and sign of this thermoelectric field reflects intrinsic properties of the 2DES including the sign of the carriers (e.g. electrons versus holes), carrier effective mass, temperature, and the energy dependence of the momentum lifetime. We denote the ratio of thermoelectric field to temperature gradient (when no current is allowed to flow) by the transport coefficient *thermopower*.

In the relatively simple case of noninteracting, free 2D electrons in the limit of zero temperature, the thermopower is given by the Mott Formula, which says thermopower is directly proportional to temperature and inversely proportional to the electron density or Fermi temperature. Significantly, in regimes where the Mott formula holds, we have that thermopower is proportional to the entropy per charge carrier of the system. In subsequent chapters, we will reconsider this relationship between thermopower and entropy in the presence of a strong magnetic field (Chapter 7) as well as when electron-electron interactions are significant (Chapters 8 and 9).

At finite temperatures, another thermoelectric effect arises in addition to the diffusion thermopower described by the Mott formula. This additional contribution, known as phonon drag, is the result of phonon-electron scattering which results in momentum transfer between the electrons and the vibrational modes of the surrounding crystal lattice. Phonon drag, which historically has dominated the thermoelectric signals of high-mobility 2DESs, obfuscates the information-rich diffusion thermopower we wish to observe. In the following chapters, which discuss our thermopower measuring techniques, we describe and evaluate various strategies for overcoming this particular challenge.

## Chapter 4

# Diving Board Technique

This chapter introduces our technique for measuring the thermopower of 2D electrons of the highest mobility. The diving board technique is also our preferred method for measuring thermopower in the presence of an externally applied magnetic field. This is due to the fact that we establish temperature gradients in these devices using phonon mediated thermal currents, which are independent of the field due to their charge neutrality. Consequently, this style of experiment is very well suited for studying the thermoelectric response of the strongly correlated phases of the 2DES that are encountered in the clean, high-field limit. Two devices are described in this chapter, diving boards A and B. Our original experiments were carried out using diving board A which suffers from long thermal relaxation times that initially limited our measurement abilities. Diving board B overcomes these limitations via an improved design. With the exception of Chapter 5, which describes an alternative thermopower measurement technique, the results presented in this thesis were acquired using these diving board devices.

The chapter begins with a description of diving board A's layout. This is followed by a discussion of the temperature calibration protocol used for both of our diving board devices. Our quasi-DC thermopower measurement technique used with diving board A is explained. We then review the thermopower results from diving board A acquired without an externally applied magnetic field. The problem of long thermal relaxation times, which limits the regimes accessible with diving board A, is then discussed, which motivates the introduction of diving board B. After reviewing the

features and thermopower measurement protocol of diving board B, we discuss a puzzle that remains unsolved regarding low-field thermopower data from this device.

## 4.1 Diving Board A

The traditional approach to achieving a temperature gradient along a 2DES is to impose either a bridge-like or diving board-like geometry onto the substrate [35, 36, 45, 46, 47, 48, 49, 41, 50, 40, 51, 42, 52, 53, 43, 54, 55]. The principle is the same for the two geometries: Attach or fabricate a resistive element onto the suspended portion of the sample such that dissipated heat flows through the substrate to a boundary that is attached to a thermal reservoir.

An illustration<sup>1</sup> of diving board A is shown in Fig. 4.1. As described in Section 1.2.2, the sample is  $3 \times 12 \text{ mm}^2$  with a substrate thinned to  $130 \text{ }\mu\text{m}$ . Following illumination<sup>2</sup>, the sample has a density of  $n = 2.9 \times 10^{11} \text{ cm}^{-2}$  and a mobility of  $\mu_e = 3.1 \times 10^7 \text{ cm}^2/\text{Vs}$ . To one end is attached a strain gauge that serves as a heater ( $315 \text{ }\Omega$  at cryogenic temperatures) while the other end is indium-soldered to a silver block that is, in turn, bolted to the cold finger of a cryostat. We pattern the GaAs/AlGaAs heterostructure to confine the 2DES to two  $3 \times 3 \text{ mm}^2$  mesas. Electrical contact is provided via six InSn ohmic contacts positioned on the periphery of each mesa to which are attached  $25 \text{ }\mu\text{m}$  diameter manganin wires. For fabrication details, see Section 1.2.2 and Appendix B.

By passing current through the strain gauge heater, a heat flux  $Q$  flows along the length of the sample to the silver block, which serves as thermal ground. This establishes a temperature gradient along the diving board that is imparted to the 2DES via phonon-electron interactions. We then observe the thermoelectric response of the 2DES by measuring voltages as shown in the figure.

---

<sup>1</sup>An actual photograph of diving board A was shown in Chapter 1 in Fig. 1.7.

<sup>2</sup>See Section 2.5 for a discussion of sample illumination.

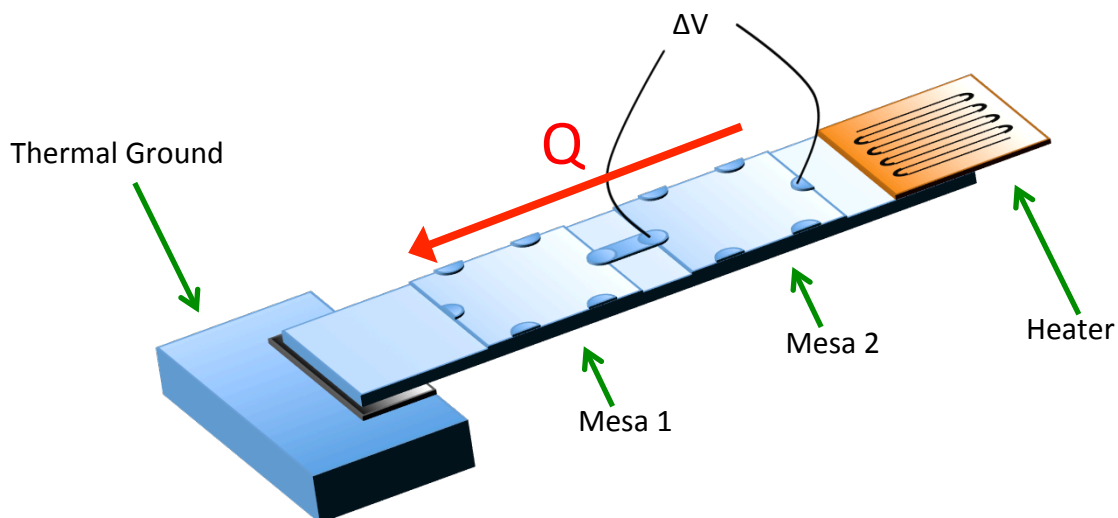


Figure 4.1: 2DES thermopower diving board technique.

### 4.1.1 Temperature Calibration

Of course, to convert measurements of thermoelectric voltages into measurements of thermopower, one must independently measure the temperature and temperature gradient of the system. Traditionally, this is achieved by attaching thermometers to the surface of the sample. Altering the sample surface in this way, however, can have the unfortunate effect of introducing inhomogeneity in the sample's thermal conductivity if phonons scatter differently in the vicinity of the attached objects. Indeed, during a previous experiment in our lab, it was found that attaching external thermometers to a diving board-style device resulted in discontinuous temperature gradients. We therefore depart from common practice by using the temperature dependence of the resistivity of the 2DES itself to provide thermometry, thereby eliminating the need to alter the sample surface. An added benefit of this approach is that observables related directly to the 2DES are used to infer its temperature

such that we need not assume the 2DES is in thermal equilibrium with an external thermometer.

Our approach is to thermally characterize the diving board by measuring the thermal conductance  $K$  along its length. Once  $K$  is established, a known temperature gradient can be imposed and the resulting thermoelectric voltages in the 2DES can be converted into measurements of thermopower. Significantly,  $K$  is overwhelmingly dominated by the transport of charge neutral phonons; diffusive heat transport by the 2DES is negligible. This allows us to employ a very useful trick provided by integer quantum Hall (IQH) physics.

In Chapter 6 we will review the impact of a strong magnetic field on 2D electrons. For now, we merely require the fact that the longitudinal resistance  $R_{xx}$  of the 2DES is highly temperature sensitive in the quantum Hall regime at particular values of magnetic field  $B$  and temperature  $T$ . To demonstrate this fact, Fig. 4.2 shows the temperature evolution of the longitudinal resistance  $R_{xx}$  as a function of magnetic field  $B$  in the vicinity of IQH filling factor  $\nu = 3$ , which is centered about  $B = 4.00$  T. As the temperature decreases, the plateau in  $R_{xy}$  (not shown) and the minimum in  $R_{xx}$  at  $\nu = 3$  broaden. This is a general feature of the IQHE that occurs in the vicinity of all integer filling factors where a strong minimum in  $R_{xx}$  is observed<sup>3</sup>.

The procedure by which we exploit this temperature dependence to determine the thermal conductance  $K$  of the diving board as a function of temperature  $T$  is as follows. For a particular  $T$ ,  $B$  is chosen such that  $R_{xx}$  is just outside a minimum associated with an IQH state (e.g. the diamonds in Fig. 4.2) for the 2DESs in both mesas. Then, in response to a small step change  $\Delta T_0$  in the cold finger temperature, the resistance changes  $\Delta R_{xx,1}$  and  $\Delta R_{xx,2}$  of each 2DES are recorded. Since this is done without applying any power to the strain gauge heater, the temperatures  $T_{1,2}$ ,

---

<sup>3</sup>To understand why this occurs, refer to the discussion on extended versus localized states in Section 6.6. When  $B$  is adjusted such that  $R_{xx}$  is just outside the minimum at an integer filling factor (e.g. the diamonds in Fig. 4.2), the 2DES behaves as an insulator in that as the temperature increases a larger population of electrons are excited from localized to extended states. Conversely, once the temperature is sufficiently low, the preponderance of electrons within the sample's interior (i.e. not in edge states) reside in localized states and  $R_{xx}$  vanishes as the sample's edge becomes an equipotential due to the edge states (see Section 6.8).

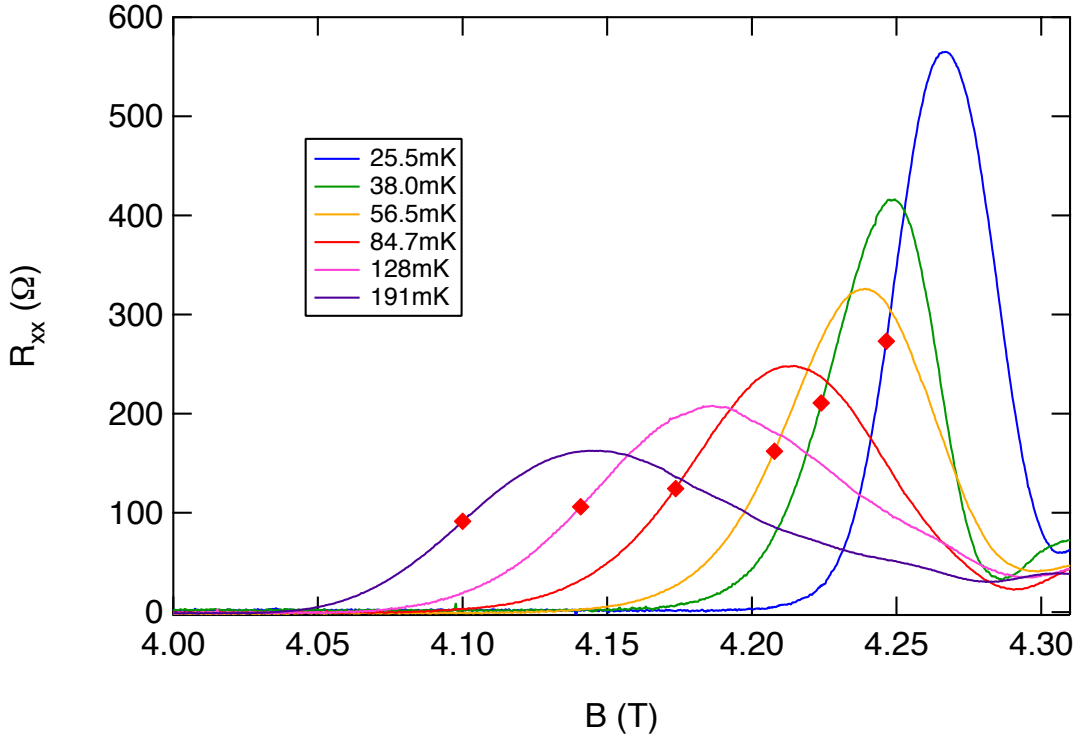


Figure 4.2: The temperature evolution of  $R_{xx}$  vs  $B$  in the vicinity of  $\nu = 3$ . The diamonds indicate where temperature calibration is performed.

and temperature changes  $\Delta T_{1,2}$ , of the two 2DES regions are assumed to be the same and equal to those of the cold finger,  $T_0$  and  $\Delta T_0$ . Next, with the cold finger temperature held constant at  $T_0$ , a small heat flux  $Q$  is applied to the strain gauge heater<sup>4</sup>.  $Q$  is chosen to render the resulting resistance changes  $\Delta R_{xx,1}$  and  $\Delta R_{xx,2}$  of the two 2DES regions comparable to those observed when the cold finger temperature was changed in the previous measurement. Comparison of these resistance changes with those observed when the cold finger temperature was changed allows the temperature rises  $\Delta T_{1,2}$  to be determined. As expected,  $\Delta T_1 < \Delta T_2$  since there is now a temperature gradient along the sample bar and mesa 2 is farther from thermal ground than is mesa 1 (see Fig. 4.1). The thermal conductances  $K_{1,2}$ , between each 2DES region and thermal ground, are then given by  $K_1 = Q/\Delta T_1$  and  $K_2 = Q/\Delta T_2$ . Note that

<sup>4</sup> $Q$  is always negligible compared to the cooling power of our dilution refrigerator. For example, at  $T_0 = 100$  mK the refrigerator cools with about  $200 \mu\text{W}$  while less than  $Q = 1$  nW is applied to the strain gauge heater.

$\Delta T_{1,2}$  is kept  $\leq 10\%$  of  $T_0$  during these thermal conductance measurements.

Importantly, we find that  $K_2/K_1 = L_1/L_2 = 0.49$  to within experimental uncertainty with  $L_1 = 3.7$  mm and  $L_2 = 7.6$  mm the distances between the midpoint of the respective 2DES mesa and the indium solder joint that connects the sample to the cold finger. This simple geometric scaling proves that the thermal resistance of the solder joint itself is negligible in comparison to that of the sample. Note that care went into ensuring that  $\Delta R_{xx}$  was linear in both  $\Delta T_0$  as well as  $Q$  for these measurements.

Figure 4.3 (a) displays the thermal conductance  $K_2$  between 2DES mesa 2 and thermal ground as a function of temperature  $T$  in a log-log plot. The figure demonstrates that  $K_2$  follows a simple power-law temperature dependence:  $K_2 \propto T^{2.56 \pm 0.05}$ . According to the kinetic theory of gases, the low-temperature phonon thermal conductance is  $K_2 = \gamma C v_{ph} \Lambda / 3$  with  $C$  the lattice specific heat of GaAs [56],  $v_{ph} = 3300$  m/s the appropriate mean acoustic phonon velocity<sup>5</sup>,  $\Lambda$  the phonon mean free path, and  $\gamma = Wt/L_2$  the cross-sectional area to length ratio of the bar. Since  $C \propto T^3$  at these low temperatures, our data demonstrate that the phonon mean free path scales roughly as  $\Lambda \propto T^{-0.44}$  over the temperature range studied here. Figure 4.3 (b) shows the deduced values of  $\Lambda$  in microns. As the temperature is reduced, the mean free path grows and approaches the diffuse boundary scattering limit,  $\Lambda_b$ , estimated to be  $\approx 720$   $\mu\text{m}$  (the dashed line in Fig. 4.3 (b)). This estimate is based on the assumption that diffuse scattering occurs only at the bottom sample surface, which is rough due to sandblasting. That  $\Lambda$  is considerably larger than the sample thickness is a result of the high aspect ratio of the sample cross-section ( $W/t \approx 23$ ) [57].

The thermal conductance data of Fig. 4.3 (a) were acquired at a variety of magnetic fields in the vicinities of the IQH states at  $\nu = 1, 2,$  and  $3$ . While minor systematic variations were found (and are evident in the data scatter in Fig. 4.3), no unambiguous magnetic field dependence emerged. This is not surprising since the thermal conductivity of our sample is heavily dominated by phonon transport.

---

<sup>5</sup>The value of  $v_{ph}$  used here, 3300 m/s, is close to the Debye velocity determined from the specific heat.

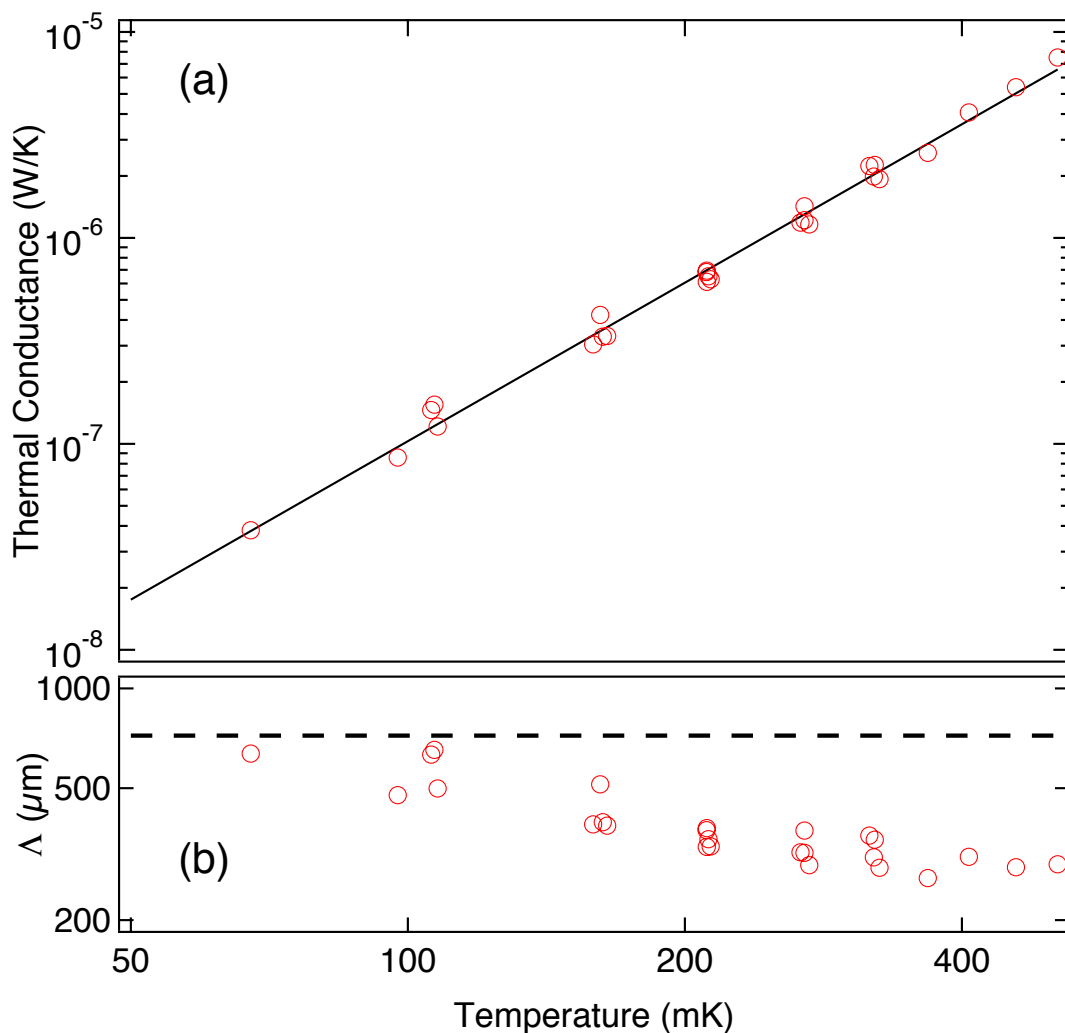


Figure 4.3: (a) Measured thermal conductance  $K_2$  between mesa 2 and thermal ground vs temperature of diving board A. The solid black line is a fit to the data and scales as  $T^{2.56 \pm 0.05}$ . (b) Phonon mean free path  $\Lambda$  inferred from the thermal conductance data. The dashed line corresponds to  $720 \mu\text{m}$ , an estimate of the diffuse boundary scattering limit. Reprinted with permission from W.E. Chickering, J.P. Eisenstein, L.N. Pfeiffer, and K.W. West, *Phys. Rev. B* **81**, 245319, (2010). Copyright 2010 by the American Physical Society.

Nevertheless, the resulting uncertainty in  $K_2(T)$  is an important source of systematic error in this type of thermopower experiment. We estimate that the uncertainty in  $K_2$  translates into a relative uncertainty of about 7 % in thermopower.

### 4.1.2 Measurement Protocol

Once the thermal conductance of the diving board is known, we can perform thermoelectric measurements, translating thermovoltages into thermopower. Applying a heat flux to the strain gauge gives rise to a temperature gradient along the length of the sample. The voltage  $\Delta V$  along a 2DES mesa is then measured. From the thermal conductance data of Fig. 4.3, along with the known cold finger temperature  $T_0$  and the applied heat flux  $Q$ , we calculate the temperature difference  $\Delta T$  between the ohmic contacts used to measure the thermovoltage as well as the mean temperature  $T$  of the 2DES to which the measurement applies. The measured longitudinal thermopower, or Seebeck coefficient, is then given by  $S(T) \equiv -\Delta V/\Delta T$ .

For much of the data acquired from diving board A the time required for the 2DES to relax to steady state following switching the heater on or off is short enough that a conventional AC lock-in technique may be used to measure the thermoelectric voltages. However, at the lowest temperatures and highest magnetic fields, extremely long thermal relaxation times are encountered. In these extreme regimes, the measured thermovoltage can take up to several minutes to reach its quiescent value immediately following the application or removal of heat. We will return to this issue shortly. For now, let it suffice to say that these relaxation times are intrinsic to diving board A. To contend with this issue, we employ a quasi-DC data acquisition and analysis technique that allows measurements at very low frequencies (e.g., 1 mHz).

At relatively high temperatures, where the thermal relaxation time of the diving board is short, the measurement protocol is straightforward. The voltage  $V_{DC}$  between two ohmic contacts is continuously recorded using a low-noise DC amplifier<sup>6</sup> while the heater is toggled on and off periodically. Figure 4.4 illustrates this with data acquired

---

<sup>6</sup>A low noise DC amplifier—specifically, an EM DC nanovoltmeter model N31—is used for all thermoelectric measurements made using diving board A.

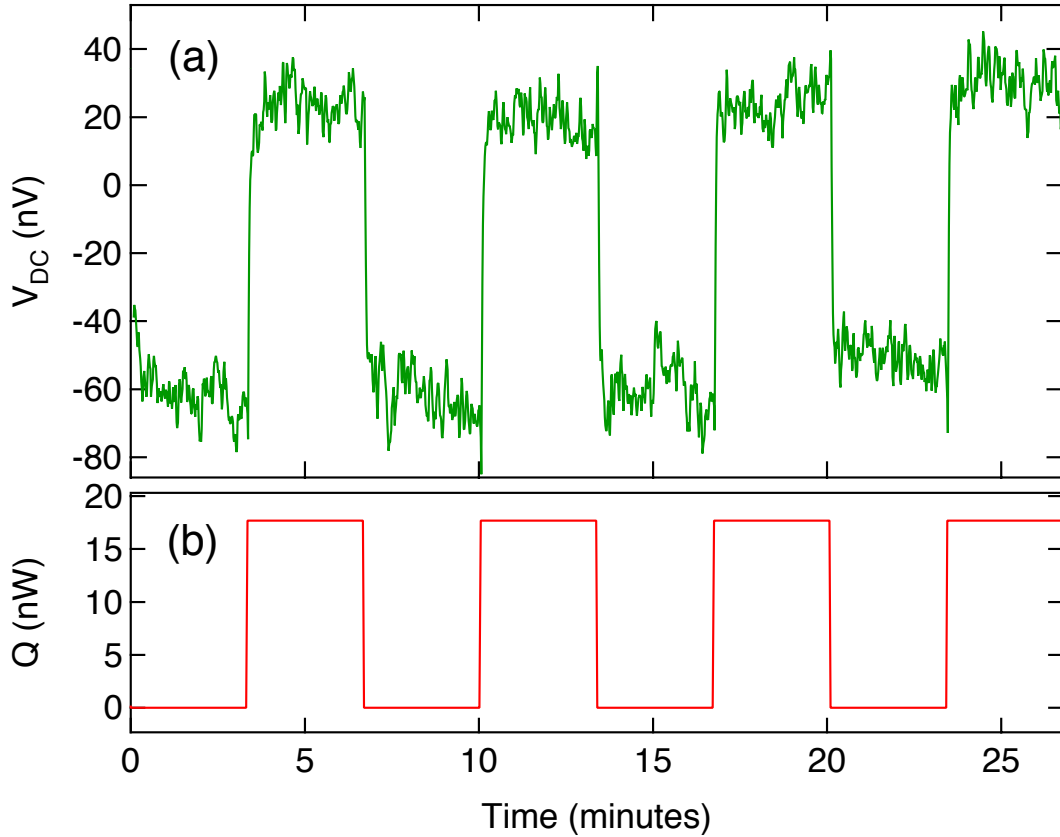


Figure 4.4: Demonstration of quasi-DC thermovoltage measurement. (a) Voltage  $V_{DC}$  measured across 2DES mesa 2 vs time as heater is toggled on and off. (b) Power  $Q$  applied to strain gauge heater vs time. In this example, taken at  $\nu = 3/2$ , the cold finger is at 120 mK such that 2DES mesa 2 is at 180 mK with  $\Delta T = 14$  mK along the mesa when heat is applied. Reprinted with permission from W.E. Chickering, J.P. Eisenstein, L.N. Pfeiffer, and K.W. West, *Phys. Rev. B* **81**, 245319, (2010). Copyright 2010 by the American Physical Society.

at Landau level filling factor  $\nu = 3/2^7$  ( $B = 8.0$  T) and  $T = 180$  mK. The figure shows the time dependence of the observed longitudinal voltage drop  $V_{DC}$  between ohmic contacts on 2DES mesa 2 as the heater power is toggled between  $Q = 0$  and 18 nW. The deduced thermoelectric voltage  $\Delta V$  is taken to be the average difference between  $V_{DC}$  with the heat on versus off; for the present example this is  $\Delta V \approx 78$  nV. In effect, this technique amounts to ex post facto lock-in detection at frequencies in

<sup>7</sup>In Chapter 8 we will discuss this many-body phase. In the present context, however, the nature of the  $\nu = 3/2$  phase is not important.

the mHz domain.

For the data shown in Fig. 4.4 the cold finger temperature was maintained at  $T_0 = 120$  mK. Integrating the thermal conductance data of Fig. 4.3 reveals that for  $Q = 18$  nW, 2DES mesa 2 is at a mean temperature of  $T_2 \approx 180$  mK with a temperature difference of  $\Delta T \approx 14$  mK between the ohmic contacts. Combining these numbers yields a thermopower of  $S = -\Delta V/\Delta T \approx -5.6\mu\text{V/K}$ .

In the above example, the thermoelectric voltage  $V_{DC}$  is measured along 2DES mesa 2 (the one farthest from thermal ground) using the ohmic contacts that lie on the central axis of the sample bar (see the Fig. 4.1). This is the case for all the measurements made using diving board A reported in subsequent chapters. In this chapter, we provide the results for zero magnetic field, in which case the net voltage difference across both 2DES mesas is recorded with the one ohmic contact they share providing the on-chip series connection. This was done in order to reduce the relative uncertainty in the distance between the ohmic contacts. This procedure was not applied at high fields owing to the slight 2DES density differences between the two mesas ( $\Delta N/N \sim 1\%$ ) which, while small, can lead to differences in Landau level filling factor that are comparable to the width of important FQH states (notably at  $\nu = 5/2$ ).

Note that all measurements of thermopower are made in regimes where both  $\Delta V$  and  $\Delta T$  are linear in the applied heat  $Q$ . This is necessary for the validity of the expression  $S = -\Delta V/\Delta T$ .

Finally, the nonzero voltages which are observed even when the heater is off, as Fig. 4.4 reveals, also deserve comment. We attribute these voltages to offsets and/or  $1/f$  noise in our DC amplifier as well as to genuine thermoelectric effects arising from a lack of perfect thermal symmetry in the measurement circuit. In any case, such background voltages, which vary slowly with time, are unrelated to thermoelectric phenomena in the 2DES and are readily subtracted.

### 4.1.3 Experimental Results at Zero Field

Before presenting our results at zero field it is worth reviewing what is arguably the best resolved measurement of the low-temperature diffusion thermopower of high-mobility 2D electrons prior to our work. Figure 4.5 shows thermopower divided by temperature as a function of temperature in a semi-log plot as reported by Fletcher et al. [42]. The data were acquired from a diving board style experiment performed on a high-mobility ( $\mu_e \approx 400,000 \text{ cm}^2/\text{Vs}$ ) 2DES within a GaAs/AlGaAs heterostructure. Recall from Section 3.3 that according to the Mott formula the diffusion thermopower  $S^d$  of a 2DES in the  $T \rightarrow 0$  limit is

$$S^d(n, T) = -\frac{\pi k_B^2 m^*}{3\hbar^2 e} (1 + p) \frac{T}{n}. \quad (4.1)$$

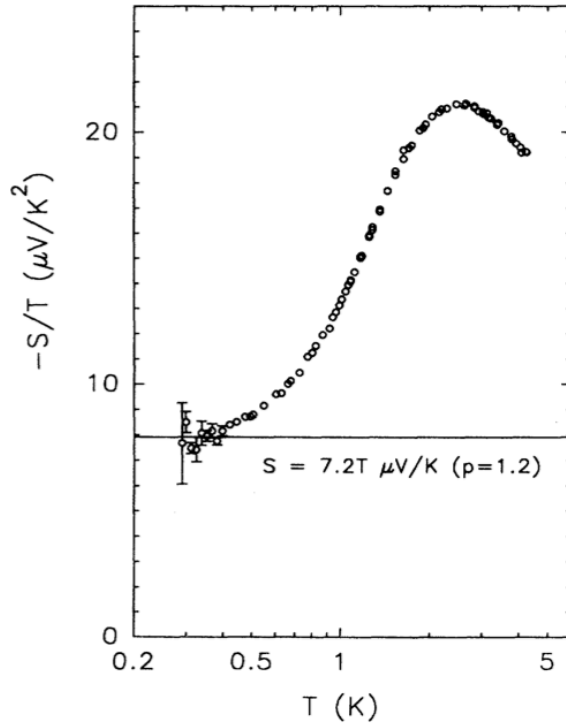


Figure 4.5:  $S/T$  vs  $T$  at  $B = 0$  in a semi-log plot. Data is from a diving board style experiment performed by Fletcher et al. on a high-mobility ( $\mu_e \approx 400,000 \text{ cm}^2/\text{Vs}$ ) 2DES. Reprinted with permission from R. Fletcher, P.T. Coleridge, and Y. Feng, *Phys. Rev. B* **52**, 2823 (1995). Copyright 1995 by the American Physical Society.

where  $p$  reflects the energy, and thus density, dependence of the momentum lifetime  $\tau_m$ :  $p = (n/\tau_m) \frac{d\tau_m}{dn}$ . The 2DES studied by Fletcher et al. has  $n \approx 1.9 \times 10^{11} \text{ cm}^{-2}$  corresponding to  $T_F \approx 80 \text{ K}$  such that  $T \ll T_F$  for the data shown in Fig. 4.5. Similarly, all 2DESs studied for this thesis are confined to  $T \ll T_F$ , the temperature regime in which Eq. 4.1 is valid.

The phonon drag contribution to thermopower, given its stronger temperature dependence (see Section 3.5), should subside rapidly as the temperature falls eventually leaving the diffusion contribution dominant. Indeed, in Fig. 4.5, below about  $T = 0.4 \text{ K}$ ,  $S/T$  appears independent of  $T$  consistent with the diffusion thermopower of Eq. 4.1. The horizontal line corresponds to the best estimate of the diffusion term predicted by Eq. 4.1 for a 2DES of this density ( $n = 1.9 \times 10^{11} \text{ cm}^{-2}$ ) corresponding to  $p = 1.2$ . (Recall that theoretically we expect  $0.4 \lesssim p \lesssim 1.5$  [33].) Above  $T = 0.4 \text{ K}$ ,  $S/T$  exceeds the horizontal line, the excess being attributed to phonon drag. It is important to note the thermopower data of Fletcher et al. shown in Fig. 4.5 is exceptional for a 2DES of this mobility in terms of the degree of attenuation of the phonon drag contribution. Indeed, this was a key point of their article.

We now turn to the results of our diving board experiment. Figure 4.6 displays the measured thermopower versus temperature at zero magnetic field in a linear plot. As the dashed line of Fig. 4.6 suggests, the observed thermopower is approximately proportional to temperature, consistent with electronic diffusion, below about 150 mK. Above about  $T = 200 \text{ mK}$ , the data begin to exceed this extrapolated linear dependence as the phonon drag contribution grows in significance. The precise crossover temperature between diffusion- and phonon-dominated thermopower is nonuniversal, depending on extrinsic factors such as the phonon mean free path  $\Lambda$  (see Eq. 3.26). Nonetheless, the crossover temperatures observed in Fig. 4.5 and Fig. 4.6 are comparable, especially when we take into consideration the uncertainty in each of these datasets. A similar crossover temperature was observed by Ying et al. [40] in their study of the thermopower of 2D hole systems in GaAs.

Fitting Eq. 4.1 to the  $T < 150 \text{ mK}$  data of Fig. 4.6 (the dashed line) yields  $p \gtrsim 0.9$  in our sample. Since the 2D density in our sample is not adjustable via electrostatic

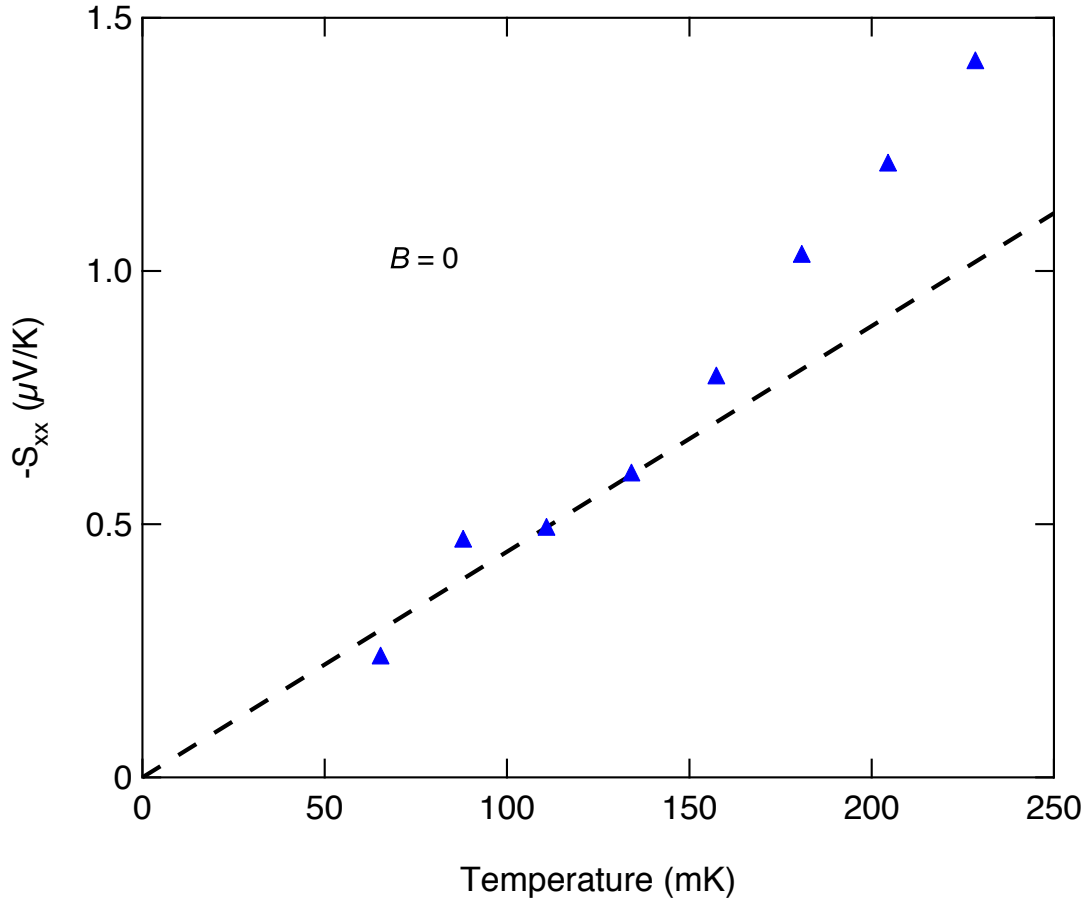


Figure 4.6: A lower bound on  $S$  vs  $T$  at  $B = 0$  of the 2DES at zero magnetic field measured using diving board A. The dashed line represents the thermopower of Eq. 4.1 for  $p = 0.9$ . Reprinted with permission from W.E. Chickering, J.P. Eisenstein, L.N. Pfeiffer, and K.W. West, *Phys. Rev. B* **81**, 245319, (2010). Copyright 2010 by the American Physical Society.

gating<sup>8</sup>, it is not possible to independently determine  $p$  from density-dependent resistivity measurements. Nonetheless, the consistency of our low-temperature data and the Mott formula (with a reasonable value of  $p$ ) gives us confidence in the reliability of our experimental technique for measuring thermopower.

A key challenge in measuring the diffusion thermopower of 2D electrons is achieving the highest possible crossover temperature between the diffusive and phonon drag

<sup>8</sup>After illumination the 2D density in our sample cannot be modified by gating. This is a common occurrence in samples of this type which are intentionally overdoped. See Sections 1.2 and 2.5 for discussions of electrostatic gating and sample illumination, respectively.

dominated regimes. In principle, a straightforward approach to minimizing phonon drag is to minimize the number of phonons required for a given temperature gradient; that is, reduce the thermal conductance of the surrounding 3D lattice. In Fig. 1.3 of Section 1.1 we illustrated how the thickness of a typical GaAs/AlGaAs heterostructure sample consists primarily of a GaAs substrate. This substrate, which provides a platform for heterostructure growth, can be mostly removed through a chemically assisted abrasive etching process described in Appendix Section B.7. In this way, we thin our diving board samples from 500 to 130  $\mu\text{m}$  to minimize thermal conductance. Moreover, to prevent specular reflection of phonons at the sample's bottom surface, we sandblast its backside to create a matte finish.

There is an important qualification to the data of Fig. 4.6. These thermopower determinations utilize the thermal conductance data of Fig. 4.3, which is acquired in a strong magnetic field as explained in Section 4.1.1. Recall that the diving board is indium-soldered to the cold reservoir. Indium is a superconductor with a critical temperature of  $T_c = 3.4$  K and critical field of  $B_c = 28$  mT. The indium comprising the solder joint is therefore assumed to be in its superconducting phase throughout the domain of Fig. 4.6. A characteristic of superconductivity is a reduction in thermal conductivity due to the suppression of the electronic contribution. The temperature gradient along the diving board inferred from the thermal conductance data of Fig. 4.3 is therefore merely an upper bound in the  $B = 0$  case. As a consequence, strictly speaking, the magnitudes shown in Fig. 4.6 are only lower bounds on the actual thermopower of the 2DES. At the same time, there remains the phonon contribution to the thermal conductivity of the indium at these temperatures. And we will now argue that this latter contribution should be sufficiently large that the discrepancy between the true thermopower and the lower limits shown in Fig. 4.6 is negligible.

Let us estimate the thermal conductance of the superconducting indium solder joint for the temperature regime of Fig. 4.6. Well into its superconducting phase (e.g.  $T \sim 100$  mK), the phonon-mediated thermal conductivity of indium has been measured as  $\kappa = \alpha_s T^3$ , with  $\alpha_s \approx 0.8$  W/cm/K<sup>4</sup> [58]. The cross-sectional area of the indium joint of diving board A is  $w \times \ell \approx 3 \times 1.5$  mm<sup>2</sup> (see Fig. 1.7). The thickness  $t$

of the indium layer is less certain; a conservative estimate is  $t \approx 0.1$  mm. We therefore estimate the thermal conductance of the joint as  $K = w\ell/t \cdot \alpha_s \cdot T^3 \approx 3.5 \cdot T^3$  W/K, with  $T$  in kelvin. For example, at  $T = 100$  mK, we have  $K \approx 3.5 \times 10^{-3}$  W/K. This is several orders larger than the measured thermal conductance of diving board A at this temperature, which Fig. 4.3 shows is only  $\sim 10^{-7}$  W/K. Given this estimate, we believe the systematic error in the thermopower of Fig. 4.6 due to the superconducting indium solder joint to be negligible.

#### 4.1.4 Long Thermal Relaxation Times

In the data acquisition example of Fig. 4.4 the thermal relaxation time is  $\tau_R \lesssim 5$  s. This is much smaller than the dwell time  $t_D = 200$  s that the heater is in the on or off state allowing straightforward measurements. Unfortunately, in certain regimes we have that  $\tau_R \sim t_D$ . If initially in steady state, the time required for the temperature profile along diving board A to arrive at its resting value immediately following a switching on/off of the heater state increases with decreasing temperature as well as with increasing magnetic field. This is evident not only through thermovoltage measurements but also the temperature dependent longitudinal resistance  $R_{xx}$  used to determine thermal conductance as explained in Section 4.1.1.

Figure 4.7 demonstrates this behavior at  $T \approx 75$  mK and  $B = 6.4$  T by showing the resistance change  $\Delta R_{xx}$  of a 2DES mesa as a function of time immediately after turning the heater off. In this example, the device is initially in steady state with the heater on such that the 2DES mesa temperature is  $\sim 10\%$  above thermal ground. At  $t = 0$  the heater is suddenly switched off and  $\Delta R_{xx}$  slowly decreases as the 2DES cools. The figure reveals that at this temperature and magnetic field more than three minutes are required for the 2DES mesa to equilibrate with thermal ground.

In this context, we may think of our system in terms of a Thévenin equivalent thermal circuit consisting of a heat source, switch, thermal resistor, thermal capacitor, and thermal ground all connected in series. The thermal relaxation time is then given by multiplying the circuit's resistance and capacitance, where the resistance

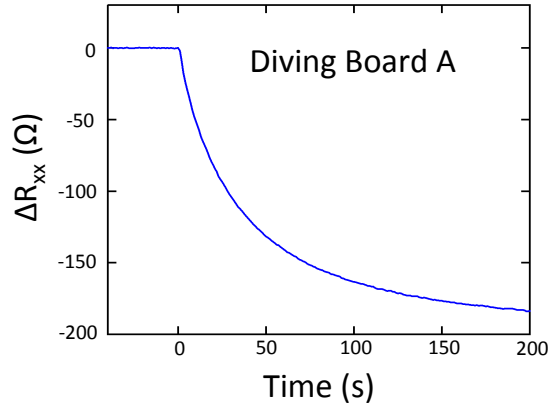


Figure 4.7: Thermal relaxation of the longitudinal resistance change  $\Delta R_{xx}$  after turning off the heater in diving board A. Data is acquired at  $T \approx 75$  mK and  $B = 6.4$  T. Reprinted with permission from W.E. Chickering, J.P. Eisenstein, L.N. Pfeiffer, and K.W. West, *Phys. Rev. B* **81**, 245319, (2010). Copyright 2010 by the American Physical Society.

is simply the inverse of the measured thermal conductance and the capacitance is the heat capacity located between the heater and thermal ground. Investigation of the temperature and magnetic field dependence of the relaxation time suggests that nuclear moments, most likely in the InSn ohmic contacts and the manganin wires attached to them, are responsible for a large heat capacity that depends strongly on temperature and magnetic field. This investigation is documented in Appendix D.

We did not anticipate these long relaxation times. Our quasi-DC data acquisition technique provides a somewhat effective work-around, however. Not only can we measure at very low frequencies (e.g. mHz), observations can be “windowed” allowing easy rejection of data acquired before the sample has reached steady state. Nonetheless, this issue ultimately limits our ability to measure thermopower using diving board A since  $1/f$  noise of even the best amplifier sets a lower limit on measurement frequency, even with the “windowing” technique. Not only does this limit the temperature at which we can measure thermopower, it also makes it impractical to measure thermopower as a continuous function of magnetic field. Following our initial thermopower studies using diving board A, a new device was designed to overcome these limitations.

## 4.2 Diving Board B

The key goal of our improved diving board design is to reduce the thermal relaxation time by minimizing the heat capacity between the heater and thermal ground. We achieve this by dramatically reducing the metallization on the surface of the GaAs/AlGaAs heterostructure. The layout of diving board B is shown in Fig. 4.8. A  $6 \times 12 \text{ mm}^2$  sample is cleaved from the same parent wafer as that used for diving board A; the 2DES has the same density and mobility for both diving boards. Once again the substrate side is thinned to a thickness of about  $130 \text{ }\mu\text{m}$  and the backside is sandblasted to ensure diffuse phonon scattering. Two independent  $3 \times 3 \text{ mm}^2$  2DES mesas are lithographically patterned and wet etched into the top surface. Instead of relatively bulky InSn ohmic contacts, six evaporated Ni/AuGe ohmic contacts are positioned at the corners and two side midpoints of each mesa. We replace diving board A's strain gauge heater with an on-chip serpentine-shaped thin film of  $640 \text{ }\Omega$  that extends across most of the diving board's width. The on-chip heater, along with each of the ohmic contacts, is electrically connected to a patch bay located at the opposite end of the sample via evaporated Ti/Au contact lines. This end of the diving board is indium-soldered, in the same manner as diving board A, to the cold finger of our dilution refrigerator such that the patch bay is at thermal ground. Fabrication details can be found in Appendix B.

The patch bay is comprised of an array of squares consisting of the same Ni/AuGe used for the ohmic contacts to the 2DES. Note that the patch bay, however, resides on an etched region of the sample where the 2DES cannot form. We use Ni/AuGe here only because this material facilitates easy attachment of external wires. The important function of the patch bay and the contact lines is the reduction in the amount of metal to thermally equilibrate when toggling the heater on/off. Comparing the two devices we find that the cross section of the contact lines is two orders of magnitude smaller than that of the manganin wires used by diving board A. Even more dramatic, we estimate<sup>9</sup> the volume of an evaporated Ni/AuGe ohmic contact on

---

<sup>9</sup>When estimating the volume of one of diving board A's InSn ohmic contacts, we model it as a sphere with a radius of  $500 \text{ }\mu\text{m}$ .

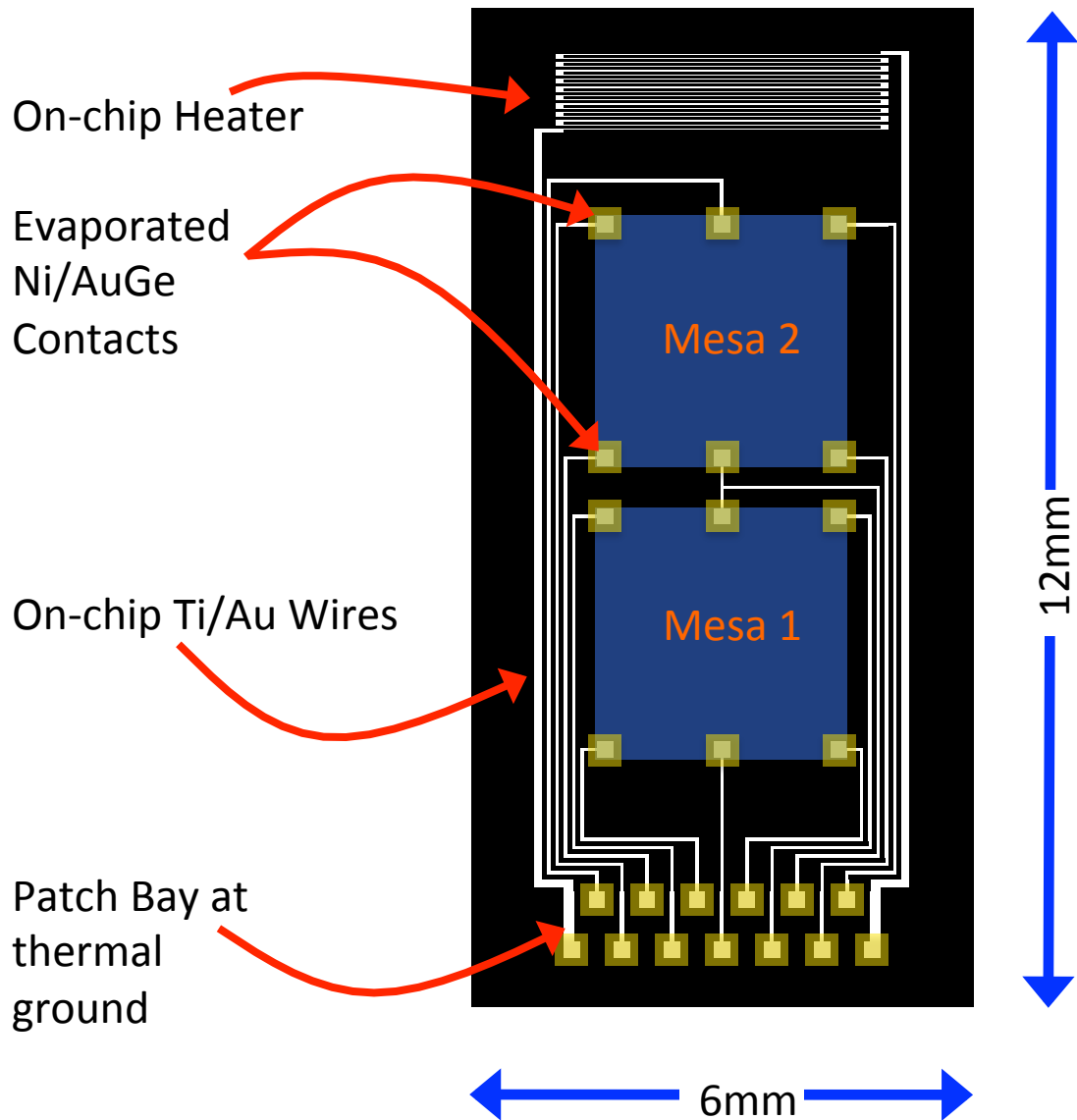


Figure 4.8: Layout of diving board B. This design aims to minimize heat capacity by dramatically reducing the metallization on the sample's surface.

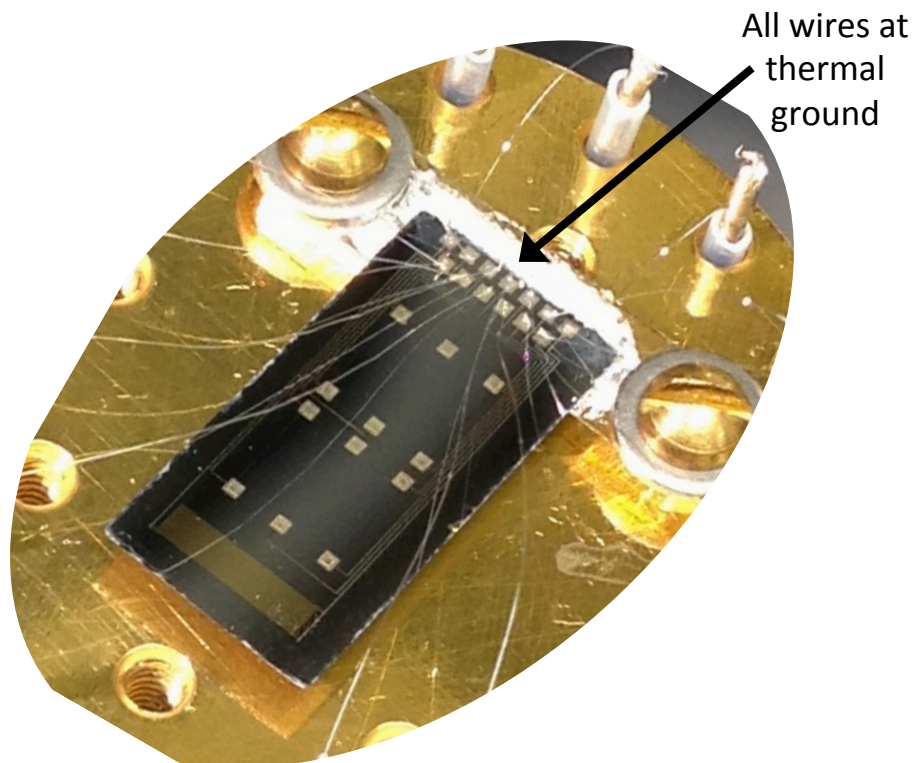


Figure 4.9: 2DES diving board B. All external wiring is connected to the patch bay at thermal ground to avoid thermal shorts.

diving board B to be four orders of magnitude less than that of a InSn ohmic contact on diving board A. A photograph of diving board B is shown in Fig. 4.9.

#### 4.2.1 Short Thermal Relaxation Times

To demonstrate the long relaxation times encountered in diving board A we showed in Fig. 4.7 how the longitudinal resistance slowly decreased after turning the heater off. The results of the same measurement made using diving board B, also at  $T \approx 75$  mK and  $B = 6.4$  T, are shown in Fig. 4.10. Only about  $200 \mu\text{s}$  are required for the new device to equilibrate following the removal of heat at  $t = 0$ . This is an improvement over diving board A of about six orders of magnitude! Of course, the exact improvement is a function of temperature and magnetic field, but the new design successfully eliminates appreciable thermal relaxation times for temperatures

as low as  $T \sim 20$  mK and fields as high as  $B \sim 12$  T.

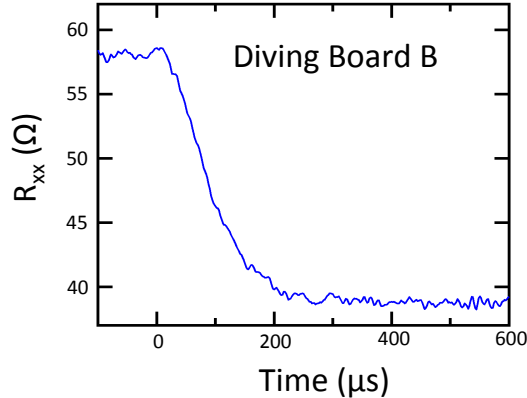


Figure 4.10: Thermal relaxation of longitudinal resistance  $R_{xx}$  after turning off heater in diving board B. An improvement of about six orders of magnitude compared to diving board A! Data acquired at  $T \approx 75$  mK and  $B = 6.4$  T.

## 4.2.2 Temperature Calibration

As with the previous device we must measure diving board B's thermal conductance in order to translate thermovoltages into measurements of thermopower. The procedure is the same as that described in Section 4.1.1 and the results are shown in Fig. 4.11 (a). Elimination of long relaxation times allows us to measure the thermal conductance at significantly lower temperatures in the new device, down to  $T = 22$  mK compared to only  $T = 68$  mK in diving board A. As expected, for  $T \geq 68$  mK we find the conductance scales with temperature in the same way in both devices and that the value for diving board B is approximately twice that of diving board A consistent with their comparative geometries. Careful inspection of the data reveals that for  $T \lesssim 50$  mK the conductance decreases more rapidly with temperature. A likely explanation for this can be found in Fig. 4.11 (b), which shows the phonon mean free path  $\Lambda$  inferred from the measured thermal conductance using kinetic gas theory as before. In the case of diving board A we found that  $\Lambda$  approached the estimated diffuse boundary scattering limit yet revealed no sign of leveling off. The dashed line once again corresponds to this limit, this time estimated using the geometry of diving

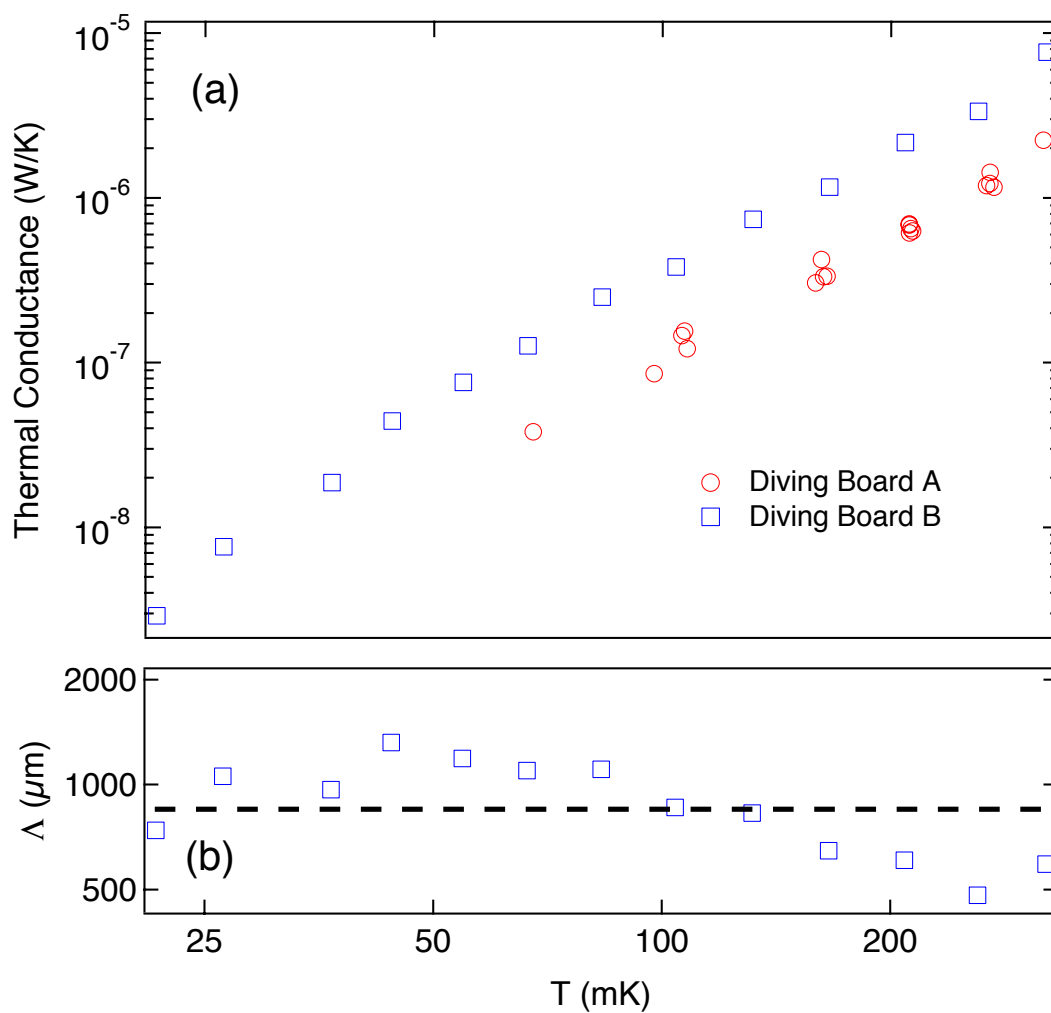


Figure 4.11: (a) Measured thermal conductance  $K_2$  between mesa 2 and thermal ground vs temperature of diving board B along with that of diving board A. (b) Phonon mean free path  $\Lambda$  inferred from the thermal conductance data of diving board B. The dashed line corresponds to  $850 \mu\text{m}$ , an estimate of the diffuse boundary scattering limit within diving board B.

board B. We find that  $\Lambda$  exceeds the estimate but then appears to saturate as the temperature further decreases suggesting the true limit has been reached. The precise temperature dependence of the conductance is not important. It only matters that we accurately know its value as a function of temperature such that we can infer the temperature profile along the diving board when measuring thermovoltages. Observing saturation of the phonon mean free path at a value comparable to our estimate of the diffuse boundary scattering limit bolsters our confidence that we indeed have an accurate measure of how the thermal conductance depends on temperature.

### 4.2.3 Measurement Protocol

Now that we have solved the problem of long thermal relaxation times, we may use low frequency AC lock-in detection to measure thermovoltages at all accessible temperatures and magnetic fields. This offers several advantages over our previous experimental setup including the ability to measure thermopower down to  $T = 22$  mK. More generally, diving board B allows faster data acquisition thereby making the exploration of a larger swath of parameter space practical. This includes the ability to measure thermopower as a continuous function of magnetic field. As will be demonstrated in subsequent chapters, observations of electrical transport coefficients (e.g. resistance) as a function of magnetic field are often made when investigating the phases and phenomena of the 2DES. It is therefore highly desirable to obtain analogous observations of thermoelectric transport coefficients.

To observe the thermoelectric response of the 2DES via lock-in detection we source a current  $I$  through the on-chip heater at a frequency  $f$  (we typically choose  $f = 13$  Hz); that is,  $I(t) = I_0 \sin(\omega t)$ , where  $\omega = 2\pi f$ . The resulting thermovoltage  $\Delta V$  is in phase with the oscillating temperature difference  $\Delta T$  along the 2DES mesa between the ohmic contacts. Given that  $\Delta T$  and the heat flux  $Q$  dissipated by the heater are in phase (i.e. the relaxation time is negligible), we have that

$$\Delta V \propto \Delta T \propto Q = I^2 R = I_0^2 R [1 - \cos(2\omega t)]/2, \quad (4.2)$$

where  $R$  is the resistance of the on-chip heater. Therefore, the voltage detected at  $2f$  with phase consistent with Eq. 4.2 is the RMS thermovoltage  $\Delta V_{\text{rms}}$ . Meanwhile, the RMS temperature difference  $\Delta T_{\text{rms}}$  that corresponds to a particular measurement is readily determined<sup>10</sup> given the applied heat flux  $Q$ , the cryostat temperature  $T_0$ , and the measured thermal conductance. Like with our quasi-DC measurement technique, we are careful to ensure that both  $\Delta V_{\text{rms}}$  and  $\Delta T_{\text{rms}}$  are linear in  $Q_{\text{rms}}$  such that the expression  $S = -\Delta V_{\text{rms}}/\Delta T_{\text{rms}}$  remains valid.

A critical diagnostic is the agreement of our quasi-DC and AC lock-in thermopower measurements. As expected, the results of these measurement protocols yield consistent results. We are also able to reproduce all thermoelectric data from diving board A with the exception of those at  $B = 0$ . Recall that measurements at  $B = 0$  in these devices merely yield a lower bound on the magnitude of the thermopower (see Section 4.1.3). The lower bounds acquired using diving board B are about a factor of two lower than those acquired using diving board A. These results are consistent with a thicker layer of superconducting indium between the heterostructure and the cold reservoir.

### 4.3 Summary

The diving board technique is an effective and relatively straightforward way to measure the thermoelectric response of a high-mobility 2DES. We combine this classic approach with a modern state of the art heterostructure sample. An important improvement in our implementation over the standard technique is the dispensing of external thermometers, which can introduce systematic errors due to how they effect phonon scattering at the sample surface. Rather, we infer the 2DES's temperature through measurements of its temperature-sensitive longitudinal resistance within the

---

<sup>10</sup>For very small values of  $Q$ , the RMS temperature difference is given by  $\Delta T_{\text{rms}} = Q_{\text{rms}}/K(T_0) = I_{\text{rms}}^2 R/\sqrt{2}K(T_0)$ , where  $K(T)$  is the thermal conductance between the two ohmic contacts used in the measurement at temperature  $T$  and  $T_0$  is the cryostat temperature. The value of  $K(T)$  is related to the measured value of  $K_2(T)$ —the conductance between the center of mesa 2 and thermal ground—by the ratio of the distance between the ohmic contacts to the distance from the center of mesa 2 and the indium solder joint of the diving board.

integer quantum Hall regime. By segregating the 2DES into two independent mesas and determining their temperatures while heat flows along the length of the diving board, we are able to measure temperature gradients within the 2DES to high precision.

Using diving board A we measured a lower bound on the magnitude of the low-temperature thermopower of an ultra-high-mobility 2DES. At the lowest temperatures, these results are consistent with Mott’s formula for diffusion thermopower assuming a reasonable value of the momentum relaxation parameter  $p$ . Above  $T \approx 200$  mK,  $S$  exceeds what is expected for diffusion thermopower. We attribute this excess to phonon drag. Indeed, the low-temperature thermopower of high-mobility 2DESs within GaAs/AlGaAs heterostructures is typically dominated by phonon drag. The most remarkable feature of our data is the degree to which phonon drag has been minimized.

As will be seen in subsequent chapters, our original high-field experiments using diving board A also yield several interesting results. Nonetheless, the regimes within which data can be acquired using diving board A—specifically at low temperatures and high magnetic fields—is limited due to the presence of long thermal relaxation times. The quasi-DC measurement technique described in this chapter accommodates this issue to an extent, but long relaxations preclude measurements of thermopower below  $T \approx 60$  mK as well as continuous measurements as a function of magnetic field  $B$ . Diving board B overcomes the problem by dramatically reducing the amount of metal whose temperature must fluctuate as we apply and remove heat. With the new device we are able to measure  $S$  at temperatures slightly above the base value for our dilution refrigerator (allowing for a small temperature gradient) and while continually varying  $B$ . The values of  $S$  acquired with diving board B for  $|B| \gtrsim 0.15$  T are consistent with those from diving board A. For  $|B| \lesssim 0.15$  T we encounter a discrepancy between the two devices. We will return to this issue in Chapter 7 when discussing our thermopower results in the quantum Hall regime. But first, we discuss a different approach to measuring the thermopower of the 2DES that dramatically reduces the role of phonon drag.

## Chapter 5

# Hot-Electron Thermocouple

In the previous chapter we saw how traditional studies of the thermopower of the 2DES impose a temperature gradient through the external application of heat. In these experiments, Joule heating of a resistive element produces phonon currents within the substrate along the length of a diving board sample. Electron-phonon scattering events thermalize the 2DES with its surrounding lattice such that in steady-state the electrons and phonons are in local equilibrium. As discussed in Section 3.5, when these phonon currents become sufficiently strong they produce a phonon drag thermopower that dominates that from the information-rich electronic diffusion. An alternative strategy for measuring diffusion thermopower involves heating the 2DES directly.

It is well known that the 2DES is readily heated out of equilibrium with its surrounding lattice if subjected to a sufficiently large electrical current. Typically we employ currents to measure the 2DES's resistivity or conductivity and appreciable resistive heating is to be avoided. When investigating thermoelectricity, however, the ability to impose temperature gradients in this way offers certain advantages, including a dramatic reduction in the generation of phonons.

This chapter introduces an alternative device and technique for measuring the thermopower of 2D electrons. We first describe the device composition and layout along with its basic working principles. This is followed by an explanation of the measurement circuit, temperature calibration technique, and thermopower measurement protocol. We then analyze our experimental results, which include both temperature

and electron density dependence. The chapter concludes with a proposal to use this new technique to study the enigmatic two-dimensional metal-insulator transition.

## 5.1 Device Layout

The basic layout of our *2D hot-electron thermocouple* is shown in Fig. 5.1 (a). Sample and fabrication details were provided in Section 1.2.1, but let us review some basic attributes. The sample has an ungated density of  $n = 1.6 \times 10^{11} \text{ cm}^{-2}$  and an electron mobility of  $\mu_e = 3.3 \times 10^6 \text{ cm}^2/\text{Vs}$ . We pattern the 2DES into a series of  $60 \text{ }\mu\text{m}$ -wide mesa-channels represented by the grey portions of the figure. At the end of each channel is a Ni-AuGe ohmic contact, to each of which we assign a number as shown. The central horizontal channel between contacts 3 and 4 is  $1 \text{ mm}$  long. The two central vertical channels have aluminum top gates  $G_1$  and  $G_2$  represented in the figure by light grey rectangles.

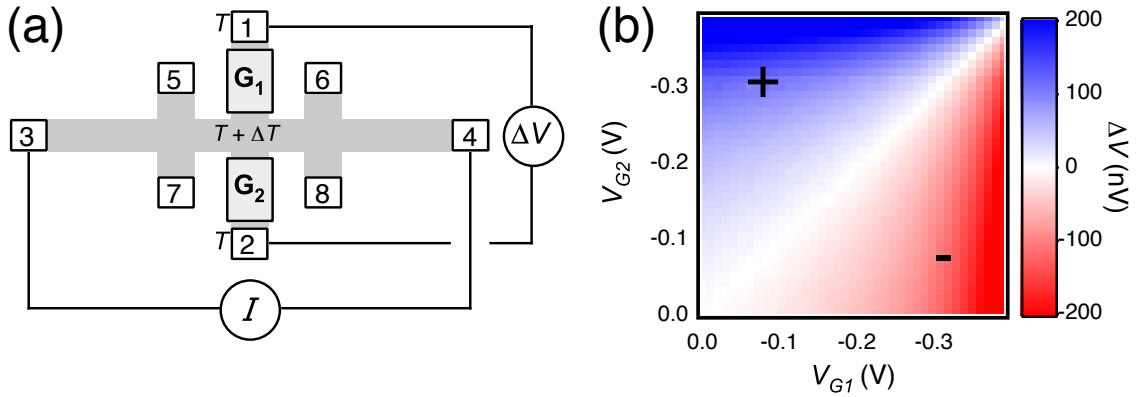


Figure 5.1: (a) Layout of 2D hot-electron thermocouple device. Numbered squares are ohmic contacts, light gray rectangles are top gates  $G_1$  and  $G_2$ . (b) Color intensity plot of thermoelectric voltage  $\Delta V$  arising from resistively heating the 2DES. Reprinted with permission from W.E. Chickering, J.P. Eisenstein, and J.L. Reno, *Phys. Rev. Lett.* **103**, 046807 (2009). Copyright 2009 by the American Physical Society.

The Ni-AuGe ohmic contacts not only provide an electrical connection to the 2DES but also serve as heat sinks pinning the local temperature of the 2DES to that of the surrounding crystal lattice,  $T$ . Away from an ohmic contact the thermal

coupling between the lattice and the 2DES is far weaker. Passing a current  $I$  between contacts 3 and 4 causes Joule heating to raise the temperature of the 2DES at the center of the device to  $T + \Delta T$ . In this way, the temperature differential  $\Delta T$  is established between the center of the device and each ohmic contact. Meanwhile, the voltage  $\Delta V = V_1 - V_2$  measured between contacts 1 and 2 will not contain a resistive component due to the symmetry of the device. Rather, any voltage seen between contacts 1 and 2 will be thermoelectric in origin. If we choose the voltage to be zero at the center of the device and impose a sufficiently small current  $I$  such that  $\Delta T \ll T$ , the voltage at contact 1 is  $V_1 = -S_1 \cdot (-\Delta T)$  (see Eq. 3.1). Similarly, the voltage at contact 2 is  $V_2 = -S_2 \cdot (-\Delta T)$ . The measured voltage is therefore

$$\Delta V = (S_1 - S_2) \cdot \Delta T. \quad (5.1)$$

The top gates  $G_1$  and  $G_2$  provide electrostatic control over the density of the 2DES beneath them. In the case where we do not bias these gates, the 2DES has a uniform density  $n$  throughout the entire device. The resulting symmetry requires that  $S_1 = S_2$ , and therefore,  $\Delta V = 0$ . By the same symmetry argument, if  $V_{G1} = V_{G2}$  for any voltage bias,  $n_1 = n_2$ , and thus  $S_1 = S_2$  such that  $\Delta V = 0$ . Only by breaking the symmetry between these gated regions can a nonzero thermovoltage arise. That is,  $\Delta V \neq 0$  if and only if  $V_{G1} \neq V_{G2}$  such that  $S_1 \neq S_2$ . As is always the case, one requires a difference in thermopowers, i.e. a thermocouple, to observe a thermovoltage.

In Fig. 5.1 (b) we show  $\Delta V$  as a function of the gate voltages  $V_{G1}$  and  $V_{G2}$  in a color intensity plot. With the device at  $T = 1$  K we source  $I = 2 \mu\text{A}$  between contacts 3 and 4 at  $f = 13$  Hz. We then measure  $\Delta V$  between contacts 1 and 2 via lock-in detection at  $2f$ , i.e. at twice the excitation frequency, since a signal resulting from Joule heating will scale as  $I^2 \propto \sin^2(\omega t) = [1 - \cos(2\omega t)]/2$ , where  $\omega = 2\pi f$ . We employ an AC lock-in technique (see Appendix C) to improve noise rejection as well as eliminate any signal offsets arising due to extrinsic or non-thermal sources. For example, any resistive voltage drops arising due to imperfections in the device symmetry appear at the excitation frequency  $f$  and are therefore rejected from the

measurement. As expected,  $\Delta V = 0$  along the diagonal where  $V_{G1} = V_{G2}$  (i.e., where  $S_1 = S_2$ ). Moreover,  $\Delta V$  exhibits the proper sign change and overall symmetry about the diagonal that is consistent with a thermovoltage given the symmetry of the device.

A photograph<sup>1</sup> of the actual hot-electron thermocouple device is presented in Fig. 5.2. The ohmic contacts are labeled with numbers showing the correspondence with the device layout in Fig. 5.1 (a). We electrically ground the top gates appearing over the channels leading to contacts 5, 6, 7, and 8 throughout the experiments discussed in this thesis such that the density of the underlying 2DES remains equal to that of the ungated regions. For this reason, we omit them from the layout in Fig. 5.1 (a). Only the top gates leading to contacts 1 and 2 are biased to modify the density, and hence the thermopower, of the 2DES beneath.

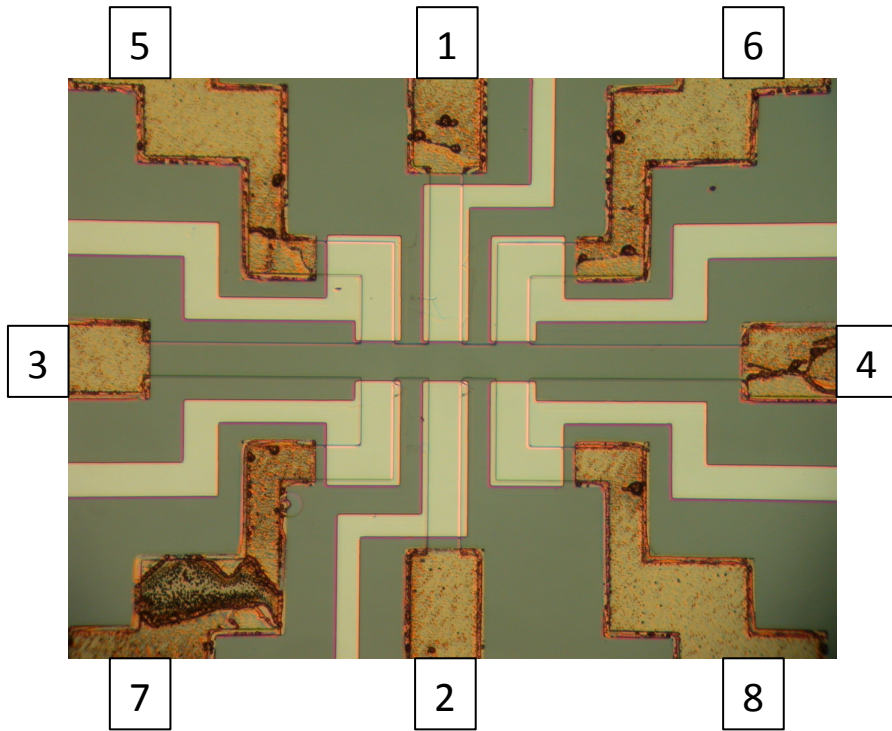


Figure 5.2: Hot-electron thermocouple device. Labeled squares are ohmic contacts numbered to show correspondence with layout shown in Fig. 5.1 (a). Central channel connecting contacts 3 and 4 is  $60 \mu\text{m}$  wide and about 1 mm long.

<sup>1</sup>This is the same device that was shown at higher magnification in Chapter 1 in Fig. 1.6 as part of a discussion about device fabrication.

Before continuing, it is worth commenting on the fact that the mobility of this sample at  $\mu_e = 3.3 \times 10^6 \text{ cm}^2/\text{Vs}$  is an order of magnitude less than that of the diving board device described in the previous chapter, which has  $\mu_e = 3.1 \times 10^7 \text{ cm}^2/\text{Vs}$ . All else being equal, we tend to prefer the highest mobility 2DES possible since the reduction in scattering events allows the manifestation of the most delicate strongly correlated phases, many of which will be discussed in subsequent chapters. The highest mobility heterostructures are inappropriate for our thermocouple, however, for two key reasons. First, as explained in Section 1.2, the highest mobility heterostructures available for this study are “over-doped” with silicon resulting in mobile carriers<sup>2</sup> in the doping layer positioned between any external metallic gates and the 2DES. Consequently, these additional carriers will screen the electrostatic fields from external metal gates such as  $G_1$  and  $G_2$  of the hot-electron thermocouple. Furthermore, even if this gateability issue were solved, higher mobility corresponds to a longer mean free path since  $\Lambda \propto \mu_e$ . The ultra-high-mobility 2DES used for our diving board devices has a tremendous mean free path of hundreds of microns. Such a 2DES confined to  $60 \mu\text{m}$  channels would exhibit ballistic transport resulting in undesirable systematic effects. By employing a lower—yet still very high—mobility for the hot-electron thermocouple, we avoid these issues.

## 5.2 Temperature Calibration

While the plot in Fig. 5.1 (b) is qualitatively consistent with our hot-electron thermocouple model, it provides insufficient information to determine the thermopower of the 2DES. For that, we require an independent determination of the electron temperature  $T_e$  at the center of the device, and hence the temperature difference  $\Delta T = T_e - T$  sensed by the thermocouple. In the  $\Delta T \ll T$  regime, the measured thermopower difference would then be the ratio of the measured thermovoltage to the measured temperature difference:  $\Delta S = S_1 - S_2 = \Delta V / \Delta T$ . Toward this end, we exploit the

---

<sup>2</sup>Note that the parallel conductance resulting from mobile carriers in the doping layers is negligible compared to that of the 2DES itself. So, while it significantly impacts the ability to electrostatically modulate the 2DES’s density, it may be ignored during most transport measurements.

temperature dependence of the 2DES's electrical resistivity  $\rho(T)$  as a thermometer<sup>3</sup>.

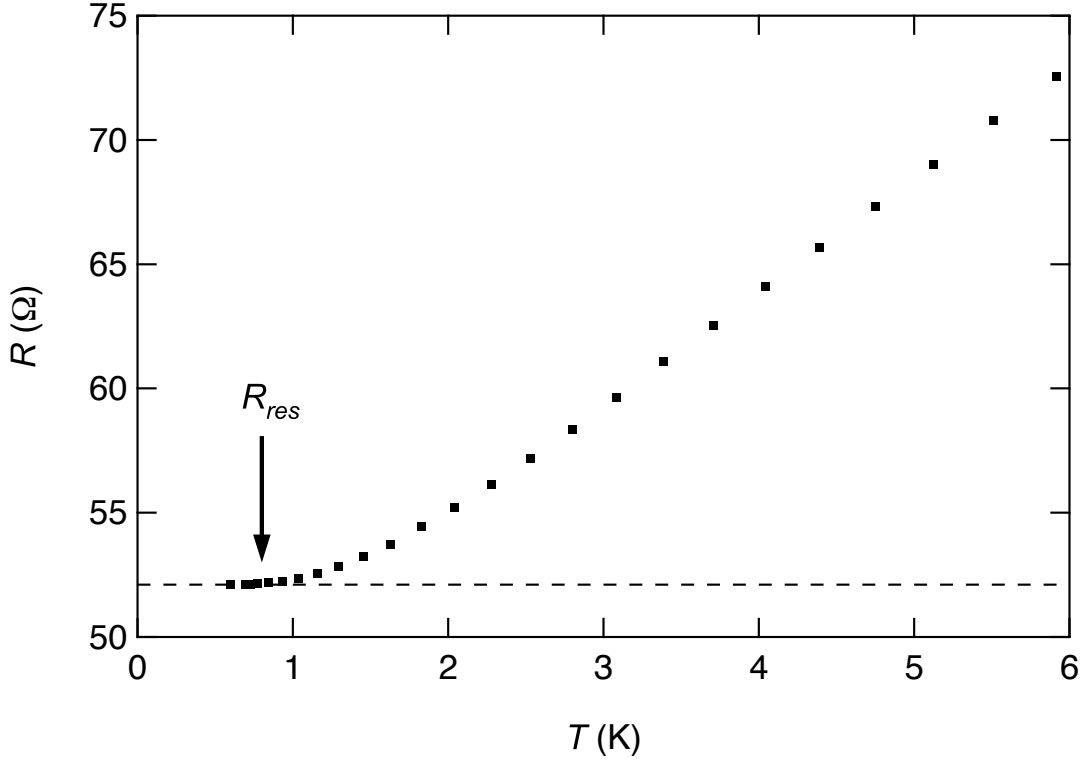


Figure 5.3:  $R$  vs  $T$  measured in the hot-electron thermocouple by sourcing  $I = 100$  nA between contacts 3 and 4 and measuring the voltage drop between contacts 5 and 6. Below  $T \approx 0.8$  K,  $R$  is independent of  $T$  with constant value  $R_{res} \approx 52 \Omega$ . Above this temperature,  $R$  serves as a thermometer.

Figure 5.3 shows the four-point<sup>4</sup> electrical resistance  $R$  versus  $T$  measured in the thermocouple device by sourcing  $I = 100$  nA between contacts 3 and 4 and measuring the voltage drop between contacts 5 and 6 (see Fig. 5.1 (a)). Keeping the current  $I$  sufficiently small we preclude appreciable Joule heating to maintain thermal equilibrium throughout the device; i.e.,  $T_e = T$  everywhere within the 2DES. We employ a calibrated Cernox resistance thermometer<sup>5</sup> that is well anchored to the cryostat cold

<sup>3</sup>This is similar to the temperature calibration strategy employed for our diving board technique (see Section 4.1.1) in that we are exploiting the temperature dependence of the 2DES's resistivity. Note, however, that in the case of the hot-electron thermocouple, thermal conductance measurements are made without applying an external magnetic field.

<sup>4</sup>See Appendix Section C.1 for elaboration on four-point resistance measurements using narrow band lock-in detection.

<sup>5</sup>Lakeshore Cryogenics, Model CX-1020-AA-03B.

finger to measure the lattice temperature  $T$ . For  $T \gtrsim 1.5$  K the 2DES's electrical resistance scales approximately linearly with  $T$ . This is the expected temperature dependence for a high-mobility 2DES within a GaAs/AlGaAs heterostructure in this temperature regime, which is the result of acoustic phonon scattering via piezoelectric coupling [59]. Below  $T \sim 1.5$  K the temperature dependence of  $R$  rapidly weakens and by  $T \approx 0.8$  K  $R$  is independent of  $T$  with constant value  $R_{res} \approx 52 \Omega$ . This remaining *residual resistance* results from screened impurities and defects within the GaAs lattice [59]. Our use of the 2DES's resistance as a thermometer is therefore limited to temperatures  $T \gtrsim 0.8$  K.

To achieve high precision measurements of electrical resistance  $R$ , and hence, electron temperature  $T_e$ , we employ a modified Zair-Greenfield (ZG) bridge [60], which is diagrammed in Fig. 5.4. The ZG bridge circuit is similar to the well-known Wheatstone bridge in that it measures an unknown electrical resistance by balancing it against a known resistance. The key advantage of the ZG bridge over the Wheatstone is that it accommodates four-point resistance measurements, a critical feature when working with 2DESs that often have relatively large contact resistances.

The thick black portion of the circuit shown in Fig. 5.4 represents the current path within our ZG bridge. We source an AC current  $I$  to contact 3 and drain it from contact 4 before passing it through the standard resistance  $R_s$  and then to electrical ground to complete the circuit. Four operational amplifiers configured as followers monitor the voltages at contacts 7 and 8 along with those just before and after  $R_s$ . The voltage followers act as buffers between the current path and the transformers of the bridge [61]. The voltage difference between the outputs of the followers monitoring contacts 7 and 8 is placed across a 1:1 isolation transformer. The outputs of the other two followers, which correspond to the voltage before and after  $R_s$ , are put across a ratio transformer. The  $V_{1f}$  lock-in detector then measures the voltage drop due to the 2DES's resistance minus the voltage drop due to the standard resistance after being inductively divided by the ratio transformer:

$$V_{1f} = I \cdot (R - \mathcal{R} \cdot R_s), \quad (5.2)$$

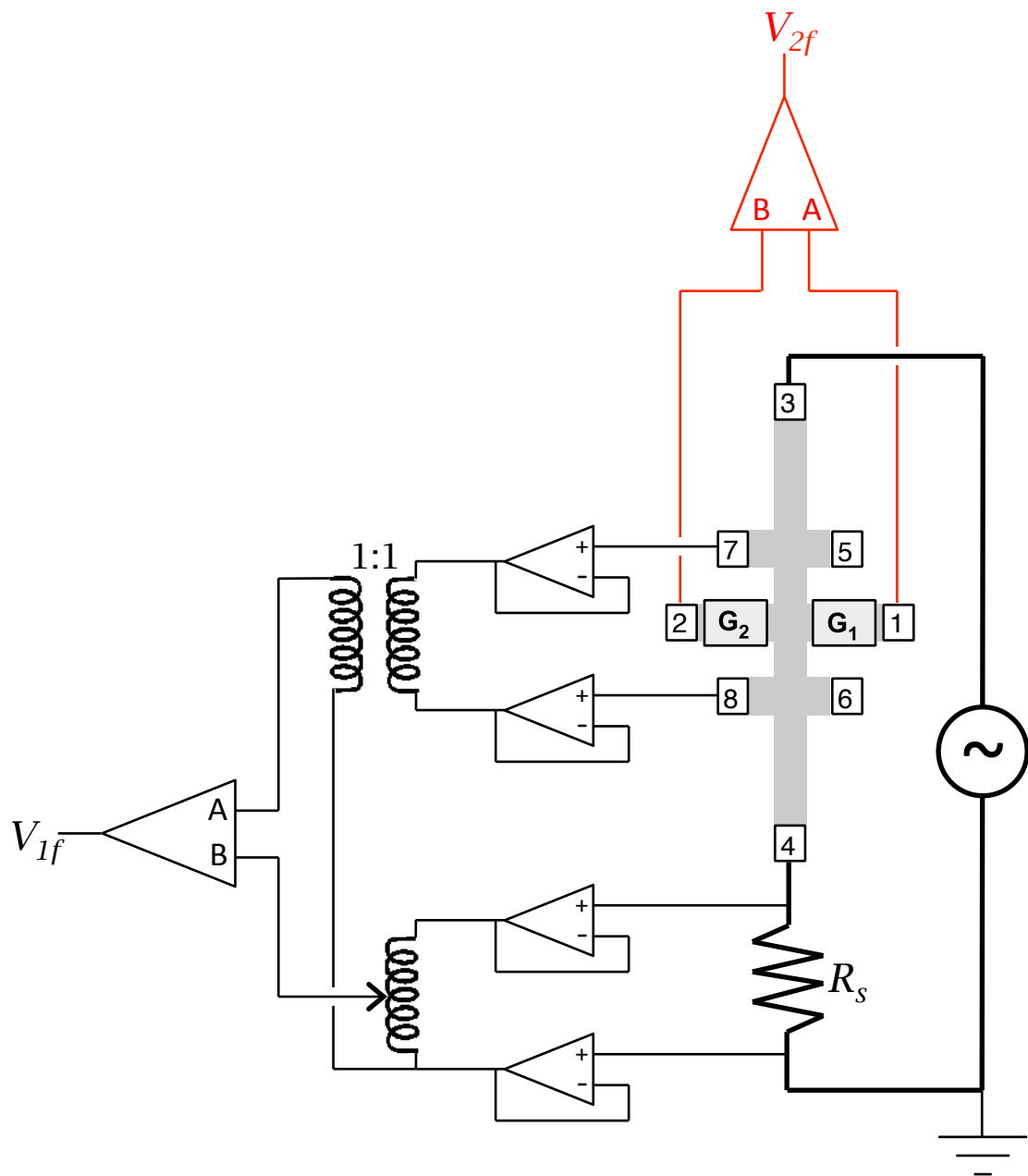


Figure 5.4: 2DES thermopower measurement circuit utilizing the hot-electron thermocouple. A modified Zaire-Greenfield bridge measures the four-point resistance of the 2DES between contacts 7 and 8 relative to the standard resistance  $R_s$  using a lock-in detector sensing the signal at  $1f$ . A second lock-in detector measures the thermovoltage by sensing the signal between contacts 1 and 2 at  $2f$ .

where  $R$ , as before, denotes the four-point resistance of the 2DES and  $\mathcal{R}$  is the adjustable setting of the ratio transformer, which has a value between 0 and 1 with five digits of precision. When the ZG bridge is balanced—i.e., when  $V_{1f} = 0$ —we have effectively measured the 2DES’s resistance as  $R = \mathcal{R} \cdot R_s$ , independent of the measurement current  $I$ .

### 5.3 Measurement Protocol

Our basic thermopower measurement protocol is as follows. We initially regulate the cryostat at  $T = T_0$  and measure  $R$  using a sufficiently small current  $I$  that Joule heating is negligible such that the electrons are in thermal equilibrium with the surrounding crystal lattice throughout the 2DES. To measure  $R$ , we balance the ZG bridge by adjusting the ratio transformer setting so that  $V_{1f} = 0$ . We then decrement the cryostat temperature by a small amount  $\Delta T_{cryo} \ll T_0$ , which causes  $R$  to decrease slightly as the 2DES cools bringing the ZG bridge out of balance. Next, we bring the ZG bridge back into balance by increasing  $I$  and thereby heating the 2DES, which increases  $R$ . Meanwhile, at the ohmic contacts the 2DES’s temperature is pinned to that of the crystal lattice  $T = T_0 - \Delta T_{cryo}$ . In this way we establish a known  $\Delta T$  within the 2DES between the center of the device and the ohmic contacts.

Naively, one would expect  $\Delta T = \Delta T_{cryo}$ . In fact, as a consequence of subtleties that arise when using narrow band lock-in detection to measure changes in resistance resulting from self-heating, it so happens that  $\Delta T = \frac{2}{3} \Delta T_{cryo}$ . We derive this factor of 2/3 in Appendix E.

Having established the temperature difference  $\Delta T$  we now measure the thermovoltage using a second lock-in detector that monitors the  $2f$  component of the signal at contacts 1 and 2 (see Fig. 5.4). The average thermovoltage  $\Delta V$  is related to the output of this lock-in amplifier  $V_{2f}$ , which is the root-mean-squared amplitude of the signal, by  $\Delta V = \sqrt{2} \cdot V_{2f}$ . With the top gates  $G_1$  and  $G_2$  biased to produce known electron densities  $n_1$  and  $n_2$  in the arms of our thermocouple, the measured differential thermopower is

$$\Delta S(\langle T \rangle, n_1, n_2) = \frac{\Delta V}{\Delta T} = \frac{3}{\sqrt{2}} \frac{V_{2f}}{\Delta T_{cryo}}, \quad (5.3)$$

where  $\langle T \rangle$  is the average temperature of the 2DES.

For each initial temperature  $T = T_0$ , we repeat the above measurement sequence for several values of  $\Delta T_{cryo}$  (all values of  $\Delta T_{cryo}$  are less than  $T_0/10$ ). And for each  $\Delta T_{cryo}$  we measure  $V_{2f}$  for several combinations of  $n_1$  and  $n_2$ . By measuring  $V_{2f}$  at fixed  $n_1$  and  $n_2$  for several values of  $\Delta T_{cryo}$ , we improve the accuracy of our thermopower determination as well as demonstrate that  $V_{2f}$  is linear in  $\Delta T_{cryo}$ . By measuring  $V_{2f}$  at fixed  $\Delta T_{cryo}$  for several combinations of  $n_1$  and  $n_2$ , we capture the density dependence of the thermopower.

## 5.4 Experimental Results

We operate the dilution refrigerator<sup>6</sup> in the “high” temperature mode described in Section 2.6, which accommodates stable regulation at temperatures between about 0.6 and 6 K. This happens to be a very convenient temperature range given that our use of the 2DES’s resistivity as a thermometer confines our measurements to above  $T \approx 0.8$  K. Using the protocol described in the previous section we measure the temperature dependence of the differential thermopower  $\Delta S$  for several combinations of 2DES densities  $n_1$  and  $n_2$  within the thermocouple arms. Figure 5.5 contains a linear plot of representative determinations of  $\Delta S/T$  versus  $T$  for three different combinations of the thermocouple arm electron densities  $n_1$  and  $n_2$ . At temperatures as high as  $T \approx 2$  K,  $\Delta S/T$  is independent of  $T$  and qualitatively consistent with diffusion thermopower. Above  $T \approx 2$  K, the magnitude of  $\Delta S/T$  increases with temperature consistent with the presence of phonon drag.

For comparison, recall Figs. 4.5 and 4.6 from the previous chapter that showed thermopower as a function of temperature as measured in two diving board style experiments. The qualitative difference between these data and those of Fig. 5.5 is

---

<sup>6</sup>An enhanced Oxford KelvinOx 25 dilution refrigerator.

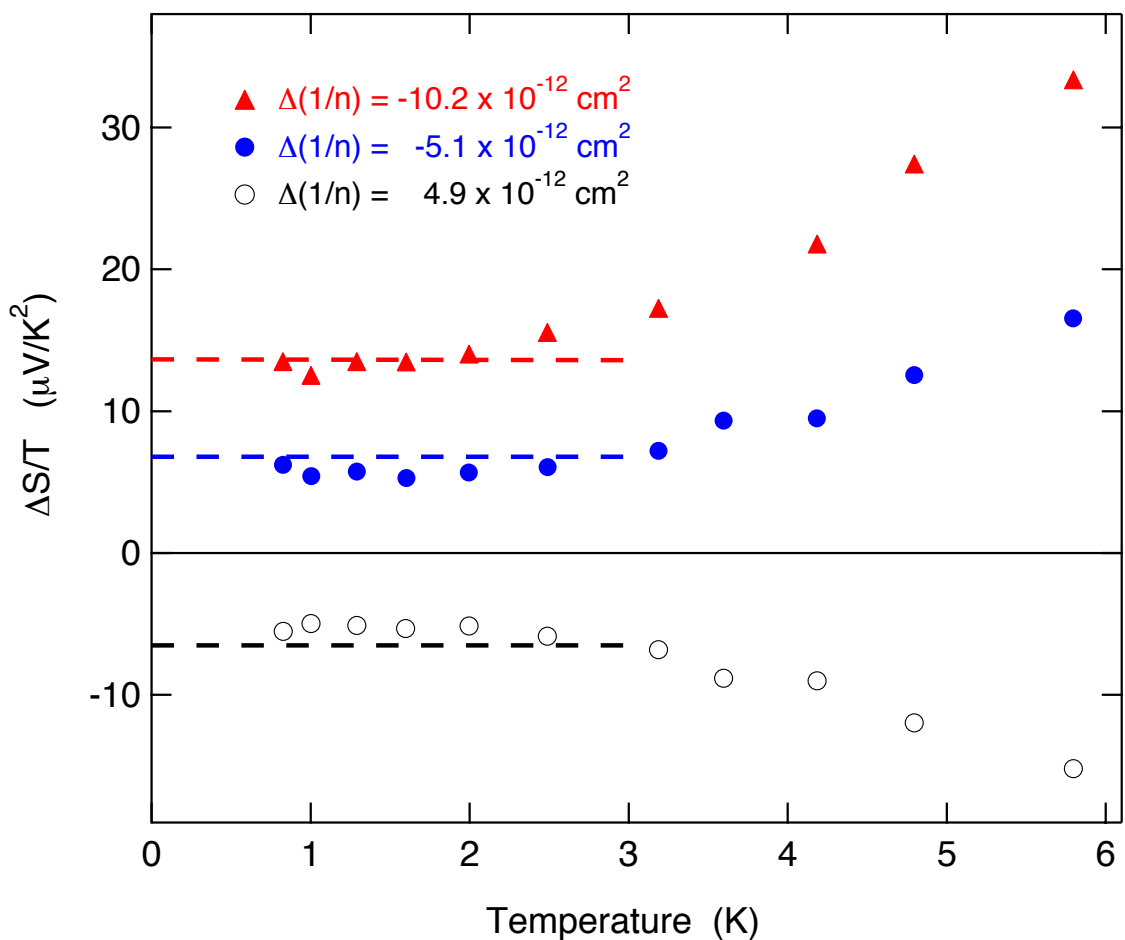


Figure 5.5:  $\Delta S/T$  vs  $T$  measured with hot-electron thermocouple for  $\Delta(1/n) = -10.2$ ,  $-5.1$ , and  $+4.9 \times 10^{-12} \text{ cm}^2$ . Dashed lines are predictions of Mott formula, Eq. 5.4. Reprinted with permission from W.E. Chickering, J.P. Eisenstein, and J.L. Reno, *Phys. Rev. Lett.* **103**, 046807 (2009). Copyright 2009 by the American Physical Society.

stark. In the diving board experiments, the crossover from the diffusion- to phonon-dominated thermopower regimes occurred between 150 and 400 mK. At  $T \approx 2$  K, due to phonon drag, the thermopower measured by Fletcher et al. shown in Fig. 4.5 reaches a maximum that is more than twice the value predicted by Mott’s formula for diffusion thermopower. In contrast, the data from the hot-electron thermocouple experiment only begins to exhibit evidence of phonon drag at this temperature. This dramatic order of magnitude difference in the crossover temperature highlights the extrinsic origins of phonon drag thermopower and how it can be greatly reduced using the hot-electron approach when investigating thermoelectric effects in low-dimensional electron systems.

Another advantage of our hot-electron technique compared to the traditional diving board setup is our ability to modulate the density of the 2DES. Indeed, the operation of the thermocouple depends upon this ability in order to establish different thermopowers  $S_1$  and  $S_2$ . We modify the density in the thermocouple arms in the conventional capacitive manner using top gates (see Section 1.2). Doing this with a diving board setup is difficult because the metallization of the gate can significantly alter the way phonons scatter off the top surface resulting in nonuniform temperature gradients, which would complicate temperature determinations. In contrast, the hot-electron thermocouple experiment does not rely upon uniform temperature gradients.

In the case of a diving board experiment, an unexpected nonuniform temperature gradient could introduce systematic errors in the measurement of  $\Delta T$ , and hence, in the determination of  $S$ . The hot-electron thermocouple technique avoids the necessity of uniform temperature gradients and merely requires a determination of the temperature of the ‘hot’ electrons at the center of the device as discussed in previous sections. Meanwhile, the ‘cold’ electrons are presumed to be in equilibrium with the cryostat cold finger whose temperature is measured using a calibrated resistance thermometer (see Section 2.4). Thus we determine  $\Delta T$  without assuming a particular temperature profile, modulo a boundary condition at the contact. This grants us liberties with regard to device fabrication such as including top gates.

Once again we provide Mott's formula as derived in Section 3.3, which says the low-temperature diffusion thermopower of a Drude metal is given by

$$S^d = - \left( \frac{\pi^2 k_B^2}{3e} \right) \left( \frac{m^*}{\pi \hbar^2} \right) T \frac{1+p}{n}, \quad (5.4)$$

where  $m^*$  is the band mass of the electrons ( $m^* = 0.067m_e$  in GaAs),  $n$  is the 2DES density and  $p \equiv (n/\tau_m) \frac{d\tau_m}{dn}$ . The data sets shown in Fig. 5.5 are qualitatively consistent with the density dependence of Eq. 5.4;  $\Delta S/T \propto \Delta(1/n) \equiv 1/n_1 - 1/n_2$ . The sign of  $\Delta S/T$  changes with the sign of  $\Delta(1/n)$  and the magnitude of  $\Delta S/T$  clearly increases with  $\Delta(1/n)$ . To examine this dependence more carefully, Fig. 5.6 displays  $\Delta S$  as a function of  $\Delta(1/n)$  at  $T = 1$  and 2 K. Although the linearity in  $\Delta(1/n)$  is not perfect, the deviations are relatively small.

Having established that our measured thermopower has the qualitative temperature and density dependence expected of  $S^d$ , we turn to the magnitude of the effect. The dashed horizontal lines in Fig. 5.5 and diagonal lines in Fig. 5.6 are the predictions of Eq. 5.4 given  $p = 0.92$  for the various data sets shown. Importantly, we independently measure this value for  $p$  in a separate device<sup>7</sup> cleaved from the same parent wafer. Equation 5.4 therefore contains no adjustable parameters.

While the overall agreement between theory and experiment is clearly quite good, there are small systematic deviations. For example, Fig. 5.5 shows that the magnitude of the measured thermopower at  $\Delta(1/n) = \pm 5 \times 10^{-12} \text{ cm}^2$  falls below the Mott result by about 20 percent for  $T \lesssim 2$  K. Similar deviations are apparent in the density dependences shown in Fig. 5.6. It is worth considering whether finite temperature corrections to Eq. 5.4, which is derived using a Sommerfeld expansion, could be responsible for this discrepancy. The next term in the expansion is  $\mathcal{O}(T/T_F)^3$ . More precisely, re-writing Eq. 5.4 in terms of  $T_F = (\pi \hbar^2/m^*)(n/k_B)$  and including this additional term we have

---

<sup>7</sup>The key feature of the device used to measure  $p$  is a gatable 2DES region that accommodates four-point resistance measurements (see Appendix C). This allows a measurement of an electrical resistance originating solely from the 2DES as a function of electron density  $n$ . Using the Drude formula  $\rho = m^*/ne^2\tau_m$ , one can determine  $p \equiv \partial \ln \tau_m / \partial \ln n$  by fitting the data.

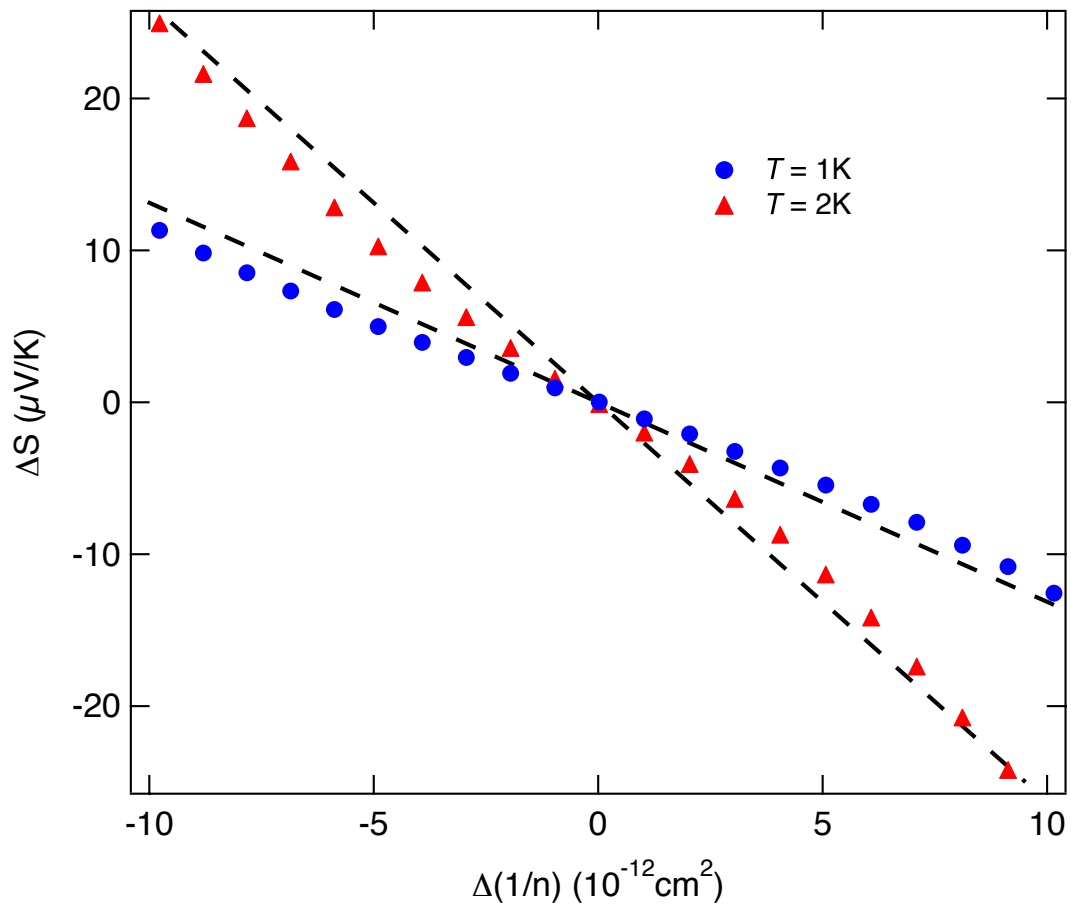


Figure 5.6:  $\Delta S$  vs  $\Delta(1/n)$  measured with hot-electron thermocouple at  $T = 1$  and  $2$  K. Solid lines are predictions of Mott formula, Eq. 5.4. Reprinted with permission from W.E. Chickering, J.P. Eisenstein, and J.L. Reno, *Phys. Rev. Lett.* **103**, 046807 (2009). Copyright 2009 by the American Physical Society.

$$S^d = - \left( \frac{\pi^2 k_B}{3e} \right) (p+1) \frac{T}{T_F} - \left( \frac{7\pi^4 k_B}{90e} \right) (p+1)(p)(p-1) \left( \frac{T}{T_F} \right)^3. \quad (5.5)$$

Notice that the additional term reduces the magnitude of  $S^d$  when  $0 < p < 1$ , such that this correction has a sign that is consistent with the deviations of Figs. 5.5 and 5.6. However, evaluating this correction for our 2DES at  $T = 1$  K and  $\Delta(1/n) = 10 \times 10^{-12} \text{ cm}^2$ , which is equivalent to  $\Delta(1/T_F) = 1/41.5 \text{ K}^{-1}$ , yields a magnitude of only 1.6 nV/K. This is orders of magnitude smaller than the discrepancies in question, which are  $\sim 1 \text{ } \mu\text{V/K}$  demonstrating that finite temperature corrections to Mott's formula cannot explain these differences between theory and experiment.

Although the origins of these deviations are so far unknown, one systematic effect that may be important deserves mention. The electron temperature determinations used here are based on resistivity measurements using voltage probes that straddle the thermocouple arms. As such, these measurements offer an average of  $T_e$  within the central region of the device. The electron temperature in this region is determined both by the ability of the 2DES to lose energy to phonons but also by the conduction of heat through the 2DES to the several ohmic contacts. Simulations of these heat transfer processes in our device suggest that the average  $T_e$  inferred from the resistivity measurements *exceeds* that sensed by the thermocouple junction by typically 10 percent. While correcting for this effect would reduce the discrepancy between our data and the Mott formula, this would increase the complexity of our data processing and we prefer to present our data in the most transparent form possible.

Finally, it is important to note that the data of Fig. 5.5 is limited to  $T \gtrsim 0.8$  K merely due to the inability to independently determine  $\Delta T$  at lower temperatures using the 2DES's resistance as explained in Section 5.2. No such limitations exist on measuring thermovoltages using the hot-electron technique, however. In fact, if we assume the Mott formula holds true at lower temperatures, the present device is able to resolve a 3 mK temperature rise at  $T_e = 30 \text{ mK}$ <sup>8</sup>. Section 2.4 described

---

<sup>8</sup>With  $\Delta S/T \approx 15 \text{ } \mu\text{V/K}^2$  (as shown in Fig. 5.5 for  $\Delta(1/n) = -10 \times 10^{-12} \text{ cm}^2$ ),  $\Delta T_e = 3 \text{ mK}$

the challenge of cooling electrons below  $T_e \sim 100$  mK. Given that conventional thermometers couple more strongly to the crystal lattice surrounding the 2DES than to the 2DES itself, the ability to directly measure differences in electron temperature has significant experimental value.

## 5.5 Future Work: Metal-Insulator Transition

The majority of this thesis focuses on the large magnetic field regime. This is largely motivated by the fact that Coulomb interactions become critically important in this regime. As discussed in Chapters 8 and 9, these interactions result in a variety of interesting correlated electron phases. In our experience, the diving board technique described in Chapter 4 is better suited than the hot-electron thermocouple for measuring thermopower in this regime. The reason being that, in the case of the hot-electron thermocouple, the “heater” is the 2DES itself, which has a resistivity that is highly sensitive to magnetic field. In the quantum limit (see Chapter 6), the situation is particularly challenging as the 2DES’s resistivity is non-uniform resulting in a complicated temperature profile within the hot-electron thermocouple. Consequently, it becomes difficult to interpret the measured thermovoltages in terms of thermopower.

Another approach to enhancing the relative importance of Coulomb interactions is through the reduction of electron density. The idea is that electron-electron interactions scale as  $\varepsilon_c \propto 1/r$ , where  $r$  is the average distance between them. In terms of electron density  $n$ , we may write  $\varepsilon_c \propto \sqrt{n}$ . Meanwhile, the kinetic energy scales as  $\varepsilon_F \propto n$  such that their ratio scales as  $\varepsilon_c/\varepsilon_F \propto 1/\sqrt{n}$ . More formally, the strength of the Coulomb interactions are often characterized by the dimensionless *Wigner-Seitz radius*:

$$r_s = \frac{1}{a_B \sqrt{\pi n}}, \quad (5.6)$$

where  $a_B$  is the effective Bohr radius ( $a_B = 10.3$  nm in GaAs). By reducing the  


---

at  $T_e = 30$  mK yields a thermoelectric voltage  $\Delta V \approx 1$  nV, which is readily detectable.

electron density we increase the Wigner-Seitz radius, and hence, the importance of Coulomb interactions.

The hot-electron thermocouple is particularly well-suited for measuring the diffusion thermopower of the 2DES in the low-density regime. Unlike the diving board technique, in which  $n$  is fixed, we can readily modulate  $n$  to arbitrarily small values within the arms of the thermocouple. Note that a 2DES of lower density is generally more susceptible to phonon drag. This is because its Fermi wave vector scales as  $k_F \propto \sqrt{n}$  and a smaller value of  $k_F$  results in an increased likelihood of backscattering by phonons. Importantly, as we have shown, the thermocouple dramatically reduces the contribution of phonon drag compared with traditional thermopower measurement techniques. In this way, our hot-electron technique provides an ideal method for observing the thermopower of a low-density 2DES while at the same time minimizing the non-diffusion component.

At sufficiently low density, a real 2DES will transition from a conducting to an insulating phase; this is generically referred to as the *metal-insulator transition*<sup>9</sup> (MIT). This MIT may seem intuitive given that even the highest mobility 2DES moves in the presence of a weak random potential. As the density is reduced, the Fermi level  $\varepsilon_F$  eventually becomes comparable to these background potential fluctuations such that at sufficiently low temperature electrons no longer populate states that extend across the sample. This is indeed expected in three dimensions and is known as *strong localization* or *Anderson localization*. However, it is not clear that such a transition should occur in two dimensions.

According to the scaling theory of localization of Abrahams et al. [63], there is no true conducting behavior in two dimensions. As such, a MIT should not occur in two dimensions. Rather, a 2DES should cross over smoothly from a regime of *weak localization*, in which localization occurs in sufficiently large samples due to quantum interference, to that of strong localization. The initial observations [64, 65] of a MIT in two dimensions were therefore unexpected. Significantly, the theory of Abrahams et al. does not account for electron-electron interactions. Theories [66] have been

---

<sup>9</sup>For a review of the MIT in two dimensions refer to [62] by Kravchenko and Sarachik.

presented in which electron-electron interactions stabilize a metallic phase and their interplay with the disorder potential results in a MIT within a 2DES. The nature of the MIT in high-mobility 2DESs, along with that of the proximate phases, remains a topic of great interest.

Thermopower offers a relatively unexplored perspective of the MIT<sup>10</sup>. Figure 5.7 illustrates our preliminary findings in the vicinity of the zero-field MIT using our hot-electron thermocouple. The figure shows  $\Delta S$  (red solid curve) versus  $n_2$ , the electron density beneath top gate  $G_2$  (see figure inset), measured at  $T = 1.0$  K. The density beneath top gate  $G_1$  is held fixed at  $n_1 = 1.5 \times 10^{11} \text{ cm}^{-2}$ . As usual, the thermovoltage is measured between contacts 1 and 2 and translated to the difference in thermopowers  $\Delta S$  given a known temperature difference  $\Delta T$  between the contacts and the center of the thermocouple. As  $n_2$  is electrostatically reduced from its ungated value of  $n_2 = 1.5 \times 10^{11} \text{ cm}^{-2}$ , the thermopower of the 2DES beneath  $G_2$  increases in magnitude such that  $\Delta S$  increases. The dashed curve in Fig. 5.7 corresponds to the diffusion thermopower of free 2D electrons as per Mott's formula (Eq 5.4). The figure demonstrates that  $\Delta S$  is in good agreement with Mott's formula for  $n_2 \gtrsim 6 \times 10^{10} \text{ cm}^{-2}$ . Note that this is consistent with the data of Figs. 5.5 and 5.6. However, as  $n_2$  is further reduced we find that  $\Delta S$  can no longer be explained in terms of free electrons.

Figure 5.7 also shows the two-point conductance  $G_{2pt}$  (blue dotted curve) measured between contacts 1 and 2.  $G_{2pt}$  vanishes for  $n_2 < 1.7 \times 10^{10} \text{ cm}^{-2}$  resulting in a divergence in the uncertainty of our  $\Delta S$  measurement. The vanishing of  $G_{2pt}$  is presumably due to a MIT that occurs at some critical density  $n_c$ , below which the conductivity of the 2DES decreases exponentially with decreasing temperature. In the vicinity of this transition, where  $1.7 \times 10^{10} \text{ cm}^{-2} < n_2 < 6 \times 10^{10} \text{ cm}^{-2}$ , we find that  $\Delta S$  exceeds what is predicted for free electrons. This excess thermopower is suggestive of an unconventional conducting phase or scattering mechanism.

A typical study of the MIT includes measurements of the resistivity  $\rho$  versus  $T$  at several densities on both sides of the transition. Metallic behavior is characterized by

---

<sup>10</sup>The author is aware of very few thermopower studies of MITs [54, 55].

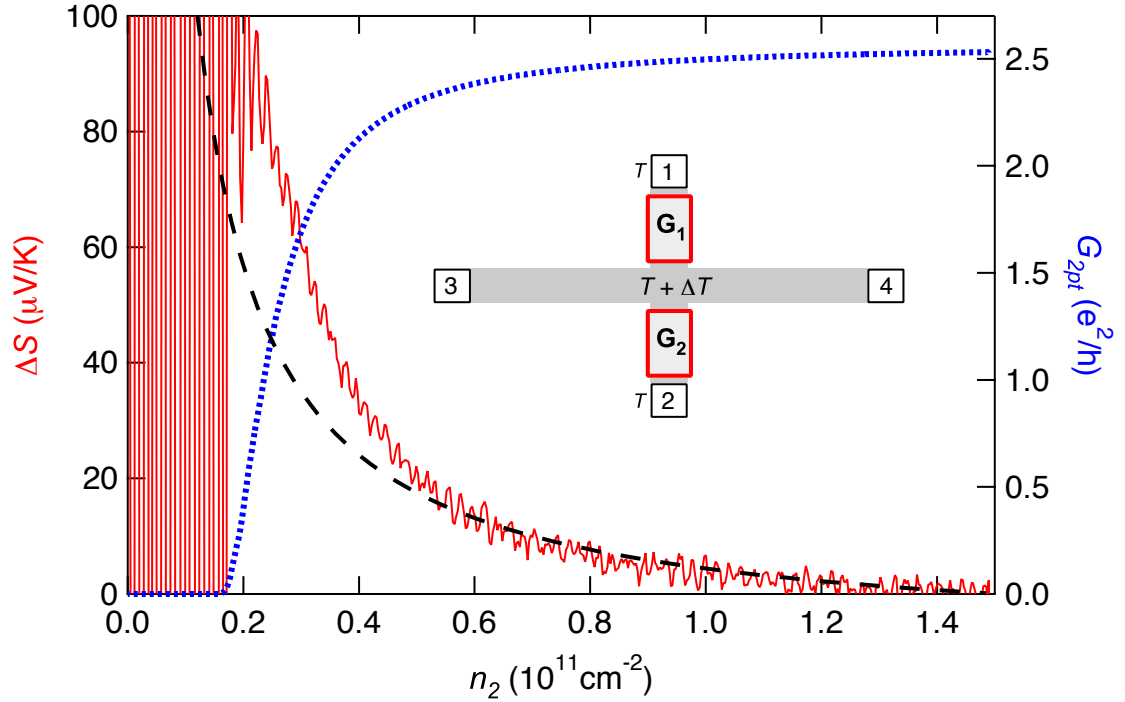


Figure 5.7: Thermopower in the vicinity of the metal-insulator transition (MIT) at  $T = 1.0$  K.  $\Delta S$  (red solid curve) versus  $n_2$ , with  $n_1$  held constant at  $n_1 = 1.5 \times 10^{11} \text{ cm}^{-2}$ , is shown together with the two-point conductivity  $G_{2pt}$  (blue dotted curve) measured between contact 1 and contact 2 (see inset for device layout). The MIT is evidenced by a vanishing  $G_{2pt}$  at a finite value of  $n_2$ . The dashed curve represents the value of  $\Delta S$  calculated for free electrons.

$d\rho/dT > 0$ , while insulating behavior is characterized by  $d\rho/dT < 0$ . A proper study that incorporates thermopower would complement these data with measurements of  $S_{xx}$  versus  $T$  at the same densities. As with  $\rho$ , we can discern whether a 2DES is metallic or insulating from the temperature dependence of  $S_{xx}$ . For example, at low temperature, a common metal has  $S_{xx} \propto T$  (see Section 3.3), while a common band insulator has  $S_{xx} \propto T^{-1}$  (see Appendix G). Furthermore, using thermopower, one can theoretically [67] recognize other prospective phases including Mott variable-range hopping, where  $S_{xx} \propto T^{1/3}$  as well as correlated hopping where  $S_{xx}$  is temperature-independent.

Rather than the 2DES used to acquire the data of Fig. 5.7, a better choice for a thermopower study of the MIT would be a two-dimensional hole system (2DHS). This

is because the effective mass of holes is typically about four times that of electrons in GaAs heterostructures [44]. Consequently, the Wigner-Seitz radius  $r_s$ —which is related to the effective mass via the effective Bohr radius  $a_B$ —is often larger for a 2DHS. For example, our ungated 2DES ( $n = 1.5 \times 10^{11} \text{ cm}^{-2}$ ) has  $r_s \approx 1.4$  and when  $G_{2pt}$  vanishes in Fig. 5.7 ( $n = 1.7 \times 10^{10} \text{ cm}^{-2}$ ) it has  $r_s \approx 4.2$ . By comparison, a GaAs/AlGaAs-based 2DHS can have  $r_s > 10$  [62]. Larger values of  $r_s$  are correlated with starker MIT features.

## 5.6 Summary

We have seen how a simple, yet novel, hot-electron thermocouple can be used to measure the thermopower of ultra-high-mobility 2D electrons in a GaAs/AlGaAs heterostructure. Our device layout facilitates direct heating of the 2DES while simultaneously measuring a thermovoltage that arises by differentially modulating the carrier density of two independently “gated” regions. By electrostatically adjusting, or “gating”, the density of the 2DES within the arms of the thermocouple, a nonvanishing thermopower difference  $\Delta S$  is established.  $\Delta S$  is determined by independently measuring a thermovoltage difference  $\Delta V$  and temperature difference  $\Delta T$  along the arms of the device.  $\Delta T$  is determined by exploiting the dependence of the 2DES’s resistivity on temperature. We utilize a modified Zair-Greenfield bridge circuit along with a carefully designed measurement protocol to optimize the precision of our temperature and thermovoltage measurements. Importantly, by heating the 2DES directly, our technique dramatically reduces the influence of phonon drag on the thermopower of our system.

We find good agreement with Mott’s formula for diffusion thermopower with respect to magnitude as well as both temperature and density dependence over the temperature range of 0.8 to 2.0 K. Above these temperatures, our measurements exceed what is expected for solely diffusion thermopower, the excess being attributed to phonon drag. In Chapter 4 we found the impact of phonons on the thermopower as measured using diving board style experiments to be significant at temperatures

as low as 200 mK. The ability to suppress appreciable phonon drag at much higher temperatures is a key advantage of this hot-electron approach. In addition to the potential of electron thermometry down to very low temperatures, this technique provides unprecedented access to high-temperature and low-density regimes of diffusion thermopower of high-mobility 2D electrons.

A potential application for our hot-electron thermocouple is the study of the enigmatic metal-insulator transition (MIT) observed in high-mobility 2D system. The MIT, which is explicitly not expected for noninteracting 2D electrons, is believed to result from the interplay of electron-electron interactions and disorder. Most studies of the MIT focus on measurements of the electrical conductivity/resistivity. The contribution of measurements of diffusion thermopower in the vicinity of the MIT will likely provide valuable new insights. The hot-electron thermocouple is particularly well-suited for measuring diffusion thermopower at low densities, which is precisely the regime where the MIT occurs. Indeed, our preliminary results show an enhancement of the thermopower relative to that of free electrons at the lowest densities, which is suggestive of an unconventional conducting phase or scattering mechanism.

## Chapter 6

# Quantum Hall Effect

When a strong magnetic field is applied to electrons confined to a plane, something truly magical occurs. The most famous manifestation of this magic are the plateaus at precise multiples of  $h/e^2$  in the transverse resistance, known as the *quantum Hall effect* (QHE). This effect, along with the concomitant periodic vanishing of the longitudinal resistance, is an example of observable macroscopic phenomena that cannot be understood in terms of classical physics but requires a quantum mechanical explanation. The discovery of the QHE provided the first example of a quantum state that did not spontaneously break symmetry. Rather, the QHE arises due to topology and is independent of sample geometry. The attention brought to this new physical paradigm has led to hopes of robust forms of quantum computing and ushered in more general research of a new class of quantum matter known as the *topological insulator*.

The QH regime offers an ideal venue for those who wish to study many-body correlated physics. As will be explained in Chapter 8, otherwise inconsequential electron-electron interactions become critically important in the presence of a quantizing magnetic field. These interactions give rise to a plethora of collective phases, several of which are explored in subsequent chapters. To understand these phases, we must first be familiar with the noninteracting picture of QH physics.

This chapter reviews the theory of noninteracting 2D electrons subjected to a strong magnetic field. We obtain initial insights from the classical picture and see how this limited model ultimately fails us. We mathematically derive quantum me-

chanical basis functions for electrons in a magnetic field. The important roles of disorder and the sample edge are then discussed. And finally, we review the key features of magnetotransport, the *integer quantum Hall effect*, and associated phenomena. The theoretical foundation provided here will be referenced and built upon in subsequent chapters. Quantum Hall phenomena comprises a tremendous amount of research, both theoretical and experimental, and addresses the most fundamental and intriguing issues in condensed matter physics. In the following chapter we will connect this topic with that of thermoelectricity by discussing the thermopower of the 2DES in the QH regime.

## 6.1 Classical Hall Effect

Classically, an electron subjected to a magnetic field experiences a *Lorentz force*  $\mathbf{F}_l$  that is proportional to its charge  $e$  and normal to both the field vector  $\mathbf{B}$  and the electron's velocity  $\mathbf{v}$  such that  $\mathbf{F}_l = -e\mathbf{v} \times \mathbf{B}$ . In the absence of additional forces the electron will therefore engage in circular motion, known as a *cyclotron orbit*, with a radius

$$r_c = \left| \frac{m^*v}{eB} \right| \quad (6.1)$$

and an angular frequency, or *cyclotron frequency*,

$$\omega_c = \left| \frac{eB}{m^*} \right|. \quad (6.2)$$

In a disordered system, however, the electrical conductivity (and mobility) is finite and scattering events disrupt cyclotron orbits, with electrons traveling in curved paths between collisions.

Let us consider what happens if we impose both a perpendicular magnetic field  $\mathbf{B}$  and an in-plane electric field  $\mathbf{E}$  on our two-dimensional electrons. More specifically, let us examine the situation where current  $I$  is sourced to one end and drained from the other end of a 2DES confined to the rectangular geometry in the  $x$ - $y$ -plane illustrated

in Fig. 6.1. The figure depicts a 2DES, subjected to a field  $\mathbf{B}$  pointing in the  $z$ -direction, with six idealized electrical contacts on its periphery. Idealized voltmeters measure both the longitudinal voltage  $V_{xx}$  and the transverse voltage  $V_{xy}$ .

By sourcing current, we enforce a spatially averaged drift velocity  $\langle \mathbf{v}_d \rangle$  that is anti-parallel (electrons have negative charge!) to the direction of the imposed current; that is,  $\langle \mathbf{v}_d \rangle$  points in the negative  $x$ -direction in Fig. 6.1. The electrons will therefore experience an average Lorentz force  $\langle \mathbf{F}_l \rangle = -e \langle \mathbf{v}_d \rangle \times \mathbf{B}$ , which points in the negative  $y$ -direction. Clearly such a force does not dissipate energy in the  $x$ -direction so the longitudinal voltage is due entirely to the intrinsic resistivity of the 2DES:

$$V_{xx} = \gamma I / \sigma(0), \quad (6.3)$$

where  $\gamma$  is a geometrical factor that is of order unity for the system in the figure and  $\sigma(0)$  is the zero magnetic field electrical conductivity.

At the same time, once in steady-state, no current is allowed to flow in the  $y$ -direction. Consequently, there must exist a force to balance the Lorentz force. The balancing force takes the form of an electric field  $\mathbf{E}_H$  pointing in the negative  $y$ -direction, established due to charge separation as electrons accumulate on one side of the system (right side of Fig. 6.1) thereby leaving an excess positive ionic charge on the other side. The magnitude of this transverse field is therefore  $E_H = \langle v_d \rangle B = \langle j \rangle B / ne$ , where  $n$  is the electron density and  $\langle j \rangle$  is the average current density. Finally, by integrating over the  $y$ -direction, we see this field results in a transverse voltage across the system

$$V_{xy} = \frac{IB}{ne}. \quad (6.4)$$

This phenomenon is known as the *classical Hall effect*. Importantly, we see in Eq. 6.4 that  $V_{xy}$  is independent of the sample geometry and depends only on the imposed current, magnetic field, carrier density, and carrier charge. This useful result can therefore be exploited to reveal both the sign and density of carriers in an arbitrarily shaped single carrier-type system (that behaves classically).

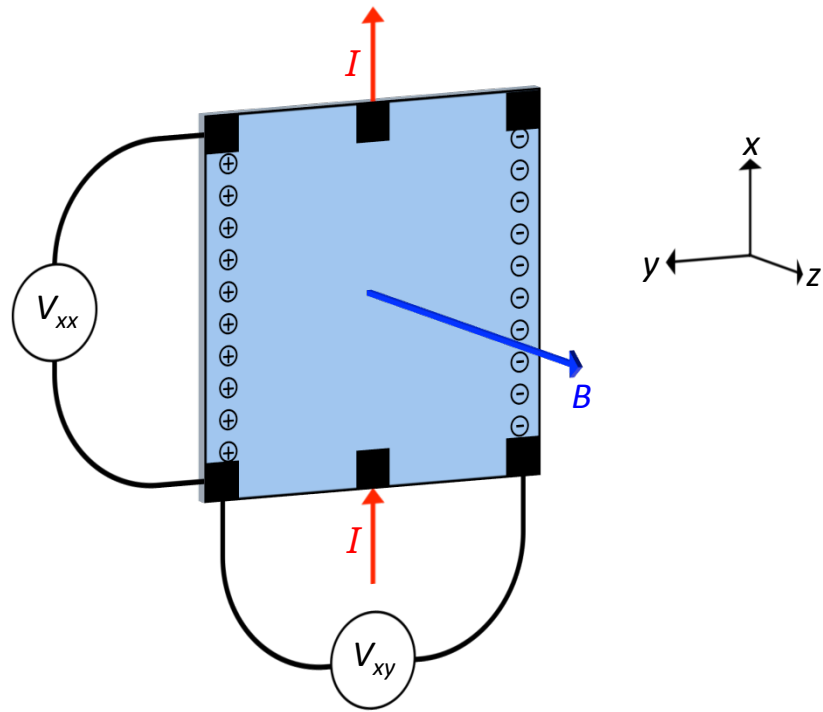


Figure 6.1: Classical magnetotransport. A rectangular 2DES is shown with six dark electrical contacts on its periphery. The 2DES is subjected to a magnetic field  $\mathbf{B}$  pointing in the  $z$ -direction. Current  $I$  is sourced to the bottom central contact and drained from the top central contact. Excess electrons accumulate on the right edge leaving an excess positive ionic charge on the left edge. Ideal voltmeters measure the longitudinal voltage  $V_{xx}$  between the corner contacts of the left edge and the transverse, or Hall, voltage  $V_{xy}$  between the corner contacts of the bottom edge.

Let us now consider what happens locally at a point near the middle of the system. Having a transverse, or Hall, component to the electric field means that it is no longer parallel to the current density, and therefore, Ohm's law for the conductivity must now be written in terms of a tensor:  $\mathbf{j} = \boldsymbol{\sigma}\mathbf{E}$ . Since we are imposing an electric current and determining the resulting electric field, it is convenient to express Ohm's law in terms of a resistivity tensor,  $\mathbf{E} = \boldsymbol{\rho}\mathbf{j}$ , where  $\boldsymbol{\rho} = \boldsymbol{\sigma}^{-1}$ . From Eq. 6.4 we see that the transverse or *Hall resistance* is  $R_{xy} = B/ne$  independent of the system's geometry. Recall that within the Drude model (see Section 3.2)  $\sigma = ne^2\tau_m/m^*$ , where  $\tau_m$  is the momentum lifetime and  $m^*$  is the electron effective mass. Applying this model to our two-dimensional resistivity tensor, we have

$$\boldsymbol{\rho} = \begin{pmatrix} \rho(0) & B/ne \\ -B/ne & \rho(0) \end{pmatrix} = \rho(0) \begin{pmatrix} 1 & \omega_c\tau_m \\ -\omega_c\tau_m & 1 \end{pmatrix}, \quad (6.5)$$

where  $\rho(0) = 1/\sigma(0) = m^*/ne^2\tau_m$  is the zero-field scalar resistivity.

Two limits deserve special attention here. First, there is the trivial limit of zero magnetic field where  $\boldsymbol{\rho}$  becomes diagonal and equivalent to the scalar  $\rho(0)$ . The other is the low disorder, high-field regime where  $\tau_m \gg 1/\omega_c$ ; that is, scattering becomes negligible. In the latter limit we may approximate the resistivity tensor as

$$\boldsymbol{\rho} \approx \begin{pmatrix} 0 & B/ne \\ -B/ne & 0 \end{pmatrix}, \quad \text{where } \tau_m \gg 1/\omega_c. \quad (6.6)$$

Here, the electric field and currents become orthogonal to each other. In the next section, we will see how the classical picture fails us in this limit.

## 6.2 Landau Level Quantization

A 2DES of sufficiently low disorder and at sufficiently high magnetic fields, is fundamentally quantum mechanical with behavior that dramatically differs from the classical picture described above. In this regime, a 2DES's constant density of states collapses into a discrete set of highly degenerate  $\delta$ -functions known as *Landau levels*.

When the Fermi-level is positioned in a region of vanishing density of states, the interior of the system becomes insulating reflecting the energy gap between adjacent Landau levels. This bulk behavior is accompanied by one or more dissipationless one-dimensional *edge states* running along the boundaries of the 2DES. The familiar manifestation of this phenomenon is the *integer quantum Hall effect* (IQHE) where the transverse, or Hall, conductance assumes values precisely quantized as integer multiples of  $e^2/h$ .

A degree of intuition for what happens in the quantum regime is offered by the classical expressions for the cyclotron radius and frequency; Eqs. 6.1 and 6.2 above. When  $\tau_m \gg 1/\omega_c$ , an electron will complete several cyclotron periods before scattering<sup>1</sup>. Only the radius of this circular motion depends on the electron's velocity, and hence, energy  $\varepsilon$ . That is,

$$r_c = \left| \frac{m^*v}{eB} \right| = \frac{\sqrt{2m^*\varepsilon}}{|eB|}, \quad (6.7)$$

while  $\omega_c = |eB/m^*|$  is independent of  $\varepsilon$ . This is reminiscent of a harmonic oscillator, and indeed, the quantum mechanical behavior of an electron in a magnetic field reflects this.

Neglecting electron-electron interactions (for now), the behavior of the 2DES in a quantizing magnetic field is given by the solution to Schrödinger's time independent equation [69]

$$\left\{ \frac{1}{2m^*} [\hat{\mathbf{p}} - q\mathbf{A}]^2 + q\phi \right\} \psi = \varepsilon\psi, \quad (6.8)$$

where  $\hat{\mathbf{p}}$  is the canonical momentum operator, which we replace with  $-i\hbar\nabla$ , and  $[\hat{\mathbf{p}} - q\mathbf{A}]$  is the mechanical momentum operator, which is associated with the kinetic energy (i.e. the first term within braces in Eq. 6.8). The term  $q\phi$ , meanwhile, is the electrostatic potential energy.

---

<sup>1</sup>Actually, a distinction should be made between the momentum lifetime  $\tau_m$  from Section 3.2 and the *quantum lifetime*  $\tau_q$ . More correctly, it is the latter that must be much larger than  $1/\omega_c$  for an electron to complete several cyclotron periods before scattering. These two lifetimes are highly correlated but different due to small angle scattering, which more significantly reduces  $\tau_q$ . Typically,  $\tau_m$  is one to two orders of magnitude larger than  $\tau_q$  [68].

To proceed, we must choose a vector potential  $\mathbf{A}$  to represent our field  $\mathbf{B}$ . A convenient choice is the so-called *Landau gauge* with  $\mathbf{A} = (0, Bx, 0)$ , which corresponds to  $\mathbf{B} = \nabla \times \mathbf{A} = B\mathbf{z}$ . Plugging this into Eq. 6.8 yields

$$\left\{ \frac{1}{2m^*} \left[ -\hbar^2 \frac{\partial^2}{\partial x^2} + \left( -i\hbar \frac{\partial}{\partial y} + eBx \right)^2 - \hbar^2 \frac{\partial^2}{\partial z^2} \right] - e\phi(z) \right\} \psi = \varepsilon\psi, \quad (6.9)$$

where  $\phi(z)$  represents the quantum well potential that confines our electrons to two dimensions (i.e. the conduction band discussed in Section 1.1). Since the confinement potential  $\phi(z)$  depends only on  $z$ , we can readily isolate the  $z$ -dependence and thereby treat the problem in two dimensions:

$$\frac{1}{2m^*} \left[ -\hbar^2 \frac{\partial^2}{\partial x^2} + \left( -i\hbar \frac{\partial}{\partial y} + eBx \right)^2 \right] u(x, y) = \varepsilon' u(x, y). \quad (6.10)$$

Expanding the terms in parentheses gives

$$\left[ -\frac{\hbar^2}{2m^*} \frac{\partial^2}{\partial x^2} - \frac{\hbar^2}{2m^*} \frac{\partial^2}{\partial y^2} - \frac{ie\hbar Bx}{m^*} \frac{\partial}{\partial y} + \frac{(eBx)^2}{2m^*} \right] u(x, y) = \varepsilon' u(x, y). \quad (6.11)$$

We see the magnetic field contributes two terms to the Hamiltonian. The first couples the  $x$  and  $\partial/\partial y$ , which is reminiscent of the Lorentz force. The second is parabolic in  $x$ , which looks like a harmonic oscillator potential. Motivated by a choice of  $\mathbf{A}$  that is independent of  $y$ , let us consider a solution of the form  $u(x, y) = f(x)e^{iky}$ . Plugging this into Eq. 6.11 we find the  $y$ -dependence cancels out:

$$\left[ -\frac{\hbar^2}{2m^*} \frac{d^2}{dx^2} + \frac{1}{2} m^* \omega_c^2 \left( x + \frac{\hbar k}{eB} \right)^2 \right] f(x) = \varepsilon' f(x). \quad (6.12)$$

This is indeed Schrödinger's equation for a one-dimensional harmonic oscillator!

Interestingly, Eq. 6.12 has the form of a harmonic oscillator with an angular frequency equal to the classical cyclotron frequency  $\omega_c = |eB/m^*|$ , but that is centered at  $x = -\hbar k/eB$ . The energy spectrum is

$$\varepsilon_{Nk} = \hbar\omega_c(N + 1/2) \quad (6.13)$$

where  $N = 0, 1, 2, 3, \dots$  is called the *Landau level* (LL). The corresponding wave functions (excluding their normalization constant) are

$$u_{Nk}(x, y) \propto H_N \left( \frac{x + \hbar k/eB}{l_B} \right) \exp \left[ -\frac{(x + \hbar k/eB)^2}{2l_B^2} \right] \exp(iky) \quad (6.14)$$

where  $H_N(x)$  are the Hermite polynomials and  $l_B \equiv \sqrt{\hbar/|eB|}$  is a characteristic length scale known as the *magnetic length*. The system has two quantum numbers,  $N$  and  $k$ , but importantly, the energy  $\varepsilon_{Nk}$  only depends on  $N$ . Each LL is therefore highly degenerate, with as many states as there are unique values of  $k$ .

In zero magnetic field, the 2DES has a constant density of states as a consequence of its parabolic dispersion relation,  $\varepsilon = \hbar^2\mathbf{k}^2/2m^*$ , together with its confinement to two dimensions. This is illustrated in Fig. 6.2 (a) where, for the moment, we ignore the electron's spin. As illustrated in Fig. 6.2 (b), with the application of a magnetic field, this constant density of states collapses into a series of  $\delta$ -functions. Each  $\delta$ -function corresponds to a LL of the energy spectrum of Eq. 6.13.

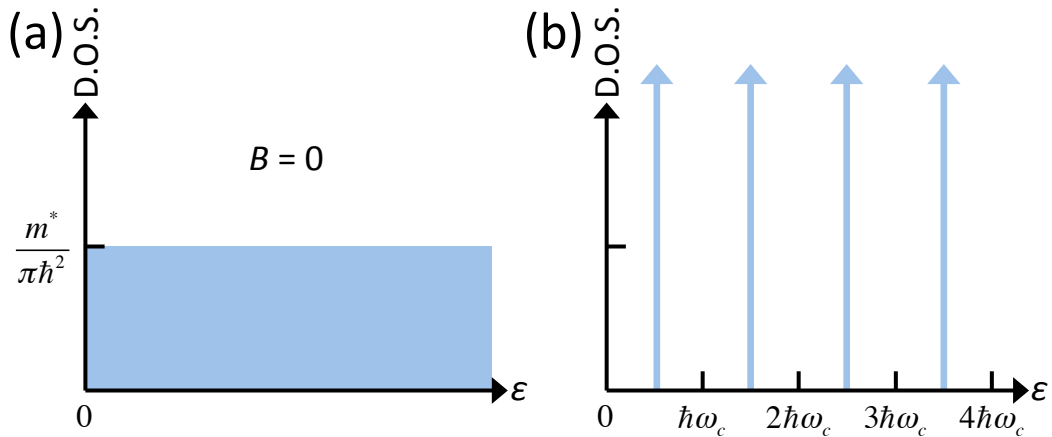


Figure 6.2: (a) Density of states as a function of energy for a 2DES in zero magnetic field (neglecting spin). (b) The application of a magnetic field collapses the density of states into a series of  $\delta$ -functions, each associated with a LL.

An ostensibly strange feature of Eq. 6.14 is that it seems to break rotational symmetry within the  $x$ - $y$ -plane. The wave functions  $u_{Nk}(x, y)$  comprise plane waves in the  $y$ -direction with traditional harmonic oscillator waveforms in the  $x$ -direction, which have  $N$  nodes and exponentially vanish sufficiently far from  $x = -\hbar k/eB$ . More specifically, the cyclotron radius, calculated as

$$r_c = \frac{v}{\omega_c} = \sqrt{\frac{2\varepsilon_{NK}}{m^*\omega_c^2}} = l_B \sqrt{2(N + 1/2)} \quad (6.15)$$

provides a characteristic length scale associated with the spread of  $u_{Nk}(x, y)$  in the  $x$ -direction. So it seems our waves form a series of parallel strips with a preferred direction. Of course, nothing physically distinguishes the  $x$ - or  $y$ -direction and this apparent directionality is merely an artifact of our gauge choice for  $\mathbf{A}$ . Every linear combination of states  $u_{Nk}(x, y)$  with equal  $N$  are degenerate and therefore are also eigenfunctions of the Hamiltonian. By mixing the waves of Eq. 6.14, it is possible to construct basis functions such as

$$u'_{Nk'}(x, y) \propto H_N \left( \frac{y + \hbar k'/eB}{l_B} \right) \exp \left[ -\frac{(y + \hbar k'/eB)^2}{2l_B^2} \right] \exp(ik'x). \quad (6.16)$$

Indeed, one can arrive at anything in between Eqs. 6.14 and 6.16, or even basis functions with rotational symmetry by exploiting the gauge freedom of the problem.

### 6.3 Electron Spin

Up to now we have neglected the electron's spin. The Zeeman interaction introduces an additional term to the Hamiltonian:  $(g\mu_B/\hbar)\mathbf{S} \cdot \mathbf{B}$ , where  $g$  is the g-factor ( $g = -0.44$  in GaAs),  $\mu_B = e\hbar/2m$  is the Bohr magneton, and  $\mathbf{S}$  is the electron's spin angular momentum. While significantly smaller than the cyclotron energy  $\hbar\omega_c$ , the Zeeman splitting  $\Delta\varepsilon_z = |g\mu_B B|$  cannot be ignored in the high-field regime. Just as important, the electron's spin degree of freedom doubles the number of available states, splitting the LLs into polarized *spin branches*.

For simplicity, we will ignore spin-splitting where possible. Unless otherwise stated, the term *Landau level*, or *LL*, in this thesis refers only to the quantization of cyclotron orbits. Where necessary, we will refer to *spin-split LLs*, or *LL spin branches*, to indicate the inclusion of electron spin. At the same time, we will adhere to the convention that *filling factor*  $\nu$  (see next section) is the fraction of filled spin-split LLs.

## 6.4 Filling Factor

In the problem as we constructed it above in Eq. 6.9, the electrons are unbound within the  $x$ - $y$ -plane, and therefore, the derived quantum number  $k$  is continuous such that each LL is infinitely degenerate. This is consistent with the notion of an infinite 2DES. In a model that includes confinement of the 2DES to a  $L_x \times L_y$  sized rectangle within the  $x$ - $y$ -plane,  $k$  would be quantized with values  $k = 2\pi M/L_y$ , where  $M$  is an integer. To determine the constraints on  $M$ , consider that the wave functions of Eq. 6.14 are each centered in the  $x$ -direction at  $x = -\hbar k/eB = -2\pi\hbar M/eBL_y$ . Confining these values of  $x$  to be within the sample—that is,  $x \in [0, L_x]$ —we find  $x = 0 \rightarrow M = 0$  and  $x = L_x \rightarrow M = -eBL_x L_y/2\pi\hbar$ . The degeneracy of each LL is therefore

$$D_{\text{LL}} = \frac{A}{2\pi l_B^2} \quad (6.17)$$

where  $A = L_x \times L_y$  is the 2DES's area and, as before,  $l_B \equiv \sqrt{\hbar/|eB|}$  is the magnetic length. By convention, the electron's spin is not included in  $D_{\text{LL}}$  as spin up and spin down are not degenerate states in a magnetic field. That is,  $D_{\text{LL}}$  is technically the degeneracy of a single LL spin branch.

Crudely speaking, we can think of  $D_{\text{LL}}$  as being the number of classical cyclotron orbits of area  $\pi l_B^2$  that fit into the area of our 2DES, modulo a factor of 2. It is useful here to invoke a quantity known as the *magnetic flux quantum*, defined as  $\phi_0 = h/e$ . The LL degeneracy may then be written as

$$D_{LL} = \frac{\phi}{\phi_0} \quad (6.18)$$

where  $\phi = AB$  is the magnetic flux applied to the 2DES. Thus a LL contains a number of states equal to the number of magnetic flux quanta that pierce the 2DES.

Figure 6.2 (b) illustrated how LLs are evenly spaced in the energy domain by the cyclotron energy  $\hbar\omega_c$ . In a typical transport measurement, the magnetic field  $B$  is slowly increased from zero. As  $B$  increases, so does  $\hbar\omega_c$ . Meanwhile, the electron density  $n = m^*\varepsilon_F/\pi\hbar^2$ , and hence, Fermi energy  $\varepsilon_F$ , remain constant such that the number of filled LLs decreases as  $B$  increases. We define the 2DES's *filling factor* as

$$\nu = 2\frac{\varepsilon_F}{\hbar\omega_c} = 2\frac{\pi\hbar n}{m^*\omega_c} = \frac{hn}{eB} = \frac{\phi_0}{B}n \quad (6.19)$$

where we include a factor of 2 for the electron's spin; that is,  $\nu$  is the number of filled LL spin branches.

As an example, our diving board devices contain 2DESs with  $n = 2.9 \times 10^{11} \text{ cm}^{-2}$ . To place all of these electrons into the lowest LL—i.e., to achieve  $\nu \leq 1$ —we would require a magnetic field  $B \geq n\phi_0/\nu \approx 12 \text{ T}$ . Incidentally, this regime, where  $\nu \leq 1$ , is known as the *extreme quantum limit*.

## 6.5 Disorder Broadening

The density of states only collapses to true  $\delta$ -functions as illustrated in Fig. 6.2 for the ideal case of a perfect, scatter-free 2DES. Real 2DESs, however, have disorder; even those within the ultra-clean samples studied for this thesis. Even if disorder could be eliminated, at finite temperatures phonons of the three-dimensional lattice will scatter electrons. Scattering events, regardless of their origin, result in an uncertainty in the energy of particular electron states. Let us define  $\tau_q$  as the average time between such scattering events, and hence, the average *quantum lifetime* of a single electron state. The result is an effective broadening of the LLs by  $\Gamma \sim \hbar/\tau_q$  as illustrated in Fig. 6.3.

It is important to distinguish between the quantum lifetime  $\tau_q$  and the momentum

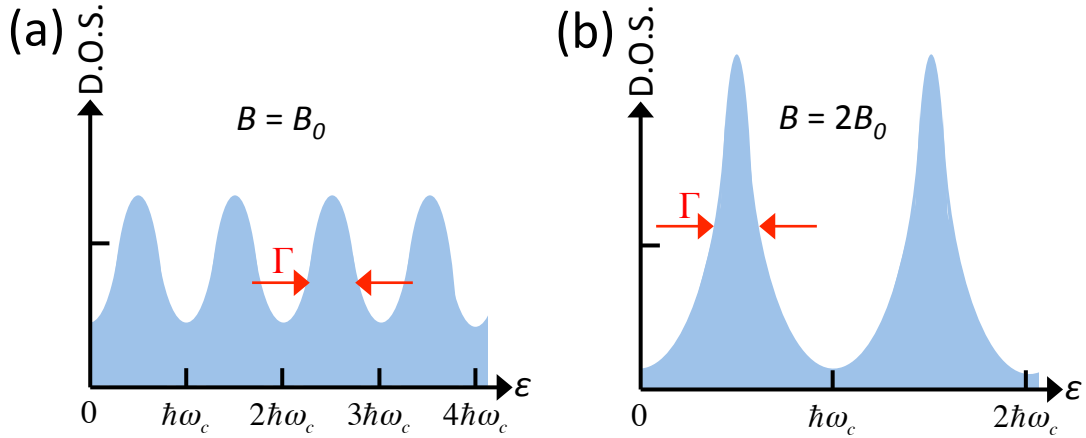


Figure 6.3: Illustration of disorder broadened LLs. (a) LLs are barely resolved at  $B = B_0$  where  $\hbar\omega_c \sim \Gamma$ . (b) LLs are well resolved at  $B = 2B_0$  where  $\hbar\omega_c \gg \Gamma$ .

lifetime  $\tau_m$ , which is related to the electron mobility via the expression  $\mu_e = e\tau_m/m^*$ . The former is the average time between *any* scattering event for a single electron whereas the latter weights scattering events by scattering angle  $\theta$ . Specifically, if  $P(\theta)$  is the probability of a scattering event occurring with angle  $\theta$  per unit time, then

$$\frac{1}{\tau_q} = \int P(\theta)d\Omega, \quad (6.20)$$

$$\frac{1}{\tau_m} = \int P(\theta)(1 - \cos\theta)d\Omega, \quad (6.21)$$

such that small angle scattering events are less impactful in the determination of  $\tau_m$ , and hence  $\mu_e$  [70]. In the case of modulation-doped GaAs/AlGaAs heterostructures at low temperatures the dominant scattering mechanism is the long-range potential associated with the donor ions. This results in predominantly small angle scattering such that  $\tau_q$  is typically  $\sim 10 - 100$  times smaller than  $\tau_m$  depending on the details of the disorder potential. So while the electron mobility  $\mu_e$  is a convenient metric, it is imperfectly correlated with the degree of LL broadening. Later in this chapter we will discuss how one measures  $\tau_q$ .

The notion of disorder broadened LLs helps us understand the transition from

the classical picture of the previous section and the QH regime. At sufficiently small fields,  $\hbar\omega_c \ll \Gamma$ , and therefore, even in the limit of zero temperature, LLs cannot be resolved and the 2DES behaves classically. Only when the field is large enough that  $\hbar\omega_c \sim \Gamma$ , as illustrated in Fig. 6.3 (a), can we begin to resolve LLs and observe the accompanying quantum behavior of the 2DES. Figure 6.3 (b) represents a doubling of the field strength relative to Fig. 6.3 (a) such that  $\hbar\omega_c \gg \Gamma$ .

## 6.6 Compressibility

Like any electronic system, the states in the vicinity of the Fermi energy  $\varepsilon_F$  will determine the transport properties of the 2DES. Let us consider the  $\hbar\omega_c \gg \Gamma$  regime, in the limit of zero temperature. When  $\nu = j + 1/2$ , for positive integer  $j$ ,  $\varepsilon_F$  is positioned at the center of a LL such that the density of states at  $\varepsilon_F$  is maximal and an infinitesimal electric field will produce a current as electrons move through a continuum of available states. In this configuration we describe the 2DES as metallic or *compressible*<sup>2</sup>. Within the system's bulk, away from the edges, only the electron's within the half filled LL can participate in electrical transport. Like electrons of a filled band, those within the  $j$  filled LLs are magnetically localized since all nearby momentum states are occupied.

In contrast to the compressible configuration at *half filling*, when  $\nu = j$ ,  $\varepsilon_F$  is centered between adjacent LLs such that the density of states at  $\varepsilon_F$  vanishes. Now the system behaves as an insulator and we describe the 2DES as *incompressible*. Like a band insulator, electrons cannot propagate without excitation across the gap dividing the full and empty LLs.

For example, our diving board devices with 2DESs of density  $n = 2.9 \times 10^{11} \text{ cm}^{-2}$

---

<sup>2</sup>Technically, the thermodynamic compressibility  $K$  of a system of volume  $V$  is given by

$$K = -\frac{1}{V} \left( \frac{\partial V}{\partial p} \right)_{T,N} = \frac{1}{n^2} \left( \frac{\partial n}{\partial \mu} \right)_{T,V}, \quad (6.22)$$

where  $p$  is pressure and  $N$  the number of particles. A 2DES with  $K > 0$  therefore has a continuum of states in the vicinity of  $\mu$ . A *compressible* 2DES is characterized by metallic behavior, while an *incompressible* ( $K = 0$ ) 2DES is characterized by insulating behavior.

have  $\nu = 3$  at  $B = 4.0$  T. The energy gap between  $\nu = 3$  and  $\nu = 4$  is a Zeeman splitting giving  $\Delta\varepsilon = |g\mu_B B| \approx 1.2$  K. Thus we require  $T \ll 1.2$  K to achieve insulating behavior in the bulk at  $\nu = 3$  in this device. Alternatively,  $\nu = 4$  occurs at  $B = 3.0$  T. The energy gap between  $\nu = 4$  and  $\nu = 6$  is approximately the cyclotron energy giving  $\Delta\varepsilon \approx \hbar\omega_c \approx 60$  K. This is comparable to  $\varepsilon_F \approx 120$  K! So once  $T$  is high enough that the gap between  $\nu = 4$  and  $\nu = 6$  can no longer be resolved, the system is so warm that it has lost its fermionic character.

In the intermediate situation, when  $\nu$  is neither at integral nor half filling, LL broadening plays a crucial role. Indeed, in the absence of any/all disorder the chemical potential would necessarily always be positioned within a LL  $\delta$ -function (e.g. see Fig. 6.2 (b) above). In real two-dimensional systems, disorder creates a potential landscape of hills and valleys that, when combined with a large magnetic field  $B$ , can localize electrons. In the case of short-ranged fluctuations that vary on a length scale comparable to  $l_B$ , the conventional theory<sup>3</sup> is that *Anderson localization* prevents the diffusion of quantum waves when  $\varepsilon_F$  is positioned away from the center of a LL [72]. When the disorder potential varies over longer length scales the 2DES is best described as having a non-uniform density, and therefore, a local value of  $\nu$  that varies spatially. The conventional picture is of an energy spectrum containing a narrow band of extended states near the center of a LL and localized states in the tails as illustrated in Fig. 6.4. When  $\varepsilon_F$  is positioned within the band of extended states, whose width vanishes in the limit of zero temperature, the 2DES's bulk is compressible. As the relative position of  $\varepsilon_F$  moves away from the center of the LL—either through a change of  $\varepsilon_F$  or  $B$ —the system undergoes a metal-insulator transition and the 2DES bulk becomes incompressible. The energy at which the extended states give way to localized states is known as a *mobility edge*.

---

<sup>3</sup>Recent experimental results by Ilani et al. [71] using a scanning single electron transistor to probe individual localized states challenge the notion that single-particle theory can explain the nature of the IQH regime.

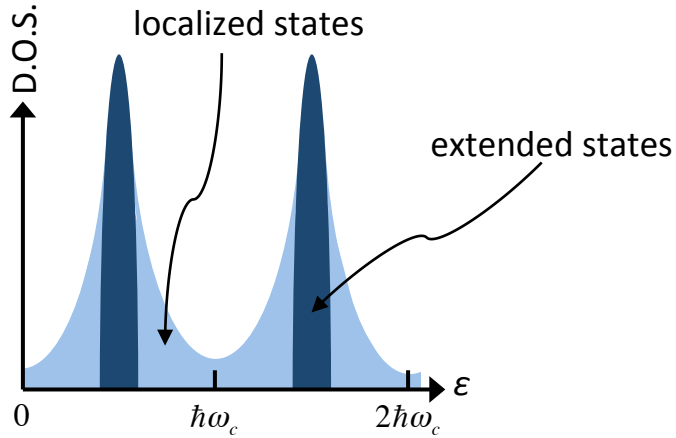


Figure 6.4: Extended and localized states within disorder broadened LLs at finite temperature.

## 6.7 Edge States

At least this is the low-temperature situation in the bulk. Near the system's edges, the bottom of the conduction band begins to rise and ultimately diverges as it must to confine the electrons. Since the LL energies are measured from the bottom of the conduction band, they too bend upward. As a consequence, when  $\nu \geq 1$ ,  $\varepsilon_F$  will intercept the filled LL energies near the edge. The result is a one-dimensional *edge state* running along the perimeter of the system for each intersection between  $\varepsilon_F$  and a LL [73].

To develop our intuition for edge states, let us briefly return to the classical picture. Consider a weakly disordered system with  $\tau_m \gg 1/\omega_c$  of sufficient size  $L^2$  that  $\langle r_c \rangle = |m^* \langle v \rangle / eB| \ll L$ . The majority of electrons will be magnetically localized, engaged in cyclotron orbits within the 2DES bulk with zero drift velocity. Near the system's edges, however, electrons will necessarily scatter, or bounce, off the confinement potential. The result is that some electrons will propagate across the system via *skipping orbits* along the edge. Figure 6.5 illustrates one possible skipping orbit. Note that in our classical model the electrons will occupy a distribution of velocities, and therefore, a range of cyclotron radii. Any electron within  $r_c$  of the

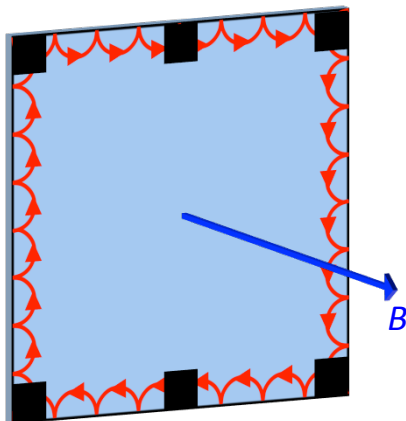


Figure 6.5: Classical skipping orbit.

edge (with  $r_c \ll L$ ) will traverse a skipping orbit; the closer to the edge, the faster the skipping.

A key feature of the skipping orbits is their *chirality*. With the magnetic field pointing out of the page (into the page), electrons propagate around the system in clockwise (counterclockwise) fashion. But alas, such a classical model is not realistic for this high-field quantum regime.

So what happens quantum mechanically? Figure 6.6 (a) illustrates the bending and ultimate divergence of LL energies for  $\nu = 2$ . Near the edges at  $y = 0$  and  $y = L_y$ ,  $\varepsilon_F$  intersects the spin-split LLs resulting in four compressible points in the plot. These compressible points correspond to one-dimensional edge states that run along the boundary of the system as shown in Fig. 6.6 (b). Like classical skipping orbits, edge states are chiral. But unlike our classical picture, the one-dimensional nature of edge states precludes back-scattering such that they are dissipationless.

Electrons propagate ballistically through these scatter-free edge channels. As a consequence, it can be shown [74] that an edge state possesses one *conductance quantum*<sup>4</sup>  $G_0 = e^2/h$ . In the low disorder, high-field, low-temperature regime, the net two-point conductance between two ideal contacts on a common edge of a 2DES

---

<sup>4</sup>Note that the conductance quantum  $G_0$  is often defined as  $G_0 = 2e^2/h$  in contexts where electron spin states are degenerate.

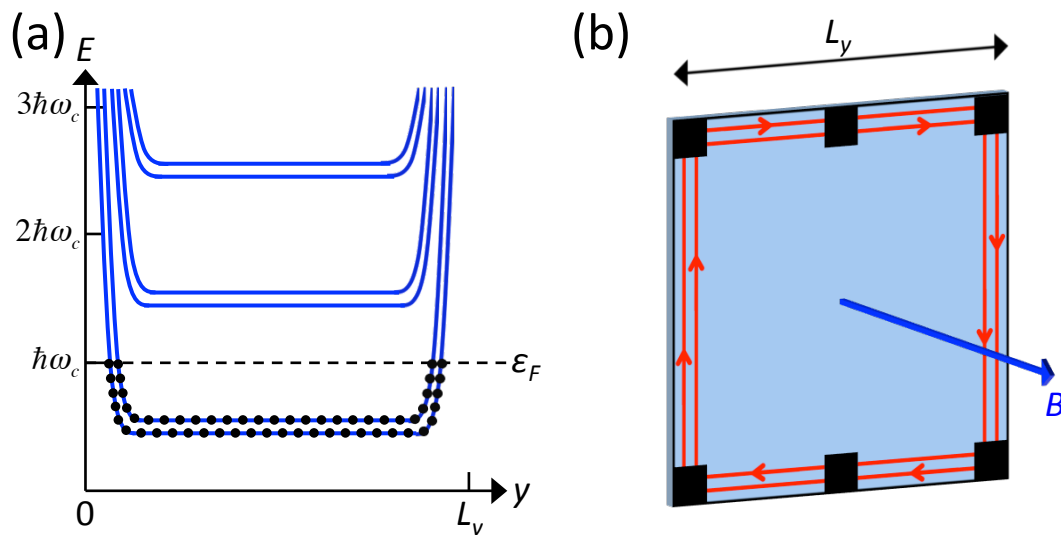


Figure 6.6: (a) Illustration of LL energy vs position. Energies diverge close to the 2DES's edges.  $\varepsilon_F$  is positioned such that  $\nu = 2$ ; that is, both spin branches of the lowest LL are completely filled. (b) Illustration of QH edge states at  $\nu = 2$ .

with integral filling factor  $\nu$  is therefore  $G = \nu e^2/h$ .

## 6.8 Quantum Magnetotransport

Now that we have outlined the physics of the 2DES in the high-field, quantum regime, let us turn to the topic of observables in the form of electrical transport. We consider the same measurement setup as in Section 6.1 shown again in Fig. 6.7 for the special case of  $\nu = 2$ . The contacts are labeled 1 through 6 in the figure. We source current  $I$  to contact 4 and drain it from contact 1, while the other contacts draw zero net current. We then measure the longitudinal voltage  $V_{xx} = V_5 - V_6$  and the transverse voltage  $V_{xy} = V_5 - V_3$ . One way to understand the voltages measured follows from our model of dissipationless edge states.

A net current passing from contact 4 to 1 translates into a net number of electrons per unit time passing from contact 1 to 4. Given the clockwise chirality of the edge channels, the current carried on the right edge (darker in Fig. 6.7) must therefore be

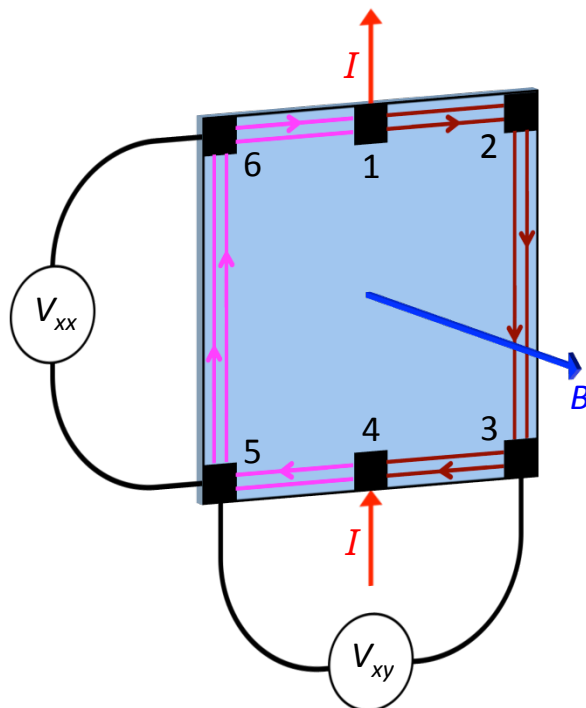


Figure 6.7: Magnetotransport measurement setup for the special case of  $\nu = 2$ . Current  $I$  is sourced to contact 4 and carried by the edge states on the right edge to contact 1 where  $I$  is drained.

larger than that on the left edge (lighter in Fig. 6.7).

Now suppose we electrically ground contact 4; that is, let  $V_4 = 0$ . To generate the current  $I$  contact 1 must therefore lower its voltage to  $V_1 = -I/(2e^2/h)$ . In the low-temperature limit, electrons injected into the edge states by contact 1 will not scatter and will enter contact 2 with a chemical potential of  $eV_1$ . Contact 2 draws no net current and so must lower its voltage to  $V_2 = V_1$  in order to emit current  $I$  onto the edge. The same situation holds for contact 3 such that  $V_3 = V_2 = V_1$ . In this way, all the contacts along the right edge arrive at the same potential  $-I/(2e^2/h)$ . By similar rational we find  $V_6 = V_5 = V_4 = 0$  such that all the contacts along the left edge arrive at electrical ground. Thus we see, for the special case of  $\nu = 2$ , that  $V_{xx} = V_5 - V_6 = 0$  and  $V_{xy} = V_5 - V_3 = I/(2e^2/h)$ .

By generalizing the above argument we conclude that for any integral filling factor

$\nu = N$ , in the low-temperature limit,  $V_{xx} = 0$  and  $V_{xy} = I/(\nu e^2/h)$ . In terms of resistances we have

$$R_{xx} = \frac{V_{xx}}{I} = 0, \quad (6.23)$$

$$R_{xy} = \frac{V_{xy}}{I} = \frac{h}{\nu e^2}, \quad (6.24)$$

where  $\nu = N$ , with  $N$  the number of filled LLs.

The above arguments explain what to expect at integral filling. So what is measured for arbitrary values of  $\nu$ ? In Fig. 6.8 we plot both  $R_{xy} = V_{xy}/I$  (left axis) and  $R_{xx} = V_{xx}/I$  (right axis) as a function of  $B$  measured at  $T \approx 300$  mK. The measured sample was cleaved from the same parent wafer as the hot-electron thermocouple device discussed in Chapter 5, which has a 2DES with  $n = 1.5 \times 10^{11}$  cm $^{-2}$  and  $\mu = 3.3 \times 10^6$  cm $^2$ /Vs. Below  $B \sim 0.1$  T,  $R_{xy}$  increases linearly with  $B$  and  $R_{xx}$  is nearly independent of  $B$ , showing only a slight decline in magnitude. This is essentially in accordance with our classical model of magnetotransport. Above  $B \sim 0.1$  T the behavior of both  $R_{xy}$  and  $R_{xx}$  dramatically changes due to the resolution of LLs.

In the quantum regime  $R_{xy}$  is characterized by a series of plateaus that form a stair-like pattern. This is the *integer quantum Hall effect* (IQHE). At the same time,  $R_{xx}$  undergoes a series of oscillations of generally increasing amplitude (though, not monotonically so) with minima that correlate with the plateaus of  $R_{xy}$ . This is known as the *Shubnikov-de Haas effect* (ShdH). From the preceding discussion about LLs and edge states we can understand the basic features of this transport data.

Recall the relationship between  $\nu$  and  $B$  for fixed electron density  $n$  (Eq. 6.19):  $\nu = 2\varepsilon_F/\hbar\omega_c = \phi_0 n/B$ , where  $\phi_0 = h/e$  is the magnetic flux quantum. As we increase  $B$  both the cyclotron energy  $\hbar\omega_c$  and Zeeman energy  $|g\mu_B B|$  separating adjacent LLs increase linearly such that they parade past  $\varepsilon_F$ . At each value of  $B$  that positions  $\varepsilon_F$  halfway between adjacent LLs,  $\nu$  acquires an integral value and  $R_{xx}$  tends to zero while  $R_{xy}$  tends to  $h/\nu e^2$  in accordance with Eqs. 6.23 and 6.24.

From Eq. 6.24 we can readily identify the integral filling factors  $\nu$  associated with

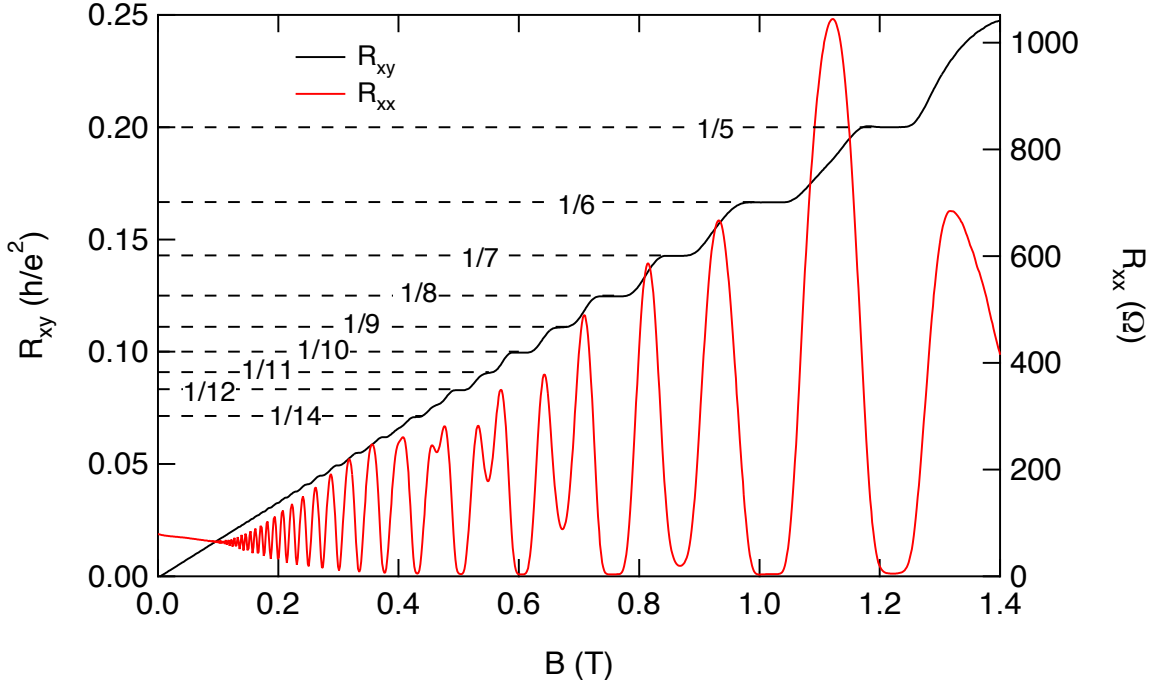


Figure 6.8: The integer quantum Hall effect. The measured transverse resistance  $R_{xy}$  (left axis) together with the longitudinal resistance  $R_{xx}$  are plotted as a function of magnetic field  $B$ . Data were acquired at  $T = 300$  mK from a sample cleaved from the same parent wafer as the hot-electron thermocouple discussed in Chapter 5.

the labeled plateaus of  $R_{xy}$  in Fig. 6.8 (e.g.  $R_{xy} = 1/5 h/e^2$  corresponds to  $\nu = 5$ ). To understand the origin of these plateaus we must return to the notion of disorder broadened LLs. In Fig. 6.4 we illustrated LLs consisting of a temperature dependent band of extended states in their centers and localized states in their flanks. The conventional theory<sup>5</sup> is that electrons within the localized states do not participate appreciably in QH transport. As a consequence,  $R_{xy}$  is constant for  $\varepsilon_F$  positioned between LLs within a range of energies corresponding to the localized states. By the same rationale  $R_{xx} \rightarrow 0$  over the same range.

The preceding idea is perhaps counterintuitive. We are claiming that the plateaus in  $R_{xy}$ , the hallmark of the IQHE, crucially depend on the presence of disorder. The corollary to this argument is that in a disorder-free 2DES  $R_{xy}$  would be linearly pro-

<sup>5</sup>Polyakov et al. [75] have argued that extended states only exist at a single energy in the center of a LL and that transport via localized states in the form of thermally activated hopping is responsible for the broadening of the longitudinal conductivity  $\sigma_{xx}$  peaks in the QH regime.

portional to  $B$ ; there would be no plateaus! Indeed, Störmer et al. [2] demonstrated in high-mobility Si MOSFETs that the plateau width increases with decreasing mobility  $\mu$ . So while too much disorder can preclude the resolution of LLs, the presence of disorder is nonetheless a critical ingredient for realizing the quantization of the Hall resistance  $R_{xy}$ .

Another key feature of Fig. 6.8 relates to spin-splitting. At  $B \sim 0.45$  T the frequency of the ShdH oscillations in  $1/B$  begins to double. This can be explained as the value of  $B$  at which the Zeeman splitting  $|g\mu_B B|$  becomes comparable to the thermal broadening  $k_B T$  such that at higher values of  $B$  LLs are spin resolved. This is quite reasonable given that at  $B = 0.45$  T the Zeeman splitting  $|g\mu_B B| \approx 130$  mK, which is indeed similar to the ambient temperature  $T \approx 300$  mK. The  $R_{xy}$  plateau values corroborate this picture. While we see the beginnings of a  $R_{xy} = 1/13$  plateau (not labeled in the figure) corresponding to  $\nu = 13$ —the lower spin branch of the  $N = 7$  LL—all resolved plateaus at lower values of  $B$  correspond to even values of  $\nu$ .

The temperature dependence of the IQHE is not captured by Fig. 6.8 but deserves comment. The formation of plateaus in  $R_{xy}$  and minima in  $R_{xx}$  is due to the resolution of LLs. At temperatures comparable to the cyclotron and/or Zeeman energy, a degenerate 2DES will have minima in  $R_{xx}$  at integral values of  $\nu$  that exhibit Arrhenius behavior consistent with thermal activation. That is,  $R_{xx,\min} \propto \exp \Delta/2k_B T$ , where  $\Delta = \Delta_0 - \Gamma$  with  $\Delta_0$  either the cyclotron or Zeeman energy for even or odd values of  $\nu$ , respectively, and with  $\Gamma$  the LL disorder broadening as before. At lower temperatures where simple activation is unlikely conduction occurs via variable range hopping—quantum tunneling between localized states with energies within about  $k_B T$  of  $\varepsilon_F$ . This results in  $R_{xx,\min} \propto \exp (T_0/T)^\gamma$ , where  $T_0$  is a constant and  $\gamma = 1/3$  or  $1/2$  depending on the details of the hopping mechanism [76, 77]. In any case, we have that the minima in  $R_{xx}$  rapidly deepen as the temperature is lowered. The formation of plateaus in  $R_{xy}$  obeys a similar temperature dependence to that of  $R_{xx}$  since these are indeed two perspectives of the same phenomenon.

Klaus von Klitzing [1] discovered this quantization of the transverse, or Hall, resistance  $R_{xy}$  in 1980 for which he was awarded the Nobel prize in 1985. We now

recognize the IQHE as the first observation of a topologically insulating system; a paradigm that has attracted a tremendous amount of interest in recent years [78]. Beyond being of fundamental interest to physicists, this phenomenon also has important applications to metrology in the form of the resistance standard known as the *von Klitzing constant*  $R_{K-90} = h/e^2 = 25812.807 \Omega$  [79].

## 6.9 Quantum Lifetime

Throughout this thesis we have repeatedly extolled the virtues of high-mobility 2DESs. By reducing the disorder in these systems we are better able to resolve their most delicate and interesting phases. It has been pointed out [80], however, that the electron mobility  $\mu_e$ , which is tantamount to the momentum lifetime since  $\mu_e = e\tau_m/m^*$ , is a suboptimal proxy for the *quality* of a 2DES. For example, a 2DES with a lower mobility may nonetheless exhibit a fragile *fractional* quantum Hall plateau that is absent in a 2DES with a higher mobility. It has been argued [80] that a measurement of  $\Gamma$ , and hence  $\tau_q$ , provides a better proxy for this *quality*.

In addition to the general value of measuring sample quality, we have a specific interest in knowing  $\Gamma$  within the context of thermopower in the QH regime. In Chapter 7 we review a generalized Mott formula for diffusion thermopower that is valid for noninteracting 2D electrons in a strong magnetic field when  $k_B T \ll \Gamma$ . A measurement of  $\Gamma$ , and hence  $\tau_q$ , therefore reveals the temperature range that this analytical expression for thermopower is potentially valid.

The value of  $\tau_q$  can be related to the peaks in  $R_{xx}$  versus  $B$  measured at low fields where the cyclotron gap governs the oscillations. Using a model that assumes the LL broadening can be represented by a Lorentzian with width  $\Gamma$  independent of energy and magnetic field such that  $\Gamma = \hbar/2\tau_q$ , Coleridge et al. derived [70] the expression

$$\Delta R_{xx}(B) = 4R_0 K(B, T) \exp\left(-\frac{\pi}{\omega_c \tau_q}\right), \quad (6.25)$$

where  $\Delta R_{xx}$  is the oscillating portion of  $R_{xx}(B)$ ,  $R_0$  is the value of  $R_{xx}$  at  $B = 0$ ,

$\omega_c = eB/m^*$  is the cyclotron frequency, and  $K(B, T)$  is a damping factor given by

$$K(B, T) = \frac{2\pi^2 k_B T / \hbar \omega_c}{\sinh(2\pi^2 k_B T / \hbar \omega_c)}. \quad (6.26)$$

A Dingle plot displays  $\ln Z$  for the maxima versus the inverse magnetic field, where

$$Z = \left( \frac{\Delta R_{xx}}{R_0} \right) \frac{1}{4K(B, T)} = \exp\left(-\frac{\pi}{\omega_c \tau_q}\right). \quad (6.27)$$

According to the model, the slope of the resulting data is therefore equal to  $-\pi m^*/e\tau_q$ .

Figure 6.9 shows the determination of  $\tau_q$  for the 2DES within diving board B. In Fig. 6.9 (a) we see  $R_{xx}$  as a function of  $B$  measured at  $T = 123$  mK for  $B \in (0.2, 0.5)$  T. As a consequence of spin-splitting, the data exhibits two sets of maxima corresponding to odd and even filling factors, respectively. Maxima occurring immediately before even filling factors are marked with blue squares<sup>6</sup>. Figure 6.9 (b) displays  $\ln Z$  versus  $1/B$  for the marked maxima. The dashed line is a least squares fit to the data. The slope of the dashed line is related to the quantum lifetime as per Eq. 6.27, and reveals that  $\tau_q = 2.99$  ps. Given the mobility of this 2DES is  $\mu_e = 3.1 \times 10^7$  cm<sup>2</sup>/Vs, its momentum lifetime is  $\tau_m = 1.2$  ns. Thus we see that  $\tau_m/\tau_q \approx 400$ !

## 6.10 Summary

This chapter introduced the rich world of quantum Hall physics. We have seen that while the classical picture provides a degree of intuition, it ultimately fails to explain key features of the magnetotransport of the 2DES. Rather, we require a quantum mechanical description of noninteracting electrons in a magnetic field, which yields the key notions of Landau levels and filling factors. By considering how disorder broadens Landau levels, we extended our model by dividing electron states into localized versus extended. This, in turn, led to a qualitative understanding of the

---

<sup>6</sup>Note that choosing the set of maxima occurring immediately before odd filling factors yields the same value for  $\tau_q$ .

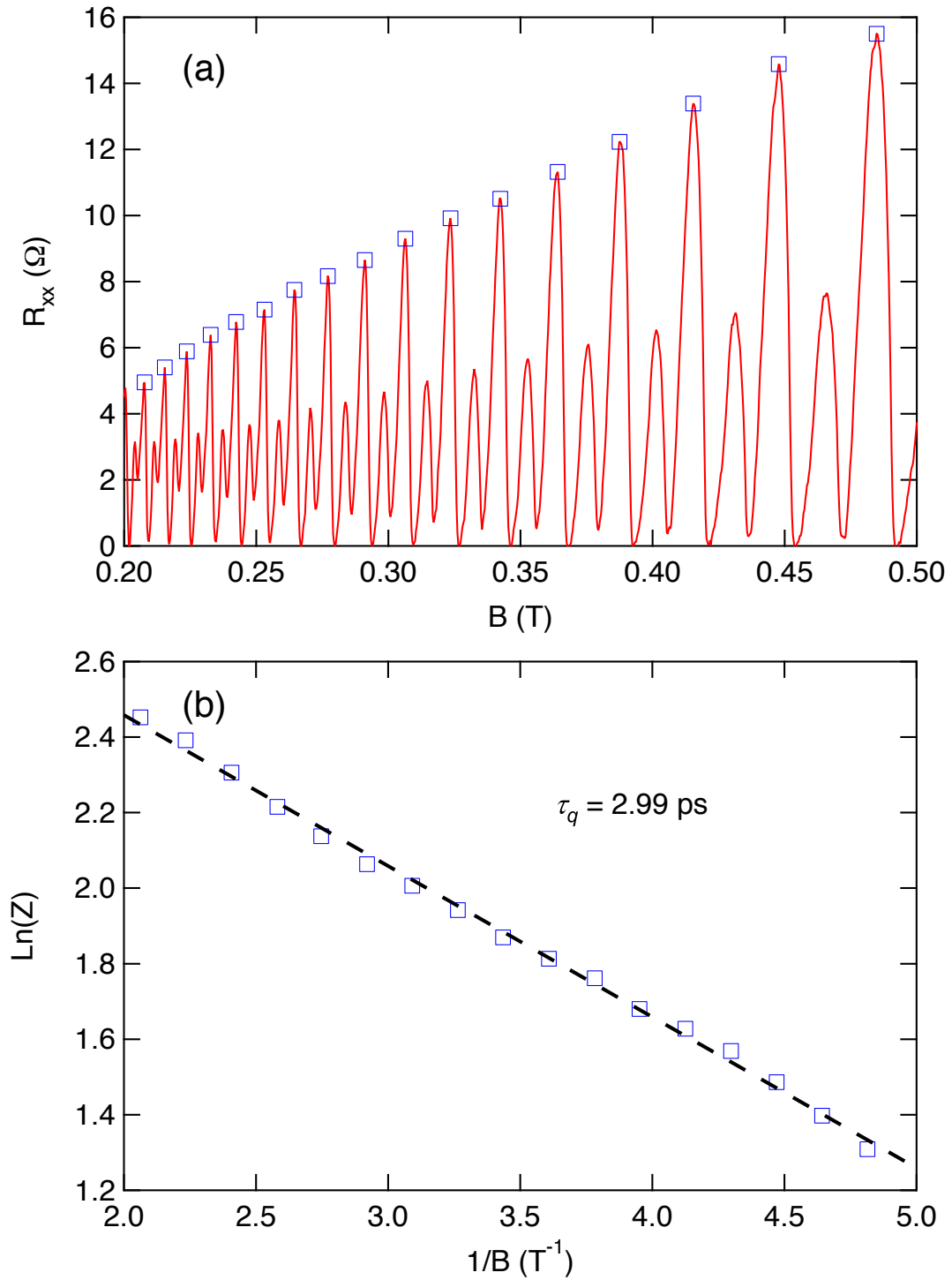


Figure 6.9: Determination of quantum lifetime  $\tau_q$  via Dingle plot. (a) The longitudinal resistance  $R_{xx}$  vs magnetic field  $B$  measured in diving board B at  $T = 123$  mK. The blue squares mark maxima associated with even filling factors. (b) Dingle plot showing the natural log of  $Z$  vs inverse magnetic field. The slope of the fitted line reveals the quantum lifetime as  $\tau_q = 2.99$  ps according to the relation  $Z = \exp\left(-\frac{\pi}{\omega_c \tau_q}\right)$ .

relationship between the magnetic field strength and system compressibility. Finally, our model anticipates the existence of one-dimensional states along the system's periphery, which are aptly referred to as *edge states*. These edge states, together with the notion of bulk compressibility, provide a picture from which the hallmarks of this regime—namely the integer quantum Hall effect—intuitively follow.

It is important to stress that all of the physics discussed in this chapter was based on single-particle theory. At the same time, the QH regime very much sets the stage for many-body correlated electronic phases. In Chapter 8 we delve into the role of electron-electron interactions and the resulting *fractional* QH phenomena. But first, in the following chapter we review the theory of thermoelectric transport within the noninteracting QH regime.

## Chapter 7

# Thermopower in the Quantum Hall Regime

We have seen how the discovery of the IQHE revolutionized our understanding of the electrical transport of 2D electrons when subjected to a strong magnetic field. It should be no surprise that a strong magnetic field dramatically alters the thermoelectric transport of the 2DES as well. This chapter provides a high-level explanation of the thermoelectric response of the 2DES within the QH regime. But first, we will discuss how a magnetic field alters the thermopower of a classical 2DES. We show how scattering behavior yields a magnetic field dependence that includes the transverse *Nernst-Ettingshausen effect*. We explain how a magnetic field produces circulating currents within the 2DES during a thermopower measurement. We then turn to the consequences of LL formation.

The collapsing of the density of states into disorder-broadened LLs yields alternating regions of compressible and incompressible QH liquids. Compared to the classical case, this quantization produces enhanced and diminished diffusion thermopower corresponding to the compressible and incompressible liquids, respectively. The result is an oscillating longitudinal and transverse diffusion thermopower as a function of magnetic field or chemical potential (at fixed magnetic field).

An important topic in this chapter is the relationship between thermopower and entropy. In Section 7.4 we derive the diffusion thermopower as a function of chemical potential for a disorder-free 2DES in a quantizing magnetic field by accepting the

premise that  $S^d$  is the entropy per electron per electron charge and calculating the entropy via a counting argument. We find that  $S^d$  derived in this way is equivalent to the derivation of Girvin and Jonson [81], which is based solely on transport physics. Using our derivation, we then investigate how the thermopower of a disorder-free noninteracting 2DES is expected to depend on  $B$  in the QH regime.

At low temperatures, we can relate this field-dependent thermopower tensor to the more familiar electrical transport coefficients via a generalization of Mott's formula. Recently, this generalized Mott formula was used in combination with a model of electrical transport to derive an analytical expression for diffusion thermopower as a function of magnetic field [82]. We review how the calculations of this model depend on parameters such as the momentum and quantum lifetime. The chapter concludes by reviewing the results of our thermoelectric measurements at several temperatures for  $|B| \leq 0.5$  T where a model of noninteracting 2D electrons reasonably describes our system. We show that our experimental results are consistent with calculations made using the recently derived analytical expression for diffusion thermopower.

## 7.1 Classical 2DES in a Magnetic Field

In Chapter 3, we derived Mott's famous result for the diffusion thermopower of noninteracting electrons in the limit of zero temperature:

$$S^d(\varepsilon_F, T) \simeq -\frac{\pi^2 k_B^2}{3e} \frac{1}{\sigma} \left. \frac{d\sigma}{d\varepsilon} \right|_{\varepsilon=\varepsilon_F} T. \quad (7.1)$$

This formula applies in the case of zero magnetic field. In the presence of a magnetic field, the transport coefficients of the 2DES become tensors. It so happens that in the limit of zero temperature, the thermopower of a classical 2DES within a magnetic field is given by [83]

$$S_{ij}^d(\varepsilon_F, T, B) \simeq -\frac{\pi^2 k_B^2}{3e} \rho_{ik} \left[ \frac{d\sigma}{d\varepsilon} \right]_{kj} \Big|_{\varepsilon=\varepsilon_F} T, \quad (7.2)$$

where subscripts refer to elements of transport tensors. Given Mott's formula, Eq. 7.2 seems like a natural generalization for the thermopower of a 2DES.

In the case of a classical 2DES we saw in Chapter 6 that the resistivity becomes

$$\boldsymbol{\rho} = \rho(0) \begin{pmatrix} 1 & \omega_c \tau_m \\ -\omega_c \tau_m & 1 \end{pmatrix}, \quad (7.3)$$

where  $\omega_c = |eB/m^*|$  is the cyclotron frequency,  $\tau_m$  is the momentum lifetime, and  $\rho(0) = 1/\sigma(0) = m^*/ne^2\tau_m$  is the zero-field scalar resistivity. To obtain the conductivity tensor, we simply invert  $\boldsymbol{\rho}$  to obtain

$$\boldsymbol{\sigma} = \frac{\sigma(0)}{1 + \omega_c^2 \tau_m^2} \begin{pmatrix} 1 & \omega_c \tau_m \\ -\omega_c \tau_m & 1 \end{pmatrix}. \quad (7.4)$$

Calculating the energy derivative of  $\boldsymbol{\rho}$  is easier than that of  $\boldsymbol{\sigma}$ . Let us therefore exploit the fact that

$$\boldsymbol{\rho} \frac{d\boldsymbol{\sigma}}{d\varepsilon} = -\frac{d\boldsymbol{\rho}}{d\varepsilon} \boldsymbol{\sigma} \quad (7.5)$$

to rewrite Eq. 7.2 as

$$S_{ij}^d(\varepsilon_F, T, B) \simeq \frac{\pi^2 k_B^2}{3e} \left[ \frac{d\rho}{d\varepsilon} \right]_{ik} \sigma_{kj} \Big|_{\varepsilon=\varepsilon_F} T. \quad (7.6)$$

Differentiating  $\boldsymbol{\rho}$  with respect to  $\varepsilon$  yields

$$\frac{d\boldsymbol{\rho}}{d\varepsilon} = -\frac{\rho(0)}{n} \frac{m^*}{\pi \hbar^2} \begin{pmatrix} 1 + p & \omega_c \tau_m \\ -\omega_c \tau_m & 1 + p \end{pmatrix}. \quad (7.7)$$

In deriving Eq. 7.7 we used the two-dimensional free electron density of states  $dn/d\varepsilon = m^*/\pi\hbar^2$  along with the empirical rule that  $d\tau_m/d\varepsilon = p \cdot \tau_m/n \cdot dn/d\varepsilon$ , where  $p$  is the impurity scattering parameter. Plugging in elements from Eqs. 7.4 and 7.7 into Eq. 7.6, we find

$$S_{xx}^d = -\frac{\pi k_B^2 m^* T}{3\hbar^2 e n} \left( 1 + \frac{p}{1 + \omega_c^2 \tau_m^2} \right) \quad (7.8)$$

and

$$S_{xy}^d = -\frac{\pi k_B^2 m^* T}{3\hbar^2 e} \frac{p\omega_c\tau_m}{n(1 + \omega_c^2\tau_m^2)}. \quad (7.9)$$

Equation 7.9 reveals that a magnetic field gives rise to a nonvanishing transverse thermopower (assuming  $p \neq 0$ ). This is known as the *Nernst-Ettingshausen effect*. Meanwhile, we see that we recover Mott's formula for the zero-field thermopower from Eqs. 7.8 and 7.9 in the limit that  $\omega_c\tau_m \rightarrow 0$ . An interesting feature of these expressions is that the magnetic field dependence is proportional to  $p$ . It follows that in the special case of  $p = 0$ ,  $\mathbf{S}^d$  remains diagonal in a magnetic field with  $S_{xx}^d = -\mathcal{S}/ne$ , the entropy per electron per electron charge. Equally interesting, these expressions imply that in the clean, high-field limit where  $\omega_c\tau_m \rightarrow \infty$ ,  $\mathbf{S}^d$  once again becomes diagonal with  $S^d \rightarrow -\mathcal{S}/ne$ ; a result originally emphasized by Obraztsov [7]. It has been suggested [36] that the fact that scattering effects disappear in the high-field limit may indicate the relationship between diffusion thermopower and entropy is rather general in this regime.

Figure 7.1 shows the diffusion thermopower, as per Eqs. 7.8 and 7.9, as a function of  $B$  at  $T = 200$  mK. The calculations use parameter values that correspond to the 2DES within our diving board devices. The dashed blue line in the figure corresponds to  $-\mathcal{S}/ne$ . These calculations show that the energy-dependent effects of scattering (i.e. finite  $p$ ) quickly subside as the magnitude of  $B$  increases. Specifically, for  $|B| \gtrsim 2$  mT,  $S_{xx}^d \approx -\mathcal{S}/ne$ , independent of  $B$ . And by  $|B| \sim 5$  mT,  $S_{xy}^d$  has nearly vanished. These results suggest that for the ultra-high-mobility 2DES in our experiments, even small magnetic fields of several milliteslas are sufficient to enter a regime where  $S_{xx}^d = -\mathcal{S}/ne$ .

Figure 7.1 also demonstrates the expected symmetries of  $S_{xx}^d$  and  $S_{xy}^d$  with respect to  $B$ . In the low temperature regime, these symmetries can be inferred from the generalized Mott formula given the well-known symmetries of the electrical transport coefficients. Equation 7.2 says that  $S_{xx}^d \propto \rho_{xx} \cdot d\sigma_{xx}/d\varepsilon - \rho_{xy} \cdot d\sigma_{xy}/d\varepsilon$ . Given that  $\rho_{xx}$  and  $\sigma_{xx}$  are even in  $B$  and that  $\rho_{xy}$  and  $\sigma_{xy}$  are odd in  $B$ , it follows that  $S_{xx}^d$  (as

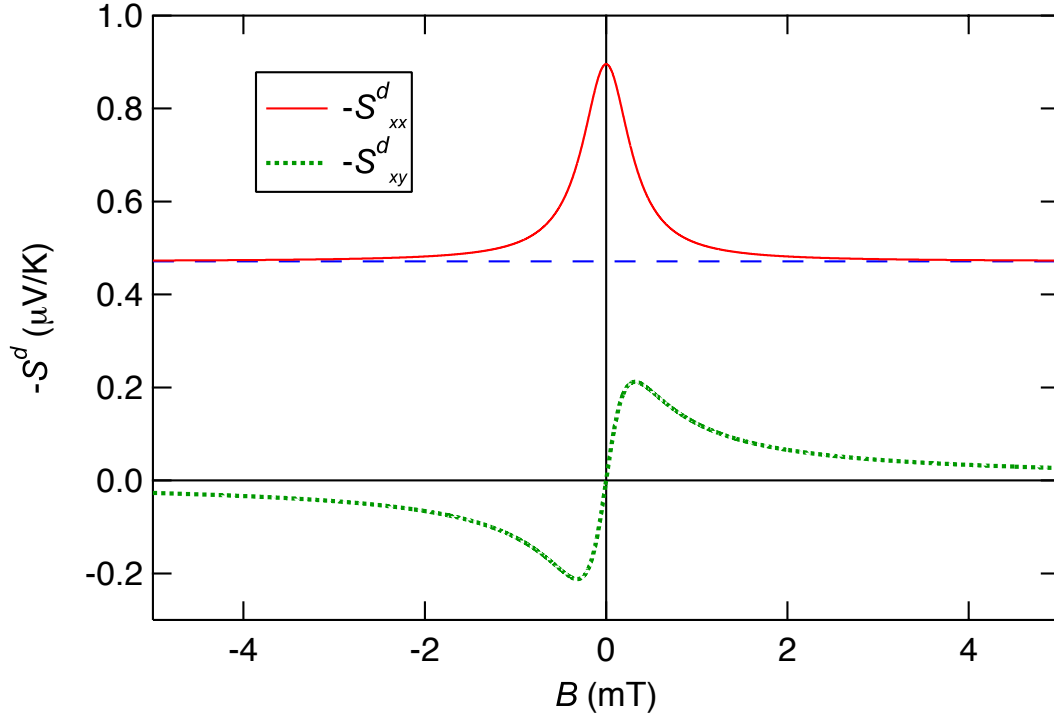


Figure 7.1: Diffusion thermopower of a classical 2DES as a function of magnetic field. Plot shows Eqs. 7.8 and 7.9 for  $T = 200$  mK with the following parameter values:  $m^* = 0.067m_0$ ,  $n = 2.9 \times 10^{11} \text{ cm}^{-2}$ ,  $p = 0.9$ ,  $\tau_m = 1.2$  ns. The dashed blue line corresponds to  $-\mathcal{S}/ne$ .

given by Eq. 7.2) is even in  $B$ . A similar analysis reveals that  $S^d_{xy}$  is odd in  $B$ . More fundamental Onsager symmetry relations can be used to show that these  $S^d_{ij}$  vs  $B$  symmetries hold at all temperatures [8].

## 7.2 Thermoelectric Currents

Let us return to the picture of mutually canceling diffusion and drift currents with which we introduced the thermoelectric effect in Chapter 3. In that chapter, we envisioned the thermoelectric field as that required to produce a drift current equal in magnitude but opposite in direction to the diffusion current that results from an applied temperature gradient. For a classical 2DES at zero magnetic field, these currents may be thought of as uniformly distributed and parallel to the electric field

and temperature gradient such that they locally cancel each other everywhere. This is no longer the case in the presence of an external magnetic field.

In Chapter 6 we described how, when subjected to a sufficiently strong magnetic field, most electrons of a classical 2DES confined to, for example, a  $L \times L$  region become localized within the interior while a fraction form skipping orbits along the region's edge (see Fig. 6.5). Suppose this 2DES is subjected to a uniform temperature gradient such that two of the edges fall along the equithermal lines at  $T = T_c$  and  $T = T_h$ , where  $T_c < T_h$ . The population of electrons within skipping orbits along the  $T = T_h$  edge will be larger than that along the  $T = T_c$  edge. This will yield a diffusion current flowing in a direction transverse to that of the temperature gradient. At sufficiently low temperatures where Eq. 7.2 is a good approximation, and at sufficiently high magnetic field that  $\sigma_{xy} \gg \sigma_{xx}$ , the magnitude of the average diffusion current density will be given by  $j_{\text{diff}} \simeq \epsilon_{xy} \cdot \nabla T$ , where

$$\epsilon_{xy} \simeq \left. \frac{\pi^2 k_B^2}{3e} \frac{d\sigma_{xy}}{d\varepsilon} \right|_{\varepsilon=\varepsilon_F} \bar{T} \quad (7.10)$$

with  $\bar{T} = (T_c + T_h)/2$  the average temperature. At the same time, if no net current is allowed to flow, a drift current must be established to cancel this diffusion current. Classically, the conductivity of the 2DES is uniform. It follows that the transversely directed drift current will be uniformly distributed throughout the 2DES with a density given by  $j_{\text{drift}} \simeq \sigma_{xy} \cdot E$ , where  $E = S_{xx} \cdot \nabla T$  is the thermoelectric field, which is antiparallel to  $\nabla T$ .

The circulating currents that flow within a classical 2DES in response to a strong out-of-plane magnetic field and a uniform in-plane temperature gradient  $\nabla T$  are illustrated in Fig. 7.2. When no *net* current is allowed to flow, the 2DES establishes a uniform electric field  $E$  that is antiparallel to  $\nabla T$ . Diffusion currents in response to  $\nabla T$  flow along the system's edge while drift currents in response to  $E$  flow uniformly through the system's interior. These circulating thermoelectric currents are in addition to any magnetization currents flowing along the edge (e.g. the electrons that would be in classical skipping orbits in the absence of the temperature gradi-

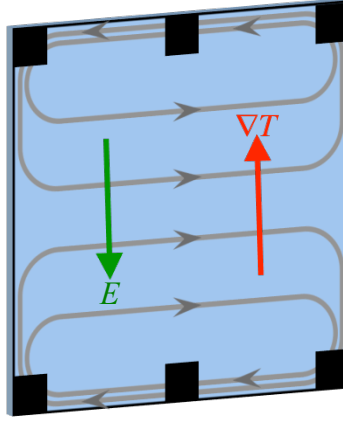


Figure 7.2: Illustration of the thermoelectric current distributions within a classical 2DES subjected to a strong magnetic field. A uniform temperature gradient  $\nabla T$  is applied and no *net* current is allowed to flow. The 2DES responds by establishing a uniform electric field  $E$  that is antiparallel to  $\nabla T$ . Diffusion currents in response to  $\nabla T$  flow along the system's edge. Drift currents in response to  $E$  flow uniformly through the system's interior.

ent). Note that while the net current is zero, the average current densities can be relatively large, reaching a magnitude corresponding to what would occur if only the temperature gradient or electric field were present.

### 7.3 Thermopower with LL Quantization

The quantization of LLs dramatically alters the thermoelectric response of the 2DES. In Chapter 6 we saw how, at sufficiently high magnetic fields and low temperatures, disorder broadened LLs resulted in a quantization of the transverse resistance  $R_{xy}$ , known as the integer quantum Hall effect (IQHE). In this regime,  $\sigma$  is approximately off-diagonal with  $\sigma_{xy} \approx R_{xy}^{-1} \approx e^2/h \cdot \nu$ , where  $\nu$  is the LL filling factor. As a function of energy,  $\sigma_{xy}$  forms a staircase pattern reflecting the filling of LLs as  $\mu$  is increased. Figure 7.3 illustrates  $\sigma_{xy}$  as a function of  $\mu$  together with the corresponding transverse thermoelectric conductivity  $\epsilon_{xy}$  (for simplicity, spin-splitting is not included). Like,  $\sigma$ ,  $\epsilon$  will be approximately off-diagonal in this regime. Equation 7.10, which says that

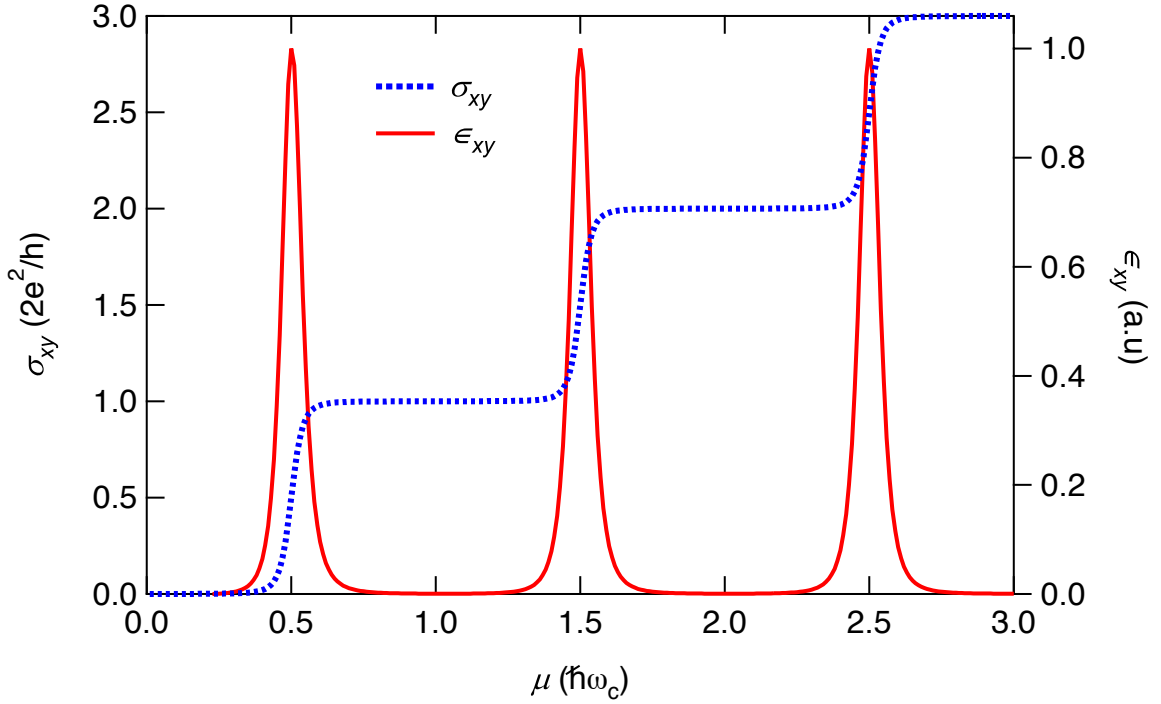


Figure 7.3: An illustration of the transverse conductivity  $\sigma_{xy}$  and thermoelectric conductivity  $\epsilon_{xy}$  as a function of chemical potential  $\mu$  in a strong magnetic field at low temperature. Spin-splitting is not included.

$\epsilon_{xy}$  is proportional to the energy derivative of  $\sigma_{xy}$ , implies that  $\epsilon_{xy}$  will vanish along the  $\sigma_{xy}$  plateaus and form peaks in between.

Let us consider the implications of Fig. 7.3 for diffusion thermopower in the QH regime. When  $\mu$  is positioned between LLs where  $\sigma_{xy}$  is quantized,  $\epsilon_{xy}$  vanishes. This indicates that no diffusion current will flow in response to a small temperature gradient. Therefore, the 2DES need not establish a canceling drift current. It follows that the diffusion thermopower vanishes in these regions. Conversely, when  $\mu$  is near the center of a LL,  $\sigma_{xy}$  increases as a function of energy resulting in a finite  $\epsilon_{xy}$ . That is, in the presence of a small longitudinal temperature gradient, a diffusion current will flow in the transverse direction. The 2DES will therefore establish an electric field to produce a canceling drift current. It follows that the diffusion thermopower is finite in these regions. Moreover, since  $\sigma$  is approximately off-diagonal, the electric field will be in the longitudinal direction. Here, the thermoelectric response of the

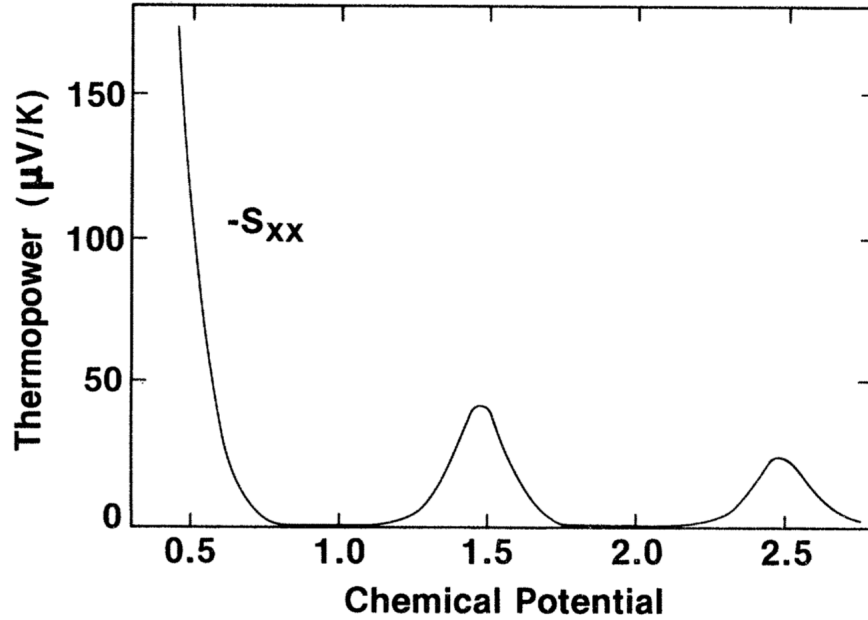


Figure 7.4: Calculated diffusion thermopower  $-S_{xx}^d$  vs chemical potential  $\mu$ , in the absence of disorder, in units where  $\hbar\omega_c = 1$  and  $k_B T = 0.05$ . This corresponds to  $T = 4.0$  K at  $B = 4.0$  T in GaAs. Spin-splitting is not included. Reprinted with permission from M. Jonson and S.M. Girvin, *Phys. Rev. B* **29**, 1939 (1984). Copyright 1984 by the American Physical Society.

2DES resembles that of a classical 2DES in that  $\mathbf{S}^d$  is approximately diagonal with canceling diffusion and drift currents flowing in the transverse direction.

The above analysis reveals that in the high field, low temperature limit,  $S_{xx}^d$  oscillates between vanishing and nonvanishing regions as a function of  $\mu$  that correspond to the incompressible and compressible phases of the QH regime. But what about the magnitude of  $S_{xx}^d$ ? Given that thermopower is  $\mathbf{S} = -\boldsymbol{\sigma}^{-1} \cdot \boldsymbol{\epsilon}$ , in this regime we have  $S_{xx}^d \approx -\epsilon_{xy}/\sigma_{xy}$ . Figure 7.3 therefore implies that  $-S_{xx}^d$  as a function of energy will have a peak at the center of each LL with a magnitude that is proportional to  $(N + 1/2)^{-1}$ , where  $N$  is the number of filled LLs. (An exception to this is the  $N = 0$  LL where  $-S_{xx}^d$  will not have a local maximum.) This is consistent with the theoretical work of Girvin and Jonson [81, 84]. In Fig. 7.4 we reproduce their calculation of  $-S_{xx}^d$  as a function of  $\mu$  for an ideal 2DES in a quantizing magnetic field. The cal-

ulation corresponds to a disorder-free 2DES at  $T = 4.0$  K and  $B = 4.0$  T in GaAs. Spin-splitting is not included. They derived a purely diagonal thermopower ( $S_{xy}^d = 0$  everywhere) that vanishes between LLs with a peak whenever  $\mu$  is centered on a LL with  $N > 0$ . As the temperature is lowered, the height of these peaks approaches the universal value  $-\ln 2(k_B/e)/(N + 1/2)$ , independent of magnetic field, electron density, effective mass, etc. Between LLs, the thermopower is thermally activated with an activation energy of the same order as the cyclotron energy  $\hbar\omega_c$  due to the QH gap at  $\mu$ .

As an aside, it is worth pointing out that this is very similar to the thermoelectric response of a quantum point contact (QPC) [85, 86, 87]. A QPC uses top gates to form an electrostatically tunable constriction within the 2DES of width comparable to  $\varepsilon_F$ . One may think of a QPC as a truncated waveguide that supports a finite number of conducting modes. The hallmark of a QPC is the quantization of its conductance to integer multiples of  $2e^2/h$ . As a function of energy, the QPC's longitudinal electrical and thermoelectric conductance qualitatively reproduce Fig. 7.3, with the cyclotron energy replaced by the eigenenergy spacing of a parabolic lateral confinement potential. Consequently, the resulting thermopower strongly resembles that of Fig. 7.4.

We now comment on the thermoelectric current distributions in the QH regime. For a noninteracting 2DES in the lowest LL, the current distributions during a thermoelectric measurement are expected to resemble the classical case illustrated in Fig. 7.2 [8]. That is, a transverse diffusion current will flow along the system edge in response to a longitudinal temperature gradient and a canceling transverse drift current will flow through the system bulk in response to a longitudinal thermoelectric field. Within excited LLs, however, the existence of edge channels must be taken into consideration. QH edge channels provide a parallel path for the canceling drift current. For instance, when  $\mu$  is centered on the  $N^{\text{th}}$  LL (ignoring spin), the edge channels provide a transverse conductance of  $N \cdot 2e^2/h$  while the bulk has a transverse conductivity of  $e^2/h$ . It follows that  $2N$  times as much of the transverse drift current flows along the edge as flows through the bulk.

## 7.4 Entropic Model

The thermopower of Fig. 7.4 was derived by examining the nonequilibrium particle-current density in a 2DES subject to a temperature gradient and magnetic field [84]. We will now derive the thermopower of Fig. 7.4 without any consideration of transport physics. Rather, we will take as our premise that  $S^d = -\mathcal{S}/en$ , where  $\mathcal{S}$  is the entropy per area and  $n$  is the two-dimensional electron density, as usual. For a disorder-free, noninteracting 2DES, calculating  $\mathcal{S}$  by counting states within LLs is relatively straightforward.

The entropy per area is given by

$$\mathcal{S} = k_B \ln \left( \prod_{N=0}^{\infty} D_N \right), \quad (7.11)$$

where  $D_N$  is the degeneracy per area of the  $N^{\text{th}}$  LL. In the absence of disorder, all *single-electron* states within a LL are degenerate. Therefore, the degeneracy of the *collection* of electrons within a LL follows from basic combinatorics as  $D_N = n_s!/(n_s - n_N)!n_N!$ , where  $n_s$  is the number of single-electron states per LL per area and  $n_N$  is the LL occupancy, or number of electrons populating the  $N^{\text{th}}$  LL per area. Applying Stirling's approximation, we have

$$\mathcal{S} \simeq k_B \sum_{N=0}^{\infty} \left( n_s \ln(n_s) - (n_s - n_N) \ln(n_s - n_N) - n_N \ln(n_N) \right). \quad (7.12)$$

From Section 6.4, we know that  $n_s$  equals the number of flux quanta per area. That is,  $n_s = B/\phi_0$ , where  $\phi_0 = h/e$  is the flux quantum. Meanwhile, the LL occupancy is given by Fermi-Dirac statistics as

$$\frac{n_N}{n_s} = \frac{1}{1 + \exp[(\hbar\omega_N - \mu)/k_B T]}, \quad (7.13)$$

where  $\hbar\omega_N = \hbar\omega_c(N + 1/2) = \hbar eB(N + 1/2)/m^*$  is the energy of the  $N^{\text{th}}$  LL. Putting all this together, the diffusion thermopower can be approximated as

$$S^d \simeq \frac{k_B}{e\nu} \sum_{N=0}^{\infty} \left( \left(1 - \frac{n_N}{n_s}\right) \ln \left(1 - \frac{n_N}{n_s}\right) + \frac{n_N}{n_s} \ln \left(\frac{n_N}{n_s}\right) \right), \quad (7.14)$$

where we used the fact that  $\nu = n/n_s$ .

Equations 7.13 and 7.14 reproduce Girvin and Jonson's  $S_{xx}$  versus  $\mu$  curve shown in Fig. 7.4 for  $B = 4.0$  T,  $T = 4.0$  K, and  $m^* = 0.067m_0$ . Remarkably, we see that even in the presence of a quantizing magnetic field the diffusion thermopower of the 2DES is equivalent to the entropy per charge carrier. This relationship between thermopower and entropy at high magnetic fields was originally recognized by Obraztsov [7] and explicitly applied to the 2DES in theoretical work by Oji [88] as well as Zawadski and Lassnig [89].

From the above analysis we can easily compute  $S^d$  as a function of  $\mu$  for a disorder-free noninteracting 2DES given parameters  $B$ ,  $T$ , and  $m^*$ . Experimentally, however, our independent variable is often  $B$  rather than  $\mu$ . To compute  $S^d$  as a function of  $B$  for fixed  $n$ , we must perform the intermediate step of determining  $\mu$  at each value of  $B$ . Toward that end, expressing  $n$  as a summation over LL occupancies provides an implicit function<sup>1</sup> for determining the value of  $\mu$ . Once we have  $\mu$ , we can compute  $S^d$  by counting degenerate states as before.

As an example, Fig. 7.5 shows  $S^d$  calculated as a function of  $B$  for a 2DES in GaAs with  $n = 1.0 \times 10^{11} \text{ cm}^{-2}$  at both  $T = 1.5$  K (red solid curve) and  $T = 0.5$  K (blue dotted curve). Several integral filling factors are labeled in the figure. This time we include spin-splitting. Odd filling factors correspond to spin-split LLs while even filling factors correspond to whole LLs. Since the Zeeman energy gap is less than the cyclotron energy gap, the Fermi statistics allow for a relatively larger number of

---

<sup>1</sup>Newton's method for root finding [90] can be used to estimate  $\mu$  given  $n$ ,  $B$ ,  $T$ ,  $m^*$ , and the electron spin g-factor  $g$ . Choose the differentiable function  $f(\mu)$  to be the difference between the constant  $\nu = \phi_0 n/B$  and the summation over spin-split LL occupancies:

$$f(\mu) = \nu - \sum_{\sigma \in (-1, +1)} \sum_{N=0}^{\infty} \frac{1}{1 + \exp[(\hbar\omega_N + \sigma g\mu_B B/2 - \mu)/k_B T]}, \quad (7.15)$$

where  $\mu_B = e\hbar/2m^*$  is the Bohr magneton. With a good initial guess—e.g.  $\mu(T = 0) = \hbar\omega_N + \sigma g\mu_B B/2$ , where  $N$  is the number of filled LLs and  $\sigma = \pm 1$  depending on valence spin branch—the method quickly converges to the value of  $\mu$  where  $f(\mu) = 0$ .

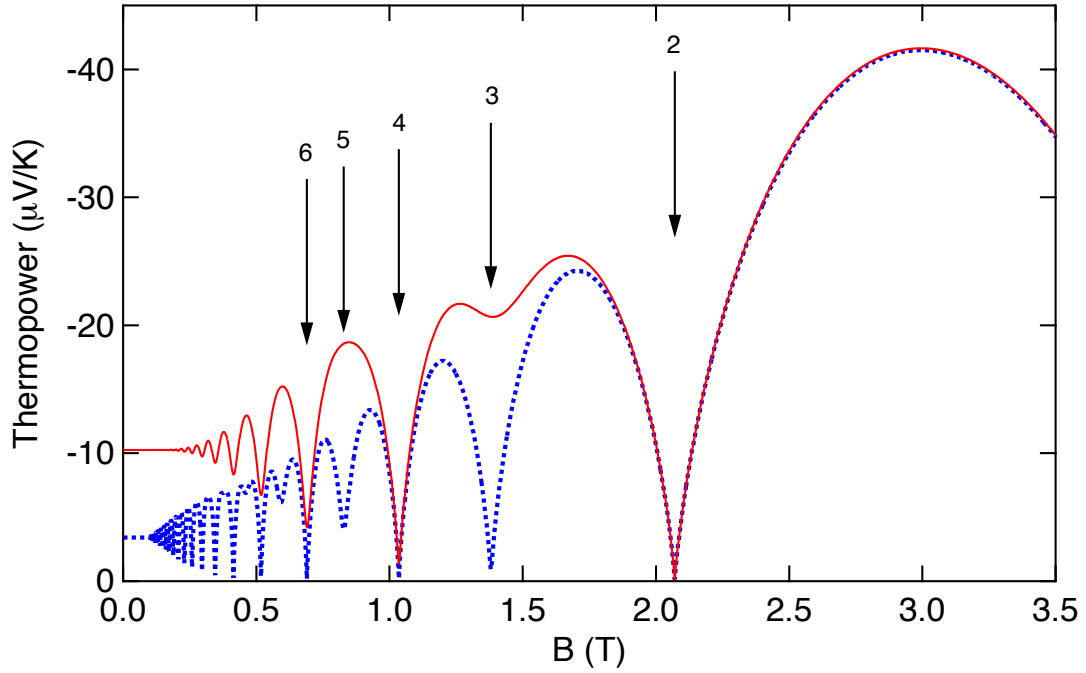


Figure 7.5: Calculated diffusion thermopower  $S^d$  vs magnetic field  $B$ , in the absence of disorder, for a noninteracting 2DES in GaAs with  $n = 1.0 \times 10^{11} \text{ cm}^{-2}$  at both  $T = 1.5 \text{ K}$  (red curve) and  $T = 0.5 \text{ K}$  (blue curve). Calculation includes spin-splitting. Several integral filling factors are labeled.

configurations at odd filling factors. This is why, for example,  $|S^d|$  is much larger at  $\nu = 3$  than at  $\nu = 4$  for the  $T = 1.5 \text{ K}$  curve.

Additional features of the  $S^d$  versus  $B$  calculations in Fig. 7.5 are worth comment. As expected, as  $B \rightarrow 0$  we recover the classical disorder-free value given by Eq. 7.8 with  $p = 0$ . Meanwhile, at sufficiently high magnetic field that  $\hbar\omega_N + \sigma g\mu_B B/2 \gg k_B T$ ,  $S^d$  becomes independent of temperature. In this latter regime, all terms in the summation over LLs in Eq. 7.14 vanish except for that corresponding to the valence LL such that  $S^d$  approaches the universal behavior

$$S^d = \frac{k_B}{e\nu} \left( (1 - \nu^*) \ln(1 - \nu^*) + \nu^* \ln(\nu^*) \right), \quad (7.16)$$

where  $\nu^* = \nu \bmod 1$  is the fractional part of  $\nu$ . Notice that Eq. 7.16 yields local extrema whenever  $\nu^* = 1/2$  equal to  $S^d = -\ln(2)k_B/e(i + 1/2)$ , where  $i$  is the

number of filled spin-split LLs. Also notice that Eq. 7.16 provides a lower-bound for a disorder-free, noninteracting 2DES and that  $|S^d|$  increases as a function of  $T$  monotonically from this universal curve. We will find monotonic temperature dependence to be a common feature of  $|S^d|$  for QH liquids even in the presence of disorder and/or interactions.

Equation 7.16 holds for a disorder-free, noninteracting 2DES in the limit of zero temperature. For fixed  $n$ , it is essentially the zero-temperature entropy as a function of  $B$ . This “universal” behavior is limited to the disorder-free case, however; the introduction of weak disorder dramatically alters  $S^d$ . For example, at  $T = 0$  and  $\nu = 3/2$ ,  $S^d \approx -40 \mu\text{V/K}$  in the disorder-free case. However, in the presence of any appreciable disorder,  $S^d \rightarrow 0$  as  $T \rightarrow 0$  for any value of  $\nu$ . In the following sections we will examine the impact that disorder has on the diffusion thermopower of a noninteracting 2DES.

## 7.5 Disorder and the Generalized Mott Formula

In Section 7.1, we asserted that the generalization of Mott’s formula for the case of a classical 2DES within a magnetic field is given by

$$S_{ij}^d \simeq -\frac{\pi^2 k_B^2}{3e} \rho_{ik} \left[ \frac{d\sigma}{d\varepsilon} \right]_{kj} \Big|_{\varepsilon=\varepsilon_F} T. \quad (7.17)$$

We then anticipated the basic features of diffusion thermopower in the QH regime by considering Eq. 7.17 in the context of the quantization of  $\sigma_{xy}$ . But is Eq. 7.17 a good approximation for  $S_{ij}^d$  within the weakly disordered QH regime? Jonson and Girvin showed [84] that this is indeed the case, at least for a noninteracting 2DES, as long as  $k_B T \ll \Gamma$ , where  $\Gamma$  is the LL broadening.

Experimentally, we are continually reducing both the accessible temperature and the amount of disorder in our systems. Therefore, it is not known a priori whether the  $k_B T \ll \Gamma$  condition can be achieved for our present samples. Recall, however, that in Section 6.9 we asserted that  $\Gamma = \hbar/2\tau_q$  for a simplified model of the QH system.

We also demonstrated a method for measuring the quantum lifetime  $\tau_q$  and found that for our diving board devices the 2DES has  $\tau_q \approx 3.0$  ps. This indicates that Eq. 7.17 is a good approximation when  $T \ll \hbar/2k_B\tau_q \approx 1.3$  K assuming phonon drag and electron-electron interactions can be ignored—a readily accessible temperature regime. Conveniently, the disorder in our ultra-clean system is not so low as to preclude the usefulness of the generalized Mott formula at dilution temperatures.

One consequence of Eq. 7.17 is a nonvanishing transverse diffusion thermopower  $S_{xy}^d$  at high magnetic fields in the presence of disorder. Classically, we expect  $S_{xy}^d$  to quickly vanish as a function of magnetic field as shown in Fig. 7.1. In the QH regime, however,  $S_{xy}^d$  should oscillate about zero with an amplitude that depends on the amount and type of disorder. In the model of Jonson and Girvin [84] the magnitude of  $S_{xy}^d$  increases with increasing disorder. In the next section we will explore a more recent model in which  $S_{xy}^d$  is impacted differently by short- and long-range disorder.

## 7.6 Computing $S_{xx}^d$ and $S_{xy}^d$

An explicit test of the generalized Mott formula is difficult for the 2DESs within our diving board devices. This is due to our inability to adjust the 2D density via electrostatic gating<sup>2</sup>, which is required to directly measure the conductivity’s energy dependence. However, Shirasaki et al. [82] recently calculated  $S_{xx}^d$  and  $S_{xy}^d$  using analytical formulas for the conductivity tensor  $\sigma$ , which allow explicit differentiation with respect to  $\varepsilon$ . The result is an integral expression that depends on  $T$ ,  $B$ ,  $n$ ,  $\tau_q$ ,  $\tau_m$ , and  $p$ , where, as usual,  $p = (n/\tau_i) \frac{d\tau_i}{dn}$  with  $i = q$  or  $m$ . Note that their model ignores spin-splitting. We do not include the expression here due to its complexity, but do provide a brief qualitative discussion of their results below. Later in this chapter, we will compare calculations made using this model to measurements made against the 2DES in diving board B.

Figure 7.6 shows an example calculation of both  $-S_{xx}^d$  and  $-S_{xy}^d$  as a function

---

<sup>2</sup>After illumination the 2D density in our sample cannot be modified by gating. This is a common occurrence in samples of this type which are intentionally overdoped. See Sections 1.2 and 2.5 for discussions of electrostatic gating and sample illumination, respectively.

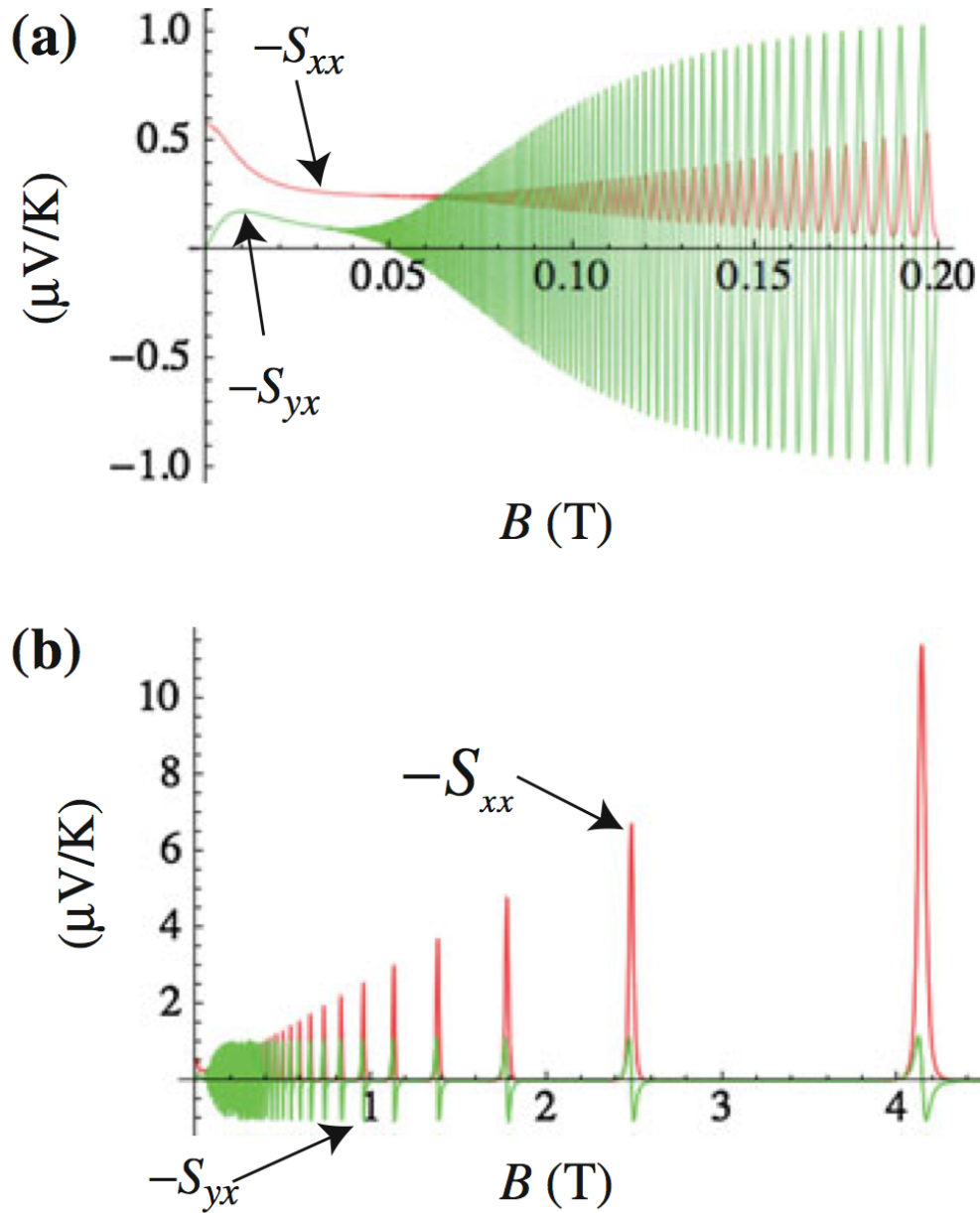


Figure 7.6: Calculated longitudinal and transverse diffusion thermopower,  $S_{xx}^d$  and  $S_{xy}^d$ , vs magnetic field  $B$  at  $T = 100$  mK in the range (a)  $0 \text{ T} < B < 0.2 \text{ T}$  and (b)  $0 \text{ T} < B < 4.5 \text{ T}$ . The calculation is made for a 2DES in GaAs with  $n = 3.0 \times 10^{11} \text{ cm}^{-2}$ ,  $\tau_q = 3.8 \text{ ps}$ ,  $\tau_m = 38 \text{ ps}$  ( $\mu_e = 1.0 \times 10^6 \text{ cm}^2/\text{Vs}$ ), and  $p = 1.5$ . Reprinted from R. Shirasaki, A. Endo, N. Hatano, and H. Nakamura, *J. Electron. Mater.* **41**, 1540 (2012) with kind permission of Springer Science and Business Media.

of  $B$  for a 2DES in GaAs with  $n = 3.0 \times 10^{11} \text{ cm}^{-2}$ ,  $\tau_q = 3.8 \text{ ps}$ ,  $\tau_m = 38 \text{ ps}$  ( $\mu_e = 1.0 \times 10^6 \text{ cm}^2/\text{Vs}$ ), and  $p = 1.5$  at  $T = 100 \text{ mK}$ . In Fig. 7.6 (a) we see the low-field regime where  $B \leq 0.20 \text{ T}$ . Observe the crossover in the vicinity of  $B \sim 0.04 \text{ T}$  from the classical to QH regimes. For  $B \lesssim 0.04 \text{ T}$ ,  $-S_{xx}^d$  and  $-S_{xy}^d$  exhibit classical behavior similar to that of Fig. 7.1. Away from the classical regime both thermopower coefficients oscillate as a function of  $B$ . These oscillations are periodic in  $1/B$  with a frequency that scales with  $n$ . Like oscillations in  $\rho_{xx}$  and  $\sigma_{xx}$ , a minimum in  $S_{xx}^d$  occurs each time  $\mu$  is positioned between LLs. In this model, the amplitude of the  $S_{xx}^d$  oscillations increases for larger  $\tau_q$ . This dependence on  $\tau_q \propto 1/\Gamma$  is consistent with the generalized Mott formula, which says that when  $\sigma_{xy} \gg \sigma_{xx}$ ,  $S_{xx}^d \propto \rho_{xy} \cdot d\sigma_{xy}/d\varepsilon$ . A cleaner 2DES (i.e. larger  $\tau_q$ ) will have sharper steps in  $\sigma_{xy}$  as a function of  $\varepsilon$  yielding larger maxima in  $d\sigma_{xy}/d\varepsilon$ , and therefore, larger maxima in  $|S_{xx}^d|$ .

$S_{xy}^d$  initially oscillates with increasing amplitude as  $B$  increases and eventually oscillates about zero. Once  $B$  is sufficiently large (e.g.  $B \gtrsim 0.10 \text{ T}$ ),  $S_{xy}^d$  passes through zero whenever an integral number of LLs are filled and again whenever a LL is half filled. In this model, the amplitude of the  $S_{xy}^d$  oscillations depends on both  $\tau_q$  and  $\tau_m$ , increasing for larger values of the former but decreasing for larger values of the latter. This is in contrast to  $S_{xx}^d$ , whose amplitudes depend on  $\tau_q$  only. This is consistent with the generalized Mott formula, which tells us that when  $\sigma_{xy} \gg \sigma_{xx}$ ,  $S_{xy}^d \propto -\rho_{xx} \cdot d\sigma_{xy}/d\varepsilon$ . Larger  $\tau_q$  yields sharper steps in  $\sigma_{xy}$  as a function of  $\varepsilon$  such that the amplitude of  $S_{xy}^d$  increases. At the same time, the magnitude of the  $\rho_{xx}$  peaks are inversely proportional to  $\tau_m$  in this model. A larger  $\tau_m$  therefore yields a smaller amplitude of  $S_{xy}^d$ .

Figure 7.6 (b) provides an expanded view of  $S_{xx}^d$  and  $S_{xy}^d$  as a function of magnetic field  $B$ . For  $B \gtrsim 0.2 \text{ T}$ , the peaks in  $|S_{xy}^d|$  are independent of  $B$ . The peaks in  $|S_{xx}^d|$  are seen to increase in magnitude in proportion to  $B$ . This is a reflection of the linear increase in the degeneracy of LLs (and hence, entropy per electron) with  $B$ . Importantly, however, unlike the disorder-free case, the magnitude of the maxima in  $|S_{xx}^d|$  are not equal to the universal values of  $\ln 2 (k_B/e) / (N + 1/2)$ , with  $N$  the number of filled LLs. Instead, within this disordered model, when  $T \ll \Gamma/k_B$ ,

$|S_{xx}^d|$  is linearly proportional to  $T$ . At higher temperatures, the peak value of  $|S_{xx}^d|$  associated with the  $N^{\text{th}}$  LL is predicted to become sublinear with respect to  $T$  before asymptotically approaching  $\ln 2 (k_B/e) / (N + 1/2)$  from below [82].

## 7.7 Phonon Drag in the QH Regime

Early experimental observations of thermopower in the QH regime yielded magnitudes far larger than any predictions made for diffusion thermopower [45, 49, 46, 47, 48]. In section 3.5 we discussed another contribution to thermopower resulting from the transfer of momentum from phonons known as phonon drag. It is now generally accepted, as in the zero-field case, that the thermoelectric signals measured in these early experiments performed within a quantizing magnetic field were nearly entirely attributable to electron-phonon interactions [37].

As an example, in Fig. 7.7 we present a comparison of the experimental results of a 1988 study [91] by Fletcher et al. and the theoretical work [92] of S. K. Lyo for a GaAs/AlGaAs heterostructure in a diving board-like configuration similar<sup>3</sup> to ours. The figure shows the measured longitudinal thermopower (dashed lines) as a function of magnetic field together with calculated phonon drag thermopower (solid lines) for  $T \in (1.61, 2.72, 4.03)$  K. The calculations treated the phonon mean free path  $\Lambda$  and the Landau level broadening  $\Gamma$  as adjustable parameters with chosen values comparable to those empirically estimated. A key point of the theoretical work was the necessity of assuming only the extended states at the center of each LL participate in the scattering of phonons; only then is good agreement achieved between the calculations and the experimental data [92].

As is true for calculations of  $S_{xx}^d$ , at sufficiently low temperatures the phonon drag contribution  $S_{xx}^g$  vanishes at integral filling factors, which occur in the figure at  $B \approx 2.6, 3.2, 4.3$ , and  $6.5$  T ( $\nu = 10, 8, 6$ , and  $4$ , respectively). And like  $S_{xx}^d$ , the magnitude of  $S_{xx}^g$  is maximum with the chemical potential centered on a LL.

---

<sup>3</sup>While the experimental setups are similar a key difference between the 2DES studied by Fletcher et al. and that studied for this thesis is the electron mobility with  $\mu_e = 1.9 \times 10^5$  cm<sup>2</sup>/Vs and  $3.1 \times 10^7$  cm<sup>2</sup>/Vs, respectively.

Indeed, it is here that the density states is greatest such that electrons are readily scattered by phonons. It is worth remarking on the most conspicuous discrepancy between the experimental data and the calculation, which occurs at  $B \approx 5.2$  T where a clear minimum in the measured thermopower is observed at  $T = 1.6$  K. This is a consequence of the calculation ignoring spin-splitting, which is only observed in the experimental data for  $\nu = 5$  at  $T = 1.6$  K (elsewhere the Zeeman energy gap  $g\mu_B B$  is much smaller than the temperature  $k_B T$ ).

The data show two ways in which  $S_{xx}^g$  significantly differs from  $S_{xx}^d$  in the low-temperature limit as per the generalized Mott formula. First, the magnitudes of the

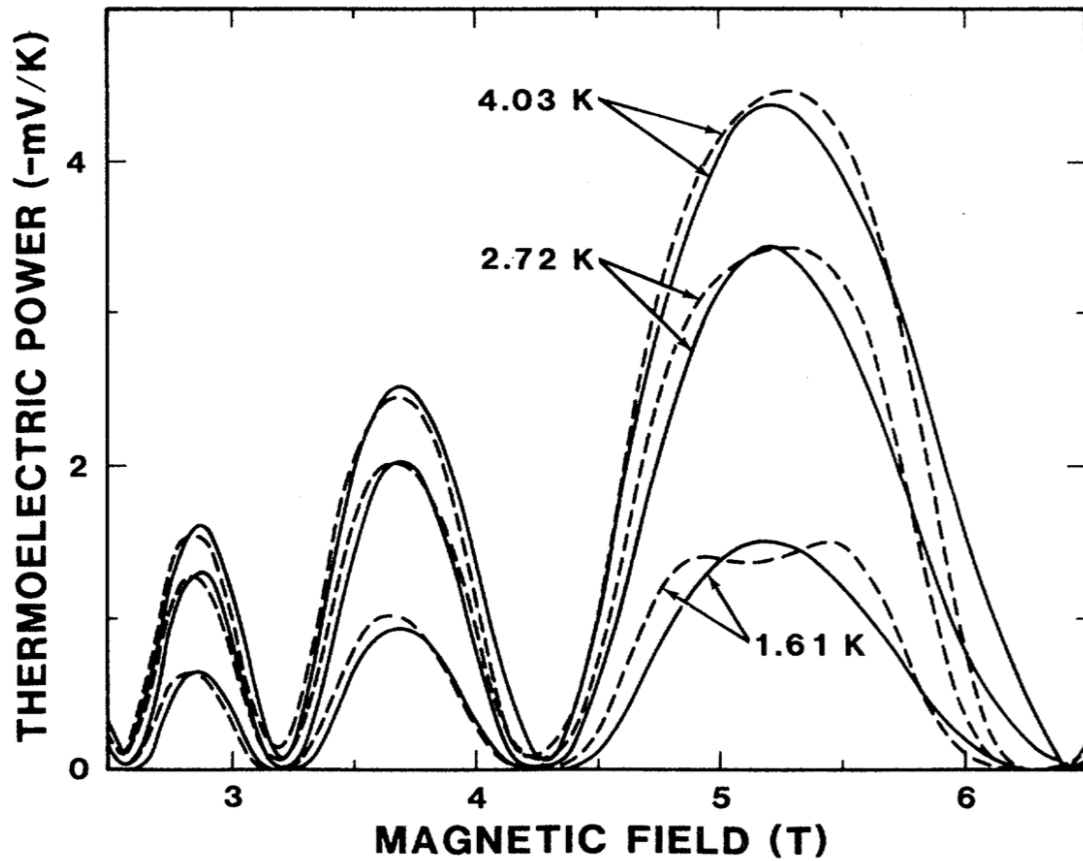


Figure 7.7: Comparison of calculated longitudinal phonon drag thermopower  $S_{xx}^g$  (solid lines) to experimental data (dashed lines) for a GaAs/AlGaAs heterostructure in the QH regime at several temperatures. Reprinted with permission from S. K. Lyo, *Phys. Rev. B* **40**, 6458 (1989). Copyright 1989 by the American Physical Society.

$|S_{xx}^g|$  maxima occurring when  $\mu$  is positioned between LLs are not linear in temperature. Rather, from  $T = 1.61$  K to  $T = 2.72$  K we see approximately a doubling in the magnitude of  $|S_{xx}^g|$  indicating superlinear temperature dependence. Moreover, from  $T = 2.72$  K to  $T = 4.03$  K—an increase in temperature of about 50%—we observe roughly an increase of 33% in  $|S_{xx}^g|$  indicating sublinear temperature dependence. Second, the magnitude of the phonon drag maxima are on the order of millivolts per Kelvin compared to only tens of microvolts per Kelvin for diffusion thermopower. With a difference of two orders of magnitude, it is no surprise that phonon drag often masks the thermoelectric effects of electronic diffusion at these temperatures.

Experimentally, phonon drag typically dominates measurements of thermopower in the QH regime at  $T \gtrsim 0.3$  K [45, 49, 46, 47, 48]. Due to the strong temperature dependence of phonon emission rates within GaAs at dilution refrigeration temperatures, at  $T \lesssim 0.3$  K a crossover from phonon drag-dominated to diffusion-dominated thermopower will occur (see Section 3.5 for more on this). The precise crossover temperature varies among experiments and can be increased by limiting the phonon mean free path through careful fabrication methods<sup>4</sup>. As in the zero-field case, it is incumbent upon the diffusion-thermopower-seeking experimentalist to minimize temperature and/or phonon emissions to mitigate this unwanted contribution.

## 7.8 Experimental Results at Low Fields

At sufficiently low fields, electron-electron interactions may be ignored such that the theoretical picture provided in this chapter applies. We show that, at sufficiently low temperatures, within the domain of  $B$  where the 2DES may be reasonably modeled as spinless noninteracting 2D electrons, the measured thermoelectric response is consistent with expectations based upon the generalized Mott formula and the model of Shirasaki et al. By demonstrating our ability to measure the expected thermopower of the 2DES within the IQH regime, we further bolster our confidence in our measure-

---

<sup>4</sup>For example, our diving board devices are thinned and the backside is sandblasted to minimize specular reflection of phonons on that surface. See Appendix Section B.7 for these fabrication details.

ment technique. In Chapter 8 we will introduce the *fractional* quantum Hall regime, which occurs at higher magnetic fields. The results discussed here are a stepping stone toward our ultimate aim of utilizing thermopower as a probe of the many-body phases found in this latter regime.

Early in our investigation we chose to focus our attention on the Seebeck effect ( $S_{xx}$ ) of 2D electrons and not pursue the Nernst-Ettingshausen effect ( $S_{xy}$ ). This decision was primarily motivated by our limitation of time and resources in conjunction with a recent prediction [93] of an enhanced Seebeck coefficient in the case of the non-abelian quasiparticle statistics that are anticipated for particular FQH states (more on this in Chapter 9). Moreover, preliminary measurements of  $S_{xy}$  did not yield reproducible results upon thermally cycling our experiment through elevated temperatures<sup>5</sup> thereby making their interpretation more difficult.

Figure 7.8 shows the measured thermovoltage  $\Delta V$  divided by the *apparent* change in temperature  $\Delta T_{\text{app}}$  along the 2DES mesa versus magnetic field  $B$  for three temperatures. In the case where  $\Delta V$  can be entirely attributed to the Seebeck effect and  $\Delta T_{\text{app}}$  is equal to the actual change in temperature  $\Delta T$ , we have that  $\Delta V/\Delta T_{\text{app}} = -S_{xx}$ . These data were acquired from diving board B using the AC lock-in technique and temperature calibration data of Section 4.2. Thermovoltages were measured using the middle ohmic contacts of mesa 1 (the mesa closest to thermal ground). Note that similar results were acquired from mesa 2. Thermovoltages at temperatures

---

<sup>5</sup>During our experimental study, our dilution refrigerator repeatedly warmed from operating temperatures of  $T < 300$  mK to  $T \sim 4$  K. This was the result of contaminants within our supply of liquid helium that would plug the intake line that delivers helium from the cryostat's main bath to the 1K pot (see Chapter 2). The 1K pot would eventually become empty causing the dilution circuit to fail. Each time this occurred the diving board sample would eventually come into thermal equilibrium with the liquid helium in the main bath. We would then clear the 1K pot intake line and slowly re-cool the experiment to operating temperatures. The upside of an otherwise frustrating situation was the opportunity to exhaustively test the reproducibility of transport measurements, both electric and thermoelectric, after cycling our sample through  $T \sim 4$  K. We believe thermally annealing our sample in this way results in a randomization of the microscopic details of the background impurity potential. From these measurements we found that the transverse electrical resistance  $R_{xy}$  and the longitudinal thermopower  $S_{xx}$  as a function of  $B$  and  $T$  were unchanged for  $T \gtrsim 50$  mK. Conversely, the high-field longitudinal electrical resistance  $R_{xx}$  and the transverse thermopower  $S_{xy}$  as a function of  $B$  and  $T$  significantly changed in magnitude. Observing changes in the magnitude of the high-field  $R_{xx}$  upon thermally cycling a 2DES is a familiar phenomenon in our laboratory. That the low-temperature, high-field  $S_{xy}$  would exhibit similar behavior is consistent with the generalized Mott formula, which says that  $S_{xy} \propto -\rho_{xx} \cdot d\sigma_{xy}/d\varepsilon$  in this regime.

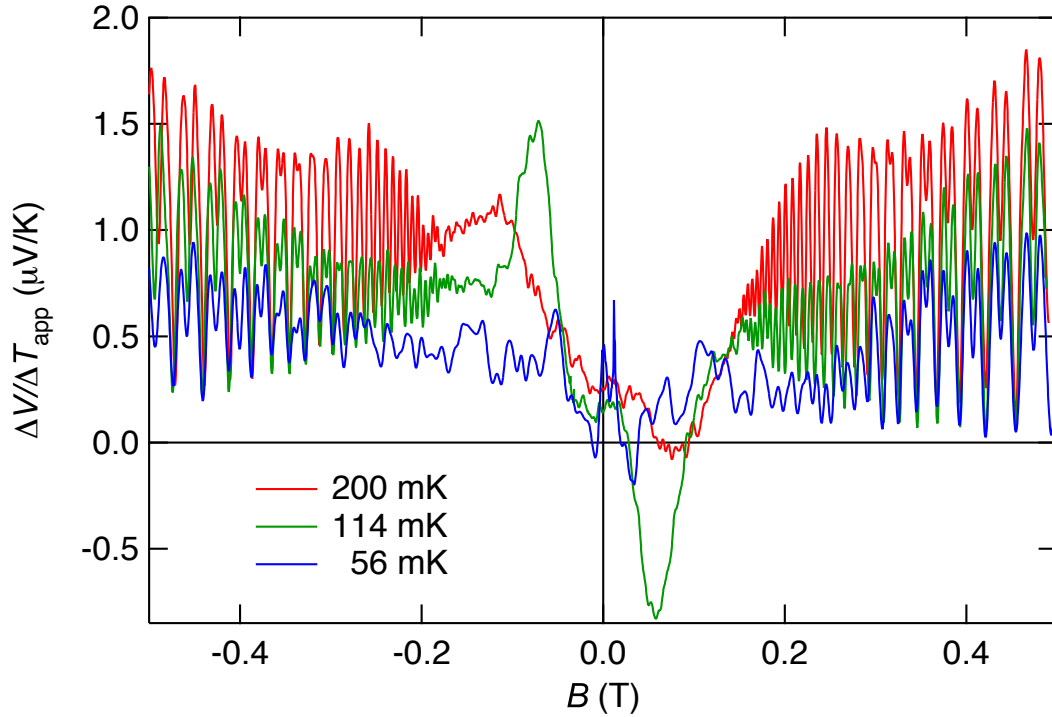


Figure 7.8: Measured thermovoltage  $\Delta V$  divided by *apparent* change in temperature  $\Delta T_{\text{app}}$  vs magnetic field  $B$  for three temperatures. For  $|B| \gtrsim 0.2$  T we attribute  $\Delta V$  entirely to the Seebeck effect and claim that  $\Delta T_{\text{app}} = \Delta T$  such that  $\Delta V/\Delta T_{\text{app}} = -S_{xx}$ . For  $|B| \lesssim 0.2$  T the data is more difficult to interpret due to superconducting phase transitions in the indium solder joint that connects the diving board to the cold reservoir.

$T \in (56, 114, 200)$  mK were measured by establishing apparent temperature differences  $\Delta T_{\text{app}} \in (3.8, 8.1, 10.3)$  mK along the 2DES mesa, respectively. These data were acquired while slowly varying the magnetic field at  $dB/dt = 5$  mT/min.

The data shown in Fig. 7.8 for  $|B| \lesssim 0.2$  T remains an unexplained mystery. At  $B = 0$ , these results are inconsistent with our thermopower measurements in diving board A. More conspicuously, the sign reversal and nearly odd-symmetry of the  $T = 114$  mK data is both surprising and suspiciously similar to what is expected for  $S_{xy}$ . This is why we emphasize the distinction between  $\Delta T_{\text{app}}$  and the actual change in temperature  $\Delta T$ . Unlike  $\Delta V$ , which is measured directly, the change in temperature is inferred using measurements of thermal conductance. Specifically,  $\Delta T_{\text{app}}$  is the change in temperature along the 2DES mesa (between the ohmic contacts) that is

calculated using the calibration data of Section 4.2.

Recall from Sec. 4.1.3 our discussion of the role of the indium solder joint that connects the diving board to the cold reservoir when inferring the temperatures along a diving board device. In principle, differences between  $\Delta T_{\text{app}}$  and  $\Delta T$  can arise due to superconducting phase transitions in the indium. At sufficiently low magnetic fields the indium is superconducting, and therefore, has a significantly reduced thermal conductance compared to when in its normal phase. Since our temperature calibration technique (see Section 4.1.1) utilizes magnetic fields that are several orders of magnitude larger than bulk indium's critical field  $B_c = 28 \text{ mT}$ , we can be confident that the indium is always in its normal phase when measuring thermal conductances. In Sec. 4.1.3 we argue that the thermal conductance of the indium in its superconducting phase should remain sufficiently large relative to the rest of the diving board that the impact of this transition is negligible. Nonetheless, the data of Fig. 7.8 suggests that we reconsider our assumptions. In our previous analysis we estimate the thickness of the indium to be  $t \sim 0.1 \text{ mm}$ . It is possible that in the case of diving board B the thickness of the indium is significantly less than this and perhaps non-uniform along the width of the indium-GaAs interface. It has been shown that the critical field of an indium film of thickness  $t \lesssim 100 \mu\text{m}$  is dependent upon  $t$  and can be significantly larger than that of bulk indium [94]. Even if superconductivity introduces systematic error to our temperature determinations near  $B = 0$ , the apparent change in temperature  $\Delta T_{\text{app}}$  can be expected to equal the actual change in temperature  $\Delta T$  above some unknown magnitude of  $B$  where the indium is necessarily in its normal phase. Consequently, the data of Fig. 7.8 can be expected to equal the negative longitudinal thermopower  $-S_{xx}$  above the same unknown magnitude of  $B$ .

Several features of the data shown in Fig. 7.8 suggest that for  $|B| \gtrsim 0.2 \text{ T}$  we have that  $\Delta V/\Delta T_{\text{app}} = -S_{xx}$ . To begin with, we expect  $S_{xx}$  to have even symmetry with respect to  $B$ . This is approximately true for all three temperatures for  $|B| \gtrsim 0.2 \text{ T}$  while clearly false for  $|B| \lesssim 0.2 \text{ T}$ . Moreover, if the critical field varies along the width of the indium solder joint due to variations in its thickness, we can no longer expect the temperature gradient to be parallel to the length of the diving board for all

values of  $B$ . This would result in a  $\Delta V$  that is a linear combination of the Seebeck and Nernst-Ettingshausen effects. As previously discussed, the latter of these is expected to have odd symmetry with respect to  $B$ . At least in the case of the  $T = 114$  mK data, for  $|B| \lesssim 0.15$  T, it is obvious that the signal could be well approximated as the sum of evenly and oddly symmetric signals. For  $|B| \lesssim 0.2$  T it may be that admixture of the Nernst-Ettingshausen effect as well as differences between  $\Delta T_{\text{app}}$  and  $\Delta T$  contribute to a discrepancy between  $\Delta V/\Delta T_{\text{app}}$  and  $-S_{xx}$ .

The temperature dependence of the data also suggests that  $\Delta V/\Delta T_{\text{app}} = -S_{xx}$  for  $|B| \gtrsim 0.2$  T. Assuming Mott-like diffusion thermopower, we expect maxima in  $-S_{xx}$  to be approximately linear in  $T$ . With data for only three temperatures, a precise measure of the temperature dependence is not available. Nonetheless, the maxima for  $|B| \gtrsim 0.2$  T are consistent with a linear temperature dependence to within experimental uncertainty. Meanwhile, the data for  $|B| \lesssim 0.2$  T fail to even exhibit monotonic temperature dependence, which makes an interpretation as  $-S_{xx}$  quite difficult.

Other features of Fig. 7.8 where  $|B| \gtrsim 0.2$  T that are consistent with  $-S_{xx}$  include the frequency of the oscillations, which are periodic in  $1/B$  with the correct frequency for a 2DES of this density ( $n = 2.9 \times 10^{11} \text{ cm}^{-2}$ ). Also, the  $T = 114$  mK and  $T = 200$  mK data both show a clear frequency doubling that can be attributed to spin-splitting of the LLs. These doublings occur at  $|B| \approx 0.25$  T and  $|B| \approx 0.30$  T for  $T = 114$  mK and  $T = 200$  mK, respectively. Due to the reduced signal-to-noise<sup>6</sup> ratio of the  $T = 56$  mK measurements, the precise onset of the doubled frequency is not clear in this data set. But for  $|B| \gtrsim 0.3$  T the  $T = 56$  mK data clearly oscillates with the doubled frequency. These are all consistent with frequency doubling observed in  $R_{xx}$  that occurs once the Zeeman splitting  $|g\mu_B B|$  is comparable to the thermal broadening  $k_B T$ .

Finally, notice the field dependence of the peaks of the  $T = 200$  mK data of

---

<sup>6</sup>For a metallic phase in which  $S \propto T$ , the signal-to-noise  $S/N$  of our thermopower measurements goes as  $S/N \propto T^2$ . This is because we approximately hold the ratio  $\Delta T/T$  fixed in an effort to maximize  $S/N$  while simultaneously remaining in a linear regime where  $\Delta T \ll T$ . We therefore have  $\Delta V = S \cdot \Delta T \propto T^2$ .

Fig. 7.8. In the region where  $0.20 \text{ T} \leq |B| \leq 0.25 \text{ T}$  the magnitude of these peaks increases approximately linearly with increasing  $|B|$ . This is qualitatively consistent with the notion that the peaks of  $S_{xx}^d$  should scale with the degeneracy of the LLs, which increases with  $|B|$ . After a period in which the peaks decrease with  $|B|$  and the frequency doubling attributed to spin-splitting occurs, we again observe a region in which the peaks increase linearly with  $|B|$ . In this latter region, which coincides with  $|B| \gtrsim 0.3 \text{ T}$ , the rate at which the peaks increase is approximately half that of the region where  $0.20 \text{ T} \leq |B| \leq 0.25 \text{ T}$ . This should be expected since the degeneracy of spin-split LLs is half that of LLs that ignore spin.

In Fig. 7.9 we compare our measurements of  $\Delta V/\Delta T_{\text{app}}$  to predictions of  $-S_{xx}^d$  from the model of Shirasaki et al. calculated using the generalized Mott formula. The right panel shows a subset of the experimental data already shown where  $0.17 \text{ T} \leq$

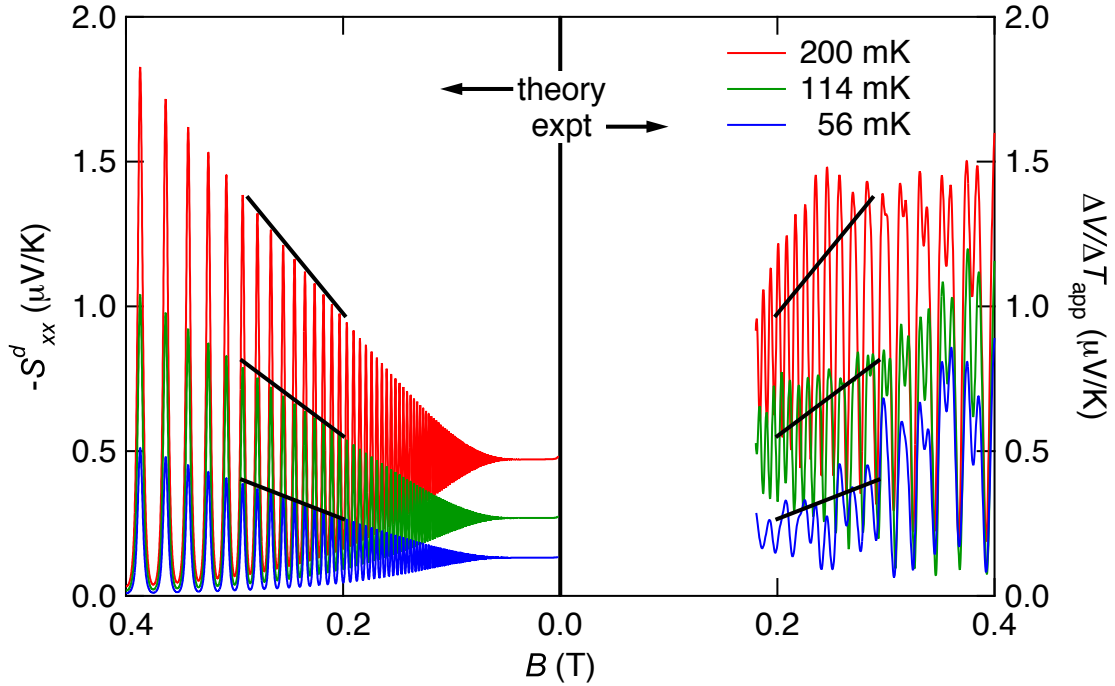


Figure 7.9: Comparison of calculations of  $-S_{xx}^d$  made using the model of Shirasaki et al. and measurements of  $\Delta V/\Delta T_{\text{app}}$ . The right panel shows the subset of experimental data where  $0.17 \text{ T} \leq B \leq 0.40 \text{ T}$ . The left panel shows calculations for the three relevant temperatures made using the following parameter values:  $n = 2.9 \times 10^{11} \text{ cm}^{-2}$ ,  $\tau_q = 3.0 \text{ ps}$ ,  $\tau_m = 1.2 \text{ ns}$ , and  $p = 0.9$ . Thick black lines are guides to the eye.

$B \leq 0.40$  T. The left panel shows calculations for the three relevant temperatures made using the following measured<sup>7</sup> quantities as parameter values:  $n = 2.9 \times 10^{11} \text{ cm}^{-2}$ ,  $\tau_q = 3.0$  ps,  $\tau_m = 1.2$  ns, and  $p = 0.9$ . Note there are no free parameters. Several thick black lines are included as guides to the eye.

Let us consider the similarities and differences between the measured data and predicted thermopowers of Fig. 7.9. We find good agreement in the periodicity for  $B \lesssim 0.3$  T in the case of  $T = 200$  mK and for  $B \lesssim 0.25$  T in the case of  $T = 114$  mK. At higher values of  $B$  we observe frequency doubling, which we attribute to the resolution of spin-split LLs, as previously discussed. Since the model ignores electron spin, this sort of frequency doubling is absent from the predicted thermopower. Meanwhile, as the thick black lines highlight, for all three temperatures the measured peaks of  $\Delta V/\Delta T_{\text{app}}$  are consistent with the predicted peaks for  $-S_{xx}$  for  $B \lesssim 0.3$  T to within experimental uncertainty. Taking into consideration the absence of electron spin from the model, these calculations further corroborate the notion that the measured  $\Delta V/\Delta T_{\text{app}}$  is indeed the negative longitudinal thermopower  $-S_{xx}$  of the 2DES. Moreover, the agreement in the magnitude of the measured signals to that predicted by the model suggests that phonon drag contributes negligibly to the measurements for  $T \lesssim 200$  mK.

## 7.9 Summary

The thermoelectric response of the 2DES within the QH regime is a rich topic and offers a perspective that is complimentary to the more familiar picture provided by electrical transport. Applying an external magnetic field to the 2DES results in circulating currents and transverse thermoelectric effects. The formation of LLs dramatically alters the thermopower of the 2DES compared to the classical case. The alternating compressible and incompressible liquids of the QH regime present profoundly different thermoelectric behavior. The former acts like a metal in that we

---

<sup>7</sup>In the case of  $p$  we merely have the lower bound  $p \gtrsim 0.9$  (see Section 4.1.3). Increasing the value of  $p$ , which has the theoretical [33] upper bound  $p \leq 1.5$ , has a negligible impact on these theoretical data away from  $B = 0$  due to the values of the other parameters.

expect linear temperature dependence. The thermally activated behavior of the latter resembles that of the longitudinal electrical resistance. But for both we expect the diffusion thermopower to remain proportional, if not equal, to the entropy per electron per electron charge.

This chapter introduced a generalized Mott formula for diffusion thermopower that holds in a magnetic field in the limit of zero temperature in the absence of electron-electron interactions and phonon drag. We reviewed the recent model of Shiraski et al. [82], which employs the generalized Mott formula to calculate diffusion thermopower as a function of magnetic field. We saw how these calculations yield a thermopower that crosses over from the classical to QH regimes. We also explored how these calculations depend on measurable parameters such as the momentum and quantum lifetimes.

We concluded the chapter by reviewing our experimental results at low magnetic fields where  $|B| \leq 0.5$  T at several temperatures. For  $|B| \lesssim 0.2$  T we are not able to understand our thermoelectric measurements in terms of thermopower. This is a consequence of the indium solder joint that connects our diving board device to the cold reservoir of the cryostat. We argue that data are compromised for  $|B| \lesssim 0.2$  T by the discrepancy between thermal conductances measured in a large magnetic field and those when the indium solder joint is in its superconducting phase. Due to our temperature calibration technique, we are limited to thermopower measurements during which the indium solder joint is in its normal phase. We contend that this is the case for  $|B| \gtrsim 0.2$  T and that our thermoelectric measurements are consistent with diffusion thermopower in this region. We show that for  $0.2 \text{ T} \gtrsim |B| \gtrsim 0.3 \text{ T}$ , our measurements at  $T \in (114, 200)$  mK are roughly consistent with the model of Shirasaki et al. We explain discrepancies between our measurements and the model for  $|B| \gtrsim 0.3$  T as consequences of spin-splitting of LLs. We observe no evidence of appreciable phonon drag for  $T \leq 200$  mK and  $|B| < 0.5$  T.

## Chapter 8

# Fractional Quantum Hall Regime

This chapter will review the fractional quantum Hall effect (FQHE), the associated thermopower, and our experimental results for the  $N = 0$  Landau level. The FQHE is a higher-order QH phenomenon resulting from electron-electron interactions. Like the IQHE, the FQHE is characterized by quantization of the Hall resistance. The latter, however, occurs at fractional values of the LL filling factor. Two theoretical frameworks will be considered that capture key features of the FQHE. The first, pioneered by Robert Laughlin, is built upon a relatively simple, parameterized wave function that describes the most prominent observed quantized fractions. A quantum statistical analysis of the quasiparticle excitations of Laughlin's original states leads to a hierarchical framework that successfully describes all observed odd-denominator FQHEs. An alternative framework recasts the problem of many strongly interacting electrons in a large magnetic field to one of many weakly interacting composite particles in a small magnetic field. We may then understand FQHEs as IQHEs of *composite fermions* (CFs), thereby arriving at a more intuitive and insightful picture of otherwise very complicated physics.

The CFs introduced by this latter theoretical framework are more than mere mathematical contrivances; they are theoretically predicted and observed to exhibit bona fide fermionic behavior, which includes their thermoelectric response. Following an overview of the FQHE, we discuss diffusion thermopower in the FQH regime leveraging the CF model whenever possible to make analogy with IQH phenomena. In particular, we will extend the disorder-free entropic model of thermopower introduced

in Chapter 7 to include CF formation. This model clearly demonstrates that CFs, formed via electron-electron interactions, can dramatically reduce the entropy and energy of a 2DES within a strong magnetic field.

The second half of this chapter is dedicated to reviewing and analyzing our experimental results within the  $N = 0$  LL. We begin at  $\nu = 3/2$  where the 2DES can be understood as a filled spin-split LL in parallel with a sea of CFs in zero effective magnetic field. We compare  $S_{xx}$  versus  $T$  at  $\nu = 3/2$  to that of noninteracting electrons in zero field. Our results are then compared to a previously reported experiment with 2D holes. We then briefly return to the model of Shirasaki et al. that was described in Section 7.6 to argue that our results at  $\nu = 3/2$  are not consistent with disordered noninteracting 2D electrons.

Our most comprehensive picture of the thermopower in the FQH regime is provided by traces of  $S_{xx}$  versus  $B$ . We compare and contrast such a trace to the more familiar longitudinal resistance  $R_{xx}$ . We show that while these transport coefficients are often correlated, they offer unique information about the underlying system. To gain a rough sense of the temperature evolution of the thermopower in this regime, we present  $S_{xx}$  versus  $B$  in the  $N = 0$  LL at three different temperatures. These data reveal strong evidence of the formation of multiple species of CFs (i.e. number of flux quanta attached to each electron). At the lowest experimentally accessible temperatures we observe novel fluctuations. We provide an example of this and offer a possible explanation. Finally, we return to our disorder-free entropic model and demonstrate good correlation with our experimental data in the vicinity of strong FQH states.

## 8.1 Fractional Quantum Hall Effect

Given the dominance of the interaction term, it cannot be treated perturbatively. At the same time, it is well known that analytically solving Schrödinger's equation for even a three-body interaction is difficult if not impossible. We may therefore consider the FQHE as *emergent phenomena* in the sense that these are energy minimizing

collective modes arising from the interactions of large numbers of electrons whose dynamics cannot be understood via a study of their microscopic details. The resulting many-body states exhibit remarkable properties. In the limit of zero temperature, FQH liquids flow without dissipation slipping around any would-be impediments. Disturbing a FQH ground state through a small deviation in the magnetic field or by elevating the temperature has the remarkable effect of producing quasiparticle excitations that carry a fraction of an electron charge. Moreover, these quasiparticles themselves can interact to yield even higher-order exotica!

### 8.1.1 Laughlin States

Given the complex nature of correlated electron states, following the discovery of the FQHE the idea that a simple description could capture its essential features seemed unlikely. Nonetheless, in 1983 Robert Laughlin managed to capture the fundamental dynamics of the  $\nu = 1/3$  state with his succinct trial wavefunction [95]

$$\Psi_{1/\eta} = \prod_{j < k} (z_j - z_k)^\eta \exp\left(-\frac{1}{4} \sum_j |z_j|^2\right) \quad (8.1)$$

where  $\eta$  is an odd integer ( $\eta = 3$  in the case of  $\nu = 1/3$ ), and  $z_j = x_j + iy_j$  is the position of the  $j^{\text{th}}$  electron expressed as a complex number in units of the magnetic length  $l_B$ .

The Laughlin wavefunction has several important attributes. Key among these, in the thermodynamic limit of many electrons it fixes the electron density at  $n = 1/2\pi\eta l_B^2$ . This is consistent with the notion that  $1/\eta = \nu = \phi_0 n/B$  (see Eq. 6.19). Equally important is how  $\Psi_{1/\eta}$  vanishes as any two electrons approach one another. In this way it acts to minimize the Coulombic potential energy of the system. Meanwhile, a requirement of any wavefunction describing a Fermionic system is that it be antisymmetric under exchange of any two particles and indeed given that  $\eta$  is odd  $\Psi_{1/\eta}$  meets this criterion in accordance with Fermi-Dirac statistics. Perhaps the most intriguing feature of Laughlin's solution, however, is its fractionally charged excitations. In the case of  $\nu = 1/3$  quasiparticles excitations have charge  $e^* = e/3$ !

Laughlin’s ansatz garnered much success not only in its description of the FQHE at  $\nu = 1/3$  but at other fractional fillings as well. Examples include observations of FQHEs at  $\nu = 1/5$  and  $1/7$  that seem well described by  $\Psi_{1/\eta}$  for  $\eta = 5$  and  $7$ , respectively. Transforming  $\Psi_{1/\eta}$  via the particle-hole symmetry of the LL yields an expression for states at  $\nu = 1 - 1/\eta$ , which appears to describe observed FQHEs such as  $\nu = 2/3$  and  $4/5$ . Moreover, taking the Zeeman splitting into consideration, Laughlin’s expression also anticipates several observed FQHEs in the upper spin branch of the lowest LL (i.e. between  $\nu = 1$  and  $2$ ). Yet many quantized fractional filling factors remained unexplained.

Building upon Laughlin’s work, other theorists—in particular, Haldane [96] and Halperin [97]—developed a picture of  $\nu = 1/3$  quasiparticles condensing to form incompressible fluids at fractions such as  $\nu = 2/5$  and  $2/7$  whose quasiparticles, constrained by fractional statistics, in turn condensed to form new incompressible modes at additional fractions and so on. This *quasiparticle-hierarchy* (QPH), while complicated, successfully included all observed odd-denominator FQH states.

### 8.1.2 Composite Fermions

In 1989, Jainendra Jain presented an alternative framework for understanding the FQHE [98, 99]. By recasting the problem in terms of new particles, Jain transformed the picture of many strongly interacting electrons in a large magnetic field into one of many weakly interacting quasiparticles in a small magnetic field. The novel quasiparticle, dubbed the *composite fermion* (CF), consists of an even number  $2m$  of magnetic flux quanta attached to an individual electron. By “capturing” flux quanta,  $^{2m}$ CFs experience a much reduced *effective magnetic field*

$$B^* = B - 2mn\phi_0, \tag{8.2}$$

where  $m$  is an integer,  $n$  is the usual electron density, and  $\phi_0$  is the flux quantum introduced in Section 6.4. We may likewise define<sup>1</sup> an effective filling factor  $\nu^* = \phi_0 n / B^*$ , from which we have the relationship

$$\nu = \frac{\nu^*}{2m\nu^* \pm 1}. \quad (8.3)$$

In this way, Jain related fractional values of  $\nu$  corresponding to FQH states of electrons to integral values of  $\nu^*$  corresponding to IQH states of CFs.

As an example, let us consider  $\nu = 1/3$  described by Laughlin's wavefunction  $\Psi_{1/3}$ . At this LL filling, a 2DES of density  $n$  requires a field  $B = \phi_0 n / \nu$ . We may recast the problem in terms of <sup>2</sup>CFs (i.e.  $m = 1$ ). Each <sup>2</sup>CF consists of two flux quanta bound to an electron, which experiences an effective field  $B^* = B - 2n\phi_0$ . These <sup>2</sup>CFs have an effective filling factor  $\nu^* = \phi_0 n / B^* = \nu / (1 - 2\nu) = 1$ . That is, we may think of the  $\nu = 1/3$  FQHE resulting from strongly interacting electrons as the  $\nu^* = 1$  IQH state produced by noninteracting <sup>2</sup>CFs.

Equation 8.1 provides wavefunctions for both  $\nu = 1$  and  $1/3$ , which correspond to  $\eta = 1$  and  $3$ , respectively. That is,

$$\Psi_{\nu=1/3} = \prod_{j < k} (z_j - z_k)^3 \exp \left( -\frac{1}{4} \sum_j |z_j|^2 \right) \quad (8.4)$$

and

$$\Phi_{\nu^*=1} = \prod_{j < k} (z_j - z_k) \exp \left( -\frac{1}{4} \sum_j |z_j|^2 \right). \quad (8.5)$$

It follows that

$$\frac{\Psi_{\nu=1/3}}{\Phi_{\nu^*=1}} = \prod_{j < k} (z_j - z_k)^2. \quad (8.6)$$

The right-hand side of Eq. 8.6 is a special case of the *Jastrow factor*, which relates Laughlin's FQH wavefunctions to Jain's integral  $\nu^*$  CF wavefunctions:

---

<sup>1</sup>Beware that the symbol  $\nu^*$  is overloaded in this thesis. In this chapter,  $\nu^*$  refers to the CF effective filling factor. In Chapter 7,  $\nu^*$  refers to the fractional part of  $\nu$ .

$$\frac{\Psi_{\nu^*/(2m\nu^*\pm 1)}}{\Phi_{\nu^*}} = \prod_{j < k} (z_j - z_k)^{2m}. \quad (8.7)$$

Interestingly, binding a pair of flux quanta to each electron is tantamount to modulating the collective wavefunction by the factor  $\prod_{j < k} (z_j - z_k)^2$ . Combining this transformation with that of the particle-hole symmetry of each LL, produces a hierarchy of fractions that includes nearly all observed odd-denominator FQH states.

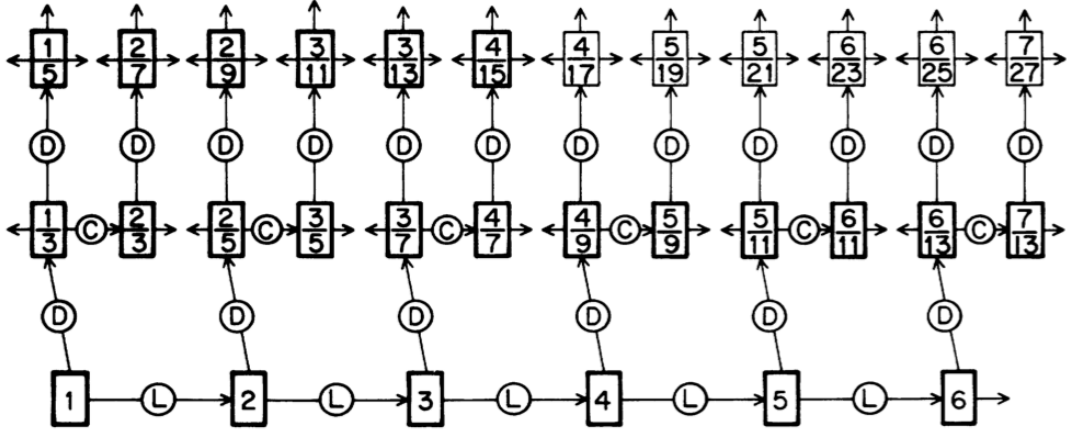


Figure 8.1: Partial hierarchy of FQH states generated from IQH states of CFs. Reprinted with permission from J.K. Jain and V.J. Goldman, *Phys. Rev. B* **45**, 1255 (1992). Copyright 1992 by the American Physical Society.

In Fig. 8.1 we reproduce a diagram from Jain and Goldman [100] showing a partial hierarchy of FQH states generated from IQH states of CFs. The  $L$  operators of the lowest level represent adding a filled LL to the system of CFs. The  $D$  operators connecting different levels correspond to multiplication by the Jastrow factor  $\prod_{j < k} (z_j - z_k)^2$ ; that is, the attachment of two flux quanta to each electron. And the  $C$  operators of the middle level indicate particle-hole transformations. Incidentally, when originally published in 1992, only those states in thick boxes had been observed experimentally. Since that time, all but  $\nu = 7/27$  has been observed [101], further reinforcing the validity of the model.

The CF hierarchical approach is far simpler and intuitive than the QPH scheme built upon excitations of the Laughlin states. But what are we to make of these CFs?

Are they simply an abstraction, a mere mathematical trick? To the contrary, a great deal of theoretical [102] and experimental [103, 104] evidence supports the existence of bona fide Fermi surfaces corresponding to CFs in this high-field regime. Specifically, consider the situation at  $\nu = 1/2$  where  $B^* = 0$  and  $\nu^* \rightarrow \infty$  for  ${}^2$ CFs. Here we have a compressible system of CFs in zero effective magnetic field. Experimental work includes transport studies of the activation energies [105] along with observations of resonances of surface acoustic waves [106] of FQH states around  $\nu = 1/2$ . The results of these investigations are consistent with a single-particle picture with a cyclotron energy gap opening as  $\nu$  deviates from half filling. Further support derives from thermopower studies pioneered by Ying et al. [40], and refined by work done for this thesis described later in this chapter.

This picture of noninteracting CFs has its limits, however. Several fragile odd-denominator FQH states including  $\nu = 4/11, 5/13, 7/11, 4/13, 6/17$ , and  $5/17$  cannot be explained as IQH states of CFs. These states, whose early observations [107] took the form of distortions in the main CF IQHE series, are believed to be the product of weak CF-CF interactions [108]. If this interpretation proves correct, these states may be regarded as the FQHE of CFs. In the next chapter we address another FQH state also believed to result from CF-CF interactions. In the case of the even-denominator state at  $\nu = 5/2$ , however, the putative nature of the CF coupling is even more surprising and exciting.

### 8.1.3 Wigner Crystal

For the sake of completeness, it is worth addressing what occurs in the 2DES in the extreme quantum limit of low disorder, high magnetic fields, and low temperatures. In this limit, the electrons become pinned due to their mutual electrostatic repulsion forming a solid known as the *Wigner crystal* (WC) [109, 3]. We may crudely understand this phenomenon as a consequence of the magnetic length  $l_B \equiv \sqrt{\hbar/|eB|}$  becoming much smaller than the average distance between electrons thereby localizing electrons at the sites of a triangular lattice [110, 111]. Experimentally, we observe

a longitudinal resistance  $R_{xx}$  that diverges as  $T \rightarrow 0$  and, interestingly, a transverse resistance  $R_{xy}$  that behaves like that of a classical metal; that is,  $R_{xy} = B/ne$ .

The competition between the FQHE and the WC has garnered significant attention [112, 113, 3]. At the lowest experimentally accessible temperatures the FQH liquid is the preferred configuration at  $\nu = 1/5$ . Adjusting the filling factor to slightly above or below  $\nu = 1/5$  causes the 2DES to enter an insulating phase as evidenced by the divergence of  $R_{xx}$ . For this reason, the insulating phase, believed to be the WC, is said to be *reentrant* about  $\nu = 1/5$ .

## 8.2 Thermopower in the FQH Regime

While most theoretical work on transport within the FQH regime focuses on electrical conductivity/resistivity, important analyses have been presented on the thermoelectric response of an interacting 2DES [114, 8, 115, 116, 117, 118, 93, 119, 120, 121]. Most of these analyses are performed within the CF picture of FQH physics. Within that picture, CFs are formed by attaching an even number of magnetic flux quanta to each electron. We have seen how this allows us to transform the difficult problem of strongly interacting electrons in a large magnetic field into the more tractable problem of weakly interacting CFs in a much smaller magnetic field. In this way we are able to understand the FQHE as the IQHE of CFs. Likewise, thermopower in the FQH regime can largely be understood in terms of CFs, in analogy with the IQH regime.

Much of the phenomenology of thermopower encountered in the IQH regime is common to the FQH regime. Key among these, as argued [8] by Cooper et al., is that for sufficiently weak impurity scattering the familiar thermopower-entropy relation

$$S^d = -\mathcal{S}/ne, \tag{8.8}$$

holds in the presence of electron-electron interactions. The question therefore arises as to what qualifies as “sufficiently weak” disorder. Cooper et al. admit that this

condition is ambiguous but do offer some guidance. A necessary but insufficient condition is that the electrical and thermoelectric conductivity tensors must be nearly off-diagonal such that the thermopower tensor is nearly diagonal. That is, we require that  $\sigma_{xy} \gg \sigma_{xx}$  and  $\epsilon_{xy} \gg \epsilon_{xx}$ . We must also be aware that Eq. 8.8 assumes the 2DES behaves as a fluid<sup>2</sup>. In Chapter 9 we will discuss solid phases of the 2DES, similar to the Wigner crystal, where Eq. 8.8 may not apply. Finally, in the case of  $B^* = 0$ , energy-dependent scattering of CFs can result in a correction to Eq. 8.8, which we discuss below.

In this section we will tour the thermopower of CFs in a manner that parallels that of the noninteracting 2DES in the previous chapter. We begin at  $B^* = 0$  where diffusion thermopower behaves similar to that of noninteracting electrons at  $B = 0$ . We then anticipate the thermopower in the vicinity of FQH states that are understood as IQH states of CFs. Using an extension of the counting argument introduced in Section 7.4, we compute the entropy per CF in order to derive the entropic thermopower in the FQH regime in the absence of disorder. Finally, we discuss the basic effects that disorder has on the diffusion thermopower in the FQH regime.

### 8.2.1 CFs at $B^* = 0$

When  $B^*$  is sufficiently small, the CFs are in a regime analogous to that of electrons where  $\hbar\omega_c \ll \Gamma$  such that disorder-broadened LLs cannot be resolved and a Fermi surface exists [102]. Therefore, one would expect the thermoelectric response of, say, <sup>2</sup>CFs at  $\nu = 1/2$  to be qualitatively similar to that of electrons at zero field. Indeed, there is strong theoretical support for this [8, 115]. Specifically, Cooper et al. showed [8] that at sufficiently low temperatures, the longitudinal diffusion thermopower at  $\nu = 1/2$  is given by the Mott-like expression

$$S_{CF}^d = -\frac{\pi k_B^2 m_{CF}}{6\hbar^2 e} (1 + p_{CF}) \frac{T}{n}, \quad (8.9)$$

---

<sup>2</sup>More specifically, Eq. 8.8 is not valid for an interacting electron system with a nonvanishing shear modulus [8].

where  $m_{CF}$  is the CF effective mass,  $p_{CF}$  is the CF scattering parameter, and  $n$  is the density of the 2DES.

As expected, Eq. 8.9 strongly resembles that for electrons at zero field:

$$S^d = -\frac{\pi k_B^2 m^*}{3\hbar^2 e} (1 + p) \frac{T}{n}. \quad (8.10)$$

One way in which Eq. 8.9 differs from Eq. 8.10 is that the factor of 3 in the denominator is replaced by a factor of 6. This follows from the assumption of complete spin polarization of the CFs. In the absence of spin polarization, additional entropy would result in an enhancement of  $S_{CF}^d$ . Another important difference is that the CF scattering parameter  $p_{CF}$  replaces the zero-field electron scattering parameter  $p$ . Recall that a nonvanishing scattering parameter yields a correction factor to the thermopower-entropy relation such that  $S^d = -\mathcal{S}(1 + p)/ne$ . Cooper et al. note [8] that scattering of CFs in modulation-doped GaAs heterostructures is only weakly energy dependent with  $p_{CF} \simeq 0.13$  being one theoretical estimate [122]. This is significantly smaller than typical values of  $p$ , which are theoretically  $0.5 \lesssim p \lesssim 1.5$  for these material systems [33].

A critical difference between the low temperature diffusion thermopower of CFs at  $B^* = 0$  and that of electrons at  $B = 0$  is that the CF effective mass  $m_{CF}$  replaces the role of the GaAs conduction-band mass  $m^* = 0.067m_0$  (with  $m_0$  the bare electron mass). The value of  $m_{CF}$ , which derives entirely from electron-electron interactions, is often much larger than  $m^*$  [102, 105, 115]. The larger mass of the CFs results in a larger entropy per carrier, and hence, larger diffusion thermopower than that of zero-field electrons.

Equation 8.9 applies whenever we have noninteracting CFs at  $B^* = 0$  [8, 118]. The values for  $m_{CF}$  and  $p_{CF}$  will vary, however. Both  ${}^2\text{CFs}$  and  ${}^4\text{CFs}$  are believed to have values of  $m_{CF}$  that scale with magnetic field as  $m_{CF} = \alpha\sqrt{B}$ , where the proportionality constant is predicted<sup>3</sup> [102] to be  $\alpha = 0.085m_e \text{ T}^{-1/2}$  in the case of

---

<sup>3</sup>A slightly higher coefficient of  $\alpha = 0.089m_e \text{ T}^{-1/2}$  is obtained if the exact diagonalization results of Morf et al. [123] are used to compute the CF mass from the energy gap of the  $\nu = 1/3$  FQH state.

${}^2\text{CFs}$ . Also note that  $\alpha$  for  ${}^4\text{CFs}$  is expected to be a factor of 2 larger than that for  ${}^2\text{CFs}$  [124]. An important feature of Eq. 8.9, however, is that the density  $n$  that appears in the denominator refers to that of *all* electrons, including those in any filled LLs, which do not form CFs [8]. This is perhaps counterintuitive and has led to confusion in the literature<sup>4</sup>. Given the analogy with electrons at zero field, one might expect to see the CF density  $n_{CF}$  in Eq. 8.9 instead of the total electron density  $n$ . In the case of CFs at  $\nu = 1/4, 1/2, \text{ or } 3/4$  this distinction is moot since the two values are equal. However, in the case of, for example,  ${}^2\text{CFs}$  at  $\nu = 3/2$  the distinction is important since  $n_{CF} = n/3$ .

The apparent breakdown at  $\nu = 3/2$  of our analogy with zero-field electrons due to the appearance of  $n$  rather than  $n_{CF}$  in Eq. 8.9 was reconciled by Karavolas et al. [118]. The 2DES at  $\nu = 3/2$  may be treated as two gases conducting in parallel. One gas is comprised of electrons that fill the lower spin branch of the  $N = 0$  LL. The other gas is comprised of electrons that halfway fill the upper spin branch of the  $N = 0$  LL and form  ${}^2\text{CFs}$ . The diffusion thermopower of such a two-gas system can be expressed as (see Eq. 3.22)

$$S_{CF}^d(3/2) = \frac{\sigma_1}{\sigma_1 + \sigma_{1/2}} S_1^d + \frac{\sigma_{1/2}}{\sigma_1 + \sigma_{1/2}} S_{1/2}^d, \quad (8.11)$$

where  $\sigma_1$  and  $S_1^d$  are the conductivity and thermopower of the electron gas filling the lower spin branch, and  $\sigma_{1/2}$  and  $S_{1/2}^d$  are the conductivity and thermopower of the  ${}^2\text{CF}$  gas. We know  $S_1^d = 0$  because the entropy of the filled spin branch is zero. By analogy with zero-field electrons (Eq. 3.16), the low-temperature entropy per area of the  ${}^2\text{CF}$  gas is

$$\mathcal{S}_{CF} = \frac{\pi k_B^2 m_{CF}}{6\hbar^2} T, \quad (8.12)$$

where the CF mass  $m_{CF}$  replaces the electron effective mass  $m^*$  and a factor of 6 replaces the factor of 3 in the denominator due to the assumption of complete spin

---

<sup>4</sup>According to Cooper et al. [8], the analysis of Ying et al. [40] is incorrect in the case of  ${}^2\text{CFs}$  at  $\nu = 3/2$  where they have replaced the total electron density  $n$  in Eq. 8.9 with the CF density  $n_{CF}$ .

polarization. Invoking the relationship between entropy and diffusion thermopower for a simple metal, we have

$$S_{1/2}^d = -(1 + p_{CF}) \frac{\mathcal{S}_{CF}}{en_{CF}} = -\frac{\pi k_B^2 m_{CF}}{6\hbar^2 e} (1 + p_{CF}) \frac{T}{n_{CF}}, \quad (8.13)$$

where  $n_{CF} = n/3$  is the density of our  ${}^2\text{CF}$  gas with  $n$  the total density of our two-gas system. Note that unlike Eq. 8.9, Eq. 8.13 fully accommodates an analogy with spinless electrons at zero field since  $n_{CF}$  replaces  $n$  in the denominator. Finally, we have that  $\sigma_{1/2} = \sigma_1/2$  allowing us to recover Eq. 8.9 for the special case of  $\nu = 3/2$ :

$$S_{CF}^d(3/2) = \frac{1}{3} S_{1/2}^d = -\frac{\pi k_B^2 m_{CF}}{6\hbar^2 e} (1 + p_{CF}) \frac{T}{n}. \quad (8.14)$$

The above analysis reveals that for  ${}^2\text{CFs}$  at  $\nu = 3/2$  a simple analogy with a zero-field Fermi gas is misleading, or at least incomplete. The correct picture must include the edge channel associated with the filled spin-split LL. This edge channel works in parallel with the compressible CFs in the bulk to conduct the drift current required to cancel the thermoelectric diffusion current produced by a temperature gradient. It is straightforward to extend the above analysis to the case of  ${}^4\text{CFs}$  at  $\nu = 5/4$  and  $7/4$ .

We now comment on the current distribution within an interacting 2DES during a thermopower measurement. In Chapter 7 we described the distribution of diffusion and drift currents within a noninteracting QH system in response to a temperature gradient and thermoelectric field. We claimed that in the lowest LL, the current distribution resembled that of a classical 2DES, with a transverse diffusion current flowing along the edge of the sample and a compensating transverse drift current flowing uniformly through the bulk. Let us now consider the distribution at  $\nu = 1/2$  for a weakly disordered, strongly interacting 2DES. At this filling factor, we may treat our system as comprised of  ${}^2\text{CFs}$  at  $B^* = 0$ . Will the diffusion current that flows in response to a temperature gradient flow uniformly through the interior as it would for a 2DES at zero field? Or will it flow along the edge as it would for a noninteracting 2DES at  $\nu = 1/2$ ? The analysis of Cooper et al. [8] reveals an

intermediate situation with precisely half the diffusion current flowing along the edge and half flowing uniformly through the bulk. Since the compensating drift current flows entirely through the bulk, half of it will cancel locally in the case of  ${}^2\text{CFs}$  at  $\nu = 1/2$ . This results in a relative reduction in the magnitude of the circulating currents in the case of an interacting 2DES compared to a noninteracting 2DES during a thermopower measurement.

### 8.2.2 Entropic Model

An important consequence of  $S^d = -\mathcal{S}/ne$  holding for a disorder-free interacting 2DES is that the counting arguments we employed for the IQH regime (see Section 7.4) are also applicable for CFs. For instance, in the case of zero disorder, at CF filling factors  $\nu^* = N^* + 1/2$ , where  $N^* \geq 0$  is the number of filled CF LLs, the low-temperature diffusion thermopower assumes the universal values [115]

$$S^d(N^* + 1/2) = -\frac{k_B}{e} \frac{\ln 2}{N^* + 1/2}, \quad (8.15)$$

in analogy with an ideal noninteracting 2DES.

As an example, let us consider CFs at effective filling  $\nu^* = 3/2$  ( $N^* = 1$ ) in the absence of disorder. Equation 8.15 says  $S^d \approx -40 \mu\text{V/K}$ . Let us compare this to the thermopower of an ideal noninteracting 2DES at the same filling factor. From Eq. 8.3 we find that  ${}^2\text{CFs}$  at  $\nu^* = 3/2$  translate to both  $\nu = 3/8$  and  $\nu = 3/4$ . From the counting argument of Section 7.4 we know that for a disorder-free noninteracting 2DES at  $\nu < 1$  the low-temperature diffusion thermopower is

$$S^d \simeq \frac{k_B}{e\nu} [(1 - \nu) \ln(1 - \nu) + \nu \ln(\nu)]. \quad (8.16)$$

Thus we have  $S^d \approx -150 \mu\text{V/K}$  and  $-65 \mu\text{V/K}$  at  $\nu = 3/8$  and  $3/4$ , respectively. The thermopower magnitude for  ${}^2\text{CFs}$  is therefore reduced from that of noninteracting electrons; in the case of  $\nu = 3/8$  it is reduced by more than a factor of three! This reduction in thermopower reflects a reduction in entropy as a consequence of the

self-organization induced by Coulomb interactions.

Figure 8.2 demonstrates more generally how CF formation reduces diffusion thermopower. The figure compares the thermopower of CFs to that of noninteracting electrons as a continuous function of  $B$  for  $\nu < 1$  in the absence of disorder. These calculations are a generalization of the exercise in Section 7.4 where we determined the entropy per carrier of noninteracting electrons by counting states within LLs. Here we extend the exercise to include CFs. The calculations correspond to a 2DES with  $n = 1 \times 10^{11} \text{ cm}^{-2}$  at  $T = 200 \text{ mK}$ . The thick black curve represents  $S^d$  for a noninteracting 2DES, similar to that previously shown in Fig. 7.5. The blue solid curve represents  $S^d$  for  ${}^2\text{CFs}$  and the red dotted curve that for  ${}^4\text{CFs}$ . Several filling factors are labeled including where  $B^* = 0$  for either  ${}^2\text{CFs}$  ( $\nu = 1/2$ ) or  ${}^4\text{CFs}$  ( $\nu = 1/4$  and  $3/4$ ). All other minima of the CF curves correspond to integral CF effective fill-

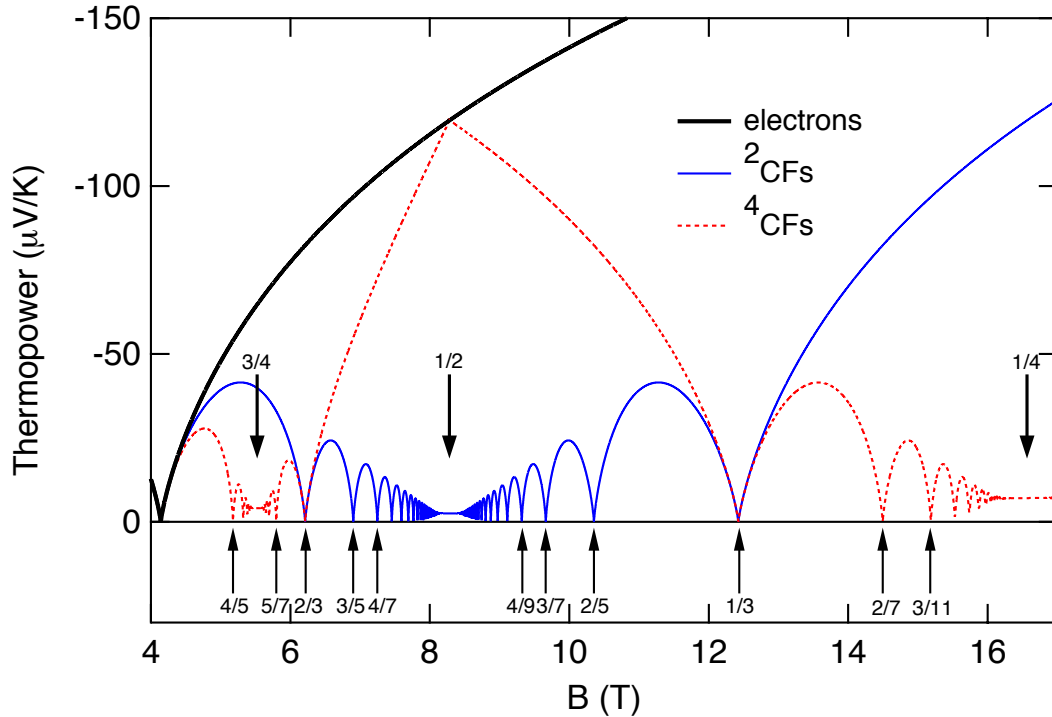


Figure 8.2: Disorder-free entropic thermopower of CFs in the lowest LL. The thick black curve corresponds to noninteracting 2D electrons. The blue solid curve corresponds to  ${}^2\text{CFs}$ . The red dotted curve corresponds to  ${}^4\text{CFs}$ . Calculation for 2DES with  $n = 1 \times 10^{11} \text{ cm}^{-2}$  at  $T = 200 \text{ mK}$ . Several filling factors are labeled.

ing factors, and hence, incompressible FQH states. Note that the complex within the  ${}^4\text{CF}$  curve about  $\nu = 3/4$  derives from states that are particle-hole conjugates of those about  $\nu = 1/4$ .

The diminished magnitude of the CF curves of Fig. 8.2, which are below the black curve everywhere, reflects the reduction in entropy achieved via the formation of CFs. Given the number of carriers is fixed and equal for all three curves, the figure reveals the relative magnitudes of the total system entropy. Moreover, given that  $T$  is also fixed and equal for all three curves, a reduction in entropy is tantamount to a reduction in energy. The system will therefore prefer the formation of  ${}^2\text{CFs}$  or  ${}^4\text{CFs}$  depending on the value of  $\nu$ . When  $1/3 \leq \nu \leq 2/3$ , the formation of  ${}^2\text{CFs}$  will minimize the system's energy. Alternatively, when  $\nu \leq 1/3$  or  $\nu \geq 2/3$ , the formation of  ${}^4\text{CFs}$  is preferred.

In Section 8.2.1 we argued that the diffusion thermopower of CFs at  $B^* = 0$  is proportional to  $m_{CF}$ . The calculations of Fig. 8.2 use the predicted [102] mass of  ${}^2\text{CFs}$  of  $m_{CF} = 0.085\sqrt{B}m_e$ . This yields  $m_{CF} = 0.24m_e$  at  $\nu = 1/2$  for the data in the figure. In the case of  ${}^4\text{CFs}$ , we introduce a factor of 2, as per [124]. This yields  $m_{CF} = 0.69m_e$  and  $0.40m_e$  at  $\nu = 1/4$  and  $3/4$ , respectively. There exists controversy [102, 105, 40, 115, 125] over the true value of  $m_{CF}$ . In the limit of zero disorder, the value of  $m_{CF}$  not only determines the magnitude of  $S^d$  at  $B^* = 0$  but also the upper limit on  $\nu^*$  where FQH states are resolved in the thermopower. For example, in the calculated curves of Fig. 8.2 we can resolve a minimum at  $\nu = 5/7$ , which corresponds to  $\nu^* = 2$  for  ${}^4\text{CF}$  holes. If we repeat the calculations with a sufficiently large  ${}^4\text{CF}$  mass, a minimum would no longer be seen at  $\nu = 5/7$ . In this context, the effect of increasing  $m_{CF}$  is equivalent to increasing the temperature.

### 8.2.3 Disorder

The disorder-free model of Fig. 8.2 is useful in that it represents a particular limiting behavior of diffusion thermopower. We have seen, however, that even a small amount of disorder dramatically alters our picture of transport. Indeed, in Chapter

6 we saw how disorder is a requirement for the observation of the IQHE. Away from  $B^* = 0$ , a small amount of disorder will reduce the magnitudes of the  $S_{xx}^d$  peaks from those of Fig. 8.2 in analogy with the IQH case. Equation 8.15 therefore provides an upper limit on the low-temperature diffusion thermopower of CFs at half-integer effective filling. Experimentally, this is useful since it suggests measured thermopowers at  $\nu^* = N^* + 1/2$  with magnitudes significantly exceeding that of Eq. 8.15 are attributable to some mechanism other than diffusion of the associated CFs. This could be the case, for example, if the disorder were so large that  $\Gamma$  were comparable to the Coulomb interaction energy such that CFs did not form; the system would consequently behave as a disordered noninteracting 2DES [102]. Alternatively, sufficiently high temperatures will result in phonon drag, which can also produce a thermopower that exceeds that of Eq. 8.15.

In Chapter 7 we introduced a generalized Mott formula that holds in the IQH regime at low temperatures given by

$$S_{ij}^d \simeq -\frac{\pi^2 k_B^2}{3e} \rho_{ik} \left[ \frac{d\sigma}{d\varepsilon} \right]_{kj} \Big|_{\varepsilon=\varepsilon_F} T. \quad (8.17)$$

Karavolas et al. demonstrated [115] that Eq. 8.17 is consistent with thermopower measured in the FQH regime—at least for  $S_{xx}^d$  measured by Bayot et al. [52] in a 2D hole gas at  $T = 169$  mK. It is well-known that the behavior of  $\rho$  and  $\sigma$  in vicinity of a FQH state resembles that of an IQH state; at sufficiently low temperatures, a plateau forms in  $\rho_{xy}$  and  $\sigma_{xy}$  while a minimum forms in  $\rho_{xx}$  and  $\sigma_{xx}$ . Therefore, Eq. 8.17 reveals that the thermopower of a FQH state will strongly resemble that of an IQH state. Moreover, it has been shown [2], in the weak-disorder regime, increasing disorder yields wider plateaus in  $\rho_{xy}$  and  $\sigma_{xy}$ . It follows from Eq. 8.17 that the width of the minima in  $S_{xx}^d$  will also increase within increasing disorder. Specifically, assuming  $\sigma_{xy} \gg \sigma_{xx}$ ,  $S_{xx}^d$  should vanish whenever a plateau in  $\sigma_{xy}$  occurs, be it due to single-particle physics or correlated phenomena.

### 8.3 Experimental Results at High Fields

The earliest experimental studies of the thermopower of the FQH regime include those by Zeitler et al. [126] and Bayot et al. [50]. These, and most subsequent experimental studies, have focused on phonon drag, which typically dominates over the diffusion contribution for high-mobility 2D systems formed in GaAs/AlGaAs heterostructures. As previously emphasized, this thesis is primarily concerned with the latter, more elusive contribution to thermopower. The diffusion thermopower of FQH states has been observed in 2D *hole* systems for  $T \lesssim 300$  mK [40, 52, 53], owing in part to the hole's larger effective mass<sup>5</sup> which translates into a larger density of states, and hence, larger entropy. At the same time, the highest mobilities achieved for 2D hole systems are far less than those of 2D electron systems<sup>6</sup>. Through a combination of fabrication and temperature calibration techniques that minimize undesirable phonon effects together with significant improvements in sample quality, we are able to measure the diffusion thermopower of electrons in the FQH regime at temperatures as high as  $T \sim 200$  mK with unprecedented resolution.

This section is outlined as follows. We begin by reviewing our experimental results at  $\nu = 3/2$  as a function of temperature. Our results are then compared to a previously reported experiment with 2D holes. As part of our analysis, we show that our measurements at  $\nu = 3/2$  are inconsistent with the disordered noninteracting model of Shirasaki et al., which was explored in Section 7.6. We then review our measurements of thermopower as a function of magnetic field in the FQH regime. These data are compared to measurements of the more familiar transport coefficient  $R_{xx}$ . Next, we consider traces of  $S_{xx}$  versus  $B$  for three temperatures in the upper spin branch of the  $N = 0$  LL to obtain a rough, but broad, sense of the temperature evolution of the thermopower in this regime. At the lowest experimentally accessible temperatures, the behavior of the thermopower is significantly altered by the appear-

---

<sup>5</sup>For example, the effective mass of the 2D holes in the thermopower study of Ying et al. is estimated to be  $m_h^* \approx 0.3m_0$ , where  $m_0$  is the bare electron mass [40]. This is a factor of about 4.5 larger than the effective mass of electrons in GaAs.

<sup>6</sup>For example, the mobility of the 2D holes in the thermopower study of Ying et al. (discussed below) is  $\mu_h \approx 7 \times 10^5$  cm<sup>2</sup>/Vs [40].

ance of fluctuations that cause  $S_{xx}$  to frequently change sign as a function of  $B$ . We present a possible explanation for this behavior that invokes the phenomenology of universal conductance fluctuations (UCFs). We conclude with a comparison of the measured  $S_{xx}$  versus  $B$  to a calculation based upon our disorder-free entropic model and attempt to explain the discrepancies between the two in terms of the effects of disorder.

### 8.3.1 $S_{xx}$ vs $T$ at $\nu = 3/2$

Figure 8.3 shows thermopower measured as a function of temperature at  $B = 8.1$  T where  $\nu = 3/2$ . The green triangles are acquired from mesa 2 of diving board A

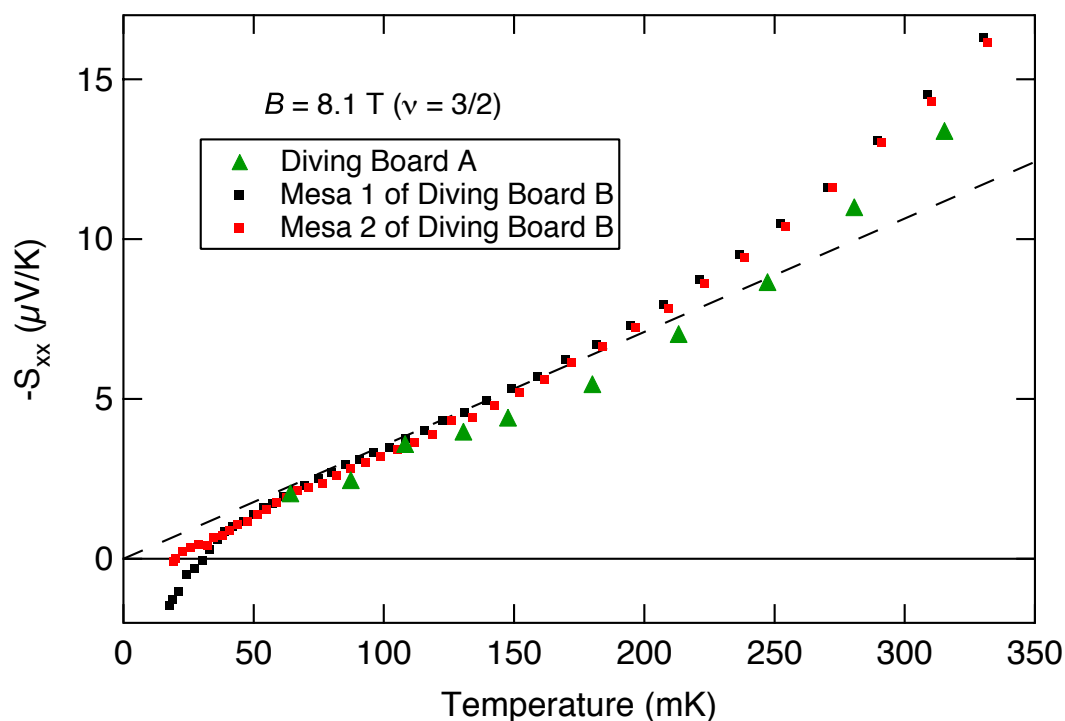


Figure 8.3: Longitudinal thermopower  $S_{xx}$  vs temperature  $T$  at  $\nu = 3/2$ . The squares are measured using diving board B while the triangles are from diving board A. The dashed line is a linear fit to the data acquired from diving board B for  $T \in [50, 200]$  mK that is forced through the origin. Reprinted with permission from W.E. Chickering, J.P. Eisenstein, L.N. Pfeiffer, and K.W. West, *Phys. Rev. B* **87**, 075302, (2013). Copyright 2013 by the American Physical Society.

using our quasi-DC protocol (see Section 4.1.2). The squares are acquired from the two 2DES mesas of diving board B using low frequency AC lock-in detection (see Section 4.2.3). All three data sets are included to demonstrate the consistency of our measurements across 2DESs and measurement techniques. Indeed, in the case of the diving board B measurements, for  $T \gtrsim 40$  mK the thermopower data extracted from the two independent 2DES mesas are virtually identical. Below  $T \approx 40$  mK the two data sets do differ and we address this later in the section.

Figure 8.3 demonstrates that  $S_{xx}$  at  $\nu = 3/2$  is linear in  $T$  for  $50 \text{ mK} \lesssim T \lesssim 200 \text{ mK}$ . This is consistent with the Mott-like thermopower behavior that Eq. 8.9 represents for CFs at  $B^* = 0$ . For  $T \gtrsim 200$  mK the thermopower exceeds linear temperature dependence, owing to the increasing importance of phonon drag. Recall that we observe a similar cross-over from linear to super-linear temperature dependence at  $B = 0$  (see Fig. 4.6). Transitioning from diffusion- to phonon-drag-dominated regimes at a temperature comparable to  $T \sim 200$  mK is typical of diving-board-style thermopower experiments with both 2D electrons and holes [41, 40, 50, 52, 42, 53].

Nonetheless, one must consider the possibility of finite temperature corrections to our Mott formula contributing to the nonlinearity above  $T \approx 200$  mK. To investigate this, let us estimate a lower bound on the Fermi energy of  ${}^2\text{CFs}$  at  $\nu = 3/2$  and compare this to the thermal broadening. The Fermi energy is given by

$$\varepsilon_F^*(3/2) = n_{CF} * \left( \frac{dn_{CF}}{d\varepsilon} \right)^{-1} \geq \frac{n}{3} \frac{\pi \hbar^2}{m_{CF}}, \quad (8.18)$$

where we use the fact the  $2/3$  of electrons in the lower spin branch of the  $N = 0$  LL do not form CFs and we use the density of states of spin *unpolarized* CFs to establish a lower bound. For the same reason, we choose  $m_{CF} = 1.7m_e$ , which is the largest theoretical [127] and experimental [125, 128] estimate of the CF mass at  $B = 8.1$  T. We conclude that  $\varepsilon_F^*(3/2)/k_B \gtrsim 1.6$  K. It therefore seems unlikely that finite temperature corrections to Eq. 8.9 contribute significantly to the nonlinearity in  $-S_{xx}$  versus  $T$  for  $T < 350$  mK.

Meanwhile, for  $T \lesssim 60$  mK only data from diving board B are available. Figure

8.3 reveals that for  $T \lesssim 40$  mK data from the independent 2DES mesas differ and individually deviate from linear temperature dependence. Indeed, in the case of mesa 1 a sign reversal is even observed at  $T \sim 30$  mK. We attribute this behavior to effects analogous to universal conductance fluctuations (UCFs) in disordered mesoscopic conductors [129, 130, 131]. In this low-temperature regime we find that  $S_{xx}$  fluctuates aperiodically with magnetic field near  $\nu = 3/2$  with the exact field dependence being very sensitive to the thermal history of the sample. These behaviors are consistent with the phenomenology of UCFs. We will return to this topic when we review our measurements of  $S_{xx}$  as a function of magnetic field.

The dashed line in Fig. 8.3 is a linear fit to the data from diving board B in the range  $T \in [50, 200]$  mK that is forced through the origin. Equation 8.9 corresponds to this fit for  $m_{CF} = 1.7m_e$  and  $p_{CF} = 0$ . Of course, assuming a larger value of  $p_{CF}$ , such as the previously mentioned theoretical estimate [122]  $p_{CF} \simeq 0.13$ , will reduce the inferred value of  $m_{CF}$ . For simplicity, we ignore energy dependent scattering effects in our analysis and set  $p_{CF} = 0$ . This estimate of  $m_{CF}$  is about 7 times larger than the predicted [102] value of  $m_{CF} = 0.085\sqrt{B[T]}m_e = 0.24m_e$  at  $B = 8.1$  T. Interestingly, but perhaps coincidentally,  $m_{CF} = 1.7m_e$  instead agrees well with a recent theoretical estimate of the so-called *CF polarization mass* [127]. However, it seems unlikely that the polarization mass, which depends on the full depth of the Fermi sea rather than just its surface properties, plays an important role in the thermoelectric response of the system.

While the origin of the discrepancy between theory and experiment regarding  $m_{CF}$  at  $\nu = 3/2$  is not known, several points are worth considering. On the theoretical side, the above estimates only apply to an infinitely thin, disorder-free 2DES at magnetic fields large enough that LL mixing is negligible. In general, violating any of these approximations tends to reduce the energy gap of FQH states. Since in the CF model these gaps are inversely proportional to  $m_{CF}$ , inclusion of these non-idealities would increase the theoretical estimates of the mass and thereby reduce the disagreement between theory and experiment. On the experimental side, the spin polarization and the value of  $p_{CF}$  at  $\nu = 3/2$  are obvious sources of uncertainty. For example, if the

spins were completely unpolarized and  $p_{CF} \sim 1$  like  $p$  at  $B = 0$ , then the value of  $m_{CF}$  inferred from our thermopower data would be reduced by a factor of 4. However, this scenario seems unlikely since spin polarization experiments [132] at  $\nu = 3/2$  indicate close to maximum polarization at  $B = 8$  T and, as previously mentioned, theoretical estimates [122] of  $p_{CF}$  are small (e.g.  $p_{CF} \approx 0.13$ ).

### 8.3.2 Comparison to Experiment on 2D Holes

It is worth comparing our results to those from a similar thermopower experiment performed on a 2D *hole* system, albeit in a lower density and mobility sample than ours. In Fig. 8.4 we reproduce the experimental results of Ying et al. [40]. They measure the longitudinal thermopower of 2D holes in a GaAs/AlGaAs heterostructure with a density of  $p_s = 6.5 \times 10^{10} \text{ cm}^{-2}$  and mobility of  $\mu_h \approx 7 \times 10^5 \text{ cm}^2/\text{Vs}$ .

Before discussing their results, we quickly review a few points regarding their experimental methods. They use a diving board technique similar to ours, although, unlike us, they use a traditional temperature calibration scheme that utilizes two carbon-paint thermometers attached to the sample. Interestingly, they do not encounter thermal time constants on the scale of those suffered by our diving board A (see Section 4.1.2 and Appendix D) and are able to measure thermovoltages using low frequency AC lock-in detection. Meanwhile, like our devices, their diving board sample is affixed to the cold finger of a cryostat using indium solder. And like us, they are not able to reliably measure  $S_{xx}$  at  $B = 0$ . We suspect this is related to the superconducting phase of the indium solder joint (see Section 4.1.3). Their solution is to measure at  $B = 0.2$  T.

Figure 8.4 shows  $S_{xx}$  versus  $T$  in a log-log plot for 2D holes at  $\nu = 1/2$  and  $B = 5.6$  T,  $\nu = 3/2$  and  $B = 1.9$  T, and  $B \approx 0$ . All three data sets follow similar temperature dependence. For  $T \lesssim 100$  mK,  $S_{xx}$  is approximately linear in  $T$  and considered diffusion-dominated. For  $T \gtrsim 100$  mK,  $S_{xx}$  is approximately proportional to  $T^3$  and considered phonon-drag-dominated. The data at  $\nu = 1/2$  and  $B = 5.6$  T for  $T \lesssim 100$  mK is consistent with Eq. 8.9 with  $m_{CF} \approx 1.3m_e$  and  $p_{CF} = 0$ . Given

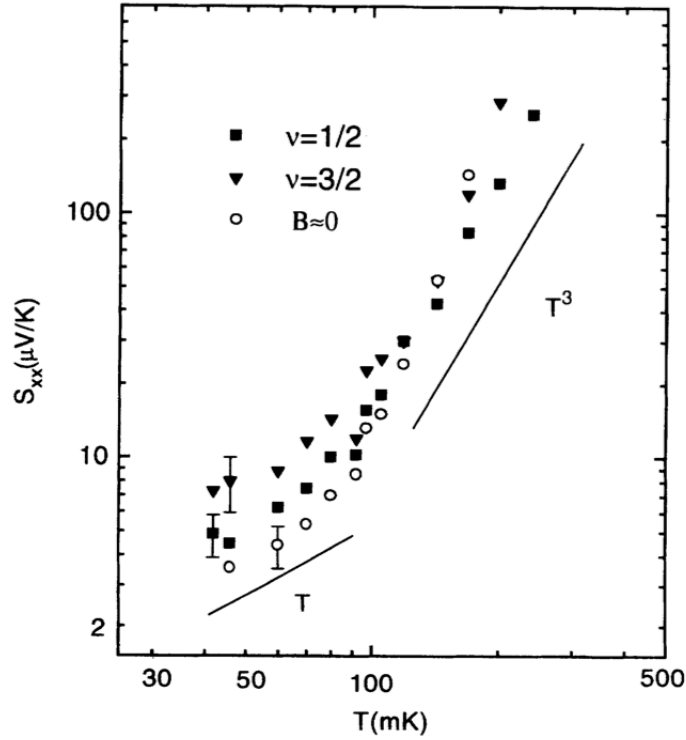


Figure 8.4: Measured thermopower versus temperature in a 2D hole system at  $\nu = 1/2$  and  $B = 5.6$  T,  $\nu = 3/2$  and  $B = 1.9$  T, and  $B \approx 0$ . Reprinted with permission from X. Ying, V. Bayot, M.B. Santos, and M. Shayegan, *Phys. Rev. B* **50**, 4969 (1994). Copyright 1994 by the American Physical Society.

that  $m_{CF}$  is expected to scale as  $\sqrt{B}$ , this would imply  $m_{CF} \approx 1.6m_e$  at  $B = 8$  T, which is roughly consistent with our  $\nu = 3/2$  data at that field. Meanwhile, the data at  $\nu = 3/2$  and  $B = 1.9$  T for  $T \lesssim 100$  mK is consistent with Eq. 8.9 with  $m_{CF} \approx 1.9m_e$  and  $p_{CF} = 0$ . This would imply  $m_{CF} \approx 3.9m_e$  at  $B = 8$  T. Naively, this is inconsistent with both our results and their measurements at  $\nu = 1/2$ . Bear in mind, however, that we are assuming the CF spins are always fully polarized. We can reconcile these results if we modify this assumption and presume the Ying et al. sample is fully unpolarized at  $\nu = 3/2$  and  $B = 1.9$  T. In this case, all three inferred measurements of  $m_{CF}$  are roughly consistent after accounting for differences in carrier density and magnetic field.

### 8.3.3 Comparison to Noninteracting Disordered Model

Our measurements are therefore consistent with those of 2D holes by Ying et al. in the context of CF diffusion thermopower, given certain presumptions regarding the spin polarizations of the measured systems. However, as previously mentioned, the inferred values of  $m_{CF}$  are about 7 times larger than those originally predicted [102]. At the same time, in Section 7.6 we described the disordered noninteracting model of Shirasaki et al., which also predicts a linear temperature dependence for the low-temperature diffusion thermopower at half-integer filling factors. Let us therefore convince ourselves that our measurements at  $\nu = 3/2$  are *not* consistent with this noninteracting model.

Adjusting<sup>7</sup> the low-temperature model of Shirasaki et al. to account for electron spin and plugging in the parameters<sup>8</sup> of our 2DES, yields  $S_{xx}^d \approx -95.5 \mu\text{V}/\text{K}^2 \cdot T$  at  $\nu = 3/2$ . For example, at  $T = 200$  mK, their model predicts  $S_{xx}^d \approx -19 \mu\text{V}/\text{K}$ . This is more than 2.5 times the measured value shown in Fig. 8.3. The reduction in magnitude of the measured thermopower at  $\nu = 3/2$  compared to the disordered noninteracting model of Shirasaki et al. is consistent with our picture of entropy reduction via CF formation.

### 8.3.4 $S_{xx}$ vs $B$ in FQH Regime

Figure 8.5 (a) shows an example trace of  $-S_{xx}$  versus  $B$ . These data are acquired via mesa 1 of diving board B (the mesa closest to thermal ground; see Fig. 4.8) using AC lock-in detection. Note that similar results are acquired from mesa 2. These data are confined to  $B \lesssim 12$  T due to the limitations of our magnet. Given the density

---

<sup>7</sup>Recall that the Shirasaki model ignores electron spin. At sufficiently high magnetic fields, we can adjust their model for comparison to our experimental results by substituting  $B/2$  for the experimental magnetic field  $B$ . To see this, recall that the  $|S_{xx}^d|$  maxima are linear in  $B$  for all  $T$  within their model. This is a reflection of the linear increase in the degeneracy of LLs. For the same reason, if one includes spin-splitting, the  $|S_{xx}^d|$  maxima—now associated with half-filled *spin-split* LLs—must also be linear in  $B$ . Moreover, the linear dependence of  $|S_{xx}^d|$  maxima versus  $B$  of the model with spin-splitting would be precisely half that of the model without spin-splitting. The end result is equivalent to adjusting  $B$  by a factor of 2.

<sup>8</sup>The following parameter values are used:  $n = 2.9 \times 10^{11} \text{ cm}^{-2}$ ,  $\tau_q = 3.0$  ps,  $\tau_m = 1.2$  ns, and  $p = 0.9$ .

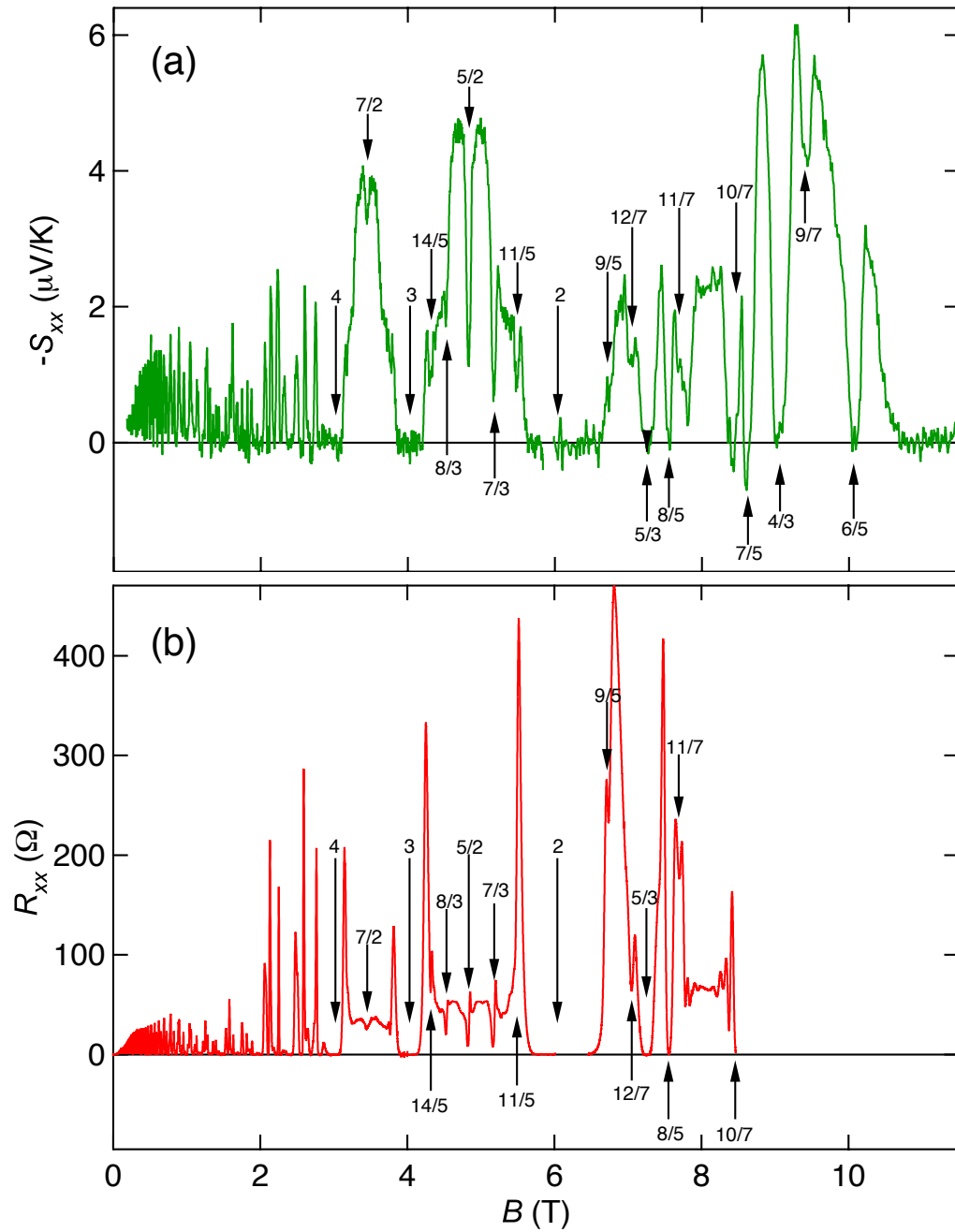


Figure 8.5: Thermopower and resistance of FQH states at  $T = 60$  mK. (a) The negative longitudinal thermopower  $-S_{xx}$  versus magnetic field  $B$ . (b) The longitudinal resistance  $R_{xx}$  versus magnetic field  $B$ . Several filling factors that coincide with a minimum in  $-S_{xx}$  and/or  $R_{xx}$  are labeled.

of our 2DES,  $n = 2.9 \times 10^{11} \text{ cm}^{-2}$ , this translates to  $\nu \gtrsim 1$ . The measurements are time averaged thermovoltage measurements that are scaled by the temperature difference of the voltage probes (see Section 4.2.3). In this example, the average temperature is  $T = 60 \text{ mK}$  such that the signatures of several FQH states are well resolved. Importantly, the broad zeros measured at integer filling factors are genuine. That is, no spurious signals are added or subtracted demonstrating that extrinsic sources of thermopower in our measurement circuit are negligible. For comparison, the longitudinal resistance  $R_{xx}$  versus  $B$ , also measured at  $T = 60 \text{ mK}$ , is included in Fig. 8.5 (b). (Unfortunately,  $R_{xx}$  at  $B \gtrsim 8.5 \text{ T}$  are not available at this temperature.) Several filling factors corresponding to a minimum in  $-S_{xx}$  and/or  $R_{xx}$  are labeled.

Comparing the longitudinal thermopowers and resistances of Fig. 8.5, one immediately notes a strong correlation between the two. This correlation results primarily from how  $S_{xx}$  and  $R_{xx}$  both tend to zero as the density of states at  $\mu$  vanishes whenever the 2DES is in an incompressible QH state. That is, the minima in both  $-S_{xx}$  and  $R_{xx}$  derive from QH energy gaps at  $\mu$ . Several filling factors corresponding to well-known incompressible IQH and FQH states are labeled in the figure. These include the IQH states at  $\nu = 2, 3$ , and 4. The rightmost minimum in Fig. 8.5 (a) is associated with  $\nu = 1$ . Several minima at higher integral filling factors are not labeled but well resolved in both  $S_{xx}$  and  $R_{xx}$ .

The labeled odd-denominator FQH states in Fig. 8.5 can be mapped to CF IQH states by inverting the transformations described in Section 8.1.2. For  $1 < \nu < 2$ , the mapping from  $\nu^*$  to  $\nu$  requires the additional transformation of adding a filled spin-split LL. The labeled filling factors in Fig. 8.5 (a) include  ${}^2\text{CF}$  IQH states at  $\nu = 4/3, 7/5$ , and  $10/7$  ( $\nu^* = 1, 2$ , and 3) along with their particle-hole conjugates<sup>9</sup> at  $\nu = 5/3, 8/5$ , and  $11/7$ . We have also labeled  ${}^4\text{CF}$  IQH states at  $\nu = 6/5$  and  $9/7$  ( $\nu^* = 1$  and 2) along with their particle-hole conjugates at  $\nu = 9/5$  and  $12/7$ .

We also observe minima in Fig. 8.5 (a) associated with FQH states in the first excited LL (i.e.  $N = 1$ , which corresponds to  $2 < \nu < 4$ ). These include states at odd-

---

<sup>9</sup>Equivalently, the FQH states at  $\nu = 5/3, 8/5$ , and  $11/7$  may be considered IQH states of  ${}^2\text{CFs}$  at  $\nu^* = 2, 3$ , and 4, respectively, as per Eq. 8.3.

denominator filling factors  $\nu = 11/5, 7/3, 8/3,$  and  $14/5,$  which can be understood as IQH states of  $^2\text{CFs}$  in a manner analogous to that of the labeled FQH states at  $\nu < 2.$  In contrast, the situation at  $\nu = 5/2$  and  $7/2$  cannot be understood in terms of noninteracting CFs. One might naively expect to observe metallic behavior at these even-denominator filling factors in analogy with  $\nu = 1/2$  and  $3/2.$  Rather, it is well-known [133] that FQH states exist at  $\nu = 5/2$  and  $7/2.$  In Chapter 9 we will discuss the nature of these states and review detailed measurements of thermopower in the vicinity of these LL filling factors.

With one exception, the labeled  $-S_{xx}$  minima in Fig. 8.5 (a) correspond to  $R_{xx}$  minima in Fig. 8.5 (b). In the case of  $\nu = 11/5$  a corresponding minimum in the  $R_{xx}$  data is not found. In our experience, it is not uncommon for the existence of  $R_{xx}$  minima associated with fragile FQH states to vary depending on the choice of voltage probes and/or current source and drain for the measurement. Indeed, an  $R_{xx}$  minimum at  $\nu = 11/5$  is observed for this 2DES using a different measurement configuration (not shown). Notably, a similar degree of variation is not encountered with measurements of  $S_{xx}$  at this temperature<sup>10</sup> upon changing voltage probes. For example, referring to Fig. 4.8, which illustrates the layout of diving board B, one can see that each 2DES mesa offers three pairs of ohmic contacts to choose from when measuring longitudinal thermovoltages; the essential features (e.g. magnitude and position of minima and maxima) shown in Fig. 8.5 (a) are independent of ohmic contact choice. The insensitivity of  $S_{xx}$  measurements to voltage probe choice is consistent with the notion that this quantity is simply related to the entropy per carrier.

The correlation between the  $-S_{xx}$  and  $R_{xx}$  data shown in Fig. 8.5 breaks down when we focus our attention on their respective maxima. The  $R_{xx}$  data is characterized by tall spikes that flank the deepest and widest minima. For instance, the two largest maxima are positioned on either side of the strongest minimum in the data set found at  $\nu = 2.$  The maxima of  $R_{xx}$  are generally highly sensitive to temperature,

---

<sup>10</sup>At  $T \lesssim 40$  mK the results of  $S_{xx}$  measurements do become sensitive to the choice of voltage probes. We address this phenomenon later in this chapter.

increasing in magnitude as the temperature is reduced (recall that we exploit this behavior during our temperature calibration method; see Section 4.1.1). No analogous features are observed in  $S_{xx}$ . In the case of  $-S_{xx}$ , maxima are observed on the flanks of  $\nu = 9/7, 4/3, 5/2,$  and  $7/2$ . The temperature dependence of these maxima is strikingly different from those of  $R_{xx}$ . The  $-S_{xx}$  maxima *decrease* as the temperature is reduced.

To broadly demonstrate the temperature dependence of  $S_{xx}$  in the FQH regime, Fig. 8.6 shows  $-S_{xx}$  versus  $B$  for the upper spin branch of the  $N = 0$  LL for  $T \in (41, 60, 114)$  mK. The rightmost and leftmost minima are associated with IQH states at  $\nu = 1$  and  $2$ , respectively. Several FQH state filling factors that coincide with a clear minimum are labeled. A key feature of these data is that, with rare exception,

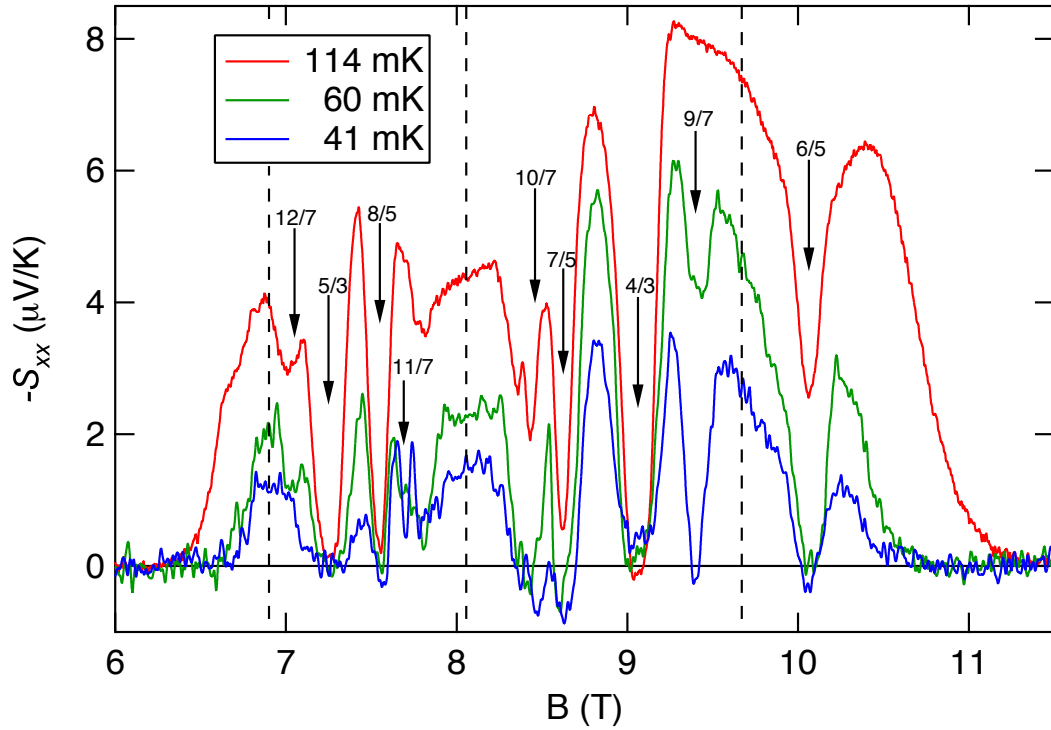


Figure 8.6: Thermopower of the upper spin branch of the  $N = 0$  LL. The negative longitudinal thermopower  $-S_{xx}$  is plotted versus magnetic field  $B$  for  $T \in (41, 60, 114)$  mK. Several FQH state filling factors that coincide with a clear minimum are labeled. The vertical dashed lines, from right to left, correspond to  $\nu = 5/4, 3/2,$  and  $7/4$ , where  $B^* = 0$  for either  ${}^2\text{CFs}$  or  ${}^4\text{CFs}$ .

the magnitude of  $S_{xx}$  decreases as the temperature is reduced. This reflects the reduction in entropy that occurs as the temperature is lowered for both compressible and incompressible QH liquids.

The dashed vertical lines in Fig. 8.6 indicate where  $B^* = 0$  for either  ${}^2\text{CFs}$  or  ${}^4\text{CFs}$ . From right to left, the lines correspond to  $\nu = 5/4, 3/2,$  and  $7/4$ . In Section 8.3.1, we reviewed our detailed study of  $S_{xx}$  versus  $T$  at  $\nu = 3/2$  and saw that for  $50 \text{ mK} \lesssim T \lesssim 200 \text{ mK}$  the thermopower exhibited linear temperature dependence consistent with a Fermi sea of  ${}^2\text{CFs}$  at  $B^* = 0$ . While limited to only three temperatures, the data of Fig. 8.6 are suggestive of similar situations at  $\nu = 5/4$  and  $7/4$  where  $B^* = 0$  for  ${}^4\text{CFs}$  and  ${}^4\text{CF}$  holes, respectively.

The minima in  $-S_{xx}$  at  $\nu = 6/5$  and  $9/7$  can be understood as IQH states of  ${}^4\text{CFs}$  at  $\nu^* = 1$  and  $2$ , respectively. We therefore expect to observe evidence of a CF metal at  $\nu = 1 + 1/4$ . The  $T = 41 \text{ mK}$  and  $60 \text{ mK}$  measurements at  $\nu = 5/4$  are consistent with linear temperature dependence. At  $T = 114 \text{ mK}$ , however, the magnitude of  $S_{xx}$  at  $\nu = 5/4$  suggests sublinear temperature dependence. At the same time, a minimum at  $\nu = 9/7$  is not observed at  $T = 114 \text{ mK}$ , so it may be that  ${}^4\text{CFs}$  are not fully formed at  $\nu = 5/4$  at this temperature. The data is therefore consistent with Mott-like behavior at  $\nu = 5/4$  below  $T \sim 60 \text{ mK}$ .

Similarly, we observe a clear minimum at  $\nu = 12/7$  for  $T = 60 \text{ mK}$  and  $114 \text{ mK}$ , which can be understood as the IQH state of  ${}^4\text{CF}$  holes at  $\nu^* = 2$ . We therefore expect to observe evidence of a CF metal at  $\nu = 2 - 1/4$ . And indeed, we find that our measurements of  $S_{xx}$  at  $\nu = 7/4$  are consistent with linear temperature dependence. The data is therefore consistent with Mott-like behavior at  $\nu = 7/4$  below  $T \sim 114 \text{ mK}$ .

In the same way we extracted an estimate of  $m_{CF}$  for  ${}^2\text{CFs}$  at  $\nu = 3/2$  from the  $-S_{xx}$  versus  $T$  data of Fig. 8.3, we can use the data of Fig. 8.6 to make crude estimates of  $m_{CF}$  for  ${}^4\text{CFs}$  at  $\nu = 5/4$  and  $7/4$ . The magnitude of  $S_{xx}$  at  $\nu = 5/4$  is roughly twice that at  $\nu = 3/2$ . (Note that a similar relationship was previously found between  $S_{xx}$  measured at  $\nu = 1/4$  and that at  $\nu = 1/2$ , although in this case the thermopower was attributed to phonon drag [134].) Assuming  $p_{CF}$  is sufficiently small that it can

be ignored, these data are consistent with Eq. 8.9 if  $m_{CF}(5/4) \approx 2 \cdot m_{CF}(3/2)$ . Since  $m_{CF}$  is expected to scale with magnetic field as  $m_{CF} = \alpha\sqrt{B}$ , we can only attribute a factor  $\sqrt{3/2}/\sqrt{5/4} \approx 1.1$  of this increase to the difference in  $B$ . Recall, however, that  $\alpha$  for  ${}^4\text{CFs}$  is expected to be a factor of 2 larger than that of  ${}^2\text{CFs}$  [124]. Our thermopower data at  $\nu = 5/4$  is therefore consistent with that at  $\nu = 3/2$  within a model of low-temperature diffusion of CFs. However, the same cannot be said for the data at  $\nu = 7/4$ , where, by the same rationale, we expect  $|S_{xx}|$  to also be twice that measured at  $\nu = 3/2$ . Instead, we find their magnitudes are roughly equal. While the origin of this discrepancy is not known, it may be that proximity to the broad minimum near  $\nu = 2$  results in a competition between this incompressible IQH state and the formation of  ${}^4\text{CFs}$  at  $\nu = 7/4$ .

### 8.3.5 Low-Temperature Fluctuations

Let us now examine the behavior of  $S_{xx}$  at the lowest experimentally accessible temperatures. As can be seen from Fig. 8.6, the maxima and minima of the  $T = 41$  mK data are well correlated with higher temperature data. The behavior of  $S_{xx}$  is distinctly altered, however, when the temperature is reduced to below  $T \approx 40$  mK. Figure 8.7 rescales the  $T = 41$  mK data and shows it together with  $-S_{xx}$  versus  $B$  at  $T = 21$  mK. The data at  $T = 21$  mK introduces aperiodic fluctuations and  $S_{xx}$  frequently reverses sign to become positive within short intervals of  $B$  (recall that the conventional sign of  $S_{xx}$  for electrons is negative). Data from the other 2DES mesa exhibits qualitatively similar behavior at this temperature. The exact field dependence differs for the two independent 2DES mesas and varies within an individual mesa depending on the thermal history of the sample. As noted during the discussion of our experimental results at  $\nu = 3/2$ , we attribute this behavior to phenomena associated with universal conductance fluctuations (UCFs).

In a disordered mesoscopic sample, quantum interference effects can yield a distinctive “magneto-fingerprint” in which the conductance fluctuates in unique way on the order of  $e^2/h$  as a function of the chemical potential  $\mu$  [129]. Given that low-

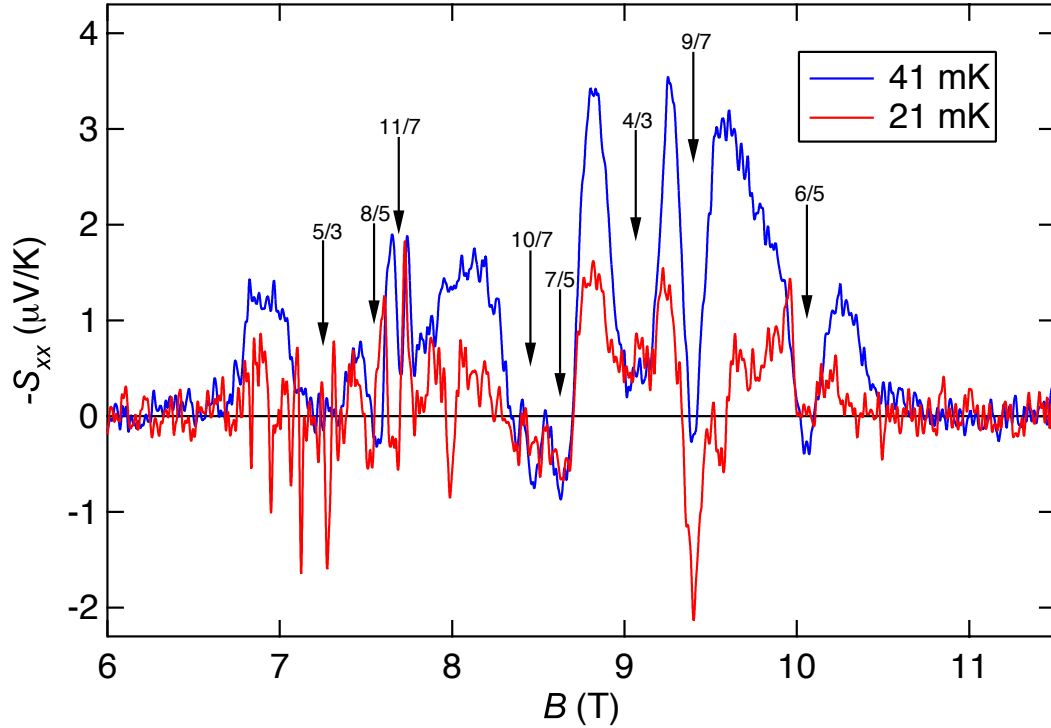


Figure 8.7: Low-temperature thermopower fluctuations in the FQH regime. The negative longitudinal thermopower  $-S_{xx}$  is plotted versus magnetic field  $B$  for  $T \in (21, 41)$  mK. Several FQH state filling factors that coincide with a clear minimum are labeled. Aperiodic fluctuations can be seen at  $T = 21$  mK.

temperature diffusion thermopower is proportional to  $d\sigma/d\mu$ , it is no surprise that UCFs are accompanied by relatively large fluctuations in thermopower [130]. While such universal thermopower fluctuations (UTFs) have been observed as a function of  $B$  in mesoscopic samples [131], we believe ours is the first observation of UTFs within the FQH regime.

We observe fluctuations believed to be UTFs in both nominally compressible and incompressible FQH liquids. In the example shown in 8.7, the fluctuations are most concentrated within  $6.8 \text{ T} \lesssim B \lesssim 7.3 \text{ T}$ , which includes a relatively strong FQH state at  $\nu = 5/3$ . Similar behavior is encountered in the vicinity of  $\nu = 3/2$  and  $\nu = 9/7$ . However, warming the sample to room temperature and then re-cooling to  $T \sim 20$  mK significantly changes the field dependence. At the same time, one persistent feature is that these fluctuations are never observed within the minima associated with the

IQH states at  $\nu = 1$  and 2. This is reasonable given the large magnitude of the energy gaps of these states, which preclude any appreciable conductance through the sample bulk, and hence, maintain  $d\sigma/d\mu = 0$  over a large range of  $B$ .

Interestingly, the nature of these fluctuations conflicts with the notion that the thermopower is the entropy per electron per electron charge. Indeed, the changing of sign of  $S_{xx}$  precludes its interpretation as  $-\mathcal{S}/ne$  since this would require the entropy per area  $\mathcal{S}$  to become negative. Cooper et al. have shown [8] that the entropic interpretation of diffusion thermopower is only valid for an interacting 2DES that behaves as a fluid (i.e. has no shear modulus). It may be that UTFs observed in an interacting 2DES are indicative of at least short-range crystalline order. This idea is supported by the fact that we observe similar fluctuations in  $S_{xx}$  in the vicinity of the reentrant integer quantum Hall effects (RIQHEs) of the  $N = 1$  LL (see Chapter 9), which are believed to result from electronic solid phases.

### 8.3.6 Comparison to Entropic Model

To further pursue whether the complicated experimental data of Fig. 8.6 can be understood in terms of noninteracting CFs, we revisit our disorder-free entropic thermopower model. While this model is clearly unrealistic since it ignores the important effects of disorder, its simplicity makes it worth consideration. We proceed in the same manner as in Section 8.2.2, where we derive the diffusion thermopower of CFs in the lower spin branch of the  $N = 0$  LL based on the premise that  $S^d = -\mathcal{S}/ne$ . In Fig. 8.8 (a) we show the results of a similar calculation for the upper spin branch of the  $N = 0$  LL. This calculation, however, uses the electron density of our diving board samples ( $n = 2.9 \times 10^{11} \text{ cm}^{-2}$ ) and our measured  ${}^2\text{CF}$  effective mass at  $\nu = 3/2$  ( $m_{CF} = 1.7m_e$ ). The  ${}^4\text{CF}$  effective masses at  $\nu = 5/4$  and  $\nu = 7/4$  are inferred from our measured  ${}^2\text{CF}$  effective mass at  $\nu = 3/2$  given that  $m_{CF} = \alpha\sqrt{B}$  together with the empirical rule [124] that  $\alpha$  for  ${}^4\text{CFs}$  is a factor of 2 larger than that for  ${}^2\text{CFs}$ . The figure displays the calculated diffusion thermopower of either  ${}^2\text{CFs}$  (solid blue curve) or  ${}^4\text{CFs}$  (red dotted curve) at  $T = 114 \text{ mK}$ . At each value of  $B$  we only show the

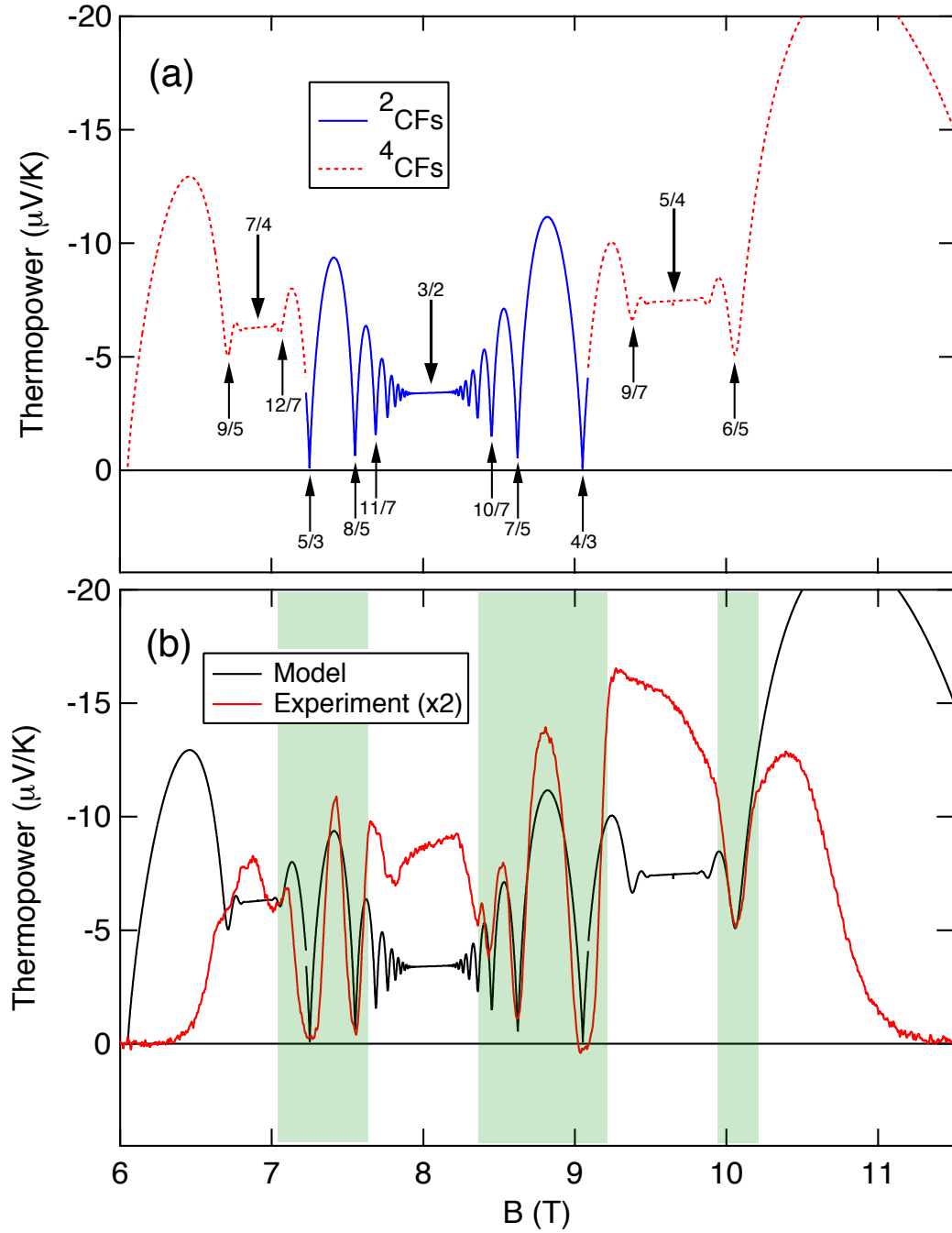


Figure 8.8: Entropic thermopower vs magnetic field of CFs in the absence of disorder. The entropic derivation is for a 2DES with  $n = 2.9 \times 10^{11} \text{cm}^{-2}$  at  $T = 114$  mK. The domain of  $B$  corresponds to the upper spin branch of the  $N = 0$  LL. In (a), the thermopower of either  ${}^2\text{CFs}$  (solid blue curve) or  ${}^4\text{CFs}$  (red dotted curve) is shown depending on which minimizes the system's entropy, and hence, energy. In (b), the disorder-free entropic model (black curve) is compared to the experimentally measured thermopower (red curve). The experimental data is multiplied by a factor of 2. Regions of strong correlation between the two datasets are shaded.

curve that minimizes the system's entropy, and hence, energy. For  $7.2 \text{ T} \lesssim B \lesssim 9.1 \text{ T}$  this corresponds to  $^2\text{CFs}$  and elsewhere in the figure to  $^4\text{CFs}$ . Several of the most prominent FQH states are labeled.

Let us compare our disorder-free entropic model to the experimentally measured thermopower. Figure 8.8 (b) shows the results of our entropic calculation together with our experimental thermopower data acquired at the same temperature,  $T = 114 \text{ mK}$ , with the latter scaled by a factor of 2. Scaled in this way, the two datasets roughly match within the shaded regions, which include the strongest FQH states in the figure (e.g.  $\nu = 6/5, 4/3, 7/5, 8/5$ , and  $5/3$ ). As in the IQH regime, a small amount of disorder will broaden the LLs and thereby reduce the entropy of a partially filled LL. That the measured thermopower is consistently about half that predicted by our disorder-free model is consistent with CF LLs with a disorder broadening parameter  $\Gamma$  that at most depends only weakly on  $B$ . The discrepancy between minima widths—most conspicuously at  $\nu = 4/3$  and  $5/3$ —can also be attributed to disorder. In analogy with the IQH regime, for a sufficiently low disorder 2DES, the width of the  $R_{xy}$  plateau associated with a FQH state will increase with increasing disorder resulting in a wider minimum in  $S_{xx}^d$ .

The comparison in Fig. 8.8 (b) reveals a different situation in the unshaded region centered at  $\nu = 3/2$  ( $B \approx 8.0 \text{ T}$ ). Here, our entropic model and the experimental data roughly converge as we approach  $\nu = 3/2$  (i.e. the red curve is about twice the black curve at  $\nu = 3/2$  in the figure). Of course, this is merely the consequence of our choice for the  $^2\text{CF}$  effective mass in the model. Similar circumstances exist for the unshaded region centered at  $\nu = 5/4$  ( $B \approx 9.7 \text{ T}$ ) where the model thermopower is governed by our choice for the  $^4\text{CF}$  effective mass.

To explain the discrepancies between our experimental data and our disorder-free model, it is important to understand how disorder impacts different regions of Fig. 8.8 (b). In the vicinity of strong FQH states (i.e. the shaded regions) a small amount of disorder will reduce the entropy of partially filled LLs, and hence, *decrease* the thermopower. However, we expect disorder to have the opposite effect where  $B^*$  is sufficiently small. As previously mentioned, the energy gaps associated with FQH

states understood as CF IQH states are inversely proportional to  $m_{CF}$ . A small amount of disorder will reduce these gaps resulting in the appearance of a larger  $m_{CF}$ , and hence, *increase* the thermopower. This might partially explain why the thermopower magnitude in the experimental data near  $B^* = 0$  (e.g.  $\nu = 5/4, 3/2$ , and  $7/4$ ) appears enhanced relative to the shaded regions when comparing to our disorder-free model. Finally, in the rightmost and leftmost unshaded regions of Fig. 8.8 (b) we find that the magnitude of the experimental data falls well short of that of our model. We attribute this to a competition between CF formation and the incompressible IQH states at  $\nu = 1$  and  $2$ , which prevail over a larger range of  $B$  in the presence of disorder.

## 8.4 Summary

In this chapter we have seen how Coulomb interactions within the 2DES result in remarkably rich physics. The hallmark of this phenomena is the fractional quantum Hall effect, in which the Hall, or transverse, resistance is quantized at fractional Landau level filling factors. Observations of FQHEs can be explained via quasiparticle-hierarchy schemes based upon Laughlin's original wavefunction. However, a simplified alternative framework is provided by the notion of composite fermions. By attaching an even number of magnetic flux quanta to each electron we can transform the complex problem of strongly interacting electrons into the more tractable problem of weakly interacting CFs.

Thermopower, like all transport, is rather complicated in the FQH regime. Fortunately, the CF model, in conjunction with the relationship between thermopower and entropy, goes a long way toward deconstructing this complex behavior. For instance, at particular filling factors (e.g.  $\nu = 1/2$  and  $3/2$ ) we may treat the 2DES as consisting of CFs in zero effective magnetic field. Here, the diffusion thermopower obeys a Mott-like formula in analogy with electrons in zero field. A key parameter for the thermoelectric response of CFs is their effective mass,  $m_{CF}$ . Unlike electrons, whose effective mass  $m^*$  results from the periodic potential of the GaAs lattice,  $m_{CF}$  derives

entirely from electron-electron interactions. Meanwhile, the low-temperature diffusion thermopower can more generally be interpreted as the entropy per CF per CF charge. We may therefore estimate the low-temperature thermopower of a disorder-free interacting 2DES by counting states within CF LLs as we did for noninteracting electrons in Chapter 7.

Our measurements of thermopower in a strong magnetic field corroborate expectations for this regime. At  $\nu = 3/2$  we find  $S_{xx}$  depends linearly on temperature for  $50 \text{ mK} \lesssim T \lesssim 200 \text{ mK}$  with a slope that is consistent with the diffusion of CFs with mass  $m_{CF} = 1.7m_e$ , where  $m_e$  is the bare electron mass. While this value of  $m_{CF}$  is about 7 times larger than originally predicted, it is consistent with values extracted from thermopower measurements performed on 2D holes, allowing for certain assumptions about the CF spin polarization. We also show that a recent disordered noninteracting thermopower model is unable to account for the small magnitude of  $S_{xx}$  measured at  $\nu = 3/2$ . Rather, we attribute the reduced thermopower is a reflection of the reduced entropy resulting from the self-organization that is CF formation. Above  $T \approx 200 \text{ mK}$ ,  $S_{xx}$  exceeds linear- $T$  dependence, which we attribute to the growing importance of phonon drag.

We also measure  $S_{xx}$  versus  $B$  to provide a more comprehensive picture of thermopower in the FQH regime. Comparing  $S_{xx}$  to  $R_{xx}$  we find the signatures of several FQH states are clearly resolved in both. The information content of these two transport coefficients differ, however, as demonstrated by the temperature evolution of  $S_{xx}$  versus  $B$ . Specifically, the measured  $S_{xx}$  exhibits linear- $T$  behavior at  $\nu = 5/4$  and  $7/4$ , in addition to  $\nu = 3/2$ , indicating the metallic nature of these QH phases. At the lowest accessible temperatures (e.g.  $T \lesssim 40 \text{ mK}$ ), we observe novel aperiodic fluctuations in  $S_{xx}$  versus  $B$  that we attribute to quantum interference effects related to universal conductance fluctuations (UCFs). Finally, we aim toward a greater understanding of our experimental data by calculating the entropic thermopower of a disorder-free interacting 2DES of the same density and at the same temperature. Assuming the formation of  ${}^2\text{CFs}$  and  ${}^4\text{CFs}$  we find good correlation between the calculation and experiment in the vicinity of strong FQH states.

## Chapter 9

# The First Excited Landau Level

Higher Landau levels display character quite distinct from that of the  $N = 0$  LL where a veritable zoo of FQHEs ultimately terminate in the Wigner crystal. No FQHEs are observed in LLs with  $N \geq 2$ . Rather, in sufficiently high quality samples, several striking features are observed in the electrical transport that cannot be explained in terms of quantum Hall physics. These include dramatic anisotropies [135, 136, 137] as well as isotropic insulating phases that yield non-monotonic “reentrant” quantization of the Hall resistance [4]. These features are generally attributed to the collective formation of liquid crystal phases or *charge density waves* (CDWs). Between these higher LLs and the  $N = 0$  LL lies the first excited ( $N = 1$ ) LL, which presents mixed character<sup>1</sup>.

In the first excited LL we find both FQHEs and *reentrant integer quantum Hall effects* (RIQHEs). In addition to odd-denominator FQH states such as those at  $\nu = 7/3$  and  $8/3$ , which can be understood in terms of noninteracting CFs, we also observe the enigmatic even-denominator state at  $\nu = 5/2$  [133, 138]. This latter state is believed to exhibit exotic quantum statistics that are of fundamental interest and could also provide an ideal venue for quantum computation [139]. In the highest mobility samples, intriguing RIQHEs are observed between the various FQH states, so-named for their non-monotonic *integer* quantization of the Hall resistance [140]. Adding to the richness of this LL, is the observation [138, 141, 142, 143] that an externally applied in-plane magnetic field destroys the FQH state at  $\nu = 5/2$  and,

---

<sup>1</sup>See Pan et al. [101] for an overview of FQHEs in the first excited LL.

initially at least, replaces it with an anisotropic phase similar to what is found at higher LLs.

In this chapter we review our thermopower results in the  $N = 1$  LL. Clear signatures of nearly all known FQH states in this LL are observed in  $S_{xx}$ . We give particular focus to the FQH state at  $\nu = 5/2$ . We examine our results in the vicinity of this filling factor for evidence of non-abelian statistics and find they are in rough quantitative agreement with a recent theory that incorporates the enhanced entropy expected from non-Abelian quasiparticle exchange statistics. We then shift our attention to the RIQHEs, which manifest themselves as an abrupt quenching of the thermopower. We argue that the temperature dependence of  $S_{xx}$  provides strong evidence for an unconventional conducting phase at temperatures just above the RIQHE transition.

This chapter also provides an overview of the first excited LL. Particular focus is applied to the FQH state at  $\nu = 5/2$ . We discuss the supposed nature of this state and the reason its quasiparticle excitations have garnered so much attention. Before presenting our results, we review a recent theory of how thermopower might reveal the true nature of the  $\nu = 5/2$  state. Our focus then shifts to the phenomena surrounding RIQHEs. After summarizing what is known about RIQHEs in higher LLs, we describe their manifestation in the  $N = 1$  LL by reviewing resistance data acquired from one of our samples. These resistance data provide context for our thermopower results.

## 9.1 FQH State at $\nu = 5/2$

Composite fermion theory successfully describes the preponderance of odd-denominator FQH states. In 1987, however, Willet et al. [133] reported magnetotransport experiments clearly showing a FQH state at *even-denominator* filling factor  $\nu = 5/2$ , which cannot be explained in terms of noninteracting CFs. Like other incompressible FQH states,  $\nu = 5/2$  is characterized by a plateau in the transverse resistance  $R_{xy}$  and simultaneous vanishing of the longitudinal resistance  $R_{xx}$  in the limit of zero tem-

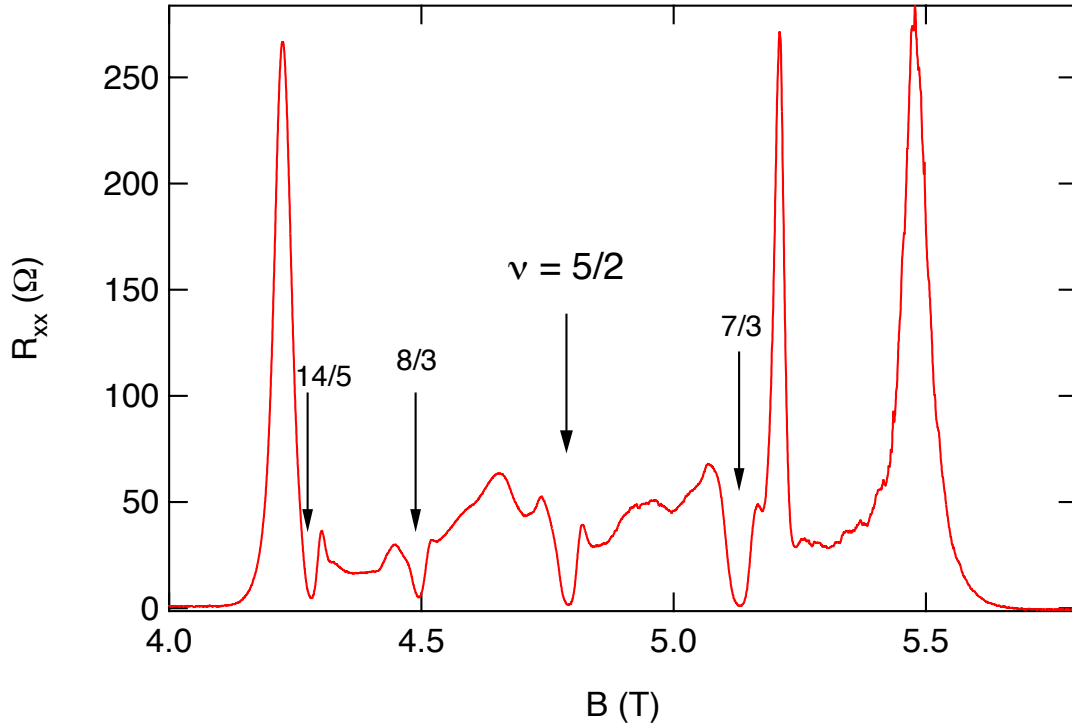


Figure 9.1: Longitudinal resistance  $R_{xx}$  vs magnetic field  $B$  at  $T = 50$  mK in the first excited LL measured in diving board A. Minima in  $R_{xx}$  at  $\nu = 7/3$ ,  $5/2$ , and  $8/3$  FQH states are indicated. Reprinted with permission from W.E. Chickering, J.P. Eisenstein, L.N. Pfeiffer, and K.W. West, *Phys. Rev. B* **81**, 245319, (2010). Copyright 2010 by the American Physical Society.

perature. The puzzle is the occurrence of this FQHE at precisely half filling of the lower spin branch of the  $N = 1$  LL. At this filling factor one would naively expect—in analogy with  $\nu = 1/2$ —to find a compressible state well described as a sea of CFs in zero effective magnetic field.

Figure 9.1 shows  $R_{xx}$  versus  $B$  measured in the lower spin branch of the first excited LL at  $T = 50$  mK using diving board A. The rightmost and leftmost minima are associated with the IQH states at  $\nu = 2$  and  $3$ , respectively. In between we label clearly formed minima<sup>2</sup> in  $R_{xx}$ , from right to left, as  $\nu = 7/3$ ,  $5/2$ ,  $8/3$ , and  $14/5$ . We see nothing about the minimum at  $\nu = 5/2$  that qualitatively distinguishes it from other FQH minima.

<sup>2</sup>In this sample, we do not observe a clearly formed minimum associated with  $\nu = 11/5$  at this temperature, but the absence of this state is not universal.

Given the adherence of all previously observed FQHEs to the *odd-denominator rule*, the discovery of an incompressible state at  $\nu = 5/2$  was quite surprising. To this day, with the exception of evidence [144] pointing toward extremely fragile quantization at  $\nu = 19/8$ , the  $\nu = 5/2$  state (and its upper spin branch manifestation at  $\nu = 7/2$ ) is the only observed even-denominator FQHE. Indeed, even the weakly quantized Hall effects mentioned in Section 8.1.2 (i.e.  $\nu = 4/11, 5/13, 7/11, 4/13, 6/17$ , and  $5/17$ ) that are interpreted as resulting from CF-CF interactions have odd denominators.

Early attempts at a theoretical understanding of the enigmatic  $\nu = 5/2$  state were ultimately disqualified [145, 6]. Today, this state is believed to be well approximated by the so-called Moore-Read (MR), or Pfaffian, wavefunction (or its particle-hole conjugate, the Anti-Pfaffian) [146, 147, 6]. At  $\nu = 5/2$ , both spin branches of the  $N = 0$  LL are filled and the lower spin branch of the  $N = 1$  LL is half filled. The electrons in the filled LL are essentially inert. The electrons in the half-filled spin branch, like at  $\nu = 1/2$  and  $3/2$ , form  ${}^2\text{CFs}$  that experience zero effective field. Unlike at  $\nu = 1/2$  and  $3/2$ , however, at sufficiently low temperatures, spin-polarized  ${}^2\text{CFs}$  at  $\nu = 5/2$  are believed to form p-wave Cooper-pairs. These Cooper-pairs then condense to form a superconductor. A most remarkable feature of this theoretical description are the quasiparticle excitations, which satisfy *non-abelian statistics* [148]. The prospect of such exotic quantum statistics is not only of great fundamental interest but also holds promise for the realization of topological quantum computation [139].

### 9.1.1 Non-Abelian Anyons

In quantum mechanics, different types of indistinguishable particles are characterized by the symmetry of their wavefunction under an exchange operation. For example, a collection of bosons occupies a symmetric state meaning their wavefunction is unchanged by swapping two particles' labels. And a collection of fermions occupies an antisymmetric state meaning their wavefunction is multiplied by  $-1$  when

we swap two particles. Given it is the modulus squared of these wavefunctions that yields a probability density, multiplication by  $\pm 1$  cannot affect observable quantities. Nonetheless, the significance of these exchange symmetries cannot be overstated. Indeed, it is these very symmetries that allow bosons to condense to form superfluids and superconductors, and fermions to obey the Pauli exclusion principal, which is fundamental to the behavior of everyday matter.

In three spatial dimensions, every particle is either a boson or a fermion. In two spatial dimensions, however, particles can exist that obey statistics that range continuously between those of bosons and fermions. Such particles are known as *anyons*. While exchanging two identical bosons or fermions modulates a wavefunction by  $\pm 1$ , exchanging two identical anyons can result in an intermediate phase factor of  $e^{i\theta}$ , where  $\theta$  is referred to as the *statistical angle* and can take a value between 0 and  $\pi$  [149, 150].

The quasiparticles of FQH states provide real-life examples of anyons [148]. In the case of a FQH state at filling factor  $\nu$  that can be understood in terms of non-interacting CFs (see Section 8.1.2), it so happens that  $\theta = \pm\nu\pi$  [151]. The sign of  $\theta$  depends on whether they are exchanged in a clockwise or counterclockwise manner. Consequently, unlike indistinguishable bosons or fermions, which always recover their original wavefunction after two exchanges that take the particles back to their original positions, these FQH quasiparticles can acquire a nontrivial phase  $e^{2i\nu\pi}$  following two sequential counterclockwise exchanges.

The quasiparticles of FQH states that can be understood in terms of noninteracting CFs are *abelian anyons*. Given a collections of such quasiparticles at filling factor  $\nu$ , after undergoing a series of exchanges, the final wavefunction gains the phase factor  $e^{i\nu\pi(b-a)}$ , where  $a$  is the number of clockwise and  $b$  is the number of counterclockwise exchanges. Importantly, it is only the number of exchanges in each direction that determines the final wavefunction; the order in which these exchanges take place is irrelevant. In other words, the exchange operators commute.

The putative situation at  $\nu = 5/2$  is more subtle and more exciting. It is believed

to be the most simple<sup>3</sup> FQH state (along with its upper spin branch manifestation at  $\nu = 7/2$ ) whose quasiparticles are *non-abelian anyons* [147], meaning their exchange operations do not commute. Instead of a single phase factor, as in the case of abelian anyons, exchanging two indistinguishable non-abelian anyons is a multidimensional unitary operation. A wavefunction describing a collection of  $\nu = 5/2$  quasiparticles is therefore sensitive to the order in which exchanges occur. Such a ground state whose excitations satisfy non-abelian statistics is the key ingredient for *topological quantum computation* in which pairwise interchanges, or *braiding*, of quasiparticles perform universal quantum computation in a fault tolerant manner [154, 139].

The non-abelian nature of the  $\nu = 5/2$  state has yet to be proven, however. Recent studies of the shot noise resulting from tunneling between quasiparticle carrying edge currents [155, 156] along with interferometric experiments [157, 158] at  $\nu = 5/2$  have demonstrated a quasiparticle charge  $e^* = e/4$  consistent with the MR Pfaffian state. Another shot noise experiment produced results suggesting backward flowing neutral edge states that appear to rule out the possibility of an abelian state [159]. Yet, an even more recent investigation of inter-edge state tunneling yielded data that strongly favored a different, abelian ground state at  $\nu = 5/2$  [160]. It may be that different ground states prevail in different specimens at this filling factor as a consequence of varying parameters such as 2DES density  $n$  and disorder broadening  $\Gamma$  such that these seemingly contradicting results can be reconciled.

### 9.1.2 Thermopower of Non-Abelian Anyons

Another approach to testing the nature of FQH state at  $\nu = 5/2$  is to probe the entropy of its perturbed ground state. A prerequisite for non-abelian anyons is a Hilbert space whose degeneracy  $D$  grows exponentially with the number of localized quasiparticles  $N_q$  in the system [139]:

$$D \propto d^{N_q}, \tag{9.1}$$

---

<sup>3</sup>The Read-Rezayi [152, 153] series of FQH states describes several non-abelian states including  $\nu = 5/2$ ,  $12/5$ , and  $13/5$ .

where  $d > 1$  is known as the *quantum dimension*. To observe evidence of this large degeneracy, measurements of the temperature dependence of the chemical potential or orbital magnetization have been proposed [161]. Alternatively, Yang and Halperin (YH) have suggested [93] exploiting the relationship between entropy and diffusion thermopower to discern the true statistical nature of the  $\nu = 5/2$  state.

In the case of a ground state with non-abelian excitations, YH predict a distinctive signature in the diffusion thermopower. The essential features of their theory are as follows. From the degeneracy of the low-level excitations (Eq. 9.1), the corresponding entropy per area is  $\mathcal{S} = k_B n_q \ln(d) + \mathcal{O}(1)$ , where  $n_q$  is the number of quasiparticles per area. In general, near the center of a QH state at low temperature, the number of quasiparticles will increase linearly with the deviation in magnetic field from the plateau center at  $B_0$ :

$$n_q = \frac{e}{e^*} \left| 1 - \frac{B}{B_0} \right| n, \quad (9.2)$$

where  $e^*$  is the quasiparticle charge. Given the diffusion thermopower equals the entropy per electron per electron charge, it follows that

$$S^d = -\mathcal{S}/en = -\frac{k_B}{e^*} \left| 1 - \frac{B}{B_0} \right| \ln(d). \quad (9.3)$$

YH point out that Eq. 9.3 is only valid as long as the temperature  $T$  satisfies

$$T_0 \ll T \ll T_1, \quad (9.4)$$

where  $T_0$  and  $T_1$  are certain temperature scales.  $T_1$  is determined by sources of entropy other than the degeneracy of non-abelian excitations such as the positional degrees of freedom of the quasiparticles. Meanwhile, quasiparticle tunneling interactions can lift the degeneracy of Eq. 9.1, which would invalidate Eq. 9.3. The strength of the coupling between quasiparticles determines the scale  $T_0$ . YH note that the strength of the coupling decays exponentially with the distance between quasiparticles such that  $T_0$  can be extremely low as  $B$  approaches  $B_0$ . While precise values for  $T_0$  and  $T_1$

are not known, YH suggest that in the case of the FQH state at  $\nu = 5/2$  the regime of Eq. 9.4 is likely to be experimentally accessible.

Equations 9.3 and 9.4 apply generally to non-abelian FQH states. In the case of the supposed MR Pfaffian, or Anti-Pfaffian, state at  $\nu = 5/2$ , we plug into Eq. 9.3 a quasiparticle charge of  $e^* = e/4$  and a quantum dimension of  $d = \sqrt{2}$  [93]. As previously mentioned, a quasiparticle charge of  $e^* = e/4$  has been measured at  $\nu = 5/2$ . This is consistent with both abelian and non-abelian candidate states, and therefore, this measurement is unable to discriminate between the two. The theory of YH can therefore be viewed as a method for measuring the quantum dimension  $d$  of the  $\nu = 5/2$  state with  $d > 1$  being the indicator of non-abelian statistics.

### 9.1.3 Experimental Results

We begin by considering the most basic features of the measured thermopower at  $\nu = 5/2$ , ignoring for the moment the question of non-abelian statistics. From a naive model of noninteracting CFs, like that explored in Chapter 8, one would expect a compressible phase at  $\nu = 5/2$  similar to what is found at  $\nu = 1/2$  and  $3/2$ . This is not the case, however, as a strong FQHE is encountered at  $\nu = 5/2$  in sufficiently clean 2DESs. As we have seen, QHEs are associated with energy gaps at the Fermi level, which greatly suppress the entropy, and hence the low temperature thermopower. Instead of the linear temperature dependence indicative of compressible, or “metallic”, behavior found at  $\nu = 1/2$  and  $3/2$ , we expect the thermopower to vanish more rapidly with decreasing temperature at  $\nu = 5/2$  in a manner similar to that observed for the FQH states of the  $N = 0$  LL.

Figure 9.2 (a) compares the temperature dependence of the thermopower at  $\nu = 5/2$  with that at  $\nu = 3/2$ . These data are acquired from mesa 2 of diving board A using our quasi-DC protocol (see Section 4.1.2). Unlike the  $\nu = 3/2$  data,  $S_{xx}$  at  $\nu = 5/2$  cannot be well fit by a straight line passing through the origin. Instead, a linear fit to the  $T < 250$  mK data, indicated by the red dashed line in the figure, extrapolates to zero at about  $T = 44$  mK. This is a reflection of the energy gap in

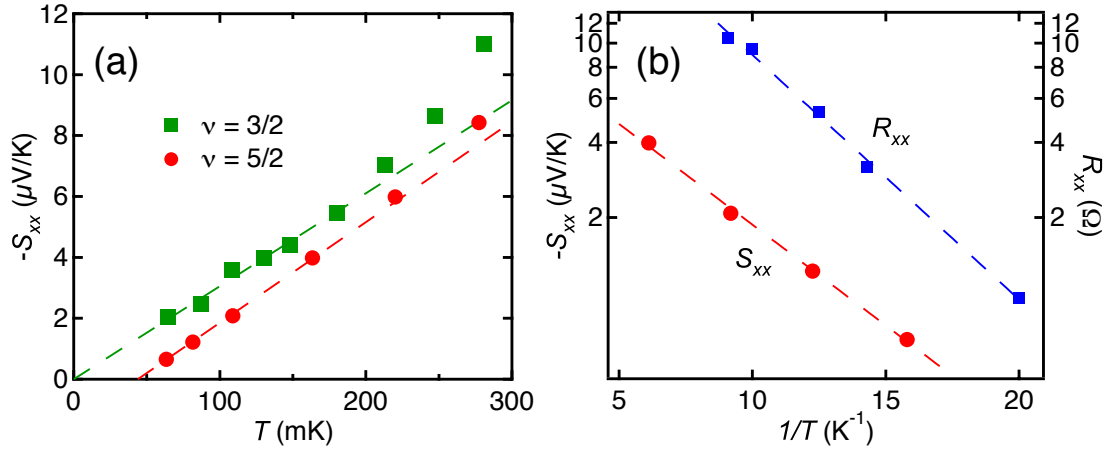


Figure 9.2: Temperature dependence of thermopower at  $\nu = 5/2$ . (a) Comparison of measured  $S_{xx}$  vs  $T$  at  $\nu = 5/2$  (red circles) and  $\nu = 3/2$  (green squares). Unlike  $S_{xx}$  at  $\nu = 3/2$ , the data at  $\nu = 5/2$  extrapolates to zero at a *nonzero* temperature. (b) Arrhenius plots of  $S_{xx}$  (red circles, left axis) and  $R_{xx}$  (blue squares, right axis) at  $\nu = 5/2$ . Dashed line fits give energy gaps of  $\Delta \approx 370$  mK and  $\Delta \approx 450$  mK for the thermopower and resistance, respectively. Reprinted with permission from W.E. Chickering, J.P. Eisenstein, L.N. Pfeiffer, and K.W. West, *Phys. Rev. B* **81**, 245319, (2010). Copyright 2010 by the American Physical Society.

the FQH state at  $\nu = 5/2$ .

Figure 9.2 (b) supports our assertion that the low-temperature thermopower at  $\nu = 5/2$  is dominated by the FQH energy gap by comparing, in an Arrhenius plot, the temperature dependence of  $S_{xx}$  and  $R_{xx}$  (both measured in mesa 2 of diving board A) at  $\nu = 5/2$ . In spite of the somewhat limited data set, it is clear from the figure that both the thermopower and the longitudinal resistance are consistent with simple thermal activation (*i.e.* both scale as  $\sim e^{-\Delta/2T}$ ) for the roughly one order of magnitude variation of each data set. From the slopes of the dashed lines in the figure, we find  $\Delta \approx 370$  mK and 450 mK for the thermopower and resistivity data, respectively. These values are quite comparable to those obtained from previous resistivity measurements at  $\nu = 5/2$  in 2DES samples of similarly high quality [140, 101, 162].

Figure 9.3 (a) shows  $S_{xx}$  measured in the lower spin branch of the  $N = 1$  LL (*i.e.* between  $\nu = 2$  and 3) at  $T = 200$  mK and  $T = 60$  mK. These data are acquired

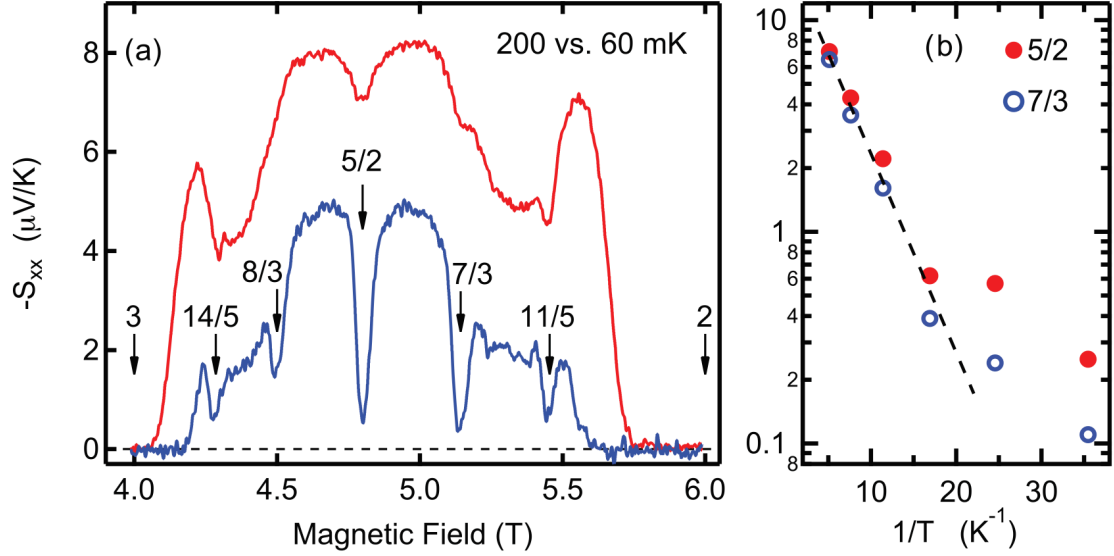


Figure 9.3: Comparison of temperature dependence of FQH states in  $N = 1$  LL. (a)  $S_{xx}$  between  $\nu = 2$  and  $\nu = 3$  at  $T = 200$  mK and  $T = 60$  mK with various quantized Hall states indicated by arrows. (b)  $S_{xx}$  at  $\nu = 5/2$  and  $\nu = 7/3$  vs.  $1/T$ . Dashed line corresponds to an energy gap of  $\Delta = 430$  mK. Reprinted with permission from W.E. Chickering, J.P. Eisenstein, L.N. Pfeiffer, and K.W. West, *Phys. Rev. B* **87**, 075302, (2013). Copyright 2013 by the American Physical Society.

from mesa 2 of diving board B (qualitatively similar results are acquired from mesa 1) using low frequency AC lock-in detection (see Section 4.2.3). Signatures of FQH states at  $\nu = 5/2$ ,  $7/3$ ,  $8/3$ ,  $11/5$ , and  $14/5$  are clearly seen with deep minima in  $S_{xx}$  at the appropriate magnetic fields developing as the temperature is reduced. This behavior is qualitatively similar to that observed for FQH states in the  $N = 0$  LL, as was seen in Chapter 8.

The temperature dependence of  $S_{xx}$  at  $\nu = 5/2$  and  $7/3$  is shown in Fig. 9.3 (b). From about  $T = 200$  mK down to roughly  $T = 50$  mK  $S_{xx}$  is thermally activated ( $S_{xx} \sim e^{-\Delta/2T}$ ) at both of these fillings. Energy gaps of  $\Delta \approx 430$  mK, for both  $\nu = 5/2$  and  $7/3$ , are estimated from the data. Statistically identical values are obtained from both mesas of diving board B. These gap values are consistent with that determined using  $R_{xx}$  measurements from diving board A (Fig. 9.2 (b)). At lower temperature  $S_{xx}$  deviates from simple thermally activated behavior, suggesting

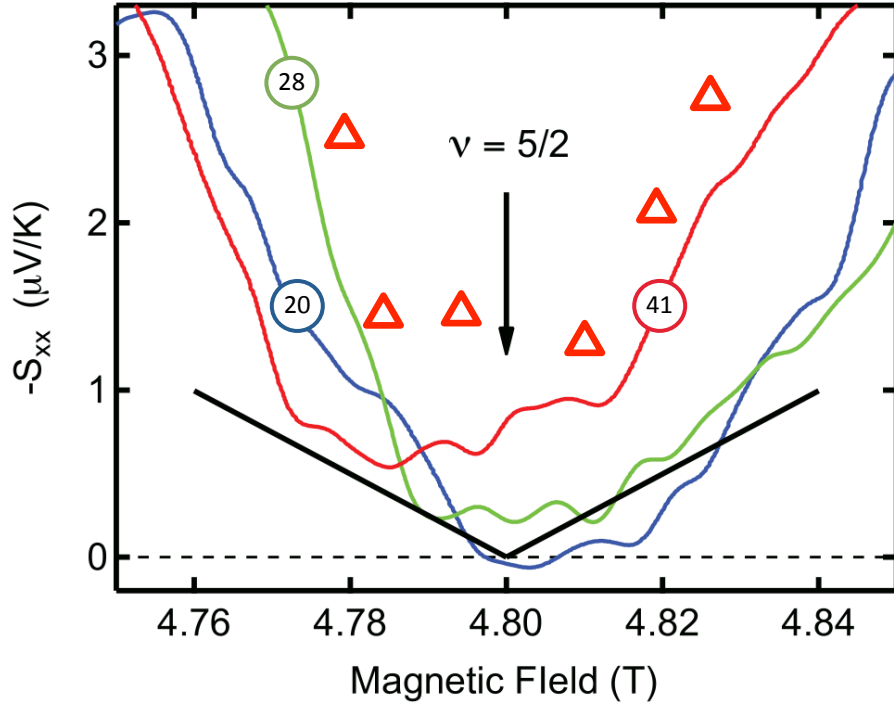


Figure 9.4:  $S_{xx}$  near  $\nu = 5/2$  at  $T = 20$  mK (blue), 28 mK (green) and 41 mK (red). Solid black lines give theoretical prediction of Yang and Halperin [93]. Reprinted with permission from W.E. Chickering, J.P. Eisenstein, L.N. Pfeiffer, and K.W. West, *Phys. Rev. B* **87**, 075302, (2013). Copyright 2013 by the American Physical Society.

the increasing importance of hopping between localized electronic states. Similar low-temperature deviations from thermal activation are commonplace in resistivity measurements in QH states.

We now turn to the question of non-abelian statistics at  $\nu = 5/2$ . Figure 9.4 compares our low-temperature  $S_{xx}$  data near  $\nu = 5/2$  with the theoretical prediction of YH [93]. The open triangles correspond to  $S_{xx}$  acquired from diving board A at  $T = 82$  mK. The colored curves correspond to  $S_{xx}$  acquired from diving board B at  $T = 20$  mK, 28 mK, and 41 mK. And the solid black lines represent the quantitative prediction of YH for the thermopower of the MR Pfaffian state at  $\nu = 5/2$ . While our data are quantitatively roughly consistent with the theory, they do not offer compelling support for it. At these low temperatures, the sub- $\mu\text{V}/\text{K}$  thermopower results in extremely small thermoelectric voltages ( $\lesssim 2$  nV at  $T = 20$  mK with  $\Delta T = 2$  mK).

Substantial signal averaging is thus required and renders the data sensitive to long-term drifts in the measurement set up. Indeed, as Fig. 9.4 shows, the location of the  $\nu = 5/2$  minimum is not precisely the same at each temperature; small, history-dependent shifts of FQH minima were frequently encountered. These difficulties prevented us from cleanly observing the expected temperature independence of  $S_{xx}$  on the flanks of the  $\nu = 5/2$  minimum.

Future thermopower experiments may clarify the situation at  $\nu = 5/2$ . In particular, Barlas and Yang recently suggested [120] that using a Corbino thermopower configuration might significantly improve our ability to distinguish non-abelian from abelian QH states. In contrast to the low-temperature Hall bar thermopower, which is proportional to the entropy per electron per electron charge, the low-temperature Corbino thermopower reflects the entropy *per quasiparticle per quasiparticle charge*. In Appendix F we review the physics of Corbino thermopower and compare it to the Hall bar thermopower.

## 9.2 Reentrant Integer Quantum Hall Effect

### 9.2.1 $N \geq 2$ LLs

We now digress from our subject of the  $N = 1$  LL to briefly discuss the peculiar many-body phases encountered at higher ( $N \geq 2$ ) LLs. The most conspicuous of these manifests itself as a strongly anisotropic magnetoresistance at half filled LLs (e.g.  $\nu = 9/2, 10/2, 11/2, \dots$ ) appearing only in samples of the highest quality at very low temperatures ( $T \lesssim 150$  mK) [135, 136, 137]. To illustrate this we reproduce a plot from an article by Cooper et al. [4] shown in Fig. 9.5. In part (a) of the figure we see the longitudinal resistances  $R_{xx}$  and  $R_{yy}$  measured with current flowing along the orthogonal crystal directions  $\langle 1\bar{1}0 \rangle$  and  $\langle 110 \rangle$ , respectively. We see a maximum in  $R_{xx}$ , but a minimum in  $R_{yy}$ , at  $\nu = 9/2$ . This dramatic anisotropy, which is absent from the  $N = 0$  and 1 LLs, lacks an explanation based solely on QH physics.

Adjacent to the anisotropic feature shown in Fig. 9.5 (a) are isotropic regions,

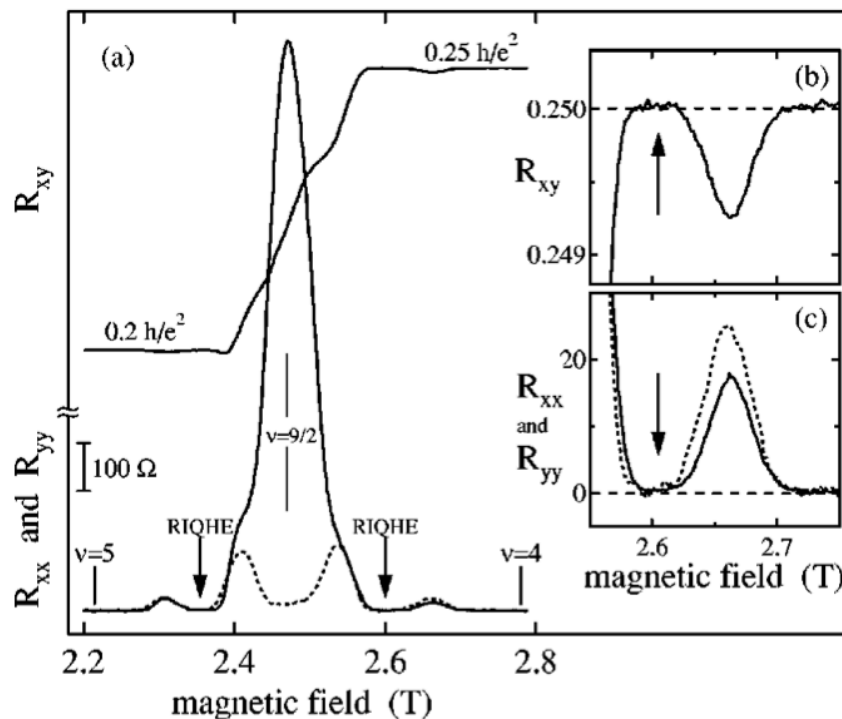


Figure 9.5: Anisotropy and the reentrant integer quantum Hall effect (RIQHE) in higher ( $N \geq 2$ ) LLs. (a) Longitudinal (solid line:  $R_{xx}$ , dotted line  $R_{yy}$ ) and Hall ( $R_{xy}$ ) resistance in the  $N = 2$  LL at  $T = 50$  mK. Arrows indicate the positions of RIQHEs. Insets (b) and (c) magnify the RIQHE region. Reprinted with permission from K.B. Cooper, M.P. Lilly, J.P. Eisenstein, L.N. Pfeiffer, and K.W. West, *Phys. Rev. B* **60**, R11285 (1999). Copyright 1999 by the American Physical Society.

labeled with arrows, where both  $R_{xx}$  and  $R_{yy}$  vanish. At the same time, the Hall resistance  $R_{xy}$  quantizes, but unlike a FQHE it assumes a value corresponding to the nearest IQHE. The inset (b) of Fig. 9.5 clearly shows this, magnifying  $R_{xy}$  in the labeled region near  $B = 2.6$  T. This surprising behavior deviates from standard QH transport in that  $R_{xy}$  is non-monotonic as a function of magnetic field  $B$  as it returns to the value of the plateau associated with the nearest integral filling factor  $\nu$ . As such, its discoverers dubbed the phenomenon the *reentrant integer quantum Hall effect* (RIQHE).

Predictions, based on Hartree-Fock theory, of energy minimizing electron density modulations collectively known as *charge density waves* (CDWs) offer a credible ex-

planation for this transport behavior [163, 164, 165]. Like the FQHE and the Wigner Crystal (WC), these CDW phases are driven by electron-electron interactions. The models describe unidirectional CDWs at half filling known as the *striped phase* resulting in strongly direction-dependent resistivity. Meanwhile, these stripes are expected to crossover into a lattice arrangement reminiscent of the WC known as the *bubble phase* as the LL filling deviates from one half. A key distinction between the WC and the bubble phase is that in the latter case multiple electrons can occupy a single lattice site. Disorder induced pinning of the bubble phase may result in an insulating 2DES bulk, a situation that would mimic the IQHE and thereby yield the RIQHE.

### 9.2.2 $N = 1$ LL

Clearly these higher LLs comprise a regime that is very differently from that of  $N = 0$  LL. Meanwhile, the  $N = 1$  LL resembles both the lowest LL and higher LLs. Like the lowest LL, we observe several FQHEs in the first excited LL including the Laughlin states at  $\nu = 2 + 1/3$  and  $2 + 1/5$  along with their particle-hole conjugate states at  $\nu = 3 - 1/3$  and  $3 - 1/5$ . Unlike the lowest LL, however, we also observe the enigmatic FQHE at  $\nu = 5/2$ , clearly demonstrating that this unique LL cannot be fully understood through simple analogy with the situation at  $N = 0$ . At the same time, shortly after the discovery of the RIQHE in higher LLs, Eisenstein et al. [140] encountered similar phenomena in the first excited LL.

In Fig. 9.6 we present  $R_{xy}$  versus  $B$  in the first excited LL measured in diving board B. At  $T = 60$  mK  $R_{xy}$  is a monotonic function of  $B$  showing wide plateaus at integral filling factors  $\nu = 2, 3,$  and  $4$  along with narrower plateaus at the fractional filling factors  $\nu = 7/3$  and  $5/2$ . At this temperature we also observe the beginning of plateau formation at several fractional filling factors including  $\nu = 11/5, 8/3,$  and  $14/5$ , while  $R_{xy}$  follows the classical Hall line between the plateaus at  $\nu = 3$  and  $4$ . At  $T = 19$  mK the shape of  $R_{xy}$  versus  $B$  is dramatically altered. Compared to  $T = 60$  mK, we now observe well formed plateaus at  $\nu = 8/3, 14/5,$  and  $7/2$ . More striking, however, are the non-monotonic features occurring between the labeled filling

factors in the figure.

The  $T = 19$  mK data shown in Fig. 9.6 strongly resembles that originally reported [140] by Eisenstein et al. in both quality as well as in the relative strengths of the integer quantization of each of the non-monotonic features with respect to filling factor. Like the RIQHE observed in the  $N \geq 2$  LLs, the Hall resistance  $R_{xy}$  demonstrates a tendency to return to the nearest IQHE plateau value. Unlike the analogous phenomenon observed in higher LLs, however, in the  $N = 1$  LL RIQHEs occur four times between integer fillings. Moreover, the onset temperature is much lower. While the RIQHE of  $N \geq 2$  LLs has been observed just below  $T = 150$  mK [135], the analogous effect in the  $N = 1$  LL requires temperatures below  $T = 50$  mK. Despite these differences, in all cases the RIQHE is consistent with the localization of electrons in the topmost, partially filled LL.

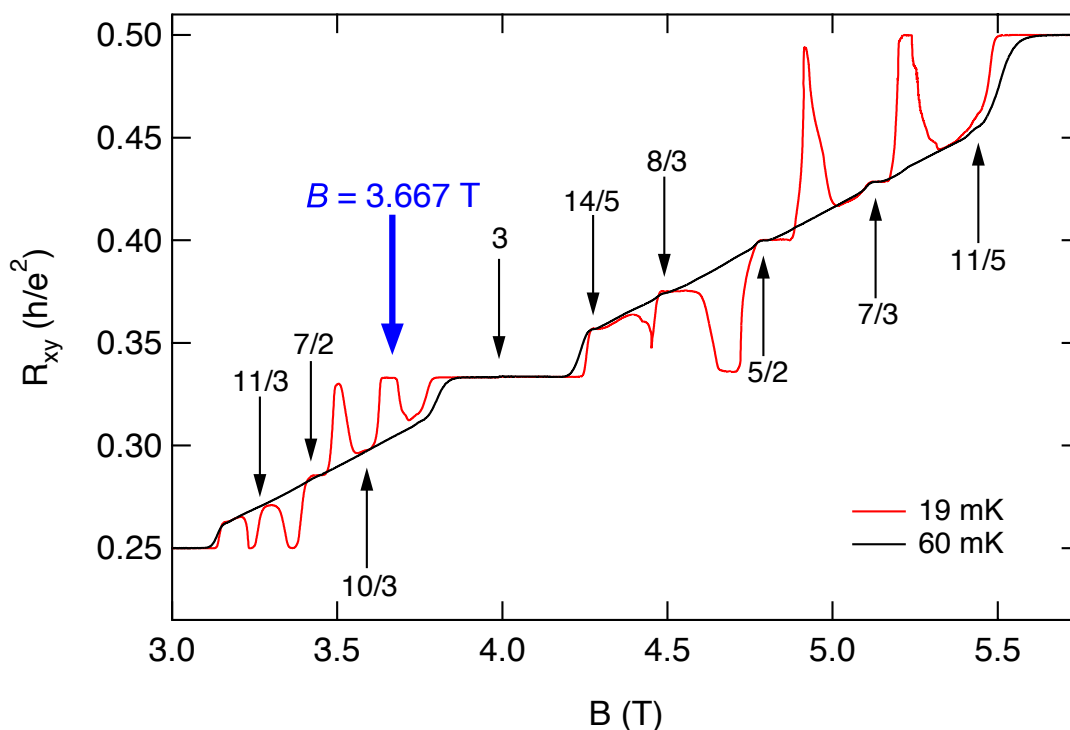


Figure 9.6: RIQHE in the  $N = 1$  LL.  $R_{xy}$  vs  $B$  is shown for both  $T = 60$  mK and 19 mK measured in diving board B. Several filling factors  $\nu$  are labeled. The thick arrow labeled  $B = 3.667$  T corresponds to the value of  $B$  in Fig. 9.7.

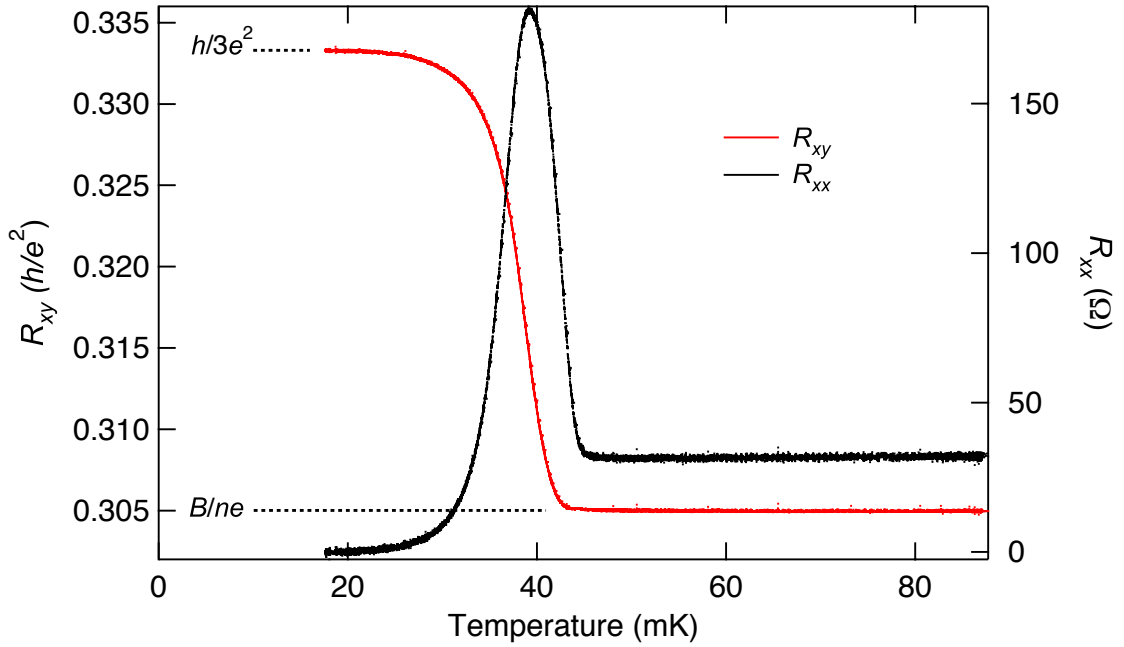


Figure 9.7: Transverse resistance  $R_{xy}$  along with longitudinal resistance  $R_{xx}$  vs temperature  $T$  at  $B = 3.667$  T where a strong RIQHE is observed at  $T \sim 20$  mK. Refer to the thick arrow in Fig. 9.6 for context.

Figure 9.7 shows the temperature dependence of both  $R_{xy}$  and  $R_{xx}$  at  $B = 3.667$  T (position in Fig. 9.6 is labeled) in diving board B. These data offer a revealing vantage point of the RIQHE in the  $N = 1$  LL. At  $T \gtrsim 45$  mK both  $R_{xy}$  and  $R_{xx}$  demonstrate no discernible temperature dependence. Below  $T = 45$  mK both coefficients exhibit rapid evolution with decreasing temperature. Between  $T = 45$  mK and 20 mK,  $R_{xy}$  jumps from its classical Hall value of  $B/ne$  to  $h/3e^2$ , the value associated with the IQHE at  $\nu = 3$ . Meanwhile,  $R_{xx}$  passes through a maximum before vanishing at  $T \sim 20$  mK. This sudden and impressive onset of the RIQHE is in stark contrast to the thermally activated behavior associated with QHEs.

A recent study by Deng et al. [166] focuses on measurements like that of Fig. 9.7 with particular attention paid to the onset temperature  $T_c$  corresponding to the peak in  $R_{xx}$  versus  $T$ . They find  $T_c$  in the lower spin branch (i.e. where  $2 < \nu < 3$ ) is consistently larger, yet follows the same trend as in the upper spin branch (i.e. where  $3 < \nu < 4$ ). Scaling  $T_c$  versus  $\nu^*$  (the fractional part of the total filling factor  $\nu$ ) by the

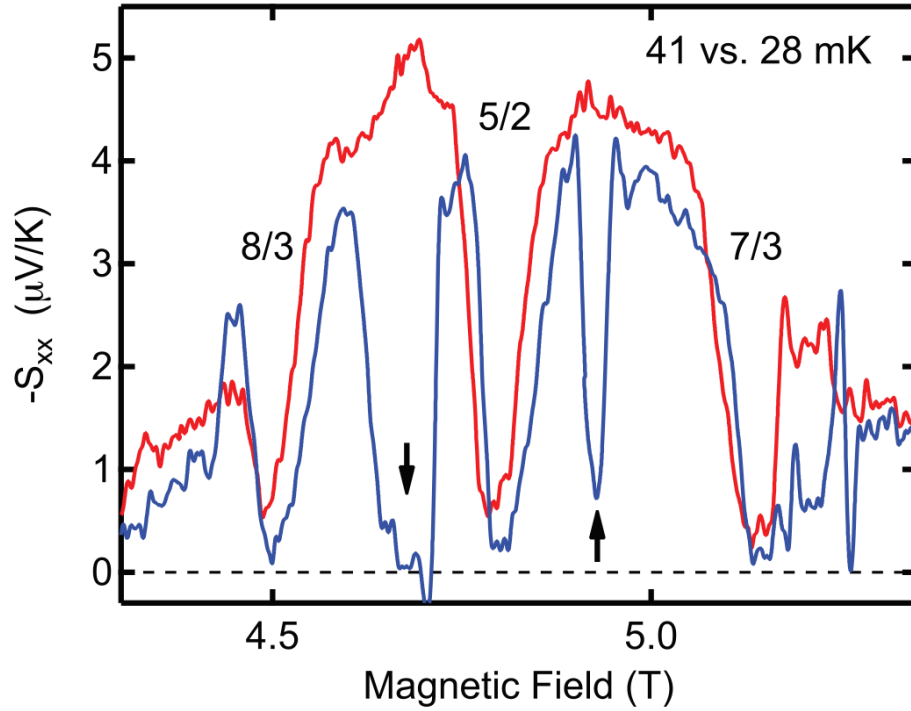


Figure 9.8:  $S_{xx}$  between  $\nu = 2$  and  $\nu = 3$  at  $T = 41$  mK and  $T = 28$  mK in diving board B. Arrows indicate field locations where a particularly strong temperature dependence is observed. Reprinted with permission from W.E. Chickering, J.P. Eisenstein, L.N. Pfeiffer, and K.W. West, *Phys. Rev. B* **87**, 075302, (2013). Copyright 2013 by the American Physical Society.

Coulomb energy  $\varepsilon_C = e^2/\epsilon l_B$ , they show the data of the two spin branches collapse onto each other providing compelling evidence that Coulomb interactions drive these RIQHEs. This is consistent with the picture of a collectively pinned bubble phase as the 2DES ground state for these filling factor ranges.

### 9.2.3 Experimental Results

We now turn to the manifestation of these RIQHEs within the thermopower. As the temperature is reduced below about  $T = 40$  mK substantial changes are observed in the thermopower in the  $N = 1$  LL. These changes are most dramatic at magnetic field locations between the prominent FQHEs at  $\nu = 5/2$  and  $7/3$  and between  $\nu = 5/2$  and  $8/3$ . Figure 9.8 illustrates the change in  $S_{xx}$  that develops between  $T = 41$  mK and

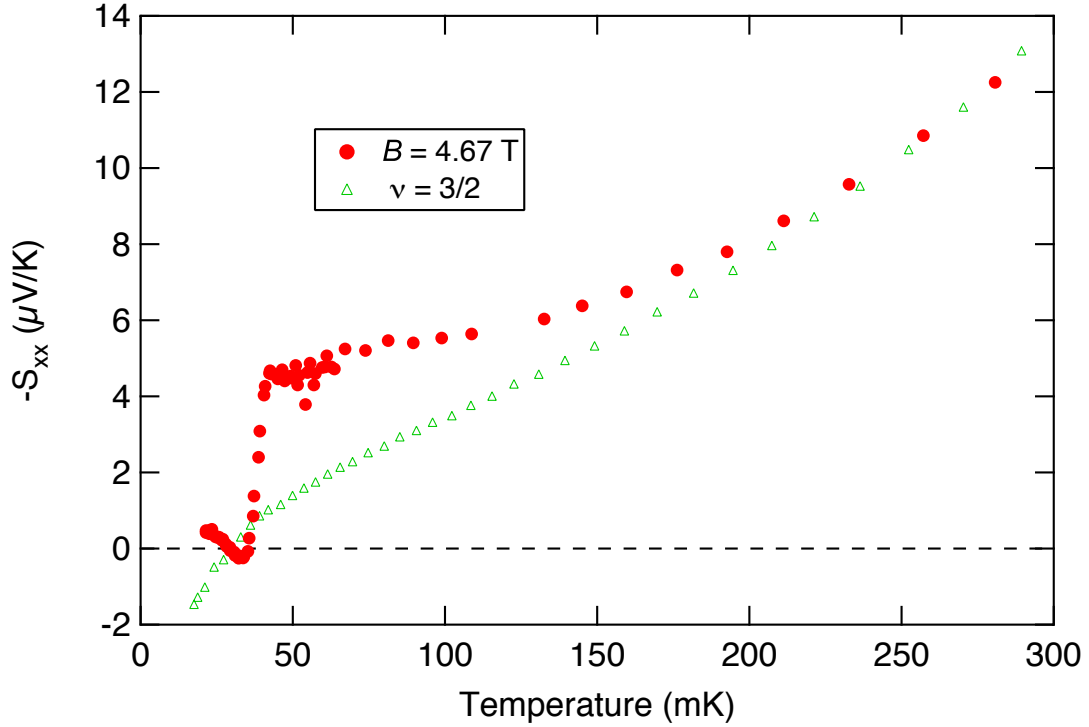


Figure 9.9: Longitudinal thermopower  $S_{xx}$  vs temperature  $T$  at  $B = 4.67$  T and  $\nu = 3/2$  ( $B = 8.1$  T) in diving board B.

28 mK as measured in diving board B. In particular around  $B = 4.67$  T and 4.93 T deep minima appear in  $S_{xx}$ . These minima develop quite suddenly as functions of temperature, with Fig. 9.9 showing the temperature dependence of  $S_{xx}$  at  $B = 4.67$  T.

Similarly abrupt collapses of  $S_{xx}$  are seen at other RIQHE states in the  $N = 1$  LL, including those adjacent to the FQH state at  $\nu = 7/2$  in the upper spin branch of the LL. In some cases  $S_{xx}$  first shows a local maximum before falling toward zero as  $T \rightarrow 0$ . We find that the collapsing of  $S_{xx}$  coincides with transitions in  $R_{xy}$  and  $R_{xx}$  like those in Fig. 9.7. These thermopower results, coupled with recent resistivity measurements [166] and prior reports of magnetic field hysteresis and non-linear transport signatures [140], strongly suggest that the RIQHE develops via finite-temperature first-order phase transitions within the 2DES.

The tendency of the thermopower to vanish during the onset of a RIQHE is consistent with the localization of the electrons or holes of the partially filled  $N =$

1 LL. These localized electrons or holes will not participate in the thermoelectric transport such that the remaining carriers fill an integral number of LLs. Thus, like an IQH state, we expect  $S_{xx}$  to vanish as  $T \rightarrow 0$ . It seems that our interpretation of the thermopower as the entropy per carrier may hold here with the caveat that only a subset of electrons—those in the filled  $N = 0$  LL—qualify as *carriers*.

The behavior of  $S_{xx}$  in the vicinity of a RIQHE differs from that of an IQH state in an important respect, however. At the lowest temperatures ( $T \sim 20$  mK) aperiodic fluctuations are observed. Moreover,  $S_{xx}$  can become positive in narrow ranges of magnetic field (the conventional sign of  $S_{xx}$  for electrons is negative). These low-temperature fluctuations are qualitatively similar to those observed in the vicinity of  $\nu = 3/2$  (see Section 8.3.1) as well as elsewhere in the  $N = 0$  LL (see Section 8.3.5). In all cases, the onset of these fluctuations occurs quickly as a function of temperature below about  $T = 40$  mK. Moreover, in all cases, the exact field dependence differs for the two independent 2DES mesas and varies within an individual mesa depending on the thermal history of the sample. Notably, such fluctuations are never observed within the  $|S_{xx}|$  minima associated with IQH states. The common onset temperature and characteristics of the fluctuations observed in the vicinity of the RIQHEs of the  $N = 1$  LL with those observed in  $N = 0$  LL suggests a common mechanism is at play. As discussed in Section 8.3.5, we attribute these fluctuations to effects analogous to universal conductance fluctuations (UCFs) in disordered mesoscopic conductors.

For comparison, we include  $S_{xx}$  versus  $T$  at  $\nu = 3/2$  in Fig. 9.9. The figure demonstrates that at high temperatures ( $T \gtrsim 200$  mK)  $S_{xx}$  at  $B = 4.67$  T strongly resembles that at  $\nu = 3/2$  in both magnitude and temperature dependence. Recall that we attribute the measured thermopower at  $\nu = 3/2$  in this temperature regime to a combination of the diffusion and phonon drag of noninteracting  $^2$ CFs (see Section 8.3.1). Given this resemblance, together with the proximity to half-filling, it seems likely that the higher temperature data in Fig. 9.9 also originates from a sea of weakly interacting  $^2$ CFs.

At lower temperatures, just above the abrupt transition, Fig. 9.9 demonstrates the stark difference between  $S_{xx}$  at  $B = 4.67$  T and that at  $\nu = 3/2$ . Surprisingly,

$S_{xx}$  at  $B = 4.67$  T is roughly temperature independent in this region. This is a strong deviation from the linear temperature dependence at  $\nu = 3/2$ . A temperature independent thermopower is not consistent with ordinary metallic or insulating behavior, but rather indicates an unconventional conducting phase. It is well-known that strongly interacting localized electrons that can be described by a Hubbard model are expected to exhibit a temperature independent thermopower [167]. However, it seems unlikely that the present system can be well described by such a model. Perhaps some insight can be gained from the liquid-solid hybrid phases predicted [168, 169] to exist between a Fermi liquid and a Wigner crystal.

### 9.3 Summary

The first excited LL provides a rich variety of correlated electron states. In addition to FQHEs, like that at  $\nu = 7/3$ , which can be understood as IQHEs of noninteracting CFs, we find exotic FQHEs at  $\nu = 5/2$  and  $7/2$ . The latter are believed to be well-described by the Moore-Read Pfaffian, or Anti-Pfaffian, wavefunction, which may be viewed as a condensate of p-wave cooper pairs of CFs. This is a particularly intriguing possibility since the excitation quasiparticles of these states obey non-Abelian statistics, which is of both fundamental interest and exciting due to its potential application to quantum computing. A recent prediction claims that the quasiparticles of these states, so-called non-Abelian anyons, will yield an enhanced entropy, and hence, an enhanced thermopower.

Unlike compressible states at  $B = 0$  and  $\nu = 3/2$ , we find the thermopower at  $\nu = 5/2$  reflects a FQH energy gap  $\Delta$ . From our measurements of the longitudinal thermopower  $S_{xx}$  versus temperature  $T$ , we are able to measure  $\Delta$ . Using our quasi-DC protocol with diving board A, we estimate  $\Delta \approx 370$  mK. Using low frequency AC lock-in detection with diving board B, we estimate  $\Delta \approx 430$  mK. These estimates are consistent with previously reported resistivity measurements as well as those made in our samples, which confirms that the incompressibility at  $\nu = 5/2$  is readily detectable via thermopower. We measured  $S_{xx}$  as a continuous function of magnetic field  $B$

through the minimum at  $\nu = 5/2$  at temperatures as low as  $T = 20$  mK. While our results are roughly consistent with the theoretical thermopower of the Moore-Read state, they do not provide convincing support for it.

The first excited LL also distinguishes itself from the lowest LL with the presence of multiple reentrant integer quantum Hall effects. These RIQHEs resemble those observed in higher LLs, which are attributed to the formation of charge density waves. At about  $T = 40$  mK, we observe an abrupt collapse of the thermopower that is coincident with the RIQHEs in both spin branches of the  $N = 1$  LL. Our results, together with recent electrical transport measurements, lend strong support to the notion that these RIQHEs develop via finite-temperature first-order phase transitions.

Finally, observation of a temperature-independent  $S_{xx}$  at temperatures just above the RIQHE transition suggests the existence of an unconventional conducting phase. At even higher temperatures ( $T \gtrsim 200$  mK)  $S_{xx}$  is consistent with that of a conventional 2D metal experiencing phonon drag as evidenced by comparison to data at  $\nu = 3/2$ . It is therefore plausible that the unconventional conducting phase resembles those predicted to be intermediate between a Fermi liquid and a Wigner crystal.

# Appendix A

## Properties of a 2DES in GaAs

<b>Units:</b> Carrier Density	$N_S$	$10^{11} \text{ cm}^{-2}$
Resistivity	$\rho$	$\Omega$ per square
Mobility	$\mu_e$	$10^6 \text{ cm}^2/\text{Vs}$
Magnetic Field	$B$	T
Energy		K or meV
Effective Mass (conduction band)	$m^*$	$= 0.067m_0$
$g$ -factor:	$g$	$= -0.44$
Dielectric constant (appx.)	$\epsilon$	$= 13 \times \epsilon_0$
Fermi Wavevector:	$k_F$	$= 7.93 \times 10^5 \times N_s^{1/2} \text{ cm}^{-1}$
Fermi Energy:	$E_F$	$= 3.58 \times N_S \text{ meV}$
	$E_F$	$= 41.5 \times N_s \text{ K}$
Fermi Velocity:	$v_F$	$= 1.37 \times 10^7 \times N_S^{1/2} \text{ cm/s}$
Mobility from Resistivity:	$\mu_e$	$= 62.4 \times N_S^{-1} \times \rho^{-1}$
Momentum Lifetime:	$\tau_m$	$= 38.1 \times \mu \text{ ps}$
Mean Free Path:	$\lambda$	$= 5.22 \times \mu \times N_S^{1/2} \text{ }\mu\text{m}$
Magnetic Length:	$\ell$	$= 257 \times B^{-1/2} \text{ }\text{\AA}$
Classical Cyclotron Radius:	$R_c$	$= 522 \times N_S^{1/2} \times B^{-1} \text{ }\text{\AA}$
$\nu = 1$ Magnetic Field:	$B_{\nu=1}$	$= 4.14 \times N_S \text{ T}$
Cyclotron Energy:	$\hbar\omega_c$	$= 20.1 \times B \text{ K}$
Zeeman Splitting:	$g\mu_B B$	$= 0.29 \times B \text{ K}$
Coulomb Energy:	$e^2/\epsilon\ell$	$= 50 \times B^{1/2} \text{ K}$

# Appendix B

## Sample Processing

This appendix provides a detailed description of the procedures used to fabricate the devices discussed in this thesis. Most of these procedures and techniques were developed and passed down by past and present members of the Eisenstein Group. For general information on the processing of GaAs samples, see Ref. [170].

### B.1 Sample Cleaving

Samples were cleaved from parent wafers of GaAs/AlGaAs heterostructures grown via MBE by either J.L. Reno<sup>1</sup> or L.N. Pfeiffer and K.W. West<sup>2</sup> onto (100)-oriented GaAs substrates. In the case of the Hot-Electron Thermocouple, a  $5 \times 5$  mm sample was cleaved. In the case of the diving board devices,  $3 \times 12$  mm and  $6 \times 12$  mm samples were cleaved. The same procedure was used in all cases.

Place the wafer onto a clean, soft surface such as a clean pad of paper or a clean sheet of paper covering a soft-cover book. A (100)-oriented substrate will readily cleave along either the [110] or  $[1\bar{1}0]$  directions. Position a metal ruler flush against a previously cleaved edge of the wafer to identify the location of the desired new cleave. Using a scribe, carefully score the corner of the wafer at the location of the desired new cleave. The score should be small, about  $100 \mu\text{m}$  long and  $50 \mu\text{m}$  deep. Next, turn the wafer over such that the shiny (heterostructure) side is face-down on the paper. Use the ruler to locate the position of the score. The scribe tool is equipped

---

<sup>1</sup>Sandia National Laboratories, Albuquerque, New Mexico 87185 USA

<sup>2</sup>Department of Electrical Engineering, Princeton University, Princeton, New Jersey 08544 USA

with a rounded end that is used to apply pressure to the backside of the wafer at the location of the score in order to produce the cleave. To more precisely localize the pressure, the rounded outside portion of fine pointed steel tweezers can be used for this purpose.

While cleaving, be careful to keep GaAs dust off the surface of the sample. Such GaAs debris can scratch the sample's surface resulting in serious damage to the device. It also important to always wear gloves when cleaving to avoid contact with GaAs dust as it is toxic.

## B.2 Cleaning the Sample

After cleaving and before any processing a sample should be cleaned. Typically, the parent wafer is pristine and sample cleaning need only consist of immersing the sample in acetone for 3 minutes followed by immersing for 1 minute in isopropyl alcohol (IPA). Be sure to minimize the time between removal from the acetone and submerging in IPA as allowing the former to dry on the sample surface can result in residue formation. After removing from the IPA, immediately blow dry with compressed nitrogen by orienting the dryer nozzle perpendicular to the sample surface at a distance of about a centimeter. In this way, the compressed nitrogen pushes the IPA off the surface taking with it any remaining 'dirt'.

In the case that the above procedure is insufficient, the sample can initially be immersed in trichloroethylene for several minutes. This solvent is highly effective at removing organic material. If necessary, sonicating the sample while immersed in acetone or trichloroethylene can provide mechanical assistance in removing material attached to a sample surface.

## B.3 Photolithography

Several processing recipes, including that for etching a mesa, creating ohmic contacts, and depositing metallic top gates, involve patterning the sample surface via

photolithography. In each case, the following procedure is used.

### **Clean Sample**

Follow the procedure of Sec. B.2.

### **Dehydration Bake**

Place directly onto hotplate set at 150° C for 10 minutes in order to evaporate any residual moisture. Remove and allow to cool to room temperature.

### **Spin Adhesion Promotor**

To minimize the likelihood of photoresist detaching from sample surface and compromising the pattern quality, apply a single drop of HMDS adhesion promotor and spin at 3000 rpm for 30 seconds.

### **Spin Resist**

Apply a single drop of AZ5214E positive photoresist and spin at 5000 rpm for 30 seconds for a  $\sim 1 \mu\text{m}$  thick layer.

### **Soft Bake**

Place sample directly onto hotplate set at 100° C for 45 seconds.

### **Expose to UV**

Align sample to photo-mask using Karl Suss MJB-3 Mask Aligner. Expose to 15 mW/cm<sup>2</sup> UV for 15 seconds. Note that since we are using a positive photoresist, the exposed regions will be removed during development.

### **Develop Pattern**

Immerse in H<sub>2</sub>O:AZ400K (4:1) solution for  $\sim 45$  seconds. For best results, visually monitor the sample while gently swirling the solution in order to perfectly time the development. Immediately following development, immerse in deionized (DI) water for 30 seconds, followed by a second immersion (fresh volume of DI water) for another 30 seconds. Gently blow dry with compressed nitrogen.

### Inspect Pattern

Inspect pattern using the mask aligner. If quality of pattern is acceptable, then continue. Otherwise, clean sample and repeat procedure.

## B.4 Etching the Mesa

All of the devices studied for this thesis require that the 2DES be confined to some geometry in the  $x$ - $y$  plane. This is achieved by patterning the sample via photolithography and chemically etching away regions where we do not want the 2DES. At cryogenic temperatures, the 2DES will only exist within the unetched region, or *mesa*.

### Photolithography

Follow the procedure of Sec. B.3.

### Hard Bake

Place sample directly onto hotplate set at 100° C for 75 seconds to bake the patterned protective layer of photoresist.

### Wet Etch

Immerse sample in etchant comprised of  $\text{H}_2\text{O} : \text{H}_3\text{PO}_4 : \text{H}_2\text{O}_2$  (50 : 5 : 1), which etches away GaAs at  $\sim 0.1 \mu\text{m}$  per minute. A 4 minute etch is therefore sufficient to remove the quantum well, and therefore, preclude the formation of the 2DES within the etched regions of the samples studied for this thesis.

### Remove Photoresist

Immerse sample in n-butyl acetate at 75° C for 15 minutes to remove the hard baked photoresist. Rinse by immersing in IPA for 1 minute and then blow dry with compressed nitrogen.

## B.5 Ohmic Contacts

Ohmic contacts provide electrical connections to the 2DES that approximately adheres to Ohm's Law. In addition, in the case of the Hot-Electron thermocouple, they

thermally ground the 2DES with respect to the surrounding GaAs/AlGaAs crystal lattice. Our group routinely employs two different recipes for processing ohmic contacts.

### **B.5.1 InSn Ohmic Contacts**

Eutectic indium-tin alloy (InSn) ohmic contacts offer the advantage of not requiring photolithography. This is preferable when quickly fabricating samples for wafer characterization or when a photomask is unavailable. Note that pure indium can be used but typically results in more resistive contacts compared with those made from InSn.

#### **Clean Sample**

Follow the procedure of Sec. B.2.

#### **Apply InSn**

With the sample viewed at low magnification through a stereo microscope, use an NT1 or NT1S soldering tip at 340° C to apply small dots of eutectic InSn (dia.  $\sim 200 - 400 \mu\text{m}$ ) onto the sample surface at the desired contact locations. The soldering tip used should be dedicated solely to this purpose to avoid contamination.

#### **Anneal Sample**

Place sample on the heating element and seal within the chamber of a rapid thermal annealer. Flow a forming gas of 85% N<sub>2</sub> and 15% H<sub>2</sub> at 2 SLPM for 5 minutes prior to applying heat to purge the chamber of oxygen. Continue to flow forming gas and anneal sample at 425° C for 5 minutes. Continue to flow forming gas and allow chamber to cool to below 40° C before turning off gas and removing sample from the chamber.

## B.5.2 Ni/AuGe Ohmic Contacts

Ni/AuGe ohmic contacts are lithographically patterned, and therefore, can be made much smaller, can be arbitrarily shaped, and require depositing much less metal as compared to the Indium variety.

### Photolithography

Follow the procedure of Sec. B.3.

### Evaporate Ni/AuGe

Use a thermal evaporator to first deposit Ni followed by AuGe without exposing the sample to atmosphere between evaporations. Deposit 135 Å of Ni at  $\sim 5$  Å/s from a tungsten boat. Then, deposit 1500 Å of AuGe (88 : 12 by weight) at  $\sim 25$  Å/s from a Al<sub>2</sub>O<sub>3</sub> coated tungsten boat (e.g. RD Mathis S35B-AO-W).

### Lift Off Ni/AuGe

Immerse sample in n-butyl acetate at 60° C for 15 minutes. Transfer to IPA and squirt surface while still submerged to provide mechanical assistance in removing excess metal. Transfer to a second volume of IPA and inspect with a microscope (e.g. mask aligner) while still submerged. If 'lift off' was successful and patterned metal is acceptable, remove sample from IPA and blow dry with compressed nitrogen. Otherwise, repeat procedure.

### Anneal Sample

Place sample on the heating element and seal within the chamber of a rapid thermal annealer. Flow a forming gas of 85% N<sub>2</sub> and 15% H<sub>2</sub> at 2 SLPM for 5 minutes prior to applying heat to purge the chamber of oxygen. Continue to flow forming gas and anneal sample at 440° C for 15 minutes. Continue to flow forming gas and allow chamber to cool to below 40° C before turning off gas and removing sample from the chamber.

## B.6 Al Top Gates

### Photolithography

Follow the procedure of Sec. B.3.

### Evaporate Al

Use a thermal evaporator to deposit 1800 Å of Al (5N purity) at  $\sim 20$  Å/s from a tungsten basket.

### Lift Off Al

Immerse sample in n-butyl acetate at 60° C for 15 minutes. Transfer to IPA and squirt surface while still submerged to provide mechanical assistance in removing excess metal. Transfer to a second volume of IPA and inspect with a microscope (e.g. mask aligner) while still submerged. If ‘lift off’ was successful and patterned metal is acceptable, remove sample from IPA and blow dry with compressed nitrogen. Otherwise, repeat procedure.

## B.7 Thin Sample

The diving board devices studied for this thesis were thinned to  $\sim 130$  μm, having most of their substrate removed, in order to reduce their thermal conductance. This was achieved using the chemical-mechanical etching process outlined here. Note that all structures on the sample surface must have a negligible profile to avoid damage during this procedure. Specifically, either use Ni/AuGe ohmic contacts or apply InSn contacts *after* the sample is thin.

### Clean Sample

Follow the procedure of Sec. B.3.

### Wax Down Sample

Using *Quickstick 135*, wax the sample, face down and centered, onto a clean quartz disc. Additionally, wax down an appropriate (4-6 depending on sample size) spacer samples uniformly distributed around the main sample. The spacer

samples will ideally consist of the same material (at minimum, the same substrate) as the main sample. Samples can be waxed down by placing the quartz disc onto a hot plate set to 150° C and depositing a few flakes of solid wax. (An industrial razor blade can be used to chip off tiny flakes of wax from a solid blob.) Place the sample, face down, onto the wax. *Carefully*, use a wooden stick with a flat end to slowly press the sample down flush onto the disc. Once all samples are waxed into place, use an acetone squirt bottle to spray wax beads surrounding the main and spacer samples. The acetone will slowly erode the excess wax. Rinse samples and disc with IPA and blow dry with compressed nitrogen. Examine with a magnifier to ensure that 1) all excess wax has been removed, and 2) the surface of main sample is completely protected by wax.

### **Prepare for Bromine-Methanol Etch**

Tightly wrap a square quartz plate ( $\sim 6 \times 6 \text{ in}^2$ ) with filter paper, securing with minimal amount of masking tape, such that one side is free of folds and edges. The filter paper will act as an ultra fine abrasive. While working under an acid hood and wearing neoprene gloves, long-sleeved lab coat, and face shield, prepare a dilute solution of bromine by adding 5 mL of bromine to 50 mL of methanol. *Be very careful to avoid direct contact with or inhalation of bromine, which is highly toxic.* Install the quartz disc containing sample into custom teflon chuck, securing with three drops of water, which hold the disc in place via capillary action. The teflon chuck has both a coarse and fine end. Initially, the coarse end should be used in which the sample is recessed  $\sim 200 \mu\text{m}$  into the chuck allowing for more aggressive etching.

### **Perform Bromine-Methanol Etch**

First saturate the filter paper covered quartz plate with methanol, then uniformly pour  $\sim 10\%$  of the bromine-methanol etchant onto the plate. Allowing only the weight of the chuck to provide the downward force, slide the sample against the etchant in a figure-eight pattern at  $\sim 1 \text{ Hz}$  for  $\sim 50$  iterations. Rinse the sample and chuck with methanol from a squirt bottle, wick away the

remaining bromine-methanol, remove quartz disc from the chuck, and then blow dry sample and disc with compressed nitrogen. Use a dial indicator to measure the sample thickness. Repeat this procedure until the sample thickness approaches  $\sim 300 \mu\text{m}$ . At this point, the fine end of the chuck should be used in which the sample is fully exposed. Continue the procedure as before except now perform only  $\sim 20$  iterations between each thickness measure to more precisely monitor your progress. Watch out for thickness gradients resulting from the torque that inevitably results from sliding the chuck against the paper covered plate. To compensate for this, a good policy is to rotate the sample  $90^\circ$  following each thickness measurement. Continue until sample thickness reaches  $130 \mu\text{m}$ .

### **Powder Blast Backside**

Powder blast the backside of the sample following the above thinning procedure with sample still waxed onto quartz disc. Using a glove box, uniformly blast sample with 600 grit brown aluminum oxide at 20 PSI holding gun  $\sim 1$  inch away. The goal is to achieve a uniform matte finish.

### **Soak Off Sample**

Immerse the disc in acetone, propping up one end such that gravity eventually separates the sample from the disc. Several hours are typically required for the acetone to dissolve all of the wax. Rinse sample in IPA and then blow dry with compressed nitrogen.

## **B.8 Mount Diving Board**

A critical procedure when fabricating a diving board device, is ‘mounting’ the board, or affixing a single end to a block of metal that acts as a heat sink to provide thermal ground. An effective mounting strategy involves a custom aluminum vacuum chuck as illustrated in Fig. B.1. The choice of aluminum offers 1) the ability to conduct heat from the heated work holder to the sample in order to assist wetting with indium, and 2) poor adhesion to indium relative to the gold-plated silver block.

Before we proceed it is important to note that the thinned sample is very fragile and must be manipulated with a gentle touch. Tweezers are a bad idea. Pieces of filter paper can be used to scoop and push the sample around without fear of chipping or cleaving it. Avoid burning the filter paper through extended contact with the hot aluminum chuck.

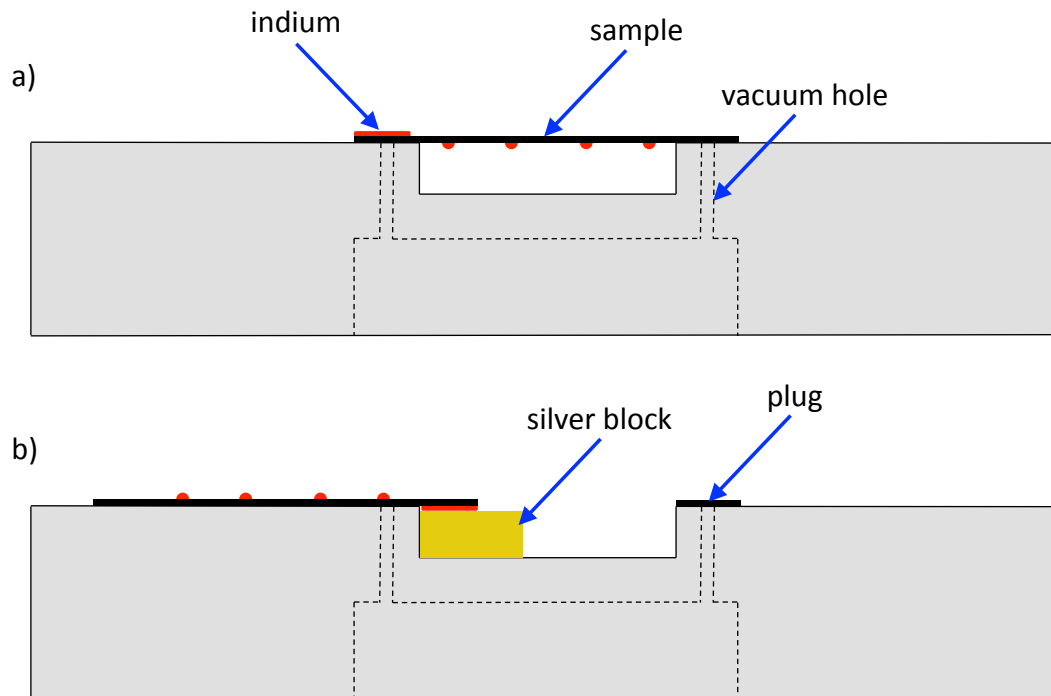


Figure B.1: Cross section of custom aluminum vacuum chuck used for mounting sample. The sample is thick black, indium is red, gold-plated silver is yellow, and aluminum is grey. a) Sample oriented for applying indium on its backside in preparation for mounting. b) Gold-plated silver block positioned within slot as sample is mounted.

First, the chuck assists in wetting the backside of the sample with indium in preparation for mounting. The milled slot allows the sample to be inverted and supported on two ends without molesting the ohmic contacts on its surface as shown in Fig. B.1 (a). But first, place the chuck onto a West Bond heated work holder set to  $110^{\circ}$  C. Carefully position the sample using filter paper. Once in place, activate the vacuum; two pin-sized vacuum holes hold the sample in place. Using a soldering

pen equipped with an NT1 tip set to  $400^\circ\text{C}$ , paint the last 2 mm of the backside of the sample with indium.

Next, use the solder pen to paint a  $\sim 2 \times 3\text{ mm}^2$  region of indium onto the center of the gold-plated silver block. Push the silver block flush against the wall of the chuck's slot as shown in Fig. B.1 (b). Note that the depth of the slot is  $\sim 200\ \mu\text{m}$  deeper than the height of the gold-plated silver block to allow room for the layer of indium. Once again using filter paper, carefully position the sample to be in its final configuration with respect to the silver mount. Plug the other vacuum hole as shown in the figure and activate the vacuum such that the sample is pulled toward the silver block (the strength of the 'vacuum' should be regulated to avoid breaking the sample). Putting the soldering pen in contact with the silver block will raise its temperature and cause the indium to flow. Capillary action in combination with the force of the vacuum bring the sample and silver block together such that upon removing the heat of the solder pen a strong indium joint is formed. Figure B.2 shows the sample after mounting and after the heater and wires have been attached (see next two sections).

## B.9 Attach Heater

In the case of diving board A, an external heater is attached to the end opposite that of thermal ground. We require a resistive element capable of dissipating enough power to impose a significant temperature gradient along the diving board at cryogenic temperatures. For this purpose, we utilize a Vishay WK-06-031CF-350 strain gauge (nominally provides  $350\ \Omega$  at room temperature in the absence of strain).

Before attaching the strain gauge, trim away the peripheral plastic such the heater has a width of  $\sim 3\text{ mm}$ . Also trim away most of the copper coated tabs leaving just enough to attach 1 mil wires to each, which should be done prior to attaching the heater to the sample. Specifically, attach 1 cm long 1 mil manganin wires following the procedure of the following section.

Once the strain gauge has been trimmed and wires are attached, use a dab of GE/IMI 7031 varnish, diluted by ethanol in the ratio 1:1, to attach it to the end

of the diving board as shown in Fig. B.2. Allow varnish to dry over night at room temperature.

## B.10 Wire Up

All of the devices studied for this thesis require multiple electrical connections. Two wire up procedures are routinely employed in our lab: 1) use soldering pen and tweezers under a stereo microscope, or 2) use the West Bond “E” Series ultrasonic wire bonder. The former option is available to most devices, however, it requires a solder joint to form the connection. This is the logical choice for diving board A, which requires that 1.5 in long, 1 mil manganin wires be attached to InSn ohmic contacts as shown in Fig. B.2. The wire bonder, when available as an option, forms a connection by wedging a wire into a metal-film-covered surface. This is typically the best option when connecting to Ni/AuGe ohmic contacts, in which case, 1 mil gold wires are a good choice.

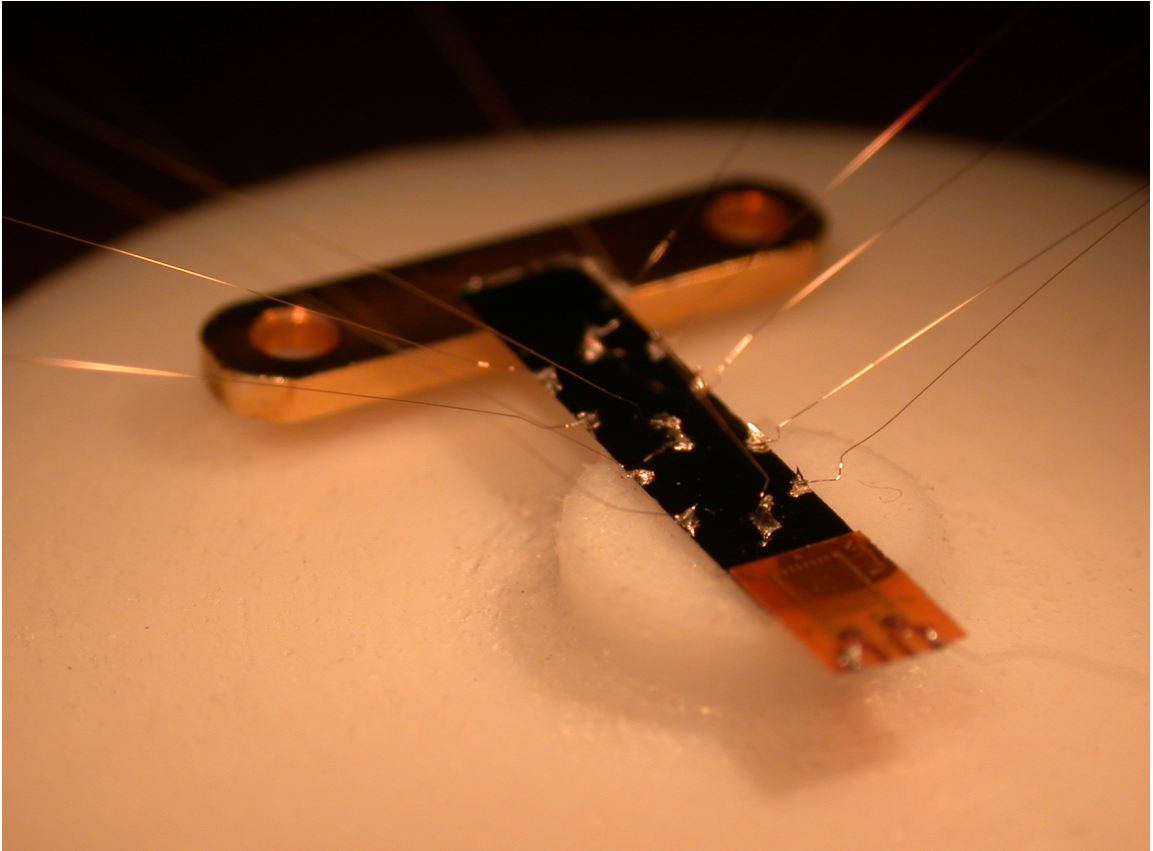


Figure B.2: 2DES diving board A on a teflon vacuum chuck after mounting, attaching strain gauge heater, and attaching wires to ohmic contacts.

## Appendix C

# Narrow Band Lock-In Detection

A key technique utilized for many of the measurements presented in this thesis is that of *narrow band lock-in detection* with which a signal with a particular frequency  $f$  and phase  $\phi$  can be extracted from a noisy environment. The details of lock-in detection, which is embodied in an instrument known as a *lock-in amplifier*, are beyond the scope of this thesis and can be found elsewhere [171]. Here we will merely summarize the essential features of this measurement method.

A lock-in amplifier works by mixing an input voltage or current with a reference signal of frequency  $f$ . Lock-in detection relies on the orthogonality of sinusoidal functions. Each sinusoidal component of frequency  $f_c$  of the amplified input signal is mixed with the reference signal yielding products of frequency  $f - f_c$  and  $f + f_c$ . Only the component with  $f_c = f$  yields a product of zero frequency. By passing the output of the mixer through a narrow band low-pass filter, the lock-in amplifier outputs a signal proportional to the amplitude of the target component times the cosine of the phase difference between the input and reference signals.

### C.1 Example: Four-Point Resistance Measurement

The use of lock-in detection requires that the target signal frequency and phase be precisely known. In transport measurements, like those performed for this thesis, this is practical since one can typically excite a sample at a well known frequency and phase using lock-in amplifier's internal oscillator. As an example, we illustrate

a four-point resistance measurement of a 2DES confined to the Hall bar geometry of Fig. C.1. A lock-in amplifier sources the current  $I$  at frequency  $f$  between contacts 1 and 2. The lock-in amplifier's input then monitors the voltage  $\Delta V$  between contacts 3 and 4 picking out the component at  $f$ , which corresponds to the resistive voltage drop. The four-point configuration allows us to measure the electrical resistance of the 2DES separate from that of the ohmic contacts. This is an extremely valuable feature given that the ohmic contact resistance of a high-mobility 2DES within a GaAs/AlGaAs heterostructure often dominates that of the 2DES itself.

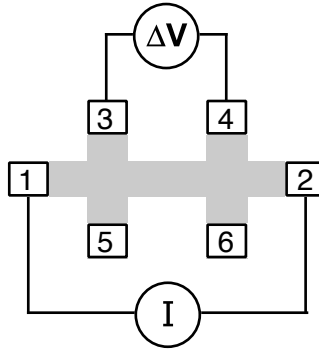


Figure C.1: Four-point resistance measurement of 2DES hall bar. Grey region represents the 2DES while numbered squares are ohmic contacts. The lock-in amplifier sources the current  $I$  at frequency  $f$  between contacts 1 and 2 and measures the voltage drop  $\Delta V$  between contacts 3 and 4.

In the case of a 2DES studied at cryogenic temperatures, extremely small excitation signals (e.g.  $\sim 10$  nA) are typically used to avoid heating the electrons out of thermal equilibrium with their surrounding lattice. These small excitations are also typically sourced at low frequency (e.g. 13 Hz) to preclude unwanted capacitive electrical currents. The ability to isolate a narrow band of a signal via lock-in detection is invaluable in these conditions where the small resistive signal of interest mixes with  $1/f$  noise.

# Appendix D

## Long Thermal Relaxation Times

At the lowest temperatures, particularly when a large magnetic field is applied, the time required for our original diving board device (diving board A) to achieve steady state following turning on or off the heater becomes very long. These long relaxation times forced us to acquire data at extremely low frequencies ( $\sim 1$  mHz, see Section 4.1.2). In this appendix we analyze the behavior of these relaxation times and arrive at a hypothesis regarding their origin.

The thermal relaxation time of diving board A is readily observed via measurements of the longitudinal resistance  $R_{xx}$  of the 2DES. After choosing a magnetic field where  $R_{xx}$  is strongly temperature dependent, its time evolution following an abrupt change in the heater power is recorded. The inset to Fig. D.1 (a) shows a typical example: After turning off the heater at  $T \approx 75$  mK and  $B = 6.4$  T,  $R_{xx}$  takes over 100 seconds to fully relax. Fitting such relaxations to a simple exponential,  $\Delta R_{xx} \propto e^{-t/\tau_R}$ , allows us to extract the relaxation time  $\tau_R$ . Figure D.1 (b) shows  $\tau_R$  versus  $T$  at various magnetic fields in a log-log plot. We find the temperature dependence of  $\tau_R$  is reasonably approximated by a simple power law,  $\tau_R \propto T^p$ , with the exponent  $p \approx -3.7$  essentially independent of magnetic field.

To more clearly illustrate the magnetic field dependence of  $\tau_R$ , Fig. D.1 (b) displays  $\tau_R$  versus  $B$  in a log-log plot. It is obvious that  $\tau_R$  versus  $B$  does not obey a simple power law. Indeed,  $\tau_R$  appears to saturate at a strongly temperature dependent value in the  $B \rightarrow 0$  limit. At high fields  $\tau_R$  becomes strongly field dependent, becoming roughly consistent with  $\tau_R \propto B^2$  beyond  $B \sim 6$  T.

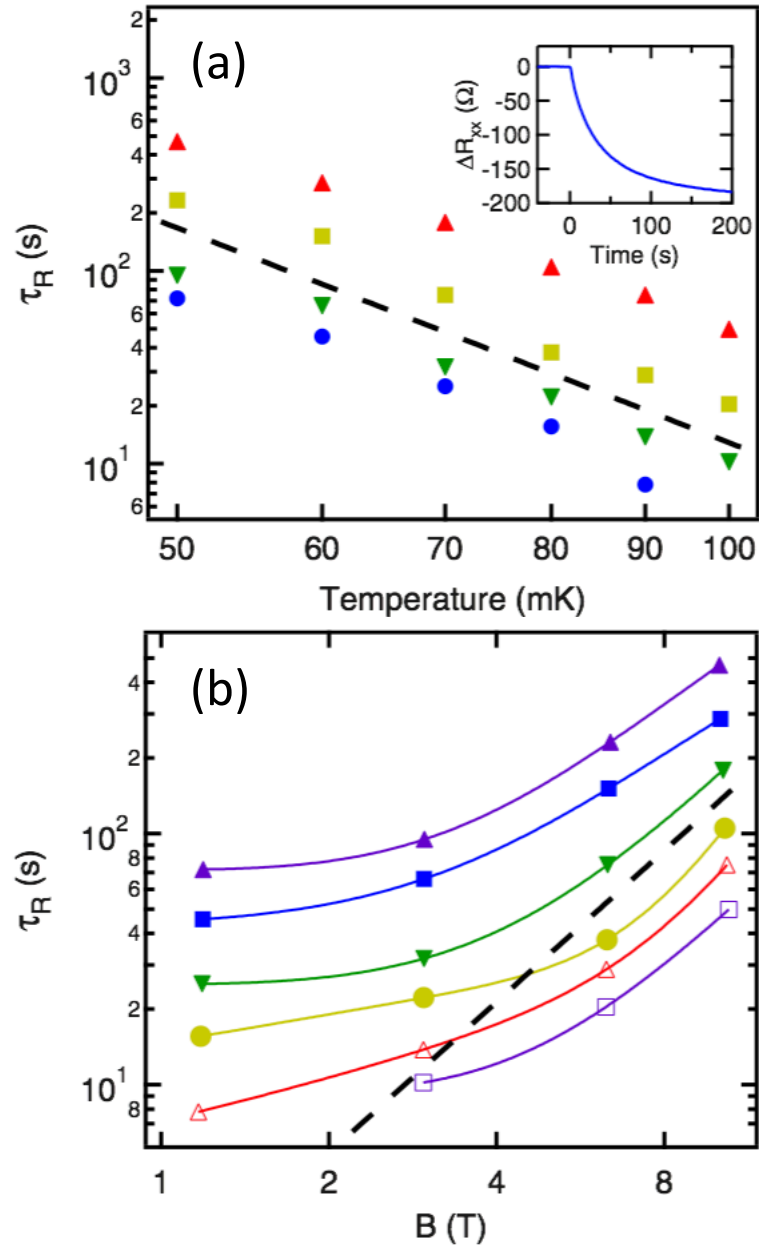


Figure D.1: (a) Thermal relaxation time  $\tau_R$  vs temperature at various magnetic fields. From top to bottom:  $B = 10.2, 6.4, 3.0,$  and  $1.2$  T. Dashed line shows a simple power law:  $\tau_R \propto T^{-3.7}$ . Inset: change in the longitudinal resistance,  $\Delta R_{xx}$ , vs time after turning off the heater (in this example, at  $T \approx 75$  mK and  $B = 6.4$  T). (b)  $\tau_R$  vs magnetic field  $B$  at several temperatures  $T$ . From top to bottom,  $T = 50, 60, 70, 80, 90,$  and  $100$  mK. Solid lines are guides to the eyes. Clearly, the magnetic field dependence of  $\tau_R$  does not obey a simple power law. The dashed line illustrates a  $B^2$  dependence. Reprinted with permission from W.E. Chickering, J.P. Eisenstein, L.N. Pfeiffer, and K.W. West, *Phys. Rev. B* **81**, 245319, (2010). Copyright 2010 by the American Physical Society.

Although the origin of the long thermal relaxation times in diving board A was not unambiguously determined, nuclear moments in the InSn contacts and the manganin wires stand out as likely culprits. At high magnetic fields and low temperatures the nuclear spin heat capacity of In and manganin scales as  $B^2/T^2$  and dwarfs that of the GaAs lattice phonons in the diving board<sup>1</sup>. Since these contacts and wires cool primarily through the phonon thermal conductance  $K \sim T^{-2.6}$  of the diving board, a thermal relaxation time  $\tau_R \sim B^2/T^{4.6}$  results. While this is a somewhat stronger temperature dependence than we observe ( $\tau_R \sim T^{-3.7}$ ), the lumped “RC” thermal model it is based on is highly oversimplified.

The above nuclear spin heat capacity model suggests that  $\tau_R$  should vanish at  $B = 0$ , in conflict with our observations. However, it is well known [172, 19] that manganin has a very large nuclear quadrupole heat capacity at  $B = 0$  which also scales as  $T^{-2}$  for  $T \lesssim 0.5$  K. This heat capacity would lead to an additional contribution to the thermal relaxation time of our device which again scales as  $T^{-4.6}$ , but now at  $B = 0$ . Rough estimates of the magnitude of the thermal relaxation time resulting from these various nuclear moments are in order-of-magnitude agreement with our observations.

Motivated by the hypothesis that these long relaxation time originate from nuclear moments in the InSn contacts and manganin wires, we designed diving board B. This new device is described in detail in Section 4.2. A key feature of diving board B is a dramatic reduction in the amount of metallization compared to diving board A. This is achieved by evaporating ohmic contacts, replacing the external heater with an on-chip heater, and using evaporated contacts lines to connect ohmic contacts and heater to an on-chip patch bay located at thermal ground. The new device succeeds in reducing the thermal relaxation time by several orders of magnitude.

---

<sup>1</sup>We specifically mention the InSn contacts and the manganin wires because they are in good thermal contact with the 2DES and have short nuclear-spin-lattice relaxation times,  $T_1$ . The spin 3/2 Ga and As nuclei in the sample also present a nuclear heat capacity and may be involved as well. Presumably, however, only those Ga and As nuclei in the quantum well containing the 2DES would have short enough  $T_1$  times to be relevant. There are far fewer such Ga and As nuclei than there are spin 9/2 In nuclei in the ohmic contacts.

## Appendix E

# Electrical Resistance as a Hot-Electron Thermometer

*I am grateful to my advisor, Jim Eisenstein, for realizing and deriving the following correction factor that arises when using electrical resistance as a hot-electron thermometer. In fact, this subtle issue goes beyond 2D electrons and thermometry and applies whenever one uses narrow band lock-in detection to measure a change in resistance resulting from Joule heating via the measurement current. Perhaps this is not a common scenario since, to the author's knowledge, it is not addressed anywhere in the literature. In any case, it is of particular importance to the hot-electron thermocouple portion of this thesis.*

### E.1 Introduction

In a typical resistance measurement using narrow band lock-in detection (see Appendix C) one keeps the excitation current sufficiently low that the resulting Joule heating may be neglected. If instead one applies a large current the sample will warm up. If the sample's resistance exhibits appreciable temperature dependence, this resistive heating will not only change the actual resistance of the sample but also yield a systematic error in the measurement of the resistance.

The hot-electron thermocouple experiment described in Chapter 5 utilizes the temperature dependence of the 2DES's four-point resistance  $R$  as an electron thermometer. The measurement protocol (see Section 5.3) presumes a one-to-one rela-

tionship between electron temperature and 2DES resistivity such that the measured four-point resistance is a simple function of the average<sup>1</sup> electron temperature at the center of the device:  $R = R(T_e)$ . A measurement of the four-point resistance  $R$  is therefore tantamount to a measurement of the electron temperature  $T_e$  at the center of the device. As such, a systematic error in the determination of  $R$  will propagate to an error in the determination of  $T_e$ . Fortunately, this error is easily corrected as explained below.

## E.2 Error in $\Delta R$ Due to Joule Heating

Let us consider the situation where the Joule heating is small such that

$$T_e = T_l + \alpha I^2 R(T_e), \quad (\text{E.1})$$

where  $T_e$  is the electron temperature at the center of the device,  $T_l$  is the temperature of the surrounding crystal lattice, and  $\alpha$  is a constant. For sufficiently small heating, the 2DES's four-point resistance may be expressed as

$$R(T_e) \simeq R(T_l) + R'(T_l) \cdot (T_e - T_l) \simeq R(T_l) + R'(T_l) \alpha I^2 R(T_l), \quad (\text{E.2})$$

where  $R'(T) = dR/dT$ . The voltage seen at the lock-in detector's input is given by Ohm's law:

$$V = IR(T_e) \simeq IR(T_l) + R'(T_l) \alpha I^3 R(T_l). \quad (\text{E.3})$$

For our lock-in measurements we source an oscillating excitation current  $I = I_0 \sin(\omega t)$ , where the frequency  $\omega = 2\pi f$  is sufficiently low that oscillations in  $T_e$  remain in phase with the Joule heating. The voltage may therefore be expressed in

---

<sup>1</sup>More specifically, the measured four-point resistance depends solely on the electron temperature spatially averaged within the region between voltage probes. As the distance between the voltage probes is small compared to the distance between the device center and any ohmic contact, we may approximate this spatially averaged electron temperature as equal to the temperature at the device center. A simple computer simulation estimated the difference between the spatially averaged temperature and that at the device center to be  $\sim 10\%$ .

the time domain as

$$V(t) = R(T_l)I_0 \sin(\omega t) + R'(T_l)R(T_l)\alpha I_0^3 \sin^3(\omega t) \quad (\text{E.4})$$

$$= R(T_l) \left[ 1 + \frac{3}{4}R'(T_l)\alpha I_0^2 \right] I_0 \sin(\omega t) - \frac{1}{4}R'(T_l)R(T_l)\alpha I_0^3 \sin(3\omega t). \quad (\text{E.5})$$

Lock-in detection at frequency  $f$  will reflect the amplitude of the  $\sin(\omega t)$  term. A naive interpretation of this measurement would suggest that  $R$  has changed due to Joule heating by the “apparent” amount  $\Delta R_{app} = \frac{3}{4}R'(T_l)R(T_l)\alpha I_0^2$ . Taking the time average of Eq. E.2

$$R(\overline{T_e}) = R(T_l) \left[ 1 + \frac{1}{2}R'(T_l)\alpha I_0^2 \right], \quad (\text{E.6})$$

however, reveals a problem, showing the “true” change in the resistance is  $\Delta R_{true} = \frac{1}{2}R'(T_l)R(T_l)\alpha I_0^2$ . That is,

$$\Delta R_{app} = \frac{3}{2}\Delta R_{true}. \quad (\text{E.7})$$

### E.3 Error in $\Delta T$ Due to Joule Heating

In the context of thermometry, the “apparent” change in temperature  $\Delta T_{app}$  is given by  $\Delta R_{app} = R'(T_l)\Delta T_{app}$  such that

$$\Delta T_{app} = \frac{3}{4}R(T_l)\alpha I_0^2. \quad (\text{E.8})$$

Meanwhile, taking the time average of Eq. E.1 shows that

$$\overline{\Delta T_{true}} = \overline{T_e} - T_l = \frac{1}{2}R(\overline{T_e})\alpha I_0^2. \quad (\text{E.9})$$

Thus we see that in a regime where  $\Delta R_{true} \ll R$  we may write  $\Delta T_{true} = \frac{1}{2}R(T_l)\alpha I_0^2$  and

$$\Delta T_{app} = \frac{3}{2} \Delta T_{true}. \quad (\text{E.10})$$

## E.4 Impact on Thermopower Measurement

In the thermopower measurement protocol described in Section 5.3, the four-point resistance  $R$  is initially measured at a temperature  $T = T_0$  using a sufficiently small excitation current  $I$  that no appreciable Joule heating occurs. For this initial measurement there is no distinction between the “apparent” and “true” resistance. Next, we decrement the cryostat temperature by  $\Delta T_{cryo} \ll T_0$  and then re-balance the ZG bridge by increasing  $I$  and thereby heating the 2DES. By re-balancing the ZG bridge we return the “apparent” resistance to its initial value:

$$R_{app} = R(T_0 - \Delta T_{cryo}) + \Delta R_{app} = R(T_0). \quad (\text{E.11})$$

The equilibrium resistance at  $T = T_0 - \Delta T_{cryo}$  may be expressed as  $R(T_0 - \Delta T_{cryo}) = R(T_0) - R'(T_0)\Delta T_{cryo}$ . This shows that  $\Delta R_{app} = R'(T_0)\Delta T_{cryo}$  from which it follows

$$\Delta T_{app} = \Delta T_{cryo}. \quad (\text{E.12})$$

The measured differential thermopower is therefore

$$\Delta S = \frac{\Delta V}{\Delta T_{true}} = \frac{3}{2} \frac{\Delta V}{\Delta T_{app}} = \frac{3}{2} \frac{\Delta V}{\Delta T_{cryo}}. \quad (\text{E.13})$$

# Appendix F

## Corbino Thermopower

This thesis focuses on the Hall bar configuration in which a continuous edge runs between our voltage probes during a thermopower measurement. As with electrical transport, appreciating the role of the system edge is critical to understanding the thermopower of a QH system. For instance, we have seen how the diffusion current that flows in response to a temperature gradient primarily flows along the system edge. Meanwhile, edge channels corresponding to filled LLs provide an important path in addition to the system bulk for the compensating drift current that flows in response to a thermoelectric field. To further elucidate the role of the system edge, and to explore an alternative vantage point of the thermoelectric response of a QH system, we now consider thermopower in the absence of edge transport.

To isolate and probe bulk properties of the 2DES, the radially symmetric *Corbino* geometry is often employed. Figure F.1 illustrates a 2DES in a Corbino geometry subjected to a strong perpendicular magnetic field and a radial temperature gradient. A key property of this geometry is that no edges connect the inner and outer ohmic contacts such that transport is confined to the bulk. We are interested in the thermopower of a QH system with  $\mu$  positioned away from the extended states at the center of Landau levels such that the 2DES in the bulk is incompressible thereby resembling a band insulator.

In Appendix G we derive the diffusion thermopower of a band insulator, which is given by

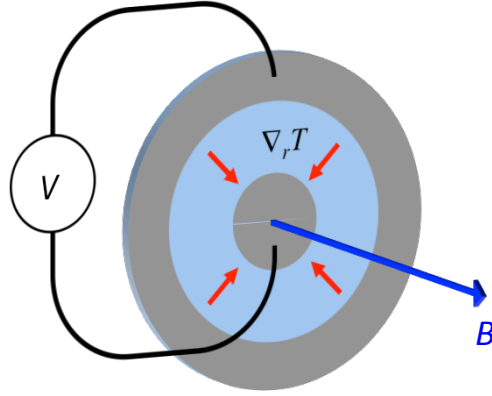


Figure F.1: Thermopower measurement of a 2DES in the Corbino configuration. The 2DES is subjected to a perpendicular magnetic field and radial temperature gradient. The thermoelectric response  $V$  of the 2DES (blue) is measured between the inner and outer ohmic contacts (grey), which do not share an edge.

$$S^d(\mu, T) = \frac{\sigma_e(\mu, T) \cdot S_e^d(\mu, T) + \sigma_h(\mu, T) \cdot S_h^d(\mu, T)}{\sigma_e(\mu, T) + \sigma_h(\mu, T)}, \quad (\text{F.1})$$

where  $\sigma_e$  and  $\sigma_h$  are the conductivities and  $S_e^d$  and  $S_h^d$  are the thermopowers of thermally activated electrons and holes, respectively. The latter are found to be

$$S_e^d(\mu, T) \simeq -\frac{\varepsilon_c - \mu}{eT} \quad (\text{F.2})$$

and

$$S_h^d(\mu, T) \simeq \frac{\mu - \varepsilon_v}{eT}, \quad (\text{F.3})$$

where  $\varepsilon_c$  is the bottom of the conduction band and  $\varepsilon_v$  is the top of the valence band. It so happens that Eqs. F.1-F.3 capture key features of the thermopower of a QH system when measured in the Corbino configuration. When  $\mu$  is positioned below the  $N^{\text{th}}$  disorder broadened LL, away from its extended states, transport in the bulk occurs via thermal activation of electrons from the  $(N - 1)^{\text{th}}$  to  $N^{\text{th}}$  LL. The heat carried by these electrons is  $Q \simeq \hbar\omega_N - \Gamma/2 - \mu$ , where  $\hbar\omega_N = \hbar\omega_c(N + 1/2)$  is the

center of the  $N^{\text{th}}$  LL and  $\Gamma$  is the LL width. The diffusion thermopower resembles a band insulator and is given by

$$S^d \simeq S_e^d = -\frac{\hbar\omega_N - \Gamma/2 - \mu}{eT}. \quad (\text{F.4})$$

Alternatively, when  $\mu$  is positioned above the  $(N - 1)^{\text{th}}$  LL, away from its extended states, transport is dominated by thermally activated holes yielding

$$S^d \simeq S_h^d = \frac{\mu - \hbar\omega_{N-1} - \Gamma/2}{eT}. \quad (\text{F.5})$$

When  $\mu$  is positioned precisely between two LLs, the contributions from electrons and holes cancel such that  $S^d = 0$ . Like an ordinary band insulator the electron and hole contributions to thermopower are proportional to an energy gap and inversely proportional to temperature and carrier charge. This behavior not only demonstrates an analogy with ordinary band insulators, but also illustrates the particle-hole symmetry that is intrinsic to QH systems.

Barlas and Yang recently calculated [120] the diffusion thermopower of a weakly disordered QH system in a Corbino setup. We reproduce their calculation of thermopower versus energy for several temperatures in Fig. F.2 (their  $Q_C$  and  $\epsilon$  are equivalent to our  $S^d$  and  $\mu$ , respectively). They ignore spin-splitting. They treat disorder in the self-consistent Born approximation (SCBA). Within SCBA, the disorder-broadened LLs are semielliptical with a semiminor axis of  $2\hbar\sigma$  ( $4\hbar\sigma$  is therefore comparable to the LL width  $\Gamma$  introduced in Chapter 6). The calculated data of Fig. F.2 are for fixed disorder with  $\hbar\sigma = 0.05\hbar\omega_c$ . The regions of the lowest LL where  $0 < \mu < 0.4\hbar\omega_c$  and  $0.6\hbar\omega_c < \mu < \hbar\omega_c$  therefore correspond to the incompressible, insulator-like regimes described above where hole- and electron-transport dominate, respectively. Their calculations in these regions are consistent with Eqs. F.4 and F.5 by setting  $\Gamma = 4\hbar\sigma$ .

Perhaps the most striking feature of the thermopower shown in Fig. F.2 is the sawtooth pattern resulting from the sharp reversals between LLs. The calculated data of Fig. F.2 corresponds to the high-field, low-temperature regime where  $\hbar\sigma \ll \hbar\omega_c$  and

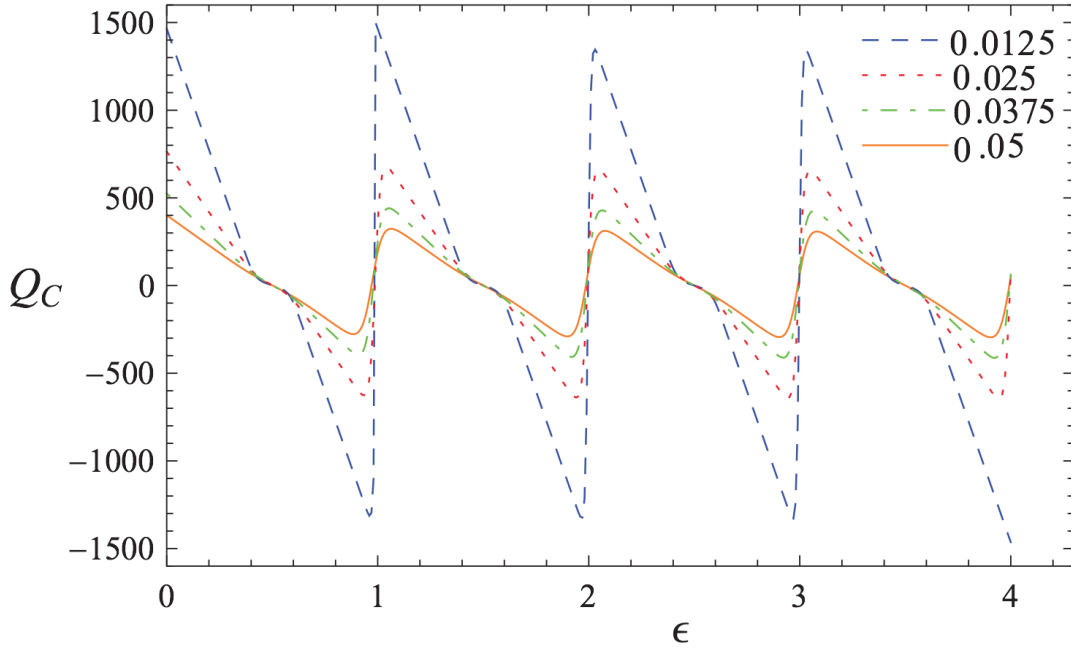


Figure F.2: Calculated diffusion thermopower as a function of energy for a weakly disordered QH system in a Corbino configuration (their  $Q_C$  and  $\epsilon$  are equivalent to our  $S^d$  and  $\mu$ , respectively). Thermopower has units of  $\mu\text{V}/\text{K}$  and energy has units of  $\hbar\omega_c$ . Calculations are shown for several temperature  $k_B T \in (0.0125, 0.025, 0.0375, 0.05)$  in units  $\hbar\omega_c$ . Reprinted with permission from Y. Barlas and K. Yang, *Phys. Rev. B* **85**, 195107 (2012). Copyright 2012 by the American Physical Society.

$k_B T \ll \hbar\omega_c$ . In this regime, between LLs, the change in energy required to transition from electron- to hole-dominated transport is much less than  $\hbar\omega_c$ . This results in a near discontinuity as  $S^d$  jumps from  $-(\hbar\omega_c/2 - 2\hbar\sigma)/eT$  to  $+(\hbar\omega_c/2 - 2\hbar\sigma)/eT$ . This dramatically contrasts with the behavior of the Hall bar thermopower. We discuss the origins of the differences between Corbino and Hall bar thermopower later in this section.

Near the center of each LL there exists a finite density of extended states. For the example in Fig. F.2, these compressible regions occur whenever  $0.4 < \mu/\hbar\omega_c - N < 0.6$ , for an integer  $N \geq 0$ . In these regions, the thermoelectric response of the QH system resembles that of a degenerate fermi gas and we recover a Mott-like expression for the thermopower [120]:

$$S^d \simeq - \frac{\pi^2 k_B^2}{3e} \frac{1}{\sigma_{xx}} \left. \frac{d\sigma_{xx}}{d\varepsilon} \right|_{\varepsilon=\mu}, \quad (\text{F.6})$$

where  $\sigma_{xx}$  is the longitudinal conductivity. As a function of  $\varepsilon$ ,  $\sigma_{xx}$  passes through a maximum near the center of the LL. Consequently,  $S^d$  is expected to change sign near the center of the LL. Like the midpoint between LLs, this sign reversal reflects a change from electron- to hole-dominated transport.

Experimentally, the Corbino geometry presents formidable technical challenges, not the least of which is the realization of a known, radially symmetric temperature gradient. In 2003, van Zelinge et al. reported [173] the first measurements of Corbino thermopower in a QH system. Heating was imposed using a scanning laserspot. Their results lacked the sign reversals expected for diffusion thermopower, however, and were attributed to phonon drag. Very recently, Kobayakawa et al. published [174] the results of another experiment in which a concentric temperature gradient within a 2DES is achieved via irradiating microwaves. Their results, obtained within the QH regime, exhibit the expected sign reversals and are otherwise consistent with the analysis of Barlas and Yang for noninteracting electrons.

## F.1 Corbino vs Hall Bar

Clearly, the diffusion thermopower of a QH system in the Corbino setup (e.g. Fig. F.2) contrasts starkly with that of the Hall bar (e.g. Fig. 7.4). This is especially true within the incompressible regions between LLs. Here, the Corbino thermopower increases with decreasing temperature while the Hall bar thermopower tends to zero. The Corbino thermopower exhibits a dramatic sign reversal at the midpoint between LLs where the magnitude of the Hall bar thermopower has a roughly symmetric minimum.

These differences can be understood in terms of the edge currents' ability to participate in charge transport. For instance, radial (longitudinal) temperature gradients during a Corbino measurement will induce azimuthal (transverse) diffusion currents

that flows along the inner or outer edge (depending on the orientation of  $\vec{\nabla}T$  and  $\vec{B}$ ). But in the Corbino configuration these circular currents are unconstrained; since they are localized, they do not participate in transport. Therefore, no compensating drift current needs to be established. The zero-current condition for Corbino thermopower therefore only applies to the radial (longitudinal) direction. In the Hall bar case, the zero-current condition applies to both longitudinal and transverse directions. Moreover, at high magnetic fields where  $\sigma_{xy} \gg \sigma_{xx}$ , it is the transverse zero-current condition that primarily determines the Hall bar thermopower.

To illustrate the profound difference between low-temperature Corbino and Hall bar thermopower due to the role of edge transport, let us consider the first excited LL where  $\hbar\omega_c < \mu < 2\hbar\omega_c$ . We can treat the 2DES as two gases conducting in parallel<sup>1</sup>. Gas 1 consists of a filled LL at zero temperature with density  $n_1 = \hbar\omega_c/\mu \cdot n$ , where  $n$  is the density of the original 2DES. Gas 2 consists of a partially filled LL at the same temperature as the original 2DES with density  $n_2 = (1 - \hbar\omega_c/\mu) \cdot n$ . This two-gas model is valid as long as  $k_B T \ll \mu - \hbar\omega_c$ . The thermopower of the 2DES can then be expressed as  $S^d = (\sigma_1 S_1^d + \sigma_2 S_2^d) / (\sigma_1 + \sigma_2)$  as per Eq. 3.22, where  $\sigma_i$  and  $S_i^d$  are the conductivity and thermopower, respectively, of gas  $i$ . For the Corbino measurement,  $\sigma_1 = 0$  such that  $S^d = S_2^d$ . That is, filled LLs do not contribute to Corbino thermopower. For the Hall bar measurement, on the otherhand,  $\sigma_1 = 2e^2/h$  due to the edge channel. At the same time,  $S_1^d = 0$  since gas 1 is a filled LL at zero temperature. In a regime where  $\sigma_{xy} \gg \sigma_{xx}$ ,  $\sigma_2 \simeq (1 - \hbar\omega_c/\mu) \cdot 2e^2/h = n_2/n \cdot 2e^2/h$ . Thus we have  $S^d \simeq n_2 S_2^d / (n + n_2)$  for the Hall bar. This reveals that, unlike the Corbino case, the edge channels of filled LLs critically impact the thermopower in a Hall bar measurement.

How do we reconcile the stark differences between the Corbino and Hall bar measurements with the entropic interpretation of diffusion thermopower? In Section 7.4 we derived the disorder-free Hall bar thermopower of a 2DES in the QH regime via an entropic argument without any consideration of edge transport. More generally, Cooper et al. argue [8] that for sufficiently weak impurity scattering, the longitudinal

---

<sup>1</sup>This two-gas approach is borrowed from Karavolas et al. [118].

Hall bar diffusion thermopower is given by  $S_{xx}^d = -\mathcal{S}/en$  in the QH regime, where  $\mathcal{S}$  is the entropy per area, as usual. If the Hall bar thermopower is the entropy per electron per electron charge, the Corbino thermopower clearly is not. Barlas and Yang argue [120] that the Corbino diffusion thermopower in the QH regime is the entropy per *quasiparticle* per *quasiparticle charge*, which is indeed consistent with our above arguments. In our simple model, the quasiparticles are thermally activated electrons and holes, which have quasiparticle charges of  $-e$  and  $e$ , respectively. The heat of transport for the quasielectrons is  $\hbar\omega_N - \Gamma/2 - \mu$ , where  $\hbar\omega_N - \Gamma/2$  is the energy of the nearest extended state. It follows that the entropy per quasielectron is given by  $(\hbar\omega_N - \Gamma/2 - \mu)/T$ . Equation F.4, and by similar argument Eq. F.5, is therefore consistent with the interpretation of Barlas and Yang. Crudely speaking, the high field diffusion thermopower is apparently equal to the entropy per *transport carrier* per *transport carrier charge*. In the Corbino case, *transport carrier* refers exclusively to thermally activated electrons and holes. In the Hall bar case, *transport carrier* refers to all electrons since those in filled LLs still contribute to transport through the establishment of edge channels.

## Appendix G

# Diffusion Thermopower of a Band Insulator

In Chapter 3, we derive a general expression for diffusion thermopower:

$$S^d(\mu, T) = -\frac{\frac{1}{e} \int_{-\infty}^{\infty} \sigma_0(\varepsilon) \frac{\partial f}{\partial T}(\varepsilon, \mu, T) d\varepsilon}{\int_{-\infty}^{\infty} \sigma_0(\varepsilon) \frac{\partial f}{\partial \varepsilon}(\varepsilon, \mu, T) d\varepsilon}, \quad (\text{G.1})$$

where  $\sigma_0(\varepsilon)$  is the electrical conductivity of carriers at energy  $\varepsilon$ , which equals the total electrical conductivity at  $T = 0$  for  $\varepsilon = \mu$ . In what follows, we will model<sup>1</sup> the energy dependence of the conductivity of the electrons in a band insulator as

$$\sigma_{e,0}(\varepsilon) = \begin{cases} 0 & \varepsilon < \varepsilon_c \\ A \cdot (\varepsilon - \varepsilon_c)^\eta & \varepsilon \geq \varepsilon_c \end{cases}, \quad (\text{G.2})$$

where  $A$  and  $\eta \gtrsim 1$  are constants that depend on material properties such as the effective mass and energy dependence of the momentum lifetime, and  $\varepsilon_c$  is the energy at the bottom of the conduction band. At low temperatures, where  $k_B T \ll \varepsilon_c - \mu$ , the contribution of electrons to the diffusion thermopower of a band insulator is then

$$S_e^d(\mu, T) \simeq -\frac{\int_{\varepsilon_c}^{\infty} (\varepsilon - \varepsilon_c)^\eta (\varepsilon - \mu)^2 \exp(-(\varepsilon - \mu)/k_B T) d\varepsilon}{eT \int_{\varepsilon_c}^{\infty} (\varepsilon - \varepsilon_c)^\eta (\varepsilon - \mu) \exp(-(\varepsilon - \mu)/k_B T) d\varepsilon}, \quad (\text{G.3})$$

where we have used the approximation that  $f(\varepsilon, \mu, T) \simeq \exp(-(\varepsilon - \mu)/k_B T)$  for  $\varepsilon \geq \varepsilon_c$  (i.e. electrons in the conduction band obey Boltzmann statistics). Note that a

---

<sup>1</sup>This model assumes a single conduction band and that the energy dependence of the scattering time follows a simple power law.

similar expression can be written for the contribution of holes in the valence band. We will return to the hole contribution in a moment; for now we will focus on electrons.

Letting  $\beta \equiv 1/k_B T$ , we may rewrite Eq. G.3 as

$$S_e^d(\mu, T) \simeq \frac{\int_{\varepsilon_c}^{\infty} (\varepsilon - \varepsilon_c)^\eta \frac{\partial^2}{\partial \beta^2} \exp(-\beta(\varepsilon - \mu)) d\varepsilon}{eT \int_{\varepsilon_c}^{\infty} (\varepsilon - \varepsilon_c)^\eta \frac{\partial}{\partial \beta} \exp(-\beta(\varepsilon - \mu)) d\varepsilon}. \quad (\text{G.4})$$

Next, we can eliminate the integrals from this expression through a change of variables: let  $x \equiv \beta(\varepsilon - \varepsilon_c)$  such that

$$S_e^d(\mu, T) \simeq \frac{\frac{\partial^2}{\partial \beta^2} \beta^{-(\eta+1)} \exp(-\beta(\varepsilon_c - \mu)) \int_0^{\infty} x^\eta \exp(-x) dx}{eT \frac{\partial}{\partial \beta} \beta^{-(\eta+1)} \exp(-\beta(\varepsilon_c - \mu)) \int_0^{\infty} x^\eta \exp(-x) dx}. \quad (\text{G.5})$$

Conveniently, the integrals cancel out. And since  $\beta(\varepsilon_c - \mu) \gg 1$  and  $\eta \sim 1$  we have that

$$\frac{\partial}{\partial \beta} \beta^{-(\eta+1)} \exp(-\beta(\varepsilon_c - \mu)) \simeq -(\varepsilon_c - \mu) \beta^{-(\eta+1)} \exp(-\beta(\varepsilon_c - \mu)) \quad (\text{G.6})$$

and

$$\frac{\partial^2}{\partial \beta^2} \beta^{-(\eta+1)} \exp(-\beta(\varepsilon_c - \mu)) \simeq (\varepsilon_c - \mu)^2 \beta^{-(\eta+1)} \exp(-\beta(\varepsilon_c - \mu)). \quad (\text{G.7})$$

Our low-temperature expression for the contribution of electrons to the diffusion thermopower of an insulator therefore simplifies to

$$S_e^d(\mu, T) \simeq -\frac{\varepsilon_c - \mu}{eT}. \quad (\text{G.8})$$

From an analogous model and argument for the holes in our insulator, one can readily arrive at their contribution as being

$$S_h^d(\mu, T) \simeq \frac{\mu - \varepsilon_v}{eT}, \quad (\text{G.9})$$

where  $\varepsilon_v$  is the energy at the top of the valence band. The total diffusion thermopower is then given by

$$S^d(\mu, T) = \frac{\sigma_e(\mu, T) \cdot S_e^d(\mu, T) + \sigma_h(\mu, T) \cdot S_h^d(\mu, T)}{\sigma_e(\mu, T) + \sigma_h(\mu, T)}, \quad (\text{G.10})$$

where  $\sigma_e(\mu, T)$  and  $\sigma_h(\mu, T)$  are the contributions to the total conductivity from electrons and holes, respectively.

Equation G.8 (G.9) tells us that, in the limit of zero temperature, the temperature dependence of the electron (hole) contribution to the diffusion thermopower of a band insulator dramatically differs from that of a metal. In the case of a metal, the Mott formula says that at low temperatures  $S^d$  increases linearly with T. Conversely, in the case of an insulator,  $S^d$  increases with *decreasing* temperature. At the same time, we have derived the low-temperature  $S^d$  for both a metal and a band insulator directly from the Cutler-Mott formula (Eq. G.1), the only difference being the energy dependence of the electrical conductivity. And in both cases, the thermopower is simply related to the entropy per charge carrier. Indeed, within an insulator, a thermally activated electron carries heat  $Q = \varepsilon_c - \mu$  such that the entropy per electron per electron charge is  $-Q/eT$ .

We have shown that the electron and hole contributions to the diffusion thermopower of an insulator are linearly proportional to the band gap and inversely proportional to temperature and carrier charge. It seems improbable, however, that the best thermoelectric materials are simply the largest gapped insulators cooled to the lowest possible temperatures. Of course, this is not the case, as Eqs. G.8 and G.9 are only valid in the thermodynamic limit of many thermally activated carriers. For a sufficiently large band gap and/or sufficiently low temperature, these equations will no longer hold. Similarly, the idea that the entropy per charge carrier is inversely proportional to temperature may seem inconsistent with the third law of thermodynamics, which requires that the entropy of our system vanish in the limit of zero temperature. To reconcile these notions, it is important to recognize that while the entropy per carrier is diverging, the number of carriers in our system is vanishing as

we approach absolute zero. Indeed, as  $T \rightarrow 0$ , we have that  $\mathcal{S} \propto nS^d \propto \sigma S^d \rightarrow 0$  as can be seen from the numerator of Eq. G.1.

# Bibliography

- [1] K. von Klitzing, G. Dorda, and M. Pepper. *Phys. Rev. Lett.*, 45:494, 1980.
- [2] H.L. Störmer, D.C. Tsui, and A.C. Gossard. *Surface Science*, 113:32, 1982.
- [3] For a review of the magnetic field induced Wigner crystal, see the chapters by H.A. Fertig and M. Shayegen. *Perspectives in Quantum Hall Effects*. edited by S. Das Sarma and A. Pinczuk, Wiley, New York, 1997.
- [4] K.B. Cooper, M.P. Lilly, J.P. Eisenstein, L.N. Pfeiffer, and K.W. West. *Phys. Rev. B*, 60:R11285, 1999.
- [5] J.P. Eisenstein and A.H. MacDonald. *Nature*, 432:691, 2004.
- [6] R.H. Morf. *Phys. Rev. Lett.*, 80:1505, 1998.
- [7] Y.N. Obraztsov. *Fiz. Tverd. Tela*, 7:573, 1965. [Sov. Phys. Solid State **7**, 455 (1965)].
- [8] N.R. Cooper, B.I. Halperin, and I.M. Ruzin. *Phys. Rev. B*, 55:2344, 1997.
- [9] J.H. Davies. *The Physics of Low-Dimensional Semiconductors*. Cambridge University Press, 1998.
- [10] W.T. Sommer. *Phys. Rev. Lett.*, 12:271, 1964.
- [11] A.K. Geim and K.S. Novoselov. *Nature Materials*, 6:183, 2007.
- [12] For an overview on heterostructures, see J. H. Davies. *The Physics of Low-Dimensional Semiconductors*, chapter 3: Heterostructures. Cambridge University Press, 1998.

- [13] R.L. Anderson. *Solid-State Electronics*, 5:341, 1962.
- [14] M.O. Watanabe, J. Yoshida, M. Mashita, T. Nakanisi, and A. Hojo. *J. Appl. Phys.*, 57:5340, 1985.
- [15] H.L. Störmer, R. Dingle, A.C. Gossard, W. Wiegmann, and M.D. Sturge. *Solid State Commun.*, 29:705, 1979.
- [16] S.M. Sze and K.K. Ng. *Physics of Semiconductor Devices*. Wiley-Interscience, 2006.
- [17] K.D.D. Rathnayaka. *J. Phys. E*, 18:380, 1985.
- [18] T. Klitzner and R.O. Pohl. *Phys. Rev. B*, 36:6551, 1987.
- [19] For a review of dilution refrigeration or cryogenic techniques more generally, see F. Pobell. *Matter and Methods at Low Temperatures, 3rd edition*. Springer-Verlag, Berlin, 2007.
- [20] O.V. Lounasmaa. *Experimental Principles and Methods Below 1K*. Academic, London, 1974.
- [21] F. Pobell. *Matter and Methods at Low Temperatures, 3rd edition*, chapter 10: Refrigeration by Adiabatic Nuclear Demagnetization. Springer-Verlag, Berlin, 2007.
- [22] H.L. Störmer, L.N. Pfeiffer, K.W. Baldwin, and K.W. West. *Phys. Rev. B*, 41:1278, 1990.
- [23] A. Mittal. *Electron-Phonon Scattering Rates in GaAs/AlGaAs 2DEGs Below 0.5K*. PhD thesis, Yale University, 1996.
- [24] J.P. Pekola, K.P. Hirvi, J.P. Kauppinen, and M.A. Paalanen. *Phys. Rev. Lett.*, 73:2903, 1994.
- [25] K.B. Cooper. *New Phases of Two-Dimensional Electrons in Excited Landau Levels*. PhD thesis, California Institute of Technology, 2003.

- [26] N.W. Ashcroft and N.D. Mermin. *Solid State Physics*, chapter 1: The Drude Theory of Metals. Saunders College Publishing, Fort Worth, TX, 1976.
- [27] G.V. Chester and A. Thellung. *Proc. Phys. Soc.*, 77:1005, 1961.
- [28] R. Kubo. *J. Phys. Soc. Jap.*, 12:570, 1957.
- [29] D.A. Greenwood. *Proc. Phys. Soc.*, 71:585, 1958.
- [30] Y. Imry and A. Amir. The localization transition at finite temperatures: Electrical and thermal transport. In E. Abrahams, editor, *50 Years of Anderson Localization*. World Scientific, 2010.
- [31] N.W. Ashcroft and N.D. Mermin. *Solid State Physics*, chapter 2: The Sommerfeld Theory of Metals. Saunders College Publishing, Fort Worth, TX, 1976.
- [32] M. Cutler and N.F. Mott. *Phys. Rev.*, 181:1336, 1969.
- [33] E.H. Hwang and S. Das Sarma. *Phys. Rev. B*, 77:235437, 2008.
- [34] C. Kittel and H. Kroemer. *Thermal Physics*, chapter 7: Fermi and Bose Gases. W.H. Freeman and Company, New York, 1980.
- [35] B.L. Gallagher and P.N. Butcher. *Handbook on Semiconductors*, volume 1. Elsevier, Amsterdam, 1992.
- [36] R. Fletcher. *Semicond. Sci. Technol.*, 14:R1, 1999.
- [37] R. Fletcher, E. Zaremba, and U. Zeitler. *Electron-Phonon Interactions in Low-Dimensional Structures*, chapter 5. Oxford Univ. Press, 2003.
- [38] R.J. Nicholas. *J. Phys. C*, 18:L695, 1985.
- [39] A. Miele, R. Fletcher, E. Zaremba, Y. Feng, C.T. Foxon, and J.J. Harris. *Phys. Rev. B*, 58:13181, 1998.
- [40] X. Ying, V. Bayot, M.B. Santos, and M. Shayegan. *Phys. Rev. B*, 50:4969, 1994.

- [41] C. Ruf, H. Obloh, B. Junge, E. Gmelin, K. Ploog, and G. Weimann. *Phys. Rev. B*, 37:6377, 1988.
- [42] R. Fletcher, P.T. Coleridge, and Y. Feng. *Phys. Rev. B*, 52:2823, 1995.
- [43] B. Tieke, U. Zeitler, R. Fletcher, S.A.J. Wieggers, A.K. Geim, J.C. Maan, and M. Henini. *Phys. Rev. Lett.*, 76:3630, 1996.
- [44] J.J. Heremans, M.B. Santos, K. Hirakawa, and M. Shayegan. *J. Appl. Phys.*, 76:1980, 1994.
- [45] H. Obloh, K. von Klitzing, and K. Ploog. *Surf. Sci.*, 142:236, 1984.
- [46] R.J. Nicholas, T.H.H. Vuong, M.A. Brummel, J.C. Portal, and M.A. Razeghi. Temperature and magnetic field dependent thermoelectric power in GaInAs-InP heterojunctions. In *Proceedings of the 17th International Conference on the Physics of Semiconductors*, page 389, 1985.
- [47] R. Fletcher, J.C. Maan, and G. Weimann. *Phys. Rev. B*, 32:8477, 1985.
- [48] R. Fletcher, J.C. Maan, K. Ploog, and G. Weimann. *Phys. Rev. B*, 33:7122, 1986.
- [49] T.H.H. Vuong, R.J. Nicholas, M.A. Brummell, J.C. Portal, M. Razeghi, F. Alexandre, J.M. Masson, K.Y. Cheng, and A.Y. Cho. *Surf. Sci.*, 170:298, 1986.
- [50] V. Bayot, X. Ying, M.B. Santos, and M. Shayegan. *Europhys. Lett.*, 25:613, 1994.
- [51] B. Tieke, R. Fletcher, S.A.J. Wieggers, U. Zeitler, J.C. Maan, C.T. Foxon, and J.J. Harris. *Physica B*, 211:414, 1995.
- [52] V. Bayot, E. Grivei, H.C. Manoharan, X. Ying, and M. Shayegan. *Phys. Rev. B*, 52:R8621, 1995.

- [53] P.A. Crump, B. Tieke, R.J. Barraclough, B.L. Gallagher, R. Fletcher, J.C. Maan, T.M. Fromhold, and M. Henini. *Surf. Sci.*, 361/362:50, 1996.
- [54] L. Moldovan, S. Melinte, V. Bayot, S.J. Papadakis, E.P. De Poortere, and M. Shayegan. *Phys. Rev. Lett.*, 85:4369, 2000.
- [55] S. Faniel, L. Moldovan, A. Vlad, E. Tutuc, N. Bishop, S. Melinte, M. Shayegan, and V. Bayot. *Phys. Rev. B*, 76:161307(R), 2007.
- [56] T.C. Cetas, C.R. Tilford, and C.A. Swenson. *Phys. Rev.*, 174:835, 1968.
- [57] M.N. Wybourne, C.G. Eddison, and M.J. Kelly. *J. Phys. C*, 17:L607, 1984.
- [58] B. Bhattacharyya and F.M. Gasparini. *Rev. Sci. Instrum.*, 53:714, 1982.
- [59] B.J.F. Lin, D.C. Tsui, M.A. Paalanen, and A.C. Gossard. *Appl. Phys. Lett.*, 45:695, 1984.
- [60] E. Zaire and A.J. Greenfield. *Rev. Sci. Instrum.*, 44:695, 1973.
- [61] P. Horowitz and W. Hill. *The Art of Electronics, 2nd edition*, chapter 4: Feedback and Operational Amplifiers. Cambridge University Press, Cambridge, 1989.
- [62] S.V. Kravchenko and M.P. Sarachik. *Int. J. Mod. Phys. B*, 24:1640, 2010.
- [63] E. Abrahams, P.W. Anderson, D.C. Licciardello, and T.V. Ramakrishnan. *Phys. Rev. Lett.*, 42:673, 1979.
- [64] T.N. Zavaritskaya and E.I. Zavaritskaya. *JTEP Lett.*, 45:609, 1987.
- [65] S.V. Kravchenko, G.V. Kravchenko, J.E. Furneaux, V.M. Pudalov, and M. D'Iorio. *Phys. Rev. B*, 50:8039, 1994.
- [66] A. Punnoose and A.M. Finkel'stein. *Science*, 310:289, 2005.
- [67] N. Van Lien and D.D. Toi. *Phys. Lett. A*, 261:108, 1999.

- [68] S. Das Sarma and F. Stern. *Phys. Rev. B*, 32:8442, 1985.
- [69] For a more detailed treatment of electrons in a magnetic field, see J. H. Davies. *The Physics of Low-Dimensional Semiconductors*, chapter 6: Electric and Magnetic Fields. Cambridge University Press, 1998.
- [70] P.T. Coleridge, R. Stoner, and Fletcher R. *Phys. Rev. B*, 39:1120, 1989.
- [71] S. Ilani, J. Martin, E. Teitelbaum, J.H. Smet, D. Mahalu, V. Umansky, and A. Yacoby. *Nature*, 427:328, 2004.
- [72] For a review of Anderson localization in the context of the quantum Hall effect, see B. Huckestein. *Rev. Mod. Phys.*, 67:357, 1995.
- [73] B.I. Halperin. *Phys. Rev. B*, 25:2185, 1982.
- [74] S. Datta. *Electronic Transport in Mesoscopic Systems*. Cambridge University Press, New York, 1997.
- [75] D.G. Polyakov and B.I. Shklovskii. *Phys. Rev. Lett.*, 70:3796, 1993.
- [76] D.C. Tsui, H.L. Störmer, and A.C. Gossard. *Phys. Rev. B*, 25:1405, 1982.
- [77] G. Ebert, K. von Klitzing, C. Probst, E. Schubert, K. Ploog, and G. Weimann. *Solid State Commun.*, 45:625, 1983.
- [78] M.Z. Hasan and C.L. Kane. *Rev. Mod. Phys.*, 82:3045, 2010.
- [79] H. Bachmair, E.O. Göbel, G. Hein, J. Melcher, B. Schumacher, J. Schurr, L. Schweitzer, and P. Warecke. *Physica E*, 20:14, 2003.
- [80] S. Das Sarma and E.H. Hwang. *Phys. Rev. B*, 90:035425, 2014.
- [81] S.M. Girvin and M. Jonson. *J. Phys. C*, 15:L1147, 1982.
- [82] R. Shirasaki, A. Endo, N. Hatano, and H. Nakamura. *J. Electron. Mater.*, 41:1540, 2012.

- [83] X. Zianni, P.N. Butcher, and M.J. Kearney. *Phys. Rev. B*, 49:7520, 1994.
- [84] M. Jonson and S.M. Girvin. *Phys. Rev. B*, 29:1939, 1984.
- [85] P. Streda. *J. Phys.: Condens. Matter*, 1:1025, 1989.
- [86] L.W. Molenkamp, H. van Houten, C.W.J. Beenakker, R. Eppenga, and C.T. Foxon. *Phys. Rev. Lett.*, 65:1052, 1990.
- [87] H.v. Houten, L.W. Molenkamp, C.W.J. Beenakker, and C.T. Foxon. *Semicond. Sci. Technol.*, 7:B215, 1992.
- [88] H. Oji. *Phys. Rev. B*, 29:3148, 1984.
- [89] W. Zawadzki and R. Lassnig. *Surf. Sci.*, 142:225, 1984.
- [90] W.H. Press, S.A. Teukolsky, W.T. Vetterling, and B.P. Flannery. *Numerical Recipes in C*, chapter 9: Root Finding and Nonlinear Sets of Equations. Cambridge University Press, 1992.
- [91] R. Fletcher, M. D'Iorio, W.T. Moore, and R. Stoner. *J. Phys. C*, 21:2681, 1988.
- [92] S.K. Lyo. *Phys. Rev. B*, 40:6458, 1989.
- [93] K. Yang and B.I. Halperin. *Phys. Rev. B*, 79:115317, 2009.
- [94] A.M. Toxen. *Phys. Rev.*, 123:442, 1961.
- [95] R.B. Laughlin. *Phys. Rev. Lett.*, 50:1395, 1983.
- [96] F.D.M. Haldane. *Phys. Rev. Lett.*, 51:605, 1983.
- [97] B.I. Halperin. *Phys. Rev. Lett.*, 52:1583, 1984.
- [98] J.K. Jain. *Phys. Rev. Lett.*, 63:199, 1989.
- [99] J.K. Jain. *Composite Fermions*. Cambridge University Press, New York, 2007.
- [100] J.K. Jain and V.J. Goldman. *Phys. Rev. B*, 45:1255, 1992.

- [101] W. Pan, J.S. Xia, H.L. Störmer, D.C. Tsui, C. Vicente, E.D. Adams, N.S. Sullivan, L.N. Pfeiffer, K.W. Baldwin, and K.W. West. *Phys. Rev. B*, 77:075307, 2008.
- [102] B.I. Halperin, P.A. Lee, and N. Read. *Phys. Rev. B*, 47:7312, 1993.
- [103] R.L. Willet. *Semicond. Sci. Technol.*, 12:495, 1997.
- [104] For a review of experimental studies of CFs, see the chapter by H.L. Störmer and D.C. Tsui. *Perspectives in Quantum Hall Effects*. edited by S. Das Sarma and A. Pinczuk, Wiley, New York, 1997.
- [105] R.R. Du, H.L. Störmer, D.C. Tsui, L.N. Pfeiffer, and K.W. West. *Phys. Rev. Lett.*, 70:2944, 1993.
- [106] R.L. Willet, R.R. Ruel, K.W. West, and L.N. Pfeiffer. *Phys. Rev. Lett.*, 71:3846, 1993.
- [107] H.L. Störmer, A.S. Yeh, W. Pan, D.C. Tsui, L.N. Pfeiffer, K.W. Baldwin, and K.W. West. *Physica E*, 3:38, 1998.
- [108] W. Pan, H.L. Störmer, D.C. Tsui, L.N. Pfeiffer, K.W. Baldwin, and K.W. West. *Phys. Rev. Lett.*, 90:016801–1, 2003.
- [109] E. Wigner. *Phys. Rev.*, 46:1002, 1934.
- [110] P.K. Lam and S.M. Girvin. *Phys. Rev. B*, 30:473, 1984.
- [111] D. Levesque, J.J. Weis, and A.H. MacDonald. *Phys. Rev. B*, 30:1056, 1984.
- [112] H.W. Jiang, R.L. Willet, H.L. Störmer, D.C. Tsui, L.N. Pfeiffer, and K.W. West. *Phys. Rev. Lett.*, 65:633, 1990.
- [113] V.J. Goldman, M. Santos, M. Shayegan, and J.E. Cunningham. *Phys. Rev. Lett.*, 65:2189, 1990.
- [114] D.V. Khveshchenko. *Phys. Rev. B*, 54:14317, 1996.

- [115] V.C. Karavolas, G.P. Triberis, and F.M. Peeters. *Phys. Rev. B*, 56:15289, 1997.
- [116] V.C. Karavolas and G.P. Triberis. *Phys. Rev. B*, 65:033307, 2001.
- [117] M. Tsaousidou and G.P. Triberis. *Physica E*, 12:112, 2002.
- [118] V.C. Karavolas and G.P. Triberis. *Phys. Rev. B*, 66:155315, 2002.
- [119] M.R. Peterson and B.S. Shastry. *Phys. Rev. B*, 82:195105, 2010.
- [120] Y. Barlas and Yang K. *Phys. Rev. B*, 85:195107, 2012.
- [121] N. d'Ambrumenil and R.H. Morf. *Phys. Rev. Lett.*, 111:136805, 2013.
- [122] D.V. Khveshchenko. *Phys. Rev. Lett.*, 77:1817, 1996.
- [123] R.H. Morf, N. d'Ambrumenil, and S. Das Sarma. *Phys. Rev. B*, 66:075408, 2002.
- [124] A.S. Yeh, H.L. Störmer, D.C. Tsui, L.N. Pfeiffer, K.W. Baldwin, and K.W. West. *Phys. Rev. Lett.*, 82:592, 1999.
- [125] W.E. Chickering, J.P. Eisenstein, L.N. Pfeiffer, and K.W. West. *Phys. Rev. B*, 81:245319, 2010.
- [126] U. Zeitler, J.C. Maan, P. Wyder, R. Fletcher, C.T. Foxon, and J.J. Harris. *Phys. Rev. B*, 47:16008, 1993.
- [127] K. Park and J.K. Jain. *Phys. Rev. Lett.*, 80:4237, 1998.
- [128] W.E. Chickering, J.P. Eisenstein, L.N. Pfeiffer, and K.W. West. *Phys. Rev. B*, 87:075302, 2013.
- [129] P.A. Lee and A.D. Stone. *Phys. Rev. Lett.*, 55:1622, 1985.
- [130] F.P. Esposito, B. Goodman, and M. Ma. *Phys. Rev. B*, 36:4507, 1987.
- [131] B.L. Gallagher, T. Galloway, P. Beton, J.P. Oxley, S.P. Beaumont, S. Thoms, and C.D.W. Wilkinson. *Phys. Rev. Lett.*, 64:2058, 1990.

- [132] I.V. Kukushkin, K. von Klitzing, and K. Eberl. *Phys. Rev. Lett.*, 82:3665, 1999.
- [133] R.L. Willet, J.P. Eisenstein, H.L. Störmer, D.C. Tsui, A.C. Gossard, and J.H. English. *Phys. Rev. Lett.*, 59:1776, 1987.
- [134] B. Tieke, R. Fletcher, U. Zeitler, M. Henini, and J.C. Maan. *Phys. Rev. B*, 58:2017, 1998.
- [135] M.P. Lilly, K.B. Cooper, J.P. Eisenstein, L.N. Pfeiffer, and K.W. West. *Phys. Rev. Lett.*, 82:394, 1999.
- [136] R.R. Du, D.C. Tsui, H.L. Störmer, L.N. Pfeiffer, and West. K.W. *Solid State Commun.*, 109:389, 1999.
- [137] W. Pan, J.S. Xia, V. Shvarts, D.E. Adams, H.L. Störmer, D.C. Tsui, L.N. Pfeiffer, and West. K.W. *Phys. Rev. Lett.*, 83:3530, 1999.
- [138] J.P. Eisenstein, R.L. Willet, H.L. Störmer, L.N. Pfeiffer, and K.W. West. *Surf. Sci.*, 229:31, 1990.
- [139] For a review of non-Abelian statistics and their application to topological quantum computation, see C. Nayak, S.H. Simon, A. Stern, M. Freedman, and S. Das Sarma. *Rev. Mod. Phys.*, 80:1083, 2008.
- [140] J.P. Eisenstein, K.B. Cooper, L.N. Pfeiffer, and K.W. West. *Phys. Rev. Lett.*, 88:076801, 2002.
- [141] J.P. Eisenstein, H.L. Störmer, D.C. Tsui, A.C. Gossard, and J.H. English. *Phys. Rev. Lett.*, 61:997, 1988.
- [142] G.A. Csáthy, J.S. Xia, C.L. Vicente, E.D. Adams, N.S. Sullivan, H.L. Störmer, D.C. Tsui, L.N. Pfeiffer, and K.W. West. *Phys. Rev. Lett.*, 94:146801, 2005.
- [143] C.R. Dean, B.A. Piot, P. Hayden, S. Das Sarma, G. Gervais, L.N. Pfeiffer, and K.W. West. *Phys. Rev. Lett.*, 101:186806, 2008.

- [144] J.S. Xia, W. Pan, C.L. Vicente, E.D. Adams, N.S. Sullivan, H.L. Störmer, D.C. Tsui, L.N. Pfeiffer, K.W. Baldwin, and K.W. West. *Phys. Rev. Lett.*, 93:176809–1, 2004.
- [145] A.H. MacDonald, D. Yoshioka, and S.M. Girvin. *Phys. Rev. B*, 39:8044, 1989.
- [146] M. Greiter, X. Wen, and F. Wilczek. *Phys. Rev. Lett.*, 66:3205, 1991.
- [147] G. Moore and N. Read. *Nucl. Phys. B*, 360:362, 1991.
- [148] For a review of both Abelian and non-Abelian statistics in the context of the quantum Hall effect, see A. Stern. *Ann. Phys.*, 323:204, 2008.
- [149] J.M. Leinaas and J. Myrheim. *Nuovo Cimento*, 37B:1, 1977.
- [150] F. Wilczek. *Phys. Rev. Lett.*, 49:14, 1982.
- [151] D. Arovas, J.R. Schrieffer, and F. Wilczek. *Phys. Rev. Lett.*, 53:722, 1984.
- [152] N. Read and E. Rezayi. *Phys. Rev. B*, 59:8084, 1999.
- [153] E.H. Rezayi and N. Read. *Phys. Rev. B*, 79:075306, 2009.
- [154] A.Y. Kitaev. *Ann. Phys.*, 303:2, 2003.
- [155] M. Dolev, M. Heiblum, V. Umansky, A. Stern, and D. Mahalu. *Nature*, 452:829, 2008.
- [156] I.P. Radu, J.B. Miller, C.M. Marcus, M.A. Kastner, L.N. Pfeiffer, and K.W. West. *Science*, 320:899, 2008.
- [157] R.L. Willet, L.N. Pfeiffer, and K.W. West. *Proc. Natl. Acad. Sci.*, 106:8853, 2009.
- [158] R.L. Willet, L.N. Pfeiffer, and K.W. West. *Phys. Rev. B*, 82:205301, 2010.
- [159] A. Bid, N. Ofek, H. Inoue, M. Heiblum, C.L. Kane, V. Umansky, and D. Mahalu. *Nature*, 466:585, 2012.

- [160] X. Lin, C. Dillard, M.A. Kastner, L.N. Pfeiffer, and K.W. West. *Phys. Rev. B*, 85:165321, 2012.
- [161] N.R. Cooper and A. Stern. *Phys. Rev. Lett.*, 102:176807, 2009.
- [162] C.R. Dean, B.A. Piot, P. Hayden, S. Das Sarma, G. Gervais, L.N. Pfeiffer, and K.W. West. *Phys. Rev. Lett.*, 100:146803, 2008.
- [163] A.A. Koulokov, M.M. Fogler, and B.I. Shklovskii. *Phys. Rev. Lett.*, 76:499, 1996.
- [164] R. Moessner and J.T. Chalker. *Phys. Rev. B*, 54:5006, 1996.
- [165] E. Fradkin and S.A. Kivelson. *Phys. Rev. B*, 59:8065, 1999.
- [166] N. Deng, A. Kumar, M.J. Manfra, L.N. Pfeiffer, K.W. West, and G.A. Csáthy. *Phys. Rev. Lett.*, 108:086803, 2012.
- [167] P.M. Chaikin and G. Beni. *Phys. Rev. B*, 13:647, 1976.
- [168] B. Spivak and S.A. Kivelson. *Phys. Rev. B*, 70:155114, 2004.
- [169] H. Falakshahi and X. Waintal. *Phys. Rev. Lett.*, 94:046801, 2005.
- [170] C. Ashby and A. Baca. *Fabrication of GaAs Devices*. The Institution of Engineering and Technology, Sandia National Laboratories, New Mexico, 2005.
- [171] C.A. Stutt. Low frequency spectrum of lock-in amplifiers. Technical Report 105, Massachusetts Institute of Technology, March 1949.
- [172] J.C. Ho, H.R. O'Neal, and N.E. Phillips. *Rev. Sci. Instrum.*, 34:782, 1963.
- [173] H. van Zelingue, R.W. van der Heijden, and J.H. Wolter. *Phys. Rev. B*, 67:165311, 2003.
- [174] A. Kobayakawa, S. Endo and Y. Iye. *J. Phys. Soc. Jpn.*, 82:053702, 2013.